Development of Functional Iron-based Nanomaterials for Biomedical and Energy Conversion Applications

Yechuan Zhang

A thesis submitted for the degree of Doctor of Philosophy

School of Chemical Engineering and Advanced Materials

Faculty of Science, Engineering, and Technology

The University of Adelaide

September 2022

I dedicate this thesis to my parents Yuxia and Mingping,

My sister Zhu

My beloved wife Yan Xia,

And my lovely son Chenxi Zhang.

Table of Contents

Abstract

Iron-based nanomaterials, an important branch of nanomaterials, are widely investigated and applied in various fields. As an essential element in the human body, iron participates in a wide range of biological processes, including oxygen transport, electron transport, biomolecule synthesis, and deoxyribonucleic acid (DNA) synthesis, so iron-derived nanomaterials have the potential for biomedical applications. Iron is a transition metal element with unfilled 3d orbitals and different valence state. The above characteristics of iron allow the formation of stable compounds and facilitate the electron transfer. Thus, the iron-based nanomaterials could be used as electrochemical catalysts in energy conversion applications. However, the potential of iron-based nanomaterials in biomedical and energy conversion applications has not been fully explored.

In this thesis, a serial of iron-based nanomaterials including iron-based metal-organic frameworks (hollow MIL-100 (Fe) and PCN-333 (Fe)), iron-based oxyhydroxide ($MoFe_{0.5}O_xCo(OH)_{2-x}$), and iron-based sulfides ($FeCo(NiS_2)_4$-C/A) have been designed and synthesized. Hollow MIL-100 (Fe) reported in Chapter 3 exhibited a high doxorubicin loading capacity and a mitochondrial targeting ability in breast cancer treatment. In addition, a green synthetic method to obtain hollow structural MIL-100 (Fe) has been proposed and realized. Based on the findings of Chapter 3, hierarchical PCN-333 (Fe) with larger pores loading with horseradish peroxidase (HRP) and 3-Indoleacetic acid (IAA) has been developed in Chapter 4. In vitro and *in vivo* experiments supported that HRP and IAA loaded PCN-333 (Fe) nanoparticles (HRP/IAA@PCN-333 (Fe)) were effective in prodrug therapy (EAPT) of breast cancer. Molybdenum-Iron-Cobalt oxyhydroxide with rich oxygen vacancies reported in Chapter 5 exhibited excellent performance in oxygen evolution reaction (OER) by tuning the composition of iron in the compounds. Furthermore, based on the findings of Chapter 5, heterostructural Iron-Cobalt-Nickel sulfides with rich crystalline/amorphous interfaces have been synthesized in the work presented

Appendix by tuning the ratio of iron in the nanostructure and they exhibited remarkable performance as a bifunctional catalyst for water splitting.

Key words: Iron-based nanomaterials, drug delivery, cancer treatment, water splitting

Preface

This thesis is submitted as a 'Thesis by Publications' in accordance with 'Specifications for Thesis 2022' of The University of Adelaide. The journal articles are listed as follow.

List of Publications:

1*. **Y.C. Zhang**, Z.X. Gu, S.H. Yun, K. Luo, J.X. Bi, Y. Jiao, H. Zhang, Green synthesis of DOX-loaded hollow MIL-100 (Fe) nanoparticles for anticancer treatment by targeting mitochondria, Nanotechnology 33(34) (2022). (**IF=3.953**)

2*. **Y.C. Zhang**, Z.X. Gu, J.X. Bi, Y. Jiao, Molybdenum-iron–cobalt oxyhydroxide with rich oxygen vacancies for the oxygen evolution reaction, Nanoscale 14(30) (2022) 10873-10879. (**IF=8.307**)

3*. Z.X. Gu, **Y.C. Zhang**, X.L. Wei, Z.Y. Duan, L. Ren, J.C. Ji, X.Q. Zhang, Y.X. Zhang, Q.Y. Gong, H. Wu, K. Luo, Unveiling the Accelerated Water Electrolysis Kinetics of Heterostructural Iron-Cobalt-Nickel Sulfides by Probing into Crystalline/Amorphous Interfaces in Stepwise Catalytic Reactions. Adv. Sci. 2022, 2201903. (**IF=17.521**, listed in the Appendix)

4. Z.X. Wei, Z.X. Gu, **Y.C. Zhang**, K. Luo, S.L. Zhao, Phase-separated CuAg alloy interfacial stress induced Cu defects for efficient N_2 activation and electrocatalytic reduction, Applied Catalysis B: Environmental (2022) 121915. (**IF: 24.319**)

List of Prepared Manuscript Ready for Submission:

5*. **Y.C. Zhang,** J.X. Bi, K. Luo, H. Zhang, Y. Jiao, Recent Advances of Iron-based Nanomaterials in Various Application Fields. (Review Article)

Intended Journal for Submission: *Nanotechnology*.

List of Submitted Manuscript:

6*. **Y.C. Zhang,** Z.X. Gu, Z.Q. Li, K. Luo, H. Zhang, J.X. Bi, Y. Jiao, Efficient Cancer Therapy Through Conversion of Encapsulated Prodrug via Immobilized Enzyme in PCN-333 (Fe).

Submitted to *Nanoscale*.

*: Publication or Manuscript included in this thesis.

Thesis Declaration

I certify that this work contains no material which has been accepted for the award of any other degree or diploma in my name, in any university or other tertiary institution and, to the best of my knowledge and belief, contains no material previously published or written by another person, except where due reference has been made in the text.

In addition, I certify that no part of this work will, in the future, be used in a submission in my name, for any other degree or diploma in any university or other tertiary institution without the prior approval of the University of Adelaide and where applicable, any partner institution responsible for the joint award of this degree. The author acknowledges that copyright of published works contained within the thesis resides with the copyright holder(s) of those works.

I give permission for the digital version of my thesis to be made available on the web, via the University's digital research repository, the Library Search and also through web search engines, unless permission has been granted by the University to restrict access for a period of time.

Name: Yechuan Zhang

Signature: Date: 05/09/2022

Acknowledgement

First of all, I give my highest respect and appreciation for my principal supervisor Associate Professor Yan Jiao for her guidance and support both in academic and daily life, for her patience and encouragement when I did not make expected progress, also for her full understanding when I had difficulties due to COVID-19 quarantine and the separation from all my family members for a long time. I will always remember this valuable experience.

I also express my deepest gratitude to my co-supervisors Professor Hu Zhang and Professor Jingxiu Bi for their instructions and support during my candidature. Professor Hu Zhang gave me the chance to start my PhD journey, and gave me as much support as he can after his position change. Professor Jingxiu Bi supported me with her professional advice on my research project and her care during my hardest time.

I would like to thank Professor Bo Jin, Professor David Lewis, Professor Katrina Falkner, and Ms. Seaneen Hopps for their support during my PhD journey.

I would like to thank all group members, Dr. Seonho Yun, Dr. Jiabin Zhang, Dr. Bi Qi, Dr. Shuang Yin, Dr. Bingyang Zhang, Dr. Yiran Qu, Dr. Heng Wang, Dr. Pei Lay Yap Dr. Gule Li, Afshin karami, Dr. Foad Farivar, Nhat Hoang Huynh, and Thai Thao Ly, for their collaboration, support, and friendship during my PhD journey at the University of Adelaide.

I appreciate the University of Adelaide for giving me a chance and scholarship for PhD degree.

Lastly, I must give my greatest appreciation to my parents, my sister, my parents-in-law, my wife Yan Xia, and my son Chenxi Zhang for their endless love throughout my life. It is the love from the family that supported me when I feel depressed, and I will always cherish this love.

Chapter 1. Introduction

1.1 Background

Iron-based nanomaterials, an important category of nanomaterials, are widely employed in various application fields. As a fundamental element in human body, iron plays an important role in the blood system that facilitates the formation of hemoglobin and myoglobin, favouring the capacity of binding and storing oxygen.[1] Therefore, Fe-based nanomaterials with excellent biocompatibility have been developed for biomedical applications including drug delivery, enzyme immobilization, imaging, biosensing, etc.[2, 3] Iron, as one of the transition metal elements, its derived nanomaterials at a low cost with great stability have been extensively utilized as electrocatalysts for water splitting, carbon dioxide reduction, nitrogen reduction, etc.[4-7] Moreover, iron is commercially available, economical, nontoxic, and environment friendly compared to other metals (Cr, Co, Ni, etc.), which also extends the application potential including drug delivery, biocatalysts, water treatment, water splitting, hydrogen storage, and carbon dioxide capture.[8-12]

However, the potential of iron-based nanomaterials remains to be explored since the advantages of incorporating iron in nanomaterials have not been well taken, and the mechanism of how iron induces different nanostructures and functions is not fully understood. Consequently, it is vital to design and fabricate unique iron-based nanomaterials to meet the demand of different applications.

To date, iron-based nanomaterials with broad applications have drawn wide attention. Following groups including 1) iron-based metal-organic frameworks (MOFs), 2) iron-based oxides, 3) iron-based sulfides, and 4) other iron-based compounds have been extensively applied in biomedical and energy conversion fields. Iron-based nanomaterials, different from iron-containing nanomaterials, iron plays an important role in forming the fundamental structure and providing the function of nanomaterials. Metal-organic frameworks (MOFs) are an emerging class of highly ordered crystalline porous materials that consist of inorganic metal centers and organic ligands.[13-15] Over the past few decades, MOFs have drawn widespread attention due to their remarkable properties such as high surface area, high porosity, preferable stability, and tailored functionality.[16-18] Among MOFs, Fe-based MOFs

have been widely utilized for their high porosity, improved stability, biocompatibility, and chemical versatility.[19-21]

Iron-based oxides with magnetic properties are commonly used as magnetic resonance imaging agents in diagnostics, also as heat mediator for the treatment of hyperthermia.[22] Additionally, iron-based oxides can be employed as drug carriers for cancer treatment due to their magnetic targeting function.[23] The multifunctional iron-based oxides resulting from the coupling with organic materials (e.g., polymers, liposomes, and micelles) have also been investigated in various phases of clinical trials of biomedical fields.[24] Moreover, with the incorporation of other metals, iron oxides can be nanostructured to form bimetallic and trimetallic oxides with superior performance in electrocatalysis.[2] Iron in the bimetallic oxides and trimetallic oxides for electrocatalysis commonly functions as an enhancer of conductivity.[25] Functions and corresponding mechanisms of iron in hybrid iron-based oxides nanomaterials require to be explored.

Iron-based sulfides nanomaterials, possessing a smaller band gap, have been studied in both energy and biomedical fields for their capabilities in electron transfer and conductivity, since they have active sites for both biological reactions and electrochemical reactions.[26-28] Iron-based sulfides can be simply categorized into three groups: simple iron sulfides, iron sulfides with different moieties, and multi-metallic sulfides generated from iron sulfides. Iron sulfides mainly comprise FeS, $Fe_{1-x}S$, FeS_{2p}, Fe_3S_4, and Fe_9S_{11}. Nanosized iron sulfides with different properties (magnetic properties, photothermal properties, etc.) and have been demonstrated with the potential in various application fields including biocatalysis, biosensing, electrocatalysis, antibacterial infection, and antitumor treatment.[3] Iron sulfides with modifications are achieved by incorporating moieties including polyethylene glycol (PEG), silica, lactose, citrate, dextran, etc. The incorporated biocompatible moieties are essential since they work as caps for nanomaterials. Multi-metallic iron-based sulfides possess the advantages of the incorporated other metal elements, which include stability and durability in acidic/alkaline solutions, conductivity, applicable morphologies, magnetism, high porosity, sulfur vacancies, and more active sites for catalysis.[29]

Therefore, multi-metallic iron-based sulfides have been widely used as drug carriers, biosensors, semi-conductors, water splitting electrodes, carbon dioxide reduction catalysts, etc.[30] In addition to the above stated iron-based nanomaterials, other categories such as iron selenide, iron nitride, and iron phosphide own different advantages over others.[31-33]

Nevertheless, the limited pore size of iron-based MOFs restrains their drug loading capacity and further application of large biological molecules delivery for cancer treatment. The stability of iron-based oxyhydroxides and sulfides also limited their performance as HER/OER catalysts. Therefore, it is of vital importance to fully understand the mechanism of iron to play its role in iron-based nanomaterials for various applications. The present thesis will focus on exploring the potential of iron-based nanomaterials in multiple application fields by rationally designing these nanomaterials and synthesizing them with facile methods.

1.2 Aims and objectives

The present thesis aims to design and develop nanostructured iron-based nanomaterials catering to specific applications, and investigate the function induced by the nature of iron (e.g., electrons in 3d orbital). Based on experimental results, general principles of designing Fe-based nanomaterials for biomedical applications and electrochemical catalysis will be concluded. The detailed objectives are:

1. To optimize the synthetic method of Fe-based MOFs by following green chemistry principles, avoiding the employment of toxic organic solvents, and decreasing the energy consumption;
2. To fabricate hollow MIL-100 (Fe) with great biocompatibility to increase the drug loading capacity of Fe-based MOFs, and achieve tumor targeting function simultaneously;
3. To develop an enzyme-triggering prodrug derived from Fe-based MOFs with large cavities. The enzyme is immobilized in the cavities of the MOFs and the drug incorporated in the pores of MOFs. The enzyme is triggered in the tumor

microenvironment for the catalysis of the prodrug, effectively releasing the free drug to kill breast cancer cells;

4. To design and synthesize Fe-based oxides with excellent stability and catalytic performance for oxygen evolution reaction of water splitting, and the mechanism of how iron facilitates the electrochemical reactions will be unveiled;
5. To design and obtain an optimal bifunctional electrocatalyst for overall splitting based on Fe-based sulfides with remarkable stability and catalytic activity, and reveal the role of iron in the electrodes.

1.3 Thesis outline

The present thesis consists of seven chapters. All chapters and connections between them are presented in Figure 1.1. Chapter 1 introduces the Fe-based nanomaterials and their broad applications. After describing the research gap, aims and objectives are illustrated. Thesis outline and key contributions of this thesis are also exhibited. Chapter 2 reviews recent advances of Fe-based nanomaterials in a variety of applications as well as the design principles of Fe-based nanomaterials catering to different applications. Chapter 3 provides a green synthesis method for fabricating a hollow Fe-based MOF (MIL-100 (Fe)) for loading anticancer drug (doxorubicin) with the mitochondrial targeting function, improving the drug loading capacity of MOF-based drug carriers. The therapeutic effect against human breast cancer by doxorubicin-loaded hollow MIL-100 (Fe) is demonstrated to be potent from in vitro studies. The function and mechanism of Fe^{2+} in the crystallization process of hollow MIL-100 (Fe) are also investigated. Chapter 4 proposes PCN-333 (Fe) as a carrier for horseradish peroxidase (HRP) immobilization and 3-indoleacetic acid (IAA) loading due to its hierarchical mesoporous structure to prepare an IAA prodrug. HRP catalyzes hydrogen peroxide in the tumor microenvironment and the prodrug IAA into reactive oxygen species (ROS) to effectively inhibit the growth of breast cancer cells. The therapeutic effect of HRP and IAA-loaded PCN-333 (Fe) is evaluated from both in vitro and *in vivo* experiments. The mechanism of the catalytic function of Fe^{3+} is also discussed in this chapter. Chapter 5 develops a novel trimetallic FeCoMo oxide as an electrocatalyst for

oxygen evolution reaction (OER), which is an important reaction of water electrolysis. The nanostructured FeCoMo oxide exhibits a nanotube morphology and provides abundant pores for the adsorption of water molecules. Work presented in the Appendix designs a trimetallic FeCoNi sulfide with sulfur vacancies and crystalline/amorphous interfaces (CAI) as a bifunctional water splitting electrocatalyst, which facilitates both hydrogen evolution reaction (HER) and OER to efficiently obtain renewable energy. The function of CAI induced by the etching effect of iron is also investigated by computational simulations to verify the conclusion drawn from the experimental results. The work in Appendix optimizes the previous catalyst in Chapter 5 and further improves the electrocatalytic performance for overall water splitting. Chapter 6 concludes key scientific contributions of the present thesis, and describes the prospects of these Fe-based nanomaterials based on this thesis.

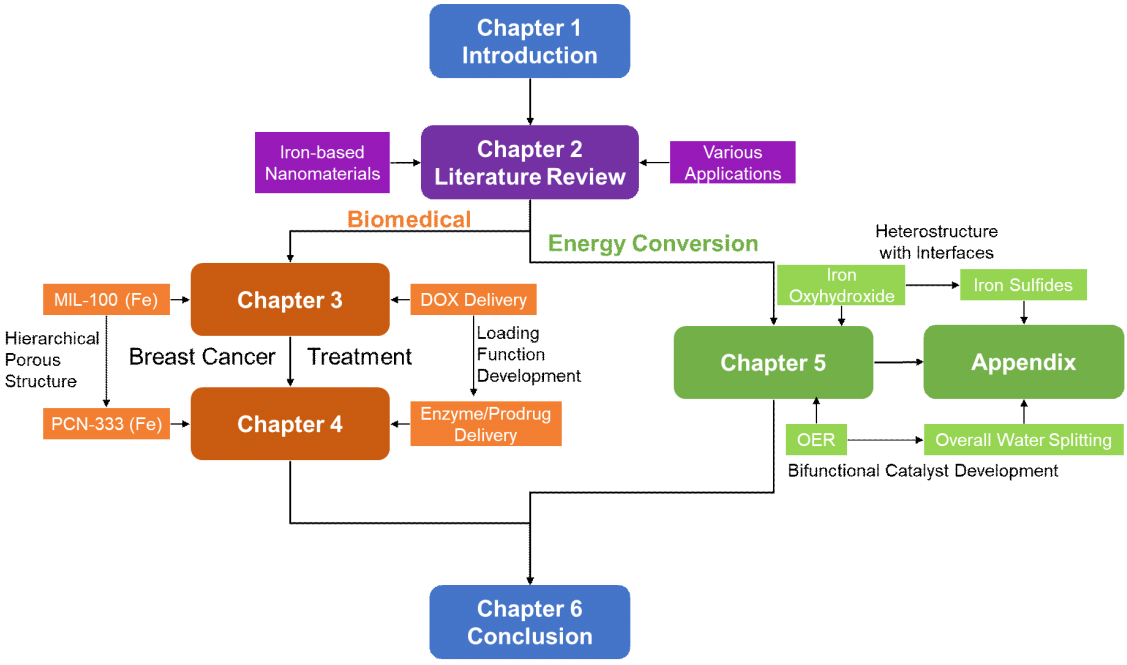

Figure 1.1 Flow chart of all chapters and connections between them.

1.4 Key contributions of this thesis

Synthetic methods of iron-based nanomaterials, namely the green synthesis method for hollow MOFs (MIL-100 (Fe), PCN-333 (Fe)), and the cation exchange method for triple-transition-metal nanotubes (FeCoMo oxyhydroxide, FeCoNi sulfides), were developed. The research outcomes contribute to the development of nanostructured functional iron-based nanomaterials for various applications, addressing the issues associated with anticancer drug delivery, enzyme immobilization, prodrug premature activation, oxygen evolution reaction, and over all water splitting. Detailed key contributions are presented as follows:

1. Hollow MIL-100 (Fe) was fabricated by a green synthetic method. The doxorubicin loading capacity was optimized to 30% and the drug-loaded MIL-100 (Fe) effectively inhibiting the growth of breast cancer cells (MDA-MB-231) through mitochondrial targeting.
2. The therapeutic effect of horseradish peroxidase and 3-indoleacetic acid-loaded PCN-333 (Fe) was found to be effective from *in vivo* experiments, confirming the feasibility of employing hierarchical iron-based MOFs as carriers for enzyme immobilization and drug encapsulation for breast cancer treatment.
3. A facile and robust cation exchange methodology was developed to synthesize a trimetallic (Fe, Mo, Co) oxyhydroxide nanotube with enriched oxygen vacancies and active metal centers for OER. The catalytic performance of the obtained catalyst was comparable to the current reported OER catalysts. The doping effect of iron and molybdenum was probed to improve the catalytic performance. This method was demonstrated to be feasible in obtaining an economical electrocatalyst with excellent performance for OER and the function and mechanism of the doping effect induced by iron and molybdenum in trimetallic oxyhydroxides were discovered.
4. A heterostructural trimetallic sulfide (Fe, Ni, Co) was developed with crystalline/amorphous interfaces and abundant active sites to perform as a bifunctional electrocatalyst for water electrolysis via a simple cation exchange route, and the mechanism of the etching effect induced by iron for the formation of crystalline/amorphous interfaces and sulfur vacancies was revealed.

Reference:

[1] N. Abbaspour, R. Hurrell, R. Kelishadi, Review on iron and its importance for human health, J Res Med Sci 19(2) (2014) 164-174.
[2] A. Figuerola, R. Di Corato, L. Manna, T. Pellegrino, From iron oxide nanoparticles towards advanced iron-based inorganic materials designed for biomedical applications, Pharmacol Res 62(2) (2010) 126-143.
[3] Y. Yuan, L.P. Wang, L.Z. Gao, Nano-Sized Iron Sulfide: Structure, Synthesis, Properties, and Biomedical Applications, Front Chem 8 (2020).
[4] Y.Y. Wang, D.D. Liu, Z.J. Liu, C. Xie, J. Huo, S.Y. Wang, Porous cobalt-iron nitride nanowires as excellent bifunctional electrocatalysts for overall water splitting, Chem Commun 52(85) (2016) 12614-12617.
[5] J.H. Yu, G.Z. Cheng, W. Luo, Ternary nickel-iron sulfide microflowers as a robust electrocatalyst for bifunctional water splitting, J Mater Chem A 5(30) (2017) 15838-15844.
[6] R.L. Cheng, E. Debroye, J. Hofkens, M.B.J. Roeffaers, Efficient Photocatalytic CO2 Reduction with MIL-100(Fe)-CsPbBr3 Composites, Catalysts 10(11) (2020).
[7] X.W. Wang, Y.Y. Zhao, L.Q. Wang, W. Peng, J.M. Feng, D.J. Li, B.J. Su, J.Y. Juang, Y.F. Ma, Y.P. Chen, F. Hou, S. Zhou, H.K. Liu, S.X. Dou, J. Liu, J. Liang, Regulating the Electronic Configuration of Supported Iron Nanoparticles for Electrochemical Catalytic Nitrogen Fixation, Adv Funct Mater (2022).
[8] Z.F. Wu, N. Hao, H. Zhang, Z.Y. Guo, R. Liu, B. He, S. Li, Mesoporous iron-carboxylate metal-organic frameworks synthesized by the double-template method as a nanocarrier platform for intratumoral drug delivery, Biomater Sci-Uk 5(5) (2017) 1032-1040.
[9] M.J. Pu, Z.Y. Guan, Y.W. Ma, J.Q. Wan, Y. Wang, M.L. Brusseau, H.Y. Chi, Synthesis of iron-based metal-organic framework MIL-53 as an efficient catalyst to activate persulfate for the degradation of Orange G in aqueous solution, Appl Catal a-Gen 549 (2018) 82-92.
[10] Y.K. Seo, J.W. Yoon, J.S. Lee, U.H. Lee, Y.K. Hwang, C.H. Jun, P. Horcajada, C. Serre, J.S. Chang, Large scale fluorine-free synthesis of hierarchically porous iron(III) trimesate MIL-100(Fe) with a zeolite MTN topology, Micropor Mesopor Mat 157 (2012) 137-145.
[11] S. Zhang, Y. Zhang, F. Baig, T.F. Liu, Synthesis and Applications of Stable Iron-Based Metal-Organic Framework Materials, Cryst Growth Des 21(5) (2021) 3100-3122.
[12] F. Zhou, X. Zhang, R.J. Sa, S. Zhang, Z.H. Wen, R.H. Wang, The electrochemical overall water splitting promoted by MoS 2 in coupled nickel iron (oxy)hydride/molybdenum sul fide/graphene composite, Chem Eng J 397 (2020).
[13] T. Simon-Yarza, M. Gimenez-Marques, R. Mrimi, A. Mielcarek, R. Gref, P. Horcajada, C. Serre, P. Couvreur, A Smart Metal-Organic Framework Nanomaterial for Lung Targeting, Angew Chem Int Edit 56(49) (2017) 15565-15569.
[14] X.C. Liu, Y.Y. Zhou, J.C. Zhang, L. Tang, L. Luo, G.M. Zeng, Iron Containing Metal-Organic Frameworks: Structure, Synthesis, and Applications in Environmental Remediation, Acs Appl Mater Inter 9(24) (2017) 20255-20275.

[15] S.L. Zhao, Y. Wang, J.C. Dong, C.T. He, H.J. Yin, P.F. An, K. Zhao, X.F. Zhang, C. Gao, L.J. Zhang, J.W. Lv, J.X. Wang, J.Q. Zhang, A.M. Khattak, N.A. Khan, Z.X. Wei, J. Zhang, S.Q. Liu, H.J. Zhao, Z.Y. Tang, Ultrathin metal-organic framework nanosheets for electrocatalytic oxygen evolution, Nat Energy 1 (2016) 1-10.
[16] A. Dhakshinamoorth, A.M. Asiri, H. Garcia, 2D Metal-Organic Frameworks as Multifunctional Materials in Heterogeneous Catalysis and Electro/Photocatalysis, Adv Mater 31(41) (2019).
[17] E. Bellido, T. Hidalgo, M.V. Lozano, M. Guillevic, R. Simon-Vazquez, M.J. Santander-Ortega, A. Gonzalez-Fernandez, C. Serre, M.J. Alonso, P. Horcajada, Heparin-Engineered Mesoporous Iron Metal-Organic Framework Nanoparticles: Toward Stealth Drug Nanocarriers, Adv Healthc Mater 4(8) (2015) 1246-1257.
[18] D.W. Feng, Z.Y. Gu, Y.P. Chen, J. Park, Z.W. Wei, Y.J. Sun, M. Bosch, S. Yuan, H.C. Zhou, A Highly Stable Porphyrinic Zirconium Metal-Organic Framework with shp-a Topology, J Am Chem Soc 136(51) (2014) 17714-17717.
[19] M.Y. Ma, H. Noei, B. Mienert, J. Niesel, E. Bill, M. Muhler, R.A. Fischer, Y.M. Wang, U. Schatzschneider, N. Metzler-Nolte, Iron MetalOrganic Frameworks MIL-88B and NH2-MIL-88B for the Loading and Delivery of the Gasotransmitter Carbon Monoxide, Chem-Eur J 19(21) (2013) 6785-6790.
[20] B.Q. Yuan, X. Wang, X. Zhou, J. Xiao, Z. Li, Novel room-temperature synthesis of MIL-100(Fe) and its excellent adsorption performances for separation of light hydrocarbons, Chem Eng J 355 (2019) 679-686.
[21] A. Lajevardi, M.H. Sadr, M.T. Yaraki, A. Badiei, M. Armaghan, A pH-responsive and magnetic Fe3O4@silica@MIL-100(Fe)/beta-CD nanocomposite as a drug nanocarrier: loading and release study of cephalexin, New J Chem 42(12) (2018) 9690-9701.
[22] J. Qi, W. Zhang, R.J. Xiang, K.Q. Liu, H.Y. Wang, M.X. Chen, Y.Z. Han, R. Cao, Porous Nickel-Iron Oxide as a Highly Efficient Electrocatalyst for Oxygen Evolution Reaction, Adv Sci 2(10) (2015).
[23] P.C. Nagajyothi, M. Pandurangan, D.H. Kim, T.V.M. Sreekanth, J. Shim, Green Synthesis of Iron Oxide Nanoparticles and Their Catalytic and In Vitro Anticancer Activities, J Clust Sci 28(1) (2017) 245-257.
[24] F.Q. Yu, L. Zhang, Y.Z. Huang, K. Sun, A.E. David, V.C. Yang, The magnetophoretic mobility and superparamagnetism of core-shell iron oxide nanoparticles with dual targeting and imaging functionality, Biomaterials 31(22) (2010) 5842-5848.
[25] J.W. Jang, C. Du, Y.F. Ye, Y.J. Lin, X.H. Yao, J. Thorne, E. Liu, G. McMahon, J.F. Zhu, A. Javey, J.H. Guo, D.W. Wang, Enabling unassisted solar water splitting by iron oxide and silicon, Nat Commun 6 (2015).
[26] S. Rahimi, S. Shahrokhian, H. Hosseini, Ternary nickel cobalt iron sulfides ultrathin nanosheets grown on 3-D nickel nanocone arrays-nickel plate current collector as a binder free electrode for fabrication of highly performance supercapacitors, J Electroanal Chem 810 (2018) 78-85.
[27] T. Kinner, K.P. Bhandari, E. Bastola, B.M. Monahan, N.O. Haugen, P.J. Roland, T.P. Bigioni, R.J. Ellingson, Majority Carrier Type Control of Cobalt Iron Sulfide

(CoxFe1-xS2) Pyrite Nanocrystals, J Phys Chem C 120(10) (2016) 5706-5713.
[28] Y.Y. Gong, J.C. Tang, D.Y. Zhao, Application of iron sulfide particles for groundwater and soil remediation: A review, Water Res 89 (2016) 309-320.
[29] A.M.K. Pasha, M. Hosseini, A. Fakhri, V.K. Gupta, S. Agarwal, Investigation of photocatalytic process for iron disulfide-bismuth oxide nanocomposites by using response surface methodology: Structural and antibacterial properties, J Mol Liq 289 (2019).
[30] S. Thinunaran, G. Gurumoorthy, R. Arulmozhi, S. Ciattini, Synthesis of nickel sulfide and nickel-iron sulfide nanoparticles from nickel dithiocarbamate complexes and their photocatalytic activities, Appl Organomet Chem 34(9) (2020).
[31] Y. Huang, L.W. Jiang, B.Y. Shi, K.M. Ryan, J.J. Wang, Highly Efficient Oxygen Evolution Reaction Enabled by Phosphorus Doping of the Fe Electronic Structure in Iron-Nickel Selenide Nanosheets, Adv Sci 8(18) (2021).
[32] B. Zhang, C.H. Xiao, S.M. Xie, J. Liang, X. Chen, Y.H. Tang, Iron-Nickel Nitride Nanostructures in Situ Grown on Surface-Redox-Etching Nickel Foam: Efficient and Ultrasustainable Electrocatalysts for Overall Water Splitting, Chem Mater 28(19) (2016) 6934-6941.
[33] L.H. Tian, X.D. Yan, X.B. Chen, Electrochemical Activity of Iron Phosphide Nanoparticles in Hydrogen Evolution Reaction, Acs Catal 6(8) (2016) 5441-5448.

Chapter 2. Recent Advances of Iron-based Nanomaterials in Biomedical and Energy conversion Fields.

2.1 Introduction and Commentary

Chapter 2 is the literature review that focuses on the various applications of iron-based nanomaterials including iron-based metal-organic frameworks (MOFs), iron-based oxides, iron-based sulfides. This literature review summarizes the advantages of different iron-based nanomaterials and their performance mainly in biomedical and energy conversion fields. The research gap related to the synthesis and nanostructure modification of iron-based nanomaterials is also illustrated.

2.2 Manuscript

This section is presented as the prepared manuscript.

Statement of Authorship

Title of Paper	Recent Advances of Iron-based Nanomaterials in Various Application Fields
Publication Status	☐ Published ☐ Accepted for Publication ☐ Submitted for Publication ☑ Unpublished and Unsubmitted work written in manuscript style
Publication Details	Ready for submission to Nanotechnology.

Principal Author

Name of Principal Author (Candidate)	Yechuan Zhang		
Contribution to the Paper	Did the literature review and wrote the manuscript.		
Overall percentage (%)	90%		
Certification:	This paper reports on original research I conducted during the period of my Higher Degree by Research candidature and is not subject to any obligations or contractual agreements with a third party that would constrain its inclusion in this thesis. I am the primary author of this paper.		
Signature		Date	09/05/2022

Co-Author Contributions

By signing the Statement of Authorship, each author certifies that:

i. the candidate's stated contribution to the publication is accurate (as detailed above);

ii. permission is granted for the candidate in include the publication in the thesis; and

iii. the sum of all co-author contributions is equal to 100% less the candidate's stated contribution.

Name of Co-Author	Hu Zhang		
Contribution to the Paper	Modified the manuscript.		
Signature		Date	09/05/2022

Name of Co-Author	Jingxiu Bi		
Contribution to the Paper	Modified the manuscript.		
Signature		Date	09/05/2022

Name of Co-Author	Kui Luo		
Contribution to the Paper	Modified the manuscript.		
Signature		Date	09/05/2022

Name of Co-Author	Yan Jiao		
Contribution to the Paper	Modified the manuscript.		
Signature		Date	09/05/2022

Please cut and paste additional co-author panels here as required.

Recent Advances of Iron-based Nanomaterials in Various Application Fields

Yechuan Zhang[1],Jingxiu Bi[1], Kui Luo[2], Hu Zhang[3], Yan Jiao[1]*

[1]*School of Chemical Engineering and Advanced Materials, University of Adelaide, SA 5005, Australia*
[2]*Huaxi MR Research Center (HMRRC), Department of Radiology, National Clinical Research Center for Geriatrics, Frontiers Science Center for Disease-Related Molecular Network, State Key Laboratory of Biotherapy, West China Hospital, Sichuan University, Chengdu 610041, China*
[3] *Riggs School of Applied Life Sciences, Keck Graduate Institute, CA 91711, USA*
[*]*Corresponding Authors.*
E-mail address: luokui@scu.edu.cn; jingxiu.bi@adelaide.edu.au; yan.jiao@adelaide.edu.au; hu_zhang@kgi.edu

Received xxxxxx
Accepted for publication xxxxxx
Published xxxxxx

Abstract

Iron-based nanomaterials have captured considerable attention owing to their intriguing architectures and multifarious functions. Iron-based nanomaterials are a broad concept including iron-based metal-organic frameworks (MOFs), iron-based oxides, iron-based sulfides, etc. In the present review, branches of iron-based nanomaterials are categorized and discussed in terms of various applications. Studying the advantages of iron-based nanomaterials based on their structures and moieties can contribute to understanding the designing principles of iron-based nanomaterials. The present study aims to provide prospects to explore the potential of iron-based nanomaterials for more practical applications with better performance.

1. Introduction

Iron, an earth-abundant element, is commercially available, non-toxic, and environment friendly. As one of the transition metals, iron plays an important role in constructing electrochemical catalysts due to the advantages of stability and electron transfer. Among all metals frequently applied in the biomedical field, Fe has the highest oral lethal dose of 30 g kg^{-1} over others (350 μg kg^{-1} for Zn, 4.1 g kg^{-1} for Zr, 1.5 g kg^{-1} for Mn, 8.1 g kg^{-1} for Mg, and 25 g kg^{-1} for Cu).[1] Moreover, iron is an essential element in human body as it participates in a wide range of metabolic processes, including oxygen transport, electron transport, biomolecule synthesis, and deoxyribonucleic acid (DNA) synthesis, endowing it with the potential of biomedical applications.[1] Therefore, iron-based nanomaterials are widely studied and applied in various fields including gas storage, sensing, energy conversion, catalysis, biomedical field, etc. Iron-based nanomaterials are one of the most vital categories among all kinds of nanomaterials due to their diversity and versatility. Based on the extensive application of iron-based

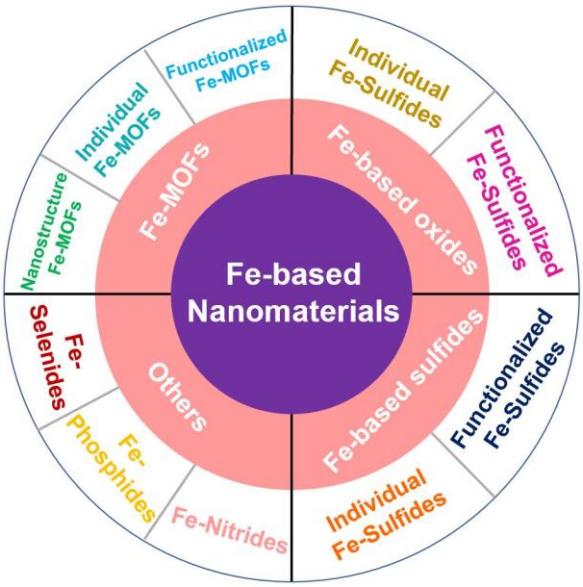

Figure 1. Scheme of the categories of Fe-based nanomaterials in the present work.

nanomaterials in recent years, this work categorizes iron-based nanomaterials into Fe-based MOFs, Fe-based oxides, Fe-based sulfides, and other Fe-based compounds (nitride, phosphide, and selenide). However, the performance of iron-based nanomaterials in both drug delivery and water splitting catalysis applications still requires improvement. For instance, the drug loading capacity of the-state-of-the-art iron-based nanomaterials regarding doxorubicin is 20%. Moreover, the composition and structure of multifunctional iron-based nanomaterials for cancer treatment is complicated, which usually involves other moieties such as hyaluronic acid to achieve tumor targeting function.

This work discusses the branches of each kind of iron-based nanomaterials (Figure 1) and the corresponding properties and advantages. The relationship between the properties of each kind of Fe-based nanomaterials and their applicable directions are also illustrated. It gives an overview regarding the development of iron-based nanomaterials in different application fields. The state-of-the-art iron-based nanomaterials applied in various applications are also introduced.

2. Fe-based MOFs

Fe-based Metal-Organic Frameworks (MOFs) are widely utilized due to their great biocompatibility, favorable stability, and ultrahigh porosity. Metal-Organic Frameworks, an emerging class of highly ordered crystalline porous materials that are composed of metal centers and organic ligands, are widely investigated due to their remarkable properties such as a high surface area, ultrahigh porosity, a hierarchical porous structure, remarkable stability, and various functionalities.[2, 3] Proper selection of metal centers and organic ligands allows different applications of MOFs, including gas adsorption, catalysis, sensing, molecular sieving, and a variety of biomedical applications.[4-6]

The key feature of MOFs is their stability in maintaining

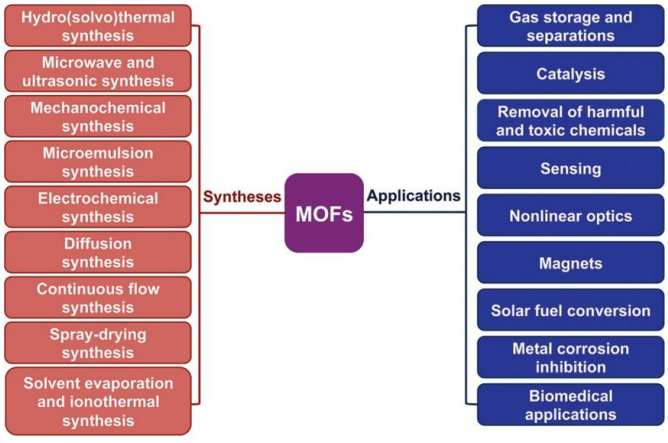

Figure 2. Scheme of the syntheses and applications of MOFs. Reused with permissions.[8] Copyright 2017, WILEY-VCH Verlag GmbH & Co. KGaA, Weinheim.

an ordered porous structure thus, their characteristic properties and functions are unchanged during their application (Figure 2).[7] MOFs exhibit their stability in various conditions including high temperature, high pressure, organic solvents, aqueous solution, corrosive media, etc.[8] Among all kinds of MOFs, Fe-based MOFs draw widespread attention due to their high porosity, tunable structure, and chemical stability and versatility.[9] Fe^{3+} is a strong Lewis acid, and the commonly applicable carboxylate ligand in MOFs is a Lewis base, thus Fe-based MOFs are stable in organic solvents or aqueous solutions. In contrast with traditional zeolite porous materials, Fe-based MOFs have posed various advantages for different applications, for example, they can be applied in the catalysis as catalysts due to their chemical stability in aqueous acidic or alkaline environments; they are employed as drug delivery carriers in biomedical applications due to their excellent stability in an aqueous solution to maintain a longer circulation for a better therapeutic effect.

2.1 Individual Stable MOFs

Unmodified Fe-MOFs are Fe-MOFs synthesized simply by Fe ions and organic ligands without any componential or structural modifications. Stability of Fe-MOFs is a key property that enables them with the potential in multiple applications. Industrial production cannot completely avoid water and moisture, and applications such as catalysis have a high demand for the chemical stability of catalysts in aqueous acidic or alkaline environment. Biomedical applications such as drug delivery require an excellent stability of carriers in aqueous solution in order to maintain a longer circulation for better therapeutic effect.

MOF-5, an important milestone in the MOF research, but it gradually disintegrates when it is exposed to water and moisture. Previous studies have demonstrated that the strength of coordination bonds in MOFs is an important factor for stabilizing the frame structure. According to Hard Soft Acids Bases (HSAB) concept, stable MOFs with strong coordination bonds can be constructed from high-valent metal ions and carboxylate-based ligands. Fe ions are high-valent metal ions, thus Fe-MOFs constructed from carboxylate-based ligands usually possess excellent stability (Table 1).

MIL series can switch the size of pores under certain external conditions (breathing effect), for example, the adsorption of molecules, the change of pressure, the fluctuation of temperature, etc. Férey et al. first developed the MIL series (MIL-53, MIL-88, MIL-100, MIL-101) MOFs using Al^{3+}, Fe^{3+}, and Cr^{3+}. MIL-53 (Fe) and MIL-100 (Fe) showed preferable stability in aqueous solution with pH of 2 to 12 (Figure 3).[10-14] MIL-101 (Fe) and other dicarboxylate-based Fe-MOFs may encounter the issue of stability under certain hydrothermal conditions. Jiang et al.

investigated MIL-53 (Fe) as a colorimetric biosensor due to its intrinsic peroxidase-like catalytic activity.[10] MIL-53 (Fe) can catalyze the oxidation process of peroxidase substrates (TMB=3,3′,5,5′-tetramethylbenzidine, OPD=*o* phenylenediamine) in the presence of hydrogen peroxide, exhibiting different colors after the catalytic reactions of different substrates.

Table 1. Examples of individual stable Fe-MOFs for various applications.

Individual Stable Fe-MOFs			
MOFs	Major Components	Application	Reference
MIL-53 (Fe)	Fe^{3+}, 1,4-BDC	Colorimetric biosensor	[10]
		Bifunctional photocatalyst for Cr^{4+}	[11]
		Ibuprofen delivery	[12]
		DOX physisorption and delivery	[13]
MIL-100 (Fe)	Fe^{3+}, 1,3,5-BTC	selective catalytic reduction of NO_x	[14]
		H_2S conversion	[15]
		AZT-TP, CDV, and DOXdelivery	[16]
MOF-74-Fe (III)	Oxidation from MOF-74-Fe (II)	Positive charged drug carrier for ibuprofen anions with high drug loading capacity	[17]
PCN-333 (Fe)	Fe^{3+}, H_3TATB	Synthetic template for PCN-333 (Cr)	[19]
		Dual exchange for PCN-333 (Cr)	[20]
		Enzyme encapsulation	[21]
PCN-426 (Fe)	Fe^{3+}, TMQPTC	Ion exchange methodology exploration	[22]
PCN-223 (Fe)	Fe^{3+}, H_2TCPP	Heterogeneous catalyst for the hetero-Diels–Alder reaction	[23]

Wu and co-workers employed MIL-53 (Fe) as a bifunctional photocatalyst for Cr^{4+} reduction and dye oxidation for its excellent photocatalytic activity under visible light ($\lambda \geq 420$ nm), proved the potential of MIL-53 (Fe) as a candidate for waste water treatment.[11] Moreover, Horcajada et al. also demonstrated the feasibility of applying MIL-53 (Fe) for ibuprofen delivery with the drug loading capacity up to 20 wt%, proving the amount of loaded drug does not depend on the metal centers of the crystalline framework.[12] Controllable-size MIL-53 (Fe) was also developed with the assistance of non-ionic surfactant PVP as the conditioning agent for doxorubicin physisorption and delivery.[13] MIL-100 (Fe), another stable porous MOF of MIL series with a larger pore size, has been proved its potential in catalysis and biomedical applications. Quan et al. utilized MIL-100 (Fe) for selective catalytic reduction of

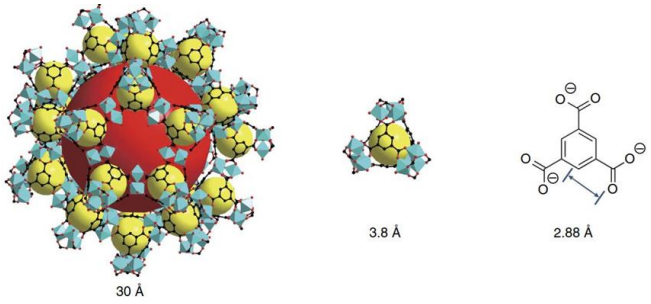

Figure 3. The largest cage, super tetrahedral unit and organic linker in MIL-100.[21] Reused with permission. Copyright 2015, Macmillan Publishers Limited.

NO_x, in which intermediate NH^{4+} reacts with NO_2 formed via NO oxidation over Fe sites. Redox properties of Fe species (Fe^{3+} + e^- ↔ Fe^{2+}) using MIL-100 (Fe) as catalyst could activate reactants in the NO_x reduction process.[14] Coordinatively unsaturated (CUS) Fe^{2+}/Fe^{3+} ions in MIL-100 (Fe) were investigated by researchers as active sites for H_2S conversion with an extreme high conversion rate and S selectivity (100%, 95.1%), which is superior to that of commercial Fe_2O_3 (42.6%, 19.4%).[15] To address the issue of a low drug loading capacity of traditional drug carriers such as micelles and vesicles, Horcajada et al. studied a series of non-toxic porous iron (III)-based MOFs to employ their high surface area and porosity for improving the loading capacity of azidothymidine triphosphate (AZT-TP), cidofovir (CDV) and doxorubicin (DOX). MIL-100 (Fe) exhibited a high loading capacity of 10.8 wt% towards DOX and sustained release up to 14 days, thus iron (III)-carboxylate ligand MOFs could be used as drug carriers for anticancer drugs.[16] Yang et al. developed a positively charged porous drug carrier MOF-74-Fe (III) after the oxidation of a neutral crystal MOF-74-Fe (II). The obtained cationic host materials showed a low cytotoxicity against PC12 cells and a high drug loading capacity of ibuprofen anions (15.9%). Synergistic physical adsorption and coordinate conjugation of ibuprofen anions facilitated flexible release of drug release from MOF-74-Fe (III) (Figure 4).[17]

Porous coordination network (PCN) MOFs are developed

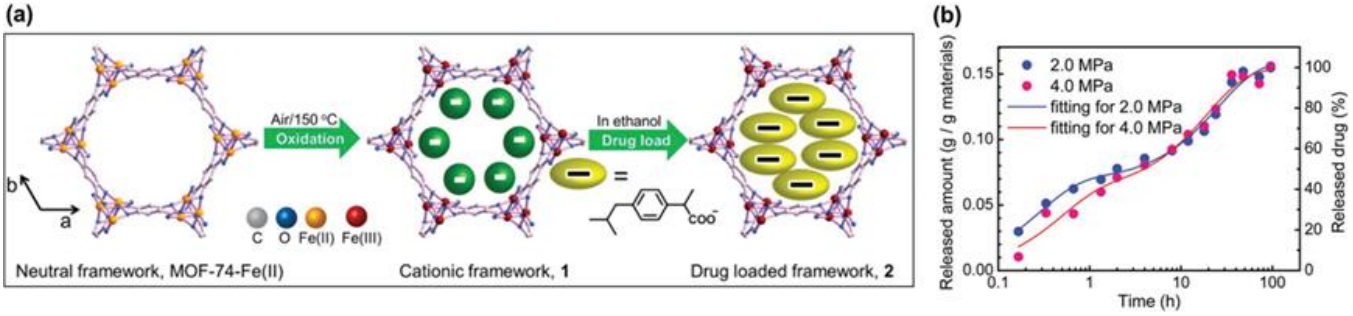

Figure 4. a) Schematic fabrication process of MOF-74-Fe (II) oxidation to crystal 1 and drug-loading. b) Release profiles of Ibu− in PBS solution under 2.0 and 4.0 MPa, respectively. Reproduced with permission.[17] Copyright 2014, American Chemical Society.

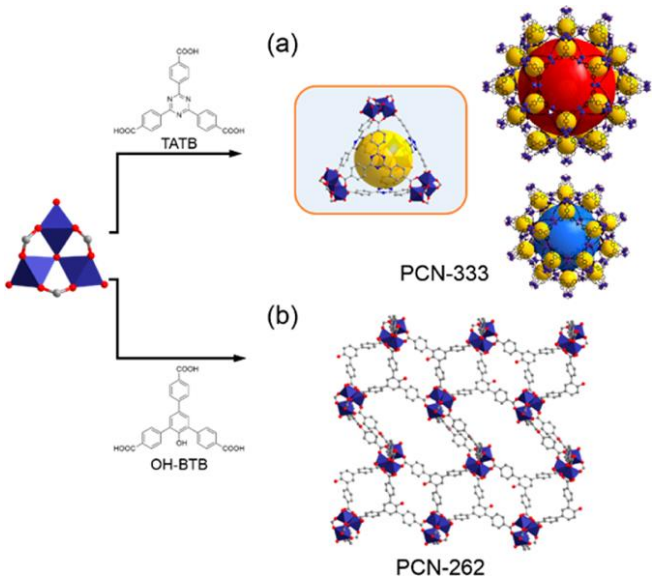

Figure 5. (a) Structure of PCN-333 with three different cages. (b) Structure of PCN-262, a direct synthesis product from OH-BTB.[23] Reused with permission. Copyright 2013, American Chemical Society.

based on dicarboxylate or tricarboxylate aromatic ligands with longer, functionalized, or extended linkers. PCN series materials contain multiple cubic octahedral nanopore cages, and form a cage-pore channel topology in space. PCN series also have the hierarchical porous structure with larger pore sizes compared to MIL series (Figure 5). For instance, PCN-333 (Al, Fe) is derived from MIL-100, and its organic ligand is 4,4′,4″-s-triazine-2,4,6-triyl-tribenzoate (TATB) linker that is developed from the organic ligand (H_3BTC) of MIL-100.[18] PCN-333 (Fe) possesses large cavities up to 4.5 nm due to the coordination between Fe^{3+} ions and extended carboxylate linkers. Excellent stability, large cavities, and a hierarchical porous structure of PCN-333 (Fe) endows it the potential for gas adsorption and drug delivery. However, there are very few studies on PCN-333 (Fe) and its application. PCN-333 (Fe) is mainly applied as a template for the synthesis of other PCN-333 MOFs series via an ion-exchange route. PCN-333 (Cr) can be obtained by the reductive labilization of Fe (III) and Cr (II), leading to the Fe (II)-Cr (II) metathesis.[19] Zhou et al. reported a dual exchange method for the synthesis of PCN-333 (Cr) with functional groups using PCN-333 (Fe) as a template, including the sequential ligand exchange and metal metathesis process. Another framework Zn-TEPP can be clicked into PCN-333 (Cr) due to its extremely large pores (~5.5 nm).[20] This dual exchange method for the synthesis of PCN-333 (Cr) can be extended as a novel synthetic methodology for the synthesis of other MOFs. The same group further investigated the potential of using PCN-333 (Fe) and PCN-333 (Al) as the carriers for enzyme encapsulation due to its large single cavity.[21] They found out that ultra-large mesopores in PCN-333 (Al) and PCN-333 (Fe) facilitated loading and immobilization of enzymes (HRP, Cyt c and MP-11) since mesopores and enzymes have a similar size. The experimental results indicated that the employment of PCN-333 (Al) and PCN-333 (Fe) as the enzyme carrier could maintain the enzymatic activity of enzymes. In addition, the Zhou group synthesized a water-stable MOF PCN-426 (Fe) using PCN-426 (Mg) as a template via a postsynthetic metathesis and oxidation method.[22] The effective exchange of Fe^{2+} and Mg^{2+} maintained the integrated structure of the original PCN-426 (Mg). After air oxidation, PCN-426 (Fe) was obtained from single-crystal transformation with a higher bonding strength resulting from high valence metal ions and carboxylates. The PCN-426 (Fe-III) product exhibited excellent water stability and permanent porosity. The same group reported successful synthesis of cationic PCN-223 (Fe) by the postsynthetic treatment, which showed a high level of stability in water with a wide range of pH, and they also demonstrated its potential as a heterogeneous catalyst for the hetero-Diels–Alder reaction.[23]

2.2 Functionalized Fe-MOFs

Although individual stable Fe-MOFs can be widely applied due to their excellent stability and permanent porous structure, a single function of those Fe-MOFs may not be adequate for complex situations. The modification method of Fe-MOFs via the introduction of functional groups and moieties is explored in order to synthesize multi-functional MOFs for various applications. Figure 6 summarized recent works of functionalized Fe-MOFs for different applications.

Functionalized Fe-MOFs are modified based on the properties of iron centers, for instance, biocompatibility, catalytic active sites, coordinatively unsaturated sites, etc. Ma et al reported a MIL-88B-Fe MOF modified with -NH_2 groups for chemical capture of carbon monoxide by removing the terminal water or chloride ligands in octahedral iron units of MIL-88B-Fe-NH_2. Fe^{3+} and Fe^{2+}, as coordinatively unsaturated metal sites, were employed for the active adsorption sites of CO, while the amino group of MIL-88B-Fe-NH_2 acted as a functional group for controlled release of CO. The captured CO on Fe^{3+} and Fe^{2+} is released into a physiological buffer solution, after which the MIL-88B-Fe-NH_2 is decomposed. The ‘gate-opening/closing’ of the porous channel induced by the ‘breathing effect’ of MIL-88B-Fe-NH_2 could achieve controlled loading/release of CO.[24] An iron-tetrakis(4-carboxyphenyl)porphyrin (Fe-TCPP) MOF was modified with albumin (bovine serum albumin, BSA) for targeting carbonic anhydrase (CA) IX of tumor cells. Sulfonamides (SAs) was used to achieve a longer circulation time for cancer therapy.[25]

The BSA/SAs-modified Fe-TCPP MOF also exhibited a T_1-T_2 weighed MRI effect (r_1 = 2.7 mM^{-1} s^{-1} and r_2 = 19.68

mM^{-1} s^{-1}), thus it offered synergetic photodynamic/photothermal tumor therapy. Horcajada et al. modified biocompatible MIL-100 (Fe) with heparin using a facile synthetic method to reduce cell recognition, prevent complementary activation, and produce reactive oxygen species. Caffeine and furazan were used as cargoes in the modified MOF and a sustained release profile was obtained. The in vitro study confirmed its excellent biocompatibility, low inflammatory responses, and successful macrophage uptake.[26] β-cyclodextrin (β-CD), a promising supramolecular macrocycle, can be coated onto MOFs as a gating moiety to regulate release of a targeted drug. For instance, the Zhang group designed a multifunctional Fe-MOF-based drug delivery platform using the one-pot synthesis method with post-synthetic surface modification of MIL-101 (Fe).[27] Azide functionalized MIL-101 (Fe)(MIL-101-N_3(Fe)) was first loaded with DOX·HCl, after which the β-CD derivative (β-CD-SS-BCN) was coated on the surface.

A peptide-functionalized polymer, Lys (adamantane)-Arg-Gly-Asp-Ser-bi-poly(ethylene glycol) (PEG) 1900 (bi = benzoic imine bond, K(ad)RGDS-PEG1900) was tethered to the surface of the nanocarrier by the host-guest interaction. The obtained modified MIL-101-N_3(Fe) possessed pH- and redox-responsiveness due to the existence of a benzoic imine bond in K(ad)RGDS-PEG1900 and a disulfide bond between

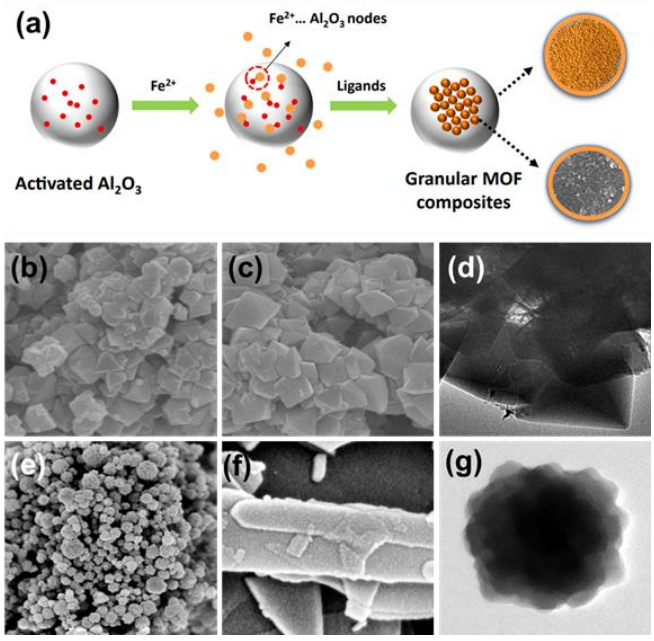

Figure 6. (a) Schematic illustration for the fabrication of granular MIL-100(Fe)@activated Al_2O_3 composites. Color coding: O, red; ferrous ion, orange; MIL-100(Fe) nanoparticles, chocolate; H atom is omitted for clarity. [28] Reproduced with permission, copyright 2021 Elsevier. (b)(c) SEM images of MIL-100 (Fe) and Fe_3O_4@MIL-100(Fe) (ration 1:4) (d) TEM images of MIL-100 (Fe).[29] Reproduced with permission, copyright 2021, Elsevier. (e)(f) SEM images of MIL-100 (Fe) and $Bi_{12}O_{17}Cl_2$ (g) TEM image of $Bi_{12}O_{17}Cl_2$/MIL-100(Fe) composites.[30]

β-CD and the nanocarrier. The constructed drug delivery system exhibited enhanced cellular uptake. The reducing agents in the tumor microenvironment triggered drug release from the modified MOF, thus achieving efficient drug delivery and cancer therapy. The surface modification further reduced the cytotoxicity of the DOX-loaded nanocarriers on normal cells from in vitro experiments, thus paving the way into clinical translation of this MOF-based drug delivery system for treating cancer.

2.3 Nanostructured Fe-MOFs

Fe-MOFs can be nanostructured to possess unique properties such as large internal cavities and higher conductivity. A core-shell nanostructure is preferable to enhance biocompatibility, drug loading capacity, and catalytic activity of Fe-MOFs. Hollow structure is usually utilized to increase the active surface area and internal space of Fe-MOFs. 2D structure is also applied in the strucural modification due to more expore of active sites. Figure 7 summarized typical nanostructured Fe-MOFs in terms of various applications.

Lin group developed an iron-carboxylate MOF MIL-101 with a core-shell structure as a theranostic platform for drug delivery and imaging. They post-synthetically modified MIL-101 (Fe) with an optical imaging contrast agent,1,3,5,7-tetramethyl-4,4-difluoro-8-bromome-thyl-4-bora-3a,4a-diaza-s-indacene (BrBODIPY), and an ethoxy-succinato-cisplatin (ESCP) prodrug, c,c,t-[$PtCl_2$ $(NH_3)_2$ (OEt) $(O_2CCH_2CH_2CO_2H)$].

A thin layer of silica was coated on the surface of the material to prevent the decomposition of drug loaded MIL-101 (Fe) in a PBS buffer. Silyl-derived c(RGDfK) was then utilized to functionalize the surface of the silica shell, thus enhancing the its cellular uptake.[31] Huang et al. reported a silica-layer-coated core-shell structural Fe-MOF (Fe-bbi) constructed from ferrous ions and 1,1′-(1,4-butanediyl) bis (imidazole) (bbi) using the deposition method. Folic acid (FA) was conjugated to Fe-bbi to endow it with pH-responsiveness and cancer cell targetability since FA could bind to the CD44 receptors on the cancer cells surface and the drug could be released at a lower pH in the tumor microenvironment.[32] A core-shell structural MIL-100 (Fe) with a Fe_3O_4 core (Fe_3O_4@MIL-100 (Fe)) was obtained by the layer-to-layer method.[33] The superparamagnetic Fe_3O_4@MIL-100 (Fe) was used as an electrochemical sensor for chlorogenic acid (CGA) and xx with a detection range of 0.1–10.0 μmol L^{-1} and 10.0–460 μmol L^{-1}, respectively. The Tang group fabricated another core-shell structural Fe-MIL-101_NH_2 with upconversion nanoparticles as the core and NH_2-PEG-COOH as the coating component for fluorescent/magnetic dual-mode targeted imaging.[34] The outer shell of Fe-MIL-101_NH_2 was used for MRI, while rare-earth-doped upconversion nanoparticles were applied to

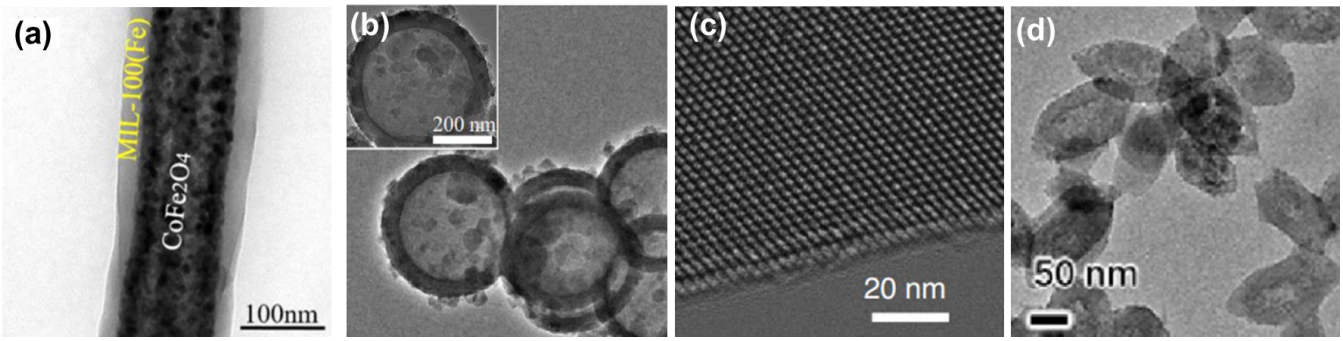

Figure 7. (a) TEM image of $CoFe_2O_4$/MIL-100 (Fe) nanofibers for visible light photocatalysis.[37] Reproduced with permission, copyright 2021, Springer Nature. (b) TEM image of hollow nano-sphere NH_2-MIL88(Fe) for remazol brilliant blue R decolorization.[38] Reproduce with permission, copyright 2020, Elsevier. (c) Cryo-EM image of a 2D Cu_3HHTT_2 plate with superb electrical conductivity.[39] Reproduced with permission from authors, copyright 2020 Springer Nature Limited 2020. (d) TEM image of hollow MIL-88B(Fe)@ZIF-8 for combined cancer imaging and therapy.[40] Reproduced with permission, copyright 2021, American Chemical Society.

display the upconversion luminescence (UCL). NH_2-PEG-COOH was employed to improve biocompatibility and stability of the entire system. In vitro and *in vivo* experimental results demonstrated the feasibility of the tumor-targeting dual-modal UCL/MR imaging nanoplatform. Another multifunctional magnetic core-shell Fe-MOF theranostic platform was reported in 2016.[35] Multifunctional Fe3O4@C@MIL-100(Fe) (FCM) nanocomposites were fabricated for the delivery of dihydroartemisinin (DHA) and Fe (III) into cancer cells. The acidic microenvironment of the tumor tissue triggered the reduction of Fe (III) ions, and Fe (II) reacted with DHA released from the FCM nanocomposites in response to a low pH in the microenvironment to generate reactive oxygen species (ROS), which induced cancer cell death. The magnetic core of Fe_3O_4@C provided the function of magnetic targeting and MRI, and it was also used to load CDs for fluorescence optical imaging (FOI). Experimental results exhibited the dual-modal pH-responsive chemotherapy with the imaging-guidance for improved cancer treatment.

A hollow nanostructure endows materials with unique properties including a low density, functional surfaces, an inner cavity, exposure of more active sites, etc. Hollow structural nanomaterials have been widely applied in various fields due to their spacial confined characteristics. Hollow structural Fe-MOFs possess advantages of their intrinsic biocompatibility and excellent stability. The hollow structure of Fe-MOFs can be generated mainly by the following methods: 1) Exterior template method; 2) Self-template method; 3) Two-phase interface method.[36]

Hollow MIL-100 (Fe) was fabricated by a layer-by-layer technique through immersing the template in a metal-ion solution and then an organic-ligand solution.[41] Liu et al. developed a hollow MIL-101 (Fe) for selective hydrogenation of α,β-unsaturated aldehyde using the in-situ growth method. Ir metal nanoclusters (NCs) were confined within hollow MOFs via in-situ growth of MOFs with metal NCs in a precursor solution. The as-prepared Ir@MIL-101(Fe) possessed an activity of 93.9%, a selectivity of 96.2%, and great recyclability for the hydrogenation of cinnamaldehyde (CAL) to cinnamyl alcohol (COL) under mild conditions. The excellent catalytic performance resulted from the electron transfer from Ir to MIL-101 (Fe) and the strong interaction between Lewis acid sites in MIL-101 (Fe) and the C=O bond. Hollow spheres of bioactive Fe-MOFs MIL-88A were designed and fabricated by an interfacial reaction based on in-droplet microfluidics for the encapsulation of enzymes and nanoparticles.[42] The hollow spheres of MIL-88A consisted of double-shell capsules. Inorganic magnetic/luminescent nanoparticles and bioactive enzymes (e.g., GDH, HRP, and AChE) were successfully encapsulated into hollow MIL-88A to form a multifunctional platform for biocatalytic microreactors. Another hollow Fe-MOF was synthesized from ferric acetylacetonate (Fe) and benzene tricarboxylic acid (BTC) ligands by a facile solvothermal method for anticancer drug (5-Fu) delivery and MRI.[43] In particular, the competitive coordination process between molybdate, thioacetamide, and the organic ligand H_3BTC destructed the long-range ordered crystal structure to form controlled pores with a size from 100-200 nm, thus achieving ultrahigh drug loading/release efficiencies of 77% and 83%. This macroporous drug delivery system exhibited excellent biocompatibility and potent therapeutic outcomes based on MTT assays and *in vivo* experiments. It was also demonstrated to be a promising MRI agent due to the intrinsic Fe element.

The development of 2D MOF nanostructures has drawn wide attention due to their higher density in the defect sites and active sites, significantly enhanced activity, and

exchangeable coordination positions around MOFs. In particular, the band gap property of certain 2D MOFs allows them to be applied as photocatalysts. 2D nanostructured Fe-MOFs have also been widely applied as traditional chemical reaction catalysts, electrocatalysts, and photocatalysts. 2D MOFs can be fabricated mainly by three methods: top-down synthesis, bottom-up synthesis, and template assisted synthesis.[44] Two mixed-valence Fe-MOF [Fe(II)/Fe(III)] nanosheets was synthesized by delaminating their bulk MOFs through sonication in methanol, leading to the formation of nanosheets at a thickness of 7 nm.[45] The template-assisted method employs in situ nucleation and growth of ultrathin 2D MOF nanosheets on certain supports. One ultrathin 2D NiFe-MOF ($Ni_{0.8}$-$Fe_{0.2}(C_{12}H_6O_4)(H_2O)_4$) nanosheet was synthesized on the Ni foam. The thickness of 3.5 nm of the NiFe-MOF was confirmed by the AFM measurement.[46] The 2D NiFe-MOF exhibited a high catalytic activity towards the overall water splitting with favorable kinetics and excellent durability. The Lin group developed 2D biomimetic Fe-MOLs (Metal-Organic Layers) by modifying the SBUs (Secondary Building Units) of MOLs with monocarboxylate compounds, which created hydrophobic/hydrophilic microenvironments near the reaction centers to control the selectivity in the photocatalytic aerobic oxidation of tetrahydrofuran (THF).[47]

Previous studies proved the feasibility of using Fe-MOFs for biomedical and energy conversion applications. However, Fe-MOFs with high loading capacity and tumor targeting function have not been well developed using a facile methodology.

3. Fe-based oxides

Iron oxides nanoparticles can be employed as a magnetic resonance imaging agent for diagnostics, a heat mediator in hyperthermia treatment, also as a magnetically targeting carrier for anticancer drug delivery due to their stable and magnetic properties.[48] The ultralow toxicity of iron and its oxides derivatives (coupling, conjugation, etc) endow them with the application potential as drug products. In addition, coupling of iron oxides to organic moieties such as polymers, liposomes, and micelles could improve the biocompatibility of the complex and enhance the versatility of iron oxides. Iron oxides doped with other metals or modified with an etching effect have also been demonstrated with a remarkable catalytic activity in the electrochemical reactions. However, the study that probes into the function and mechanism of iron in the compounds in terms of their performance for different applications is still limited.

3.1 Individual Fe-based oxides

Hematite (α-Fe_2O_3), a natural ore of iron, is the fourth most abundant element in the earth crust with a percentage of 6.3% by weight. Apart from the environmental friendliness,

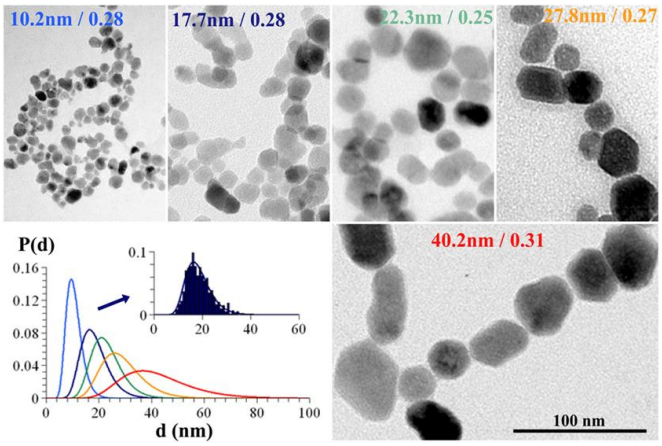

Figure 8. TEM pictures for different Fe_2O_3 samples and corresponding distributions of the major axis approximated by log-normal distributions.[58] Reused with permission. Copyright 2008, IOP Publishing.

Fe_2O_3 possesses favorable properties such as chemical stability in an aqueous solution, and a band gap (1.9-2.2 eV) for light harvesting. Therefore, Fe_2O_3 has been explored as a photoanode. However, Fe_2O_3 in the form of a thin film or a bulk structure has been demonstrated with a low efficiency due to competition between its low minority diffusion length (2-10 nm) and a high absorption depth (~120 nm at 550 nm wavelength) required to convert a large amount of incident energy.[49,50]The low hole diffusion length determines that holes generated within a few nanometers of the Fe_2O_3 electrolyte-interface can be significant for water oxidation.[49, 50]

Cheon and co-workers experimentally demonstrated that the magnetization of Fe_3O_4 nanoparticles increases with the increase of their average size and so does the T_2-weighted image contrast.[51] Monodispersed superparamagnetic

with a size ranging from 4 to 12 nm were obtained by the decomposition method using an organic solvent. It was found that smaller SPM Fe_3O_4 nanoparticles would prolong the circulation time after they were administrated into an animal model compared to larger iron oxide nanoparticles with reduced doses. Nevertheless, the choice of materials as an MRI agent has to be carefully balanced between higher magnetization of the MRI agent and its longer circulation time with reduced doses. Hypothermia therapy based on

Table 2. Summary of individual Fe oxides and applications.

Individual Fe Oxides		
Category	Application	Reference
Fe_2O_3	Water oxidation	[49] [50]
Fe_3O_4	T_2-weighted image contrast	[51]
	Hypothermia therapy	[52] [57]
SPM γ-Fe_2O_3	Hyperthermia therapy	[58]
α-FeOOH	PCB28 degradation	[59]
α-Fe_2O_3	Fenton-like reactions catalysts	[59]
Fe_3O_4	Fenton-like reactions catalysts	[59]
$H_2Fe_2O_4$	Fenton-like reactions catalysts	[59]

magnetic nanoparticles is an effective approach for selective apoptosis of tumor cells by controlled heating of the damaged tissues. After application of an external static magnetic field that alternates with a high enough frequency, the magnetization of magnetic nanoparticles is frequently reversed, which converts magnetic energy to thermal energy, therefore, the heat is generated and released into the surrounding tumor tissues. If the temperature can be maintained above the threshold of 42°C for more than 30 min, the tumor tissue can be ablated.[52] Ma et al. investigated the heating capacity of Fe_3O_4 and revealed the variations in the specific absorption rate

(SAR) and the coercivity of Fe_3O_4 nanoparticles with a size ranging from 7 to 400 nm. The experimental results indicated that 50-nm-Fe_3O_4 nanoparticles had the highest SAR and coercivity among the investigated sizes.[57] Moreover, the optimal diameter for SPM γ-Fe_2O_3 nanoparticles to reach the maximum SAR value was close to 16 nm (Figure 8).[58] Iron oxides are also widely investigated in the Fenton-reaction related catalysis due to the function of iron ions. Goethite, hematite, magnetite, and ferrihydrite, different forms of iron oxides, have been utilized to catalyze H_2O_2 to generate reactive free radicals and degrade organic compounds at pH from 3 to 7. Zhao et al. investigated the catalytic performance of different iron oxides in the degradation process of 2,4,4'-trichlobiphenyl (PCB28) based on the Fenton-like reactions.[59] The catalytic performance exhibited an order of goethite > magnetite > hydrated iron (III) oxide > hematite. The degradation efficiency of hexachloroethane (HCE) was 76.8%, 58.7%, 46.1% and 37.6% for magnetite, goethite, hematite, and hydrated iron (III) oxide, respectively, indicating the reducibility of iron oxides systems has an order of magnetite/H_2O_2 > goethite/H_2O_2 > hematite/H_2O_2 > hydrated iron (III) oxide/H_2O_2. Experimental results of HCE degradation suggested that the reductive species ($HO^{2\cdot}/O^{2\cdot-}$) and oxidative species (·OH) synergistically facilitated the degradation of PCB28 in four iron oxide-catalyzed Fenton-like reactions.

3.2 Functionalized Fe-based oxides

Coupling with organic moieties, metal doping/mixing, and nanostructure re-construction are main methodologies for optimizing the properties of iron oxide nanomaterials for various applications. For instance, the stability of iron oxide nanoparticles can be compromised due to a higher ionic strength in the physiological media. The increasing ionic strength in the aqueous solution can retain an electric double layer around the charged nanoparticles, leading to the aggregation of the nanoparticles. Moreover, although individual iron oxides nanoparticles are stable in acidic or alkaline electrolytes, the catalytic capability of electrochemical catalysis still require improvement.

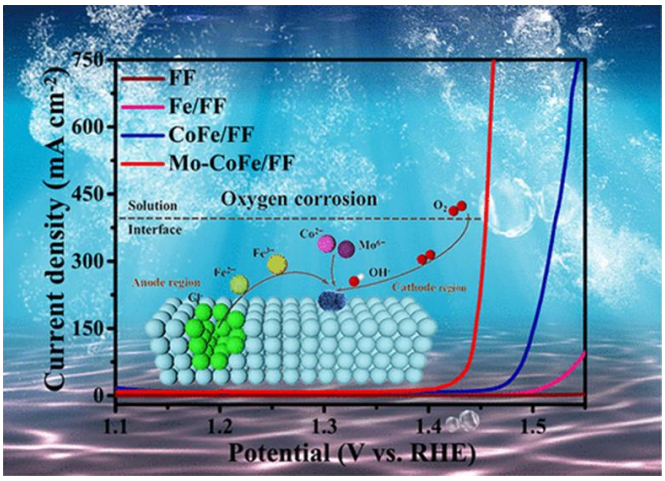

Figure 9. OER performance of Mo-CoFe/FF and the scheme of catalytic process.[71] Reused with permission. Copyright 2021, American Chemical Society.

Therefore, iron oxide nanomaterials have been modifed with multi-functions. Figure 10 summarized the recent works of functionalized Fe-based oxides from the perpective of nanostructures.

A typical surface modification method is to construct a core-shell structure of iron oxides. In this structure, iron oxide cores are encapsulated into different types of coatings for various purposes. Yu and co-workers synthesized carboxymethyldextran (CMD) coated monodispersed iron oxides nanoparticles (MION) with a core-shell structure as a MRI agent and a drug delivery carrier with magnetism-aided targetability.[60] *In vivo* experiments confirmed the feasibility of using the CMD-coated MION to provide high contrast MR images of brain tumors in a rat model. Zhang and Zhan reported a shell-core structure CdSe@Fe_2O_3 NPs by a one-step seeded growth approach. These nanoparticles possessed semiconducting and magnetic functions, enabling their potential for biosensing and biomedical application.[61]

The metal doping/mixing method usually endows iron oxides with additional properties or unique nanostructures. In order to optimize the properties of MRI agents, Lee et al. developed a potential alternative to iron oxides as a MRI agent based on the modification of iron oxides. They synthesized monodispersed ferrite nanoparticles at 12 nm based on a general formula of MFe_2O_4, where M represents +2 cation of Mn, Fe, Co or Ni.[62] Experimental results showed that both Co/Fe ferrites and $MnFe_2O_4$ exhibited the highest magnetization value of 110 emu/g as well as the highest relaxivity values, hence possessing the sharpest imaging contrast. $CoFe_2O_4$ nanoparticles at 7 nm were demonstrated to have a higher T_2-weighted image contrast than $MnFe_2O_4$ nanoparticles at a similar size.[63] The employment of a Janus structure is another method by utilizing anisotropic surface chemical compositions. Dumbbell-like Au-Fe_3O_4 and Pt- Fe_3O_4 NPs were fabricated with a tunable size from 2 to 8 nm for Au and Pt, and 4 nm to

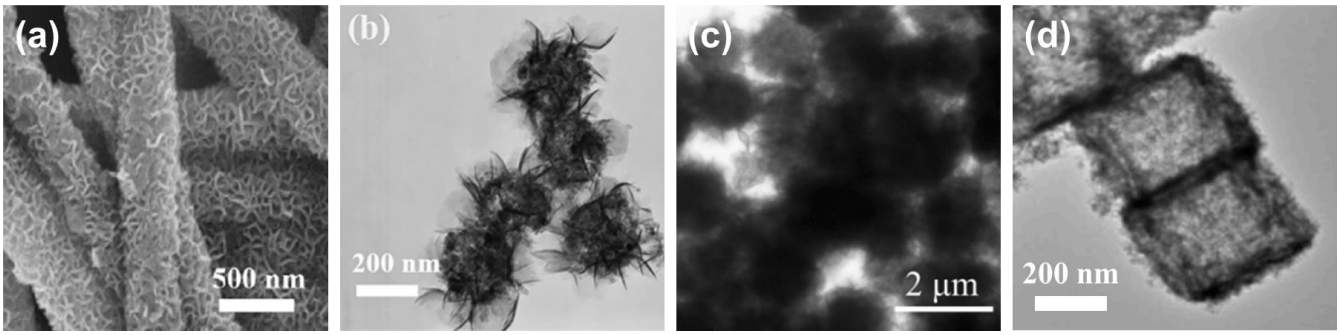

Figure 10. (a) hierarchical Fe_3O_4/Fe@C@MoS_2 core-shell nanofibers for microwave absorption.[53] Reproduced with permission, copyright 2021, Elsevier. (b) TEM image of MoS_2@Fe_3O_4 nanoparticles as microwave absorbers.[54] Reproduced with permission, copyright 2021, Elsevier. (c) TEM image of Fe_3O_4@MoS_2-Ag composite nanoparticles for antibacterial application.[55] Reproduced with permission, copyright 2021, Elsevier. (d) HR-TEM image of Fe_3O_4@MnO_x for the recovery of uranium from simulated seawater.[56] Reproduced with permission, copyright 2021, Elsevier.

20 nm for Fe_3O_4, respectively.[64,65] These Janus nanoparticles were applied in target-specific platin delivery.[66] Magnetic γ-Fe_2O_3|SiO_2 Janus particles using the flame synthesis method presented excellent aqueous dispersibility, thus providing a means for manipulation of Janus particles to form multifunctional assembled structures.[67] A porous Ni-Fe oxide was synthesized with the assistance of an organic surfactant Tween 85 for highly efficient water oxidation.[68] Ni-Fe oxide exhibited small overpotentials of 328 and 420 mV to reach current densities of 10 and 50 mA cm^{-2} in the OER process, respectively. The material maintained a current density of ≈10.2 mA cm^{-2} under 1.62 V electrolysis. The remarkable catalytic performance resulted from a porous structure, homogeneous Fe incorporation, ameliorative crystallinity, and low mass transfer resistance.

Iron oxyhydroxide, an important branch of iron oxides, has attracted wide attention in electrochemical applications. As early as in 1978 and 1981, iron oxyhydroxide had been used to adsorb metal ions such as Cd, Cu, Zn, and Pb on multiple adsorption sites.[69,70] The Li group reported a corrosion-engineered Mo-containing FeCo-oxyhydroxide electrocatalysts for superior oxygen evolution reaction. The introduction of high-valence Mo improved the conductivity and optimized the electronic coordination environment around Fe and Co, which favored its catalytic activity towards OER (Figure 9).[71] Zhou et al. developed $NiFeO_x(OH)_y$ with vertically-oriented MoS_2 nanosheets on a rGO matrix as a bifunctional electrocatalyst for water splitting. Ni and Fe, 3d transitional metal elements, favor the electron transfer, while Mo can regulate the electronic structure of $NiFeO_x(OH)_y$ to achieve excellent HER and OER performance.[72] Arrigo and co-workers employed experimental and computational studies to unveil the formation of multicarbon products generated from the reduction of polarized carbon dioxide at the interface of iron oxyhydroxide and CO_2. The combined study indicated that not only metallic Cu but also thin oxide films on a conductive support could help the formation of a C_{2+} product, and controlling the availability of reactants via dispersive interaction involving support surface chemistry could be a vital factor for the formation of C_{2+} products.[73]

4. Fe-based sulfides

Iron sulfides, an important branch of iron-based nanomaterials, are rich in mackinawite (FeS), pyrrhotite ($Fe_{1-x}S$), pyrite (FeS_2), and greigite (Fe_3S_4) in nature. They have more variability than iron oxides that contain only Fe_2O_3 and Fe_3O_4. With a smaller band gap than iron oxides, iron sulfides have favourable electron transfer and conductivity, which endows them with the potential in electrochemical catalysis.[74-76] Moreover, iron-sulfur clusters are important cofactors in many enzymes, serving as active centers for electron transfer in catalytic process as well as respiratory chain reactions.[79] Iron-based sulfides also

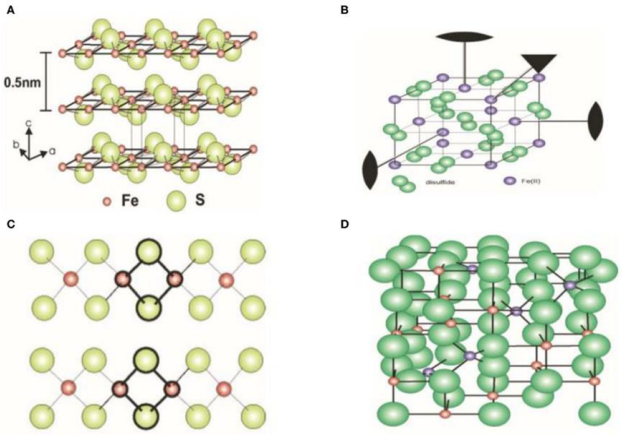

Figure 11. Crystal structure of iron sulfide. (A) FeS. (B) FeS_2. (C) Fe_2 S_2. (D) Fe_3S_4.[80] Reproduced with permissions. Copyright 2007, American Chemical Society.

possess various properties such as magnetic properties, photothermal properties, antibaterial properties, enzyme-like properties, etc (Figure 11).[80] Consequently, iron-based sulfides play an important role in biomedical application, and electrochemical catalysis.

4.1 Individual iron sulfides

To fully utilize the potential of iron sulfides, the reactivity of iron sulfides should be well understood. An iron sulfide is highly reactive to N_2 and H_2S, which can occur at room temperature. The adsorption of N_2 to FeS is dependent on its surface property and the electronic state of N_2. A decrease in the absorbed N_2 and H_2S results from the formation of ammonia.[81] Fe_7S_8 exhibits a similar reactivity as FeS. The reactivity of FeS_2 regarding the absorption of gaseous H_2O and O^{2-} was also reported.[82] The gaseous H_2O can lead to the generation of iron hydroxides on FeS_2, while the sequence of different exposures results in different products such as SO_4^{2-} and $Fe(OH)_3$.[83] Recently, FeS_2 has been speculated to play a vital role in the prebiotic chemistry since its highly reactive surface can facilitate the adsorption of amino acids.[84] Water molecules, a common probe, have also been used to test the reactivity of FeS_2.[85] Different phases of iron sulfides have a wide range of reactivities to chlorinated solvents. Therefore, FeS_2 nanoparticles were used to remove the chlorinated solvents in water.[86] The interaction between FeS, Fe_3S_4 and CO_2 has also been studied. CO_2 molecules can be activated by FeS_2 due to the charge transfer. Nevertheless, CO_2 is not reactive to Fe_3S_4.[87] A though bare iron sulfides have various reactivities and different properties, their long-term stability is quite poor in acidic environment since bare iron sulfides nanomaterials as nanocrystal cores are prone to photochemical degradation. Therefore, functionalized iron-based sulfides are developed to improve their stability for better performance.

Table 3. Examples of individual Fe sulfides for different applications.

Individual Fe Sulfides		
Category	Application	Reference
FeS	Sensitive amperometric sensor for H_2O_2	[74]
-	N_2 and H_2S absorption	[81]
FeS_2	Stability study	[75]
-	Surfactant-assisted hydrothermal	[76]
-	synthesis	[82]
-	Absorption of gaseous H_2O and O^{2-}	[84]
Fe_3S_4	Absorption of amino acids	[87]
-	CO_2 activation	[87]
Fe_7S_8	N_2 and H_2S absorption	[81]

4.2 Functionalized Fe-based sulfides

Apart from an unstable nanostructure of bare iron sulphides, they exhibit a high level of toxicity. Therefore, biocompatible moieties have been explored to coat onto the bare iron sulphides, including polyethylene glycol (PEG), silica, lactose, citrate, and dextran.[88] Moieties that contribute to the optimization of Fe-based sulfides for improving their catalytic performance were also developed (Figure 12). However, modifications on iron sulfides may lead to adverse effects on nanomaterials.

The incorporation of CTAB may inhibit the continuous growth of Fe_3S_4 nanoparticles. Previous studies reported synthesis, characterizations, cytotoxicity, biodistribution, and *in vivo* experiments of FeS/PEG nanoplates.[89] PEGylated FeS (FeS-PEG) nanoplates showed a high level of near infrared (NIR) absorbance, which could be utilized in photothermal therapy (PTT). Through infrared (IR) thermal imaging, the temperature in the tumor tissue reached about 70°C within 5 min. Moreover, FeS-PEG possesses the strongest photothermal conversion efficiency compared to reported iron oxides. Chlorin e6 (Ce6) was utilized to conjugate with FeS2 using the template of bovine serum albumin (BSA). FeS_2@BSA-Ce6 nanodots (7 nm) exhibited excellent performance in *in vivo* photoacoustic (PA) imaging, MRI, and cellular uptake.[90] FeS_2 was reported to have the antibacterial function based on the mechanism of forming H_2O_2. The same group also demonstrated this mineral in FeS_2@BSA-Ce6 nanodots induced the generation of reactive oxygen species (ROS).[91] Rapid absorption of Fe^{2+} influenced the metabolism of bacteria, and the oxidation of Fe^{2+} to Fe^{3+} resulted in the production of ROS and biomolecular damage. Therefore, iron sulfides could be used as effective antibacterial agents in preventing bacterial infections.

In 2018, the Arenas-Arrocena group fabricated $Fe_{x-1}S$ NPs and demonstrated their antibacterial and cytotoxic activity against S. aureus, E. coli and E. faecalis.[92] The antibacterial properties of FeS_2-Bi_2O_3 against pathogenic microorganisms including Mycobacterium tuberculosis and Salmonella have also been observed.[93] Diksha and co-workers found that FeS NPs could increase bacterial intracellular ROS levels triggered by light irradiation, which revealed primary mechanism of FeS NPs for antibacterial application.[94] Moreover, PEG Fe_3S_4 (GMNCs) NPs modified with β-cyclodextrin (β-CD) were employed as anticancer drug carriers since β-CD and PEG were used as surfactants to control the shape and size of GMNCs.[95] The biocompatibility of GMNCs was also enhanced by the organic moieties. The entrapment efficiency for the anticancer drug doxorubicin was 58.7%. The therapeutic effect of doxorubicin-loaded GMNCs was determined to be very potent after intravenous injection into an mice model.

Inorganic moieties are essential for iron sulfides since they can equip nanomaterials with better stability, extra active centers, special morphologies, etc. For example, an adsorption-reduction method was employed to load silver onto the surface of 3-aminopropyltriethoxysilanemodified 3-

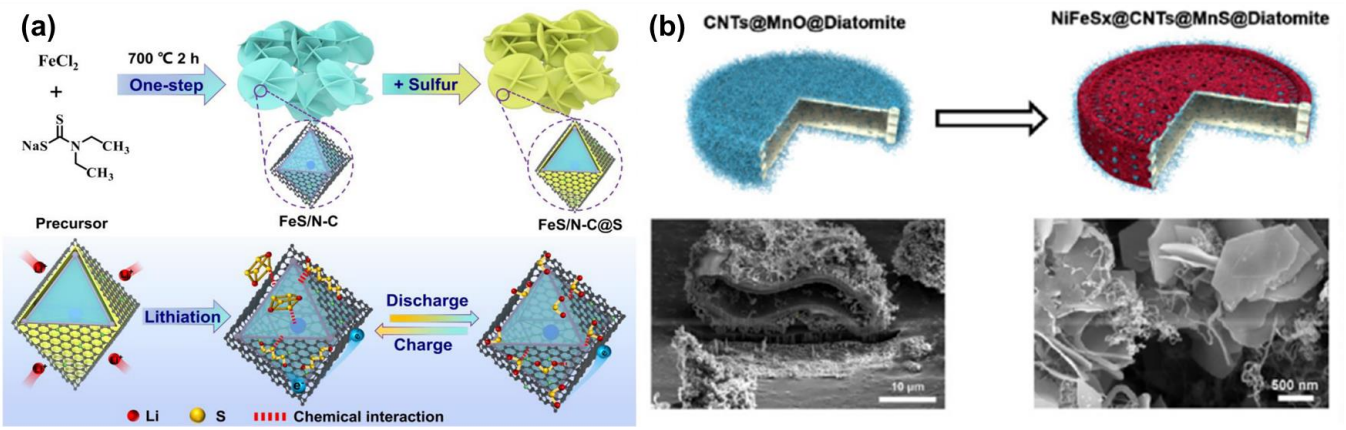

Figure 12. (a) Schematic illustration of the synthesis of N-doped carbon-coated iron sulfide (FeS/N-C) and FeS/N-C@sulfur nanocomposite and its strong interaction with lithium polysulfides (LiPSs) during the charge/discharge process of the Li–S battery.[77] Reproduced with permission, copyright 2021, Elsevier. (b) Nickel–iron sulfide nanosheets (NiFeSx) and carbon nanotubes (CNTs) were synthesized on diatomite using chemical vapor deposition and a two-step hydrothermal method (scheme and SEM images).[78] Reproduced with permission, copyright 2021, Elsevier.

aminopropyl triethoxysilane (APTES)-modified Fe_3S_4 particles, producing magnetic nanoparticles of Fe_3S_4/Ag, which was used as an antibacterial agent with magnetic targeting function.[99] The Ellingson group synthesized cobalt iron sulfide ($Co_xFe_{1-x}S_2$) pyrite nanocrystals (NCs) by probing into the majority of the carrier material. In contrast with FeS_2 NCs, the size of the obtained $Co_xFe_{1-x}S_2$ NCs was significantly smaller. This study provided different synthesis methods for cobalt iron sulfide NCs with unique electronic properties.[100] Wang and co-workers developed a York-shell iron sulfide-carbon nanosphere for the application in sodium-iron sulfide batteries. The York-shell nanostructure consisted of an iron sulfide yolk (~170 nm), a porous carbon shell (~30 nm) and an extra void space (~20 nm) in between. This system exhibited excellent capacity of of ~545 mA h g^{-1} over 100 cycles at 0.2 C (100 mA g^{-1}), delivering an ultrahigh energy density of ~438 Wh kg^{-1}.[103]

The Luo group synthesized 3D ternary nickel iron sulfide microflowers with a hierarchically porous structure. The flower was grown on the Ni foam using a facile two-step method. They were utilized as electrocatalysts for both HER and OER. After the incorporation of Ni, a unique 3D morphology was obtained. A strong electron interaction between Fe, Ni, and S was achieved. $Ni_{0.7}Fe_{0.3}S_2$ delivered an overpotential of 198 mV at a current density of 10 mA cm^{-2} toward the OER in an alkaline electrolyte, and possessed a low cell voltage of 1.625 V to reach 10 mA cm^{-2} for overall water splitting.[104] Rahimi et al. introduced Ni and Co into FeS to obtain 3D ternary metal sulfides nanosheets (Ni-Co-Fe-S) by using nickel nanocone arrays (NCAs) as supercapacitors (2159.7 F/g at 7 A/g and 1461 F/g at 35 A/g) with excellent rate capabilities. An asymmetric supercapacitor system was constructed by using Ni-Co-Fe-S@NCAs-NP as a positive electrode and the nickel foam coated with reduced graphene oxides (rGO-NF) as a negative electrode. It showed a high energy density of 35.9 Wh kg^{-1} at a power density of 375 W kg^{-1}.[105]

5. Other Fe-based nanomaterials

In addition to the above stated iron-based nanomaterials, other iron-based compounds such as iron nitrides, iron phosphides, and iron selenides, also possess special properties that can be utilized in different applications. In this section, other iron-based nanomaterials are discussed. Typical properties, their potential applications, their unique structures and the inherent mechanisms are discussed after the incorporation of iron.

5.1 Fe-based nitrides

Due to the versatility of chemistry, magnetic properties, and crystallinity,[106,107] iron nitride nanoparticles have drawn wide attention in the field of catalysis,[108, 109] battery, and biomedicine.[110] A low cost and physicochemical forms of Fe−N compounds endow them with many advantages compared to noble-metal nanoparticles, such as gold or platinum. Figure 13 summarized recent advances of Fe-based nitrides regarding the energy conversion applications.

The Fe-N based nanoparticles have many ferromagnetic forms, such as γ′-Fe_4N, α″- $Fe_{16}N_2$, or ε-Fe_3N, while FeN is paramagnetic. The most conventional synthesis method of Fe_xN nanoparticles are liquid-based processes with multiple reduction, filtration, and purification steps. Organic solvents, lengthy reaction time, and high energy consumption are often involved in the processes. Novel methods are needed to simplify the fabrication of functional iron nitride nanoparticles. Haye and coworkers used a low-pressure

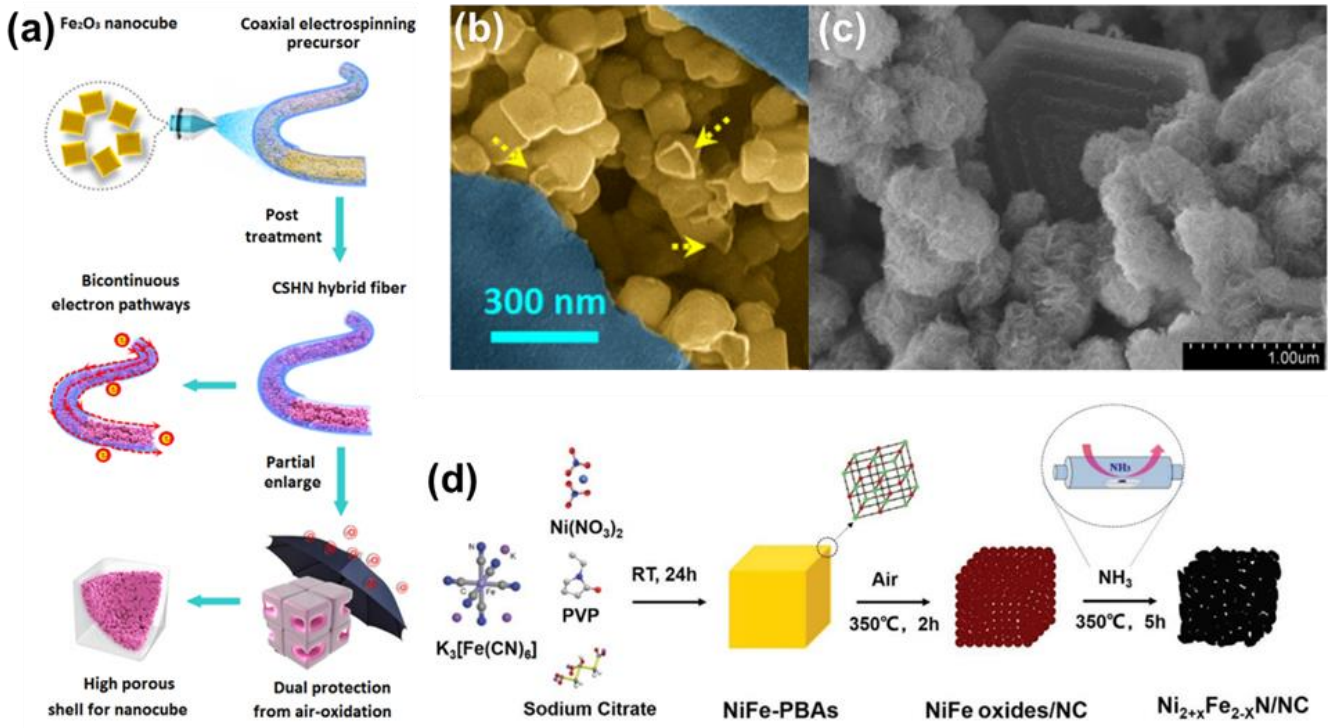

Figure 13. (a) (b) Synthetic scheme of core−shell hybrid fibers (CSHN fiber) filled with iron nitride@C hollow nanocubes for superior lithium/sodium storages and corresponding SEM image.[96] Reproduced with permission, copyright 2021, American Chemical Society. (c) SEM image of γ′-Fe$_x$N for enhanced reductive dechlorination of trichloroethylene.[97] Reproduced with permission, copyright 2022, American Chemical Society. (d) Synthetic scheme of nickel-iron nitride nanocrystals armored with amorphous N-doped carbon nanoparticles nanocubes for enhanced overall water splitting.[98] Reproduced with permission, copyright 2022, Wiley-VCH GmbH.

plasma synthesis method to tune the magnetism of iron nitride nanoparticles in the application as pervaporative membranes.

Magnetic iron nitridenanoparticles (ε-Fe3Nx) were deposited on a carbon xerogel (CXG) through plasma-induced degradation of iron acetylacetonate in a nitrogen-based plasma discharge (Ar/NH3). The results showed that the organometallic precursor was degraded through multiple reactions with the reactive species in the plasma, progressively leading to the growth of Fe$_x$N nanoparticles. Finally, the optimized Fe$_x$N/CXG composite was applied as an effective filler for the alginate membrane for pervaporative ethanol dehydration. At an optimum loading of 3% w/w, the performance of a pristine alginate membrane was considerably enhanced, in terms of the selectivity, separation index, and flux.[111] Liang and co-workers prepared CD3 antibody-conjugated graphene oxide-coated iron nitride magnetic beads (GO@FeN-IMB) as immunomagnetic beads for T cell separation. The anti-CD3-GO@FeN-IMBs were incubated with a cell mixture containing human T cells. The T cells were successfully separated from the cell mixture by the aid of a magnetic stand. The separated T cells were intact and could proliferate by the activation of the IMBs.[112] Wang et al. developed the nanoparticle-stacked cobalt-incorporated iron nitride (NSP-Co_3FeN_x) nanowires as bifunctional electrocatalysts for water splitting. NSP-Co_3FeN_x exhibited excellent OER and HER activities with a low overpotential of 222 mV at 20 mA cm^{-2} and 23 mV at 10 mA cm^{-2}, respectively. The electrocatalytic performance was ascribed to unique structural advantages with grain boundaries, defects, and dislocations.[113]

5.2 Fe-based phosphides

Iron-based phosphide materials as earth-abundant transition-metal phosphides have emerged as potential alternatives to noble metal catalysts in the electrochemical field. Figure 14 summarized two schemes of synthetic process of functionalized Fe-based phosphides for energy conversion applications.

To explore the synthesis mechanism of FeP nanoparticles, Qian et al. discovered a solution-phase route to synthesize single-crystalline iron phosphide nanorods and nanowires. They have found that the mixture of trioctylphosphine oxide (TOPO) and trioctylphosphine (TOP), commonly used as solvents for semiconductor nanocrystal synthesis, is not completely inert. Moreover, the experimental results revealed that both TOP and TOPO were essential for the formation of

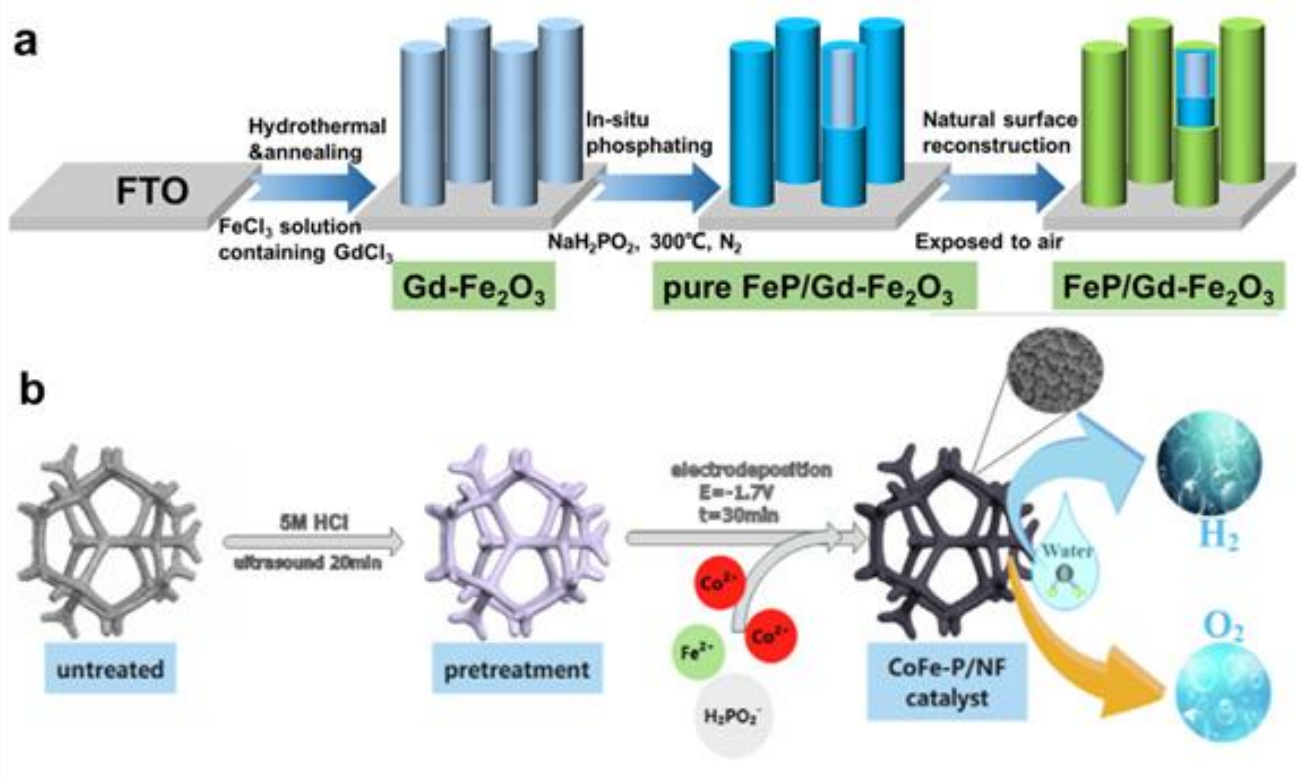

Figure 14. (a) Scheme of illustrating the essential role of iron phosphide and its surface-evolved species in the photoelectrochemical water oxidation by Gd-doped hematite photoanode.[101] Reproduced with permission, copyright 2022, Wiley-VCH GmbH. (b) Synthetic process of cobalt/iron phosphide on nickle foam by potentiostat electrodeposition for over water splitting.[102] Reproduced with permission, copyright 2022, Elsevier.

FeP nanowires and their ratio appeared to tune the morphology of the produced FeP, thus unveiling the growth mechanism of FeP nanostructures.[114] The Schaak group synthesized uniform FeP nanoparticles with a hollow morphology for HER catalysis. The as-synthesized hollow FeP nanoparticles exhibited high HER activities in both acidic and neutral-pH aqueous solutions.[115] The Chen group reported a phenomena that the HER performance of FeP nanoparticles was enhanced after a stability test owing to reduced surface-charge-transfer resistance in the HER process. The synthetic temperature and reactant ratio were vital for surface-charge-transfer resistance, electrochemically active surface area, and HER activity. Hydrogenation apparently optimized the HER performance of FeP nanoparticles verified by the reduced surface-charge- transfer resistance, overpotential, and Tafel slope.[116]

Iron phosphide (FeP) nanorods have also been synthesized via a facile hydrothermal route using iron oxyhydroxide precursors, followed by a simple phosphorization process. The obtained FeP nanorods dispersed on carbon fiber paper as current collectors showed remarkable catalytic activity and favorable long-term stability toward OER.[117] FeP_2 and FeP_4 were fabricated and characterized for their application in a non-aqueous Na ion battery. FeP_2 showed no significant electrochemical reactivity in the Na-cell. However, the FeP_4 electrode with a sodium polyacrylate binder exhibited a reversible capacity of 1137 $mAh \cdot g^{-1}$ with a Coulombic efficiency of 84.0% during the first cycle under a current density of 89 $mA \cdot g^{-1}$. The high capacity was maintained for 30 cycles, and the FeP_4 composite electrode also presented a good rate capability, which indicated its capability of charging and discharging.[118]

5.3 Fe-based selenides

Early in 1959, Okazaki reported the superstructures of Fe_7Se_8 and found that iron vacancies in Fe_7Se_8 were confined to the alternate iron layers parallel to the *c* plane of the fundamental lattice with the NiAs structure. The origin of the ferrimagnetism of Fe_7Se_8 (T_c=187°C) can be ascribed to this ordered arrangement. Two different superstructures were found at low and high temperatures. This exploration of iron selenide nanomaterials revealed the potential of using iron selenide as superconductors.[119] In 2002, Hamdadou et al. proposed a synthetic method of an iron selenide film by selenization of the evaporated iron thin films for the potential application as superconductors. It was shown that the films were mainly composed of tetragonal FeSe, while there were crystallites of orthorhombic $FeSe_2$. After annealing for 2 h at 773 K under vacuum, the films were crystallized in the

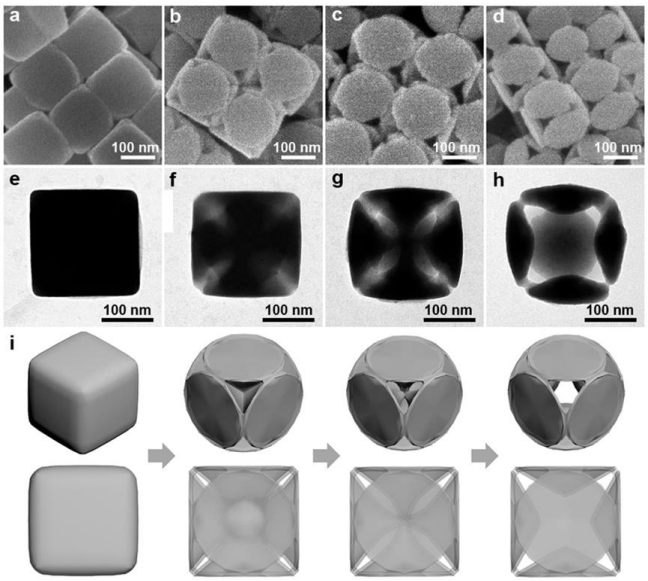

Figure 15. a–h) FESEM (a–d) and TEM (e–h) images of the Ni–Fe mixed diselenide cubic nanocages obtained in the etching procedure for the fabrication of the Ni–Fe Prussian-blue analog (PBA) nanocages at 0 min (a,e), 1 min (b,f), 3 min (c,g), and 5 min (d,h). i) The corresponding schematics illustrate the structural evolution of the exterior and interior of the Ni–Fe PBA nanocubes to form nanocages.[123] Reused with permission. Copyright 2017, WILEY-VCH Verlag GmbH & Co. KGaA, Weinheim.

hexagonal structure of FeSe, while no $FeSe_2$ was detected. The Se/Fe ratio became close to 1. When they were annealed in the same condition but in a selenium atmosphere, the product was $FeSe_2$ films.[120]

Superconductivity, exhibits exactly zero electrical resistivity below a certain temperature known as the critical temperature (Tc). Due to the magnetic ordering at a low temperature in the Fe based compounds, their potential of superconductivity at 8 K is promising. It has been reported that superconductivity in the FeSe exists in a very narrow range of the Se deficiency and this behavior shows obvious difference from other Fe based superconductors. This range has been first quantitatively reported from $FeSe_{0.82}$ to $FeSe_{0.88}$, while another report suggested it could be up to $FeSe_{0.92}$. Guo and co-workers reported the superconductivity in a FeSe-layer compound, $K_{0.8}Fe_2Se_2$ (nominal composition), at above 30 K achieved by intercalating metal K between FeSe layers. It was confirmed that the observed superconductivity at above 30 K was due to this FeSe-based 122 plane.[121]

Researchers also discover the potential of iron-based selenides in electrochemical application. Wang et al. fabricated porous nickel-iron selenide nanosheets as highly efficient electrocatalysts for oxygen evolution reaction.[122] The porous nickel-iron bimetallic selenide nanosheets ($(Ni_{0.73}Fe_{0.23})Se_2$) were grown on a carbon fiber cloth (CFC) by the selenization of the ultrathin NiFe-based nanosheet precursor. The as-synthesized OER catalytic electrode exhibited a small overpotential of 255 mV at 35 mA cm^{-2} and a low Tafel slope of 47.2 mV dec^{-1} and maintained high stability after 28-h measurements in an alkaline solution. Nai et al. obtained Ni–Fe mixed diselenide nanocages as a superior oxygen evolution electrocatalyst (Figure 15).[123] These nickel-iron selenide nanomaterials exhibited remarkable catalytic performance toward OER are mainly ascribed to: (1) a special structure and morphology, leading to a large electrochemical specific surface area and more reaction sites for catalytic reactions; (2) the catalytic active γ-NiOOH species generated in situ on the surface of iron-based selenides. Fe^{3+} tunes the electronic structure of the intermediate γ-NiOOH active phase by inducing partial charge transfer, changing the cation and the intermediates involved in OER chemical bonds, thus reducing the OER overpotential. The Se anion affects the electronic structure and conductivity of the metal site and modifies the catalytic activity; (3) growth of iron-based selenide catalysts directly on a conductive nickel foam, optimizing the overall conductivity and mechanical strength.

6. Summary and Future Perspectives

The iron-based nanomaterials have a wide range of applications mainly based on the following properties of iron: (1) magnetic property, (2) porous structure with a remarkable surface area, (3) excellent biocompatibility, (4) transition metal property and (5) stability. The magnetic property endows iron-based materials with the potential as a MRI agent, a magnetism-responsive drug carrier, a magnetic hyperthermia agent, etc. The porous structure with a remarkable surface area can expose more metal centers and active sites for catalysis, and it also has a high loading capacity for the application of drug delivery. Excellent biocompatibility supports iron-based nanomaterials to be utilized in the biomedical field. The transition metal property enables iron-based nanomaterials with favorable electron transfer capability for both oxidation and reduction in electrochemical catalysis. The excellent stability of iron-based nanomaterials is fundamental for all applications.

Nevertheless, there are many issues of using iron-based materials in biomedical application and electrochemical catalysis. For instance, the drug loading capacity of iron-based nanocarriers is often very low, which can diminish the therapeutic effect of anticancer drug-loaded nanocarriers. Although previous studies have modified iron-based MOFs with different moieties to enable them with targeting function, the entire drug delivery system becomes more complicated, and the biocompatibility can be compromised. Therefore, it is important to develop a facile drug delivery system with a high drug loading capacity, a specific targeting function, and a simplified structure. For electrochemical applications, the stability and catalytic performance can be improved. The catalytic mechanism of these iron-based nanomaterials remains unclear, especially intermediates in terms of

successive steps. Factors that affect the catalytic performance and electrochemical stability should be further explored. The relationship between intermediates, iron nodes, and nanostructures needs to be demonstrated. In addition, facile and effective approaches to obtain proposed iron-based nanomaterials need to be developed. The role of iron in iron-based nanomaterials should be revealed through fundamental studies on the structure-to-function relationship.

Conflict of Interest The authors declare that they have no conflict of interest.

Acknowledgements

This work is supported by the University of Adelaide International Wildcard Scholarship.

References:

[1] N. Abbaspour, R. Hurrell, R. Kelishadi, Review on iron and its importance for human health, J Res Med Sci 19(2) (2014) 164-174.
[2] O.M. Yaghi, H.L. Li, Hydrothermal Synthesis of a Metal-Organic Framework Containing Large Rectangular Channels, Journal of the American Chemical Society 117(41) (1995) 10401-10402.
[3] O.M. Yaghi, M. O'Keeffe, N.W. Ockwig, H.K. Chae, M. Eddaoudi, J. Kim, Reticular synthesis and the design of new materials, Nature 423(6941) (2003) 705-714.
[4] A.R. Millward, O.M. Yaghi, Metal-organic frameworks with exceptionally high capacity for storage of carbon dioxide at room temperature, Journal of the American Chemical Society 127(51) (2005) 17998-17999.
[5] R. Banerjee, A. Phan, B. Wang, C. Knobler, H. Furukawa, M. O'Keeffe, O.M. Yaghi, High-throughput synthesis of zeolitic imidazolate frameworks and application to CO2 capture, Science 319(5865) (2008) 939-943.
[6] H. Furukawa, K.E. Cordova, M. O'Keeffe, O.M. Yaghi, The Chemistry and Applications of Metal-Organic Frameworks, Science 341(6149) (2013) 974-+.
[7] S. Lee, E.A. Kapustin, O.M. Yaghi, Coordinative alignment of molecules in chiral metal-organic frameworks, Science 353(6301) (2016) 808-811.
[8] S.R. Tavares, N. Ramsahye, G. Maurin, A.A. Leitao, Computational exploration of the structure, stability and adsorption properties of the ZIF-9 metal-organic framework, Micropor Mesopor Mat 254 (2017) 170-177.
[9] P. Horcajada, S. Surble, C. Serre, D.Y. Hong, Y.K. Seo, J.S. Chang, J.M. Greneche, I. Margiolaki, G. Ferey, Synthesis and catalytic properties of MIL-100(Fe), an iron(III) carboxylate with large pores, Chemical communications (27) (2007) 2820-2822.
[10] L.H. Ai, L.L. Li, C.H. Zhang, J. Fu, J. Jiang, MIL-53(Fe): A Metal-Organic Framework with Intrinsic Peroxidase-Like Catalytic Activity for Colorimetric Biosensing, Chem-Eur J 19(45) (2013) 15105-15108.
[11] R.W. Liang, F.F. Jing, L.J. Shen, N. Qin, L. Wu, MIL-53(Fe) as a highly efficient bifunctional photocatalyst for the simultaneous reduction of Cr(VI) and oxidation of dyes, J Hazard Mater 287 (2015) 364-372.
[12] P. Horcajada, C. Serre, G. Maurin, N.A. Ramsahye, F. Balas, M. Vallet-Regi, M. Sebban, F. Taulelle, G. Ferey, Flexible porous metal-organic frameworks for a controlled drug delivery, Journal of the American Chemical Society 130(21) (2008) 6774-6780.
[13] A.X. Li, X.X. Yang, J. Chen, A novel route to size-controlled MIL-53(Fe) metal-organic frameworks for combined chemodynamic therapy and chemotherapy for cancer, Rsc Adv 11(18) (2021) 10540-10547.
[14] P. Wang, H.M. Zhao, H. Sun, H.T. Yu, S. Chen, X. Quan, Porous metal-organic framework MIL-100(Fe) as an efficient catalyst for the selective catalytic reduction of NOx with NH3, Rsc Adv 4(90) (2014) 48912-48919.
[15] X.X. Zheng, L.Y. Zhang, Z.J. Fan, Y.N. Cao, L.J. Shen, C.T. Au, L.L. Jiang, Enhanced catalytic activity over MIL-100(Fe) with coordinatively unsaturated Fe2+/Fe3+ sites for selective oxidation of H2S to sulfur, Chem Eng J 374 (2019) 793-801.
[16] P. Horcajada, T. Chalati, C. Serre, B. Gillet, C. Sebrie, T. Baati, J.F. Eubank, D. Heurtaux, P. Clayette, C. Kreuz, J.S. Chang, Y.K. Hwang, V. Marsaud, P.N. Bories, L. Cynober, S. Gil, G. Ferey, P. Couvreur, R. Gref, Porous metal-organic-framework nanoscale carriers as a potential platform for drug delivery and imaging, Nature materials 9(2) (2010) 172-178.
[17] Q. Hu, J.C. Yu, M. Liu, A.P. Liu, Z.S. Dou, Y. Yang, A Low Cytotoxic Cationic Metal-Organic Framework Carrier for Controllable Drug Release, J Med Chem 57(13) (2014) 5679-5685.
[18] D. Zhao, D.J. Timmons, D.Q. Yuan, H.C. Zhou, Tuning the Topology and Functionality of Metal-Organic Frameworks by Ligand Design, Accounts Chem Res 44(2) (2011) 123-133.
[19] X.Z. Lian, D.W. Feng, Y.P. Chen, T.F. Liu, X. Wang, H.C. Zhou, The preparation of an ultrastable mesoporous Cr(III)-MOF via reductive labilization, Chem Sci 6(12) (2015) 7044-7048.
[20] J.Y. Park, D.W. Feng, H.C. Zhou, Dual Exchange in PCN-333: A Facile Strategy to Chemically Robust Mesoporous Chromium Metal-Organic Framework with Functional Groups, Journal of the American Chemical Society 137(36) (2015) 11801-11809.
[21] D.W. Feng, T.F. Liu, J. Su, M. Bosch, Z.W. Wei, W. Wan, D.Q. Yuan, Y.P. Chen, X. Wang, K.C. Wang, X.Z. Lian, Z.Y. Gu, J. Park, X.D. Zou, H.C. Zhou, Stable metal-organic frameworks containing single-molecule traps for enzyme encapsulation, Nat Commun 6 (2015).
[22] T.F. Liu, L.F. Zou, D.W. Feng, Y.P. Chen, S. Fordham, X. Wang, Y.Y. Liu, H.C. Zhou, Stepwise Synthesis of Robust Metal-Organic Frameworks via Postsynthetic Metathesis and Oxidation of Metal Nodes in a Single-Crystal to Single-Crystal Transformation, J Am Chem Soc 136(22) (2014) 7813-7816.
[23] J. Park, D.W. Feng, H.C. Zhou, Structure-Assisted Functional Anchor Implantation in Robust Metal–Organic Frameworks with Ultralarge Pores, Journal of the American Chemical Society 2015 137 (4), 1663-1672.
[24] M.Y. Ma, H. Noei, B. Mienert, J. Niesel, E. Bill, M. Muhler, R.A. Fischer, Y.M. Wang, U. Schatzschneider, N. Metzler-Nolte, Iron MetalOrganic Frameworks MIL-88B and NH2-MIL-88B for the Loading and Delivery of the Gasotransmitter Carbon Monoxide, Chem-Eur J 19(21) (2013) 6785-6790.
[25] W. Zhu, Y. Liu, Z. Yang, L. Zhang, L.J. Xiao, P. Liu, J. Wang, C.F. Yi, Z.S. Xu, J.H. Ren, Albumin/sulfonamide stabilized iron porphyrin metal organic framework nanocomposites: targeting tumor hypoxia by carbonic anhydrase IX inhibition and T-1-T-2 dual mode MRI guided photodynamic/photothermal therapy, J Mater Chem B 6(2) (2018) 265-276..

[26] E. Bellido, T. Hidalgo, M.V. Lozano, M. Guillevic, R. Simon-Vazquez, M.J. Santander-Ortega, A. Gonzalez-Fernandez, C. Serre, M.J. Alonso, P. Horcajada, Heparin-Engineered Mesoporous Iron Metal-Organic Framework Nanoparticles: Toward Stealth Drug Nanocarriers, Adv Healthc Mater 4(8) (2015) 1246-1257.
[27] X.G. Wang, Z.Y. Dong, H. Cheng, S.S. Wan, W.H. Chen, M.Z. Zou, J.W. Huo, H.X. Deng, X.Z. Zhang, A multifunctional metal-organic framework based tumor targeting drug delivery system for cancer therapy, Nanoscale 7(38) (2015) 16061-16070.
[28] C. Yang, Y. Zhu, J. Wang, W. Sun, L. Yang, H. Lin, S. Lv, A novel granular MOF composite with dense and ordered MIL-100(Fe) nanoparticles grown on porous alumina: Green synthesis and enhanced adsorption of tetracycline hydrochloride, Chem Eng J 426 (2021) 131724.
[29] W. He, Z. Li, S. Lv, M. Niu, W. Zhou, J. Li, R. Lu, H. Gao, C. Pan, S. Zhang, Facile synthesis of Fe3O4@MIL-100(Fe) towards enhancing photo-Fenton like degradation of levofloxacin via a synergistic effect between Fe3O4 and MIL-100(Fe), Chem Eng J 409 (2021) 128274.
[30] C. Zhao, J. Wang, X. Chen, Z. Wang, H. Ji, L. Chen, W. Liu, C.C. Wang, Bifunctional Bi12O17Cl2/MIL-100(Fe) composites toward photocatalytic Cr(VI) sequestration and activation of persulfate for bisphenol A degradation, Sci Total Environ 752 (2021) 141901.
[31] K.M.L. Taylor-Pashow, J. Della Rocca, Z.G. Xie, S. Tran, W.B. Lin, Postsynthetic Modifications of Iron-Carboxylate Nanoscale Metal-Organic Frameworks for Imaging and Drug Delivery, Journal of the American Chemical Society 131(40) (2009) 14261-+.
[32] P.F. Gao, L.L. Zheng, L.J. Liang, X.X. Yang, Y.F. Li, C.Z. Huang, A new type of pH-responsive coordination polymer sphere as a vehicle for targeted anticancer drug delivery and sustained release, J Mater Chem B 1(25) (2013) 3202-3208.
[33] Y.L. Chen, W. Huang, K.J. Chen, T. Zhang, Y. Wang, J.M. Wang, A novel electrochemical sensor based on core-shell-structured metal-organic frameworks: The outstanding analytical performance towards chlorogenic acid, Talanta 196 (2019) 85-91.
[34] Y.T. Li, J.L. Tang, L.C. He, Y. Liu, Y.L. Liu, C.Y. Chen, Z.Y. Tang, Core-Shell Upconversion Nanoparticle@Metal-Organic Framework Nanoprobes for Luminescent/Magnetic Dual-Mode Targeted Imaging, Adv Mater 27(27) (2015) 4075-4080.
[35] D.D. Wang, J.J. Zhou, R.H. Chen, R.H. Shi, G.L. Xia, S. Zhou, Z.B. Liu, N.Q. Zhang, H.B. Wang, Z. Guo, Q.W. Chen, Magnetically guided delivery of DHA and Fe ions for enhanced cancer therapy based on pH-responsive degradation of DHA-loaded Fe3O4@C@MIL-100(Fe) nanoparticles, Biomaterials 107 (2016) 88-101.
[36] D. Liu, J.W. Wan, G.S. Pang, Z.Y. Tang, Hollow Metal-Organic- Framework Micro/Nanostructures and their Derivatives: Emerging Multifunctional Materials, Adv Mater 31(38) (2019).
[37] J. Liu, M. Sun, M.-J. Chang, S.-M. Fan, Q. Hui, F.-R. Ni, B. Yuan, Highly Uniform Core/Shell Structured CoFe2O4/MIL-100(Fe) Nanofibers for Efficient Visible Light Photocatalysis, Fibers and Polymers 22(2) (2021) 345-353.
[38] Y. Zhang, P. Hu, Y. Muhammad, Y. Tang, S. Shao, Z. Gao, J. Wang, R. Wang, Y. Hu, L. Kuang, Z. Zhao, Z. Zhao, High-density immobilization of laccase on hollow nano-sphere NH2-MIL88(Fe) host with interfacial defects to improve enzyme activity and stability for remazol brilliant blue R decolorization, Chem Eng J 405 (2021) 127003.
[39] J.H. Dou, M.Q. Arguilla, Y. Luo, J. Li, W. Zhang, L. Sun, J.L. Mancuso, L. Yang, T. Chen, L.R. Parent, G. Skorupskii, N.J. Libretto, C. Sun, M.C. Yang, P.V. Dip, E.J. Brignole, J.T. Miller, J. Kong, C.H. Hendon, J. Sun, M. Dinca, Atomically precise single-crystal structures of electrically conducting 2D metal-organic frameworks, Nat Mater 20(2) (2021) 222-228.
[40] X. Zeng, B. Chen, Y. Song, X. Lin, S.F. Zhou, G. Zhan, Fabrication of Versatile Hollow Metal-Organic Framework Nanoplatforms for Folate-Targeted and Combined Cancer Imaging and Therapy, ACS Appl Bio Mater 4(8) (2021) 6417-6429.
[41] A.L. Li, F. Ke, L.G. Qiu, X. Jiang, Y.M. Wang, X.Y. Tian, Controllable synthesis of metal-organic framework hollow nanospheres by a versatile step-by-step assembly strategy, Crystengcomm 15(18) (2013) 3554-3559.
[42] G.Y. Jeong, R. Ricco, K. Liang, J. Ludwig, J.O. Kim, P. Falcaro, D.P. Kim, Bioactive MIL-88A Framework Hollow Spheres via Interfacial Reaction In-Droplet Microfluidics for Enzyme and Nanoparticle Encapsulation, Chem Mater 27(23) (2015) 7903-7909.
[43] R.X. Cui, P.F. Zhao, Y.L. Yan, G. Bao, A. Damirin, Z.L. Liu, Outstanding Drug-Loading/Release Capacity of Hollow Fe-Metal-Organic Framework-Based Microcapsules: A Potential Multifunctional Drug-Delivery Platform, Inorg Chem 60(3) (2021) 1664-1671.
[44] A. Dhakshinamoorth, A.M. Asiri, H. Garcia, 2D Metal-Organic Frameworks as Multifunctional Materials in Heterogeneous Catalysis and Electro/Photocatalysis, Adv Mater 31(41) (2019).
[45] S. Benmansour, A. Abherve, P. Gomez-Claramunt, C. Valles-Garcia, C.J. Gomez-Garcia, Nanosheets of Two-Dimensional Magnetic and Conducting Fe(II)/Fe(III) Mixed-Valence Metal-Organic Frameworks, Acs Appl Mater Inter 9(31) (2017) 26210-26218.
[46] J.J. Duan, S. Chen, C. Zhao, Ultrathin metal-organic framework array for efficient electrocatalytic water splitting, Nat Commun 8 (2017).
[47] W.J. Shi, L.Y. Cao, H. Zhang, X. Zhou, B. An, Z.K. Lin, R.H. Dai, J.F. Li, C. Wang, W.B. Lin, Surface Modification of Two-Dimensional Metal-Organic Layers Creates Biomimetic Catalytic Microenvironments for Selective Oxidation, Angew Chem Int Edit 56(33) (2017) 9704-9709.
[48] A. Figuerola, R. Di Corato, L. Manna, T. Pellegrino, From iron oxide nanoparticles towards advanced iron-based inorganic materials designed for biomedical applications, Pharmacol Res 62(2) (2010) 126-143.
[49] Gurudayal, P.S. Bassi, T. Sritharan, L.H. Wong, Recent progress in iron oxide based photoanodes for solar water splitting, J Phys D Appl Phys 51(47) (2018).
[50] M. Barroso, S.R. Pendlebury, A.J. Cowan, J.R. Durrant, Charge carrier trapping, recombination and transfer in hematite (alpha-Fe2O3) water splitting photoanodes, Chem Sci 4(7) (2013) 2724-2734.
[51] Y.W. Jun, Y.M. Huh, J.S. Choi, J.H. Lee, H.T. Song, S. Kim, S. Yoon, K.S. Kim, J.S. Shin, J.S. Suh, J. Cheon, Nanoscale size effect of magnetic nanocrystals and their utilization for cancer diagnosis via magnetic resonance imaging, J Am Chem Soc 127(16) (2005) 5732-5733.
[52] V.S. Kalambur, B. Han, B.E. Hammer, T.W. Shield, J.C. Bischof, In vitro characterization of movement, heating and visualization of magnetic nanoparticles for biomedical applications, Nanotechnology 16(8) (2005) 1221-1233.

[53] Z. Tong, Z. Liao, Y. Liu, M. Ma, Y. Bi, W. Huang, Y. Ma, M. Qiao, G. Wu, Hierarchical Fe3O4/Fe@C@MoS2 core-shell nanofibers for efficient microwave absorption, Carbon 179 (2021) 646-654.
[54] X. Zhang, Y. Dong, F. Pan, Z. Xiang, X. Zhu, W. Lu, Electrostatic self-assembly construction of 2D MoS2 wrapped hollow Fe3O4 nanoflowers@1D carbon tube hybrids for self-cleaning high-performance microwave absorbers, Carbon 177 (2021) 332-343.
[55] F. Wei, X. Cui, Z. Wang, C. Dong, J. Li, X. Han, Recoverable peroxidase-like Fe3O4@MoS2-Ag nanozyme with enhanced antibacterial ability, Chem Eng J 408 (2021) 127240.
[56] T. Zhang, J. Chen, H. Xiong, Z. Yuan, Y. Zhu, B. Hu, Constructing new Fe3O4@MnOx with 3D hollow structure for efficient recovery of uranium from simulated seawater, Chemosphere 283 (2021) 131241.
[57] M. Ma, Y. Wu, H. Zhou, Y.K. Sun, Y. Zhang, N. Gu, Size dependence of specific power absorption of Fe3O4 particles in AC magnetic field, J Magn Magn Mater 268(1-2) (2004) 33-39.
[58] M. Levy, C. Wilhelm, J.M. Siaugue, O. Horner, J.C. Bacri, F. Gazeau, Magnetically induced hyperthermia: size-dependent heating power of gamma-Fe2O3 nanoparticles, J Phys-Condens Mat 20(20) (2008).
[59] L. Zhao, Z.R. Lin, X.H. Ma, Y.H. Dong, Catalytic activity of different iron oxides: Insight from pollutant degradation and hydroxyl radical formation in heterogeneous Fenton-like systems, Chem Eng J 352 (2018) 343-351.
[60] F.Q. Yu, L. Zhang, Y.Z. Huang, K. Sun, A.E. David, V.C. Yang, The magnetophoretic mobility and superparamagnetism of core-shell iron oxide nanoparticles with dual targeting and imaging functionality, Biomaterials 31(22) (2010) 5842-5848.
[61] F.M. Zhan, C.Y. Zhang, Bifunctional nanoparticles with superparamagnetic and luminescence properties, J Mater Chem 21(13) (2011) 4765-4767.
[62] J.H. Lee, Y.M. Huh, Y. Jun, J. Seo, J. Jang, H.T. Song, S. Kim, E.J. Cho, H.G. Yoon, J.S. Suh, J. Cheon, Artificially engineered magnetic nanoparticles for ultra-sensitive molecular imaging, Nat Med 13(1) (2007) 95-99.
[63] D.H. Kim, H.D. Zeng, T.C. Ng, C.S. Brazel, T-1 and T-2 relaxivities of succimer-coated MFe23+O4 (M=Mn2+, Fe2+ and Co2+) inverse spinel ferrites for potential use as phase- contrast agentsin medical MRI, J Magn Magn Mater 321(23) (2009) 3899-3904.
[64] H. Yu, M. Chen, P.M. Rice, S.X. Wang, R.L. White, S.H. Sun, Dumbbell-like bifunctional Au-Fe3O4 nanoparticles, Nano Lett 5(2) (2005) 379-382.
[65] C. Wang, H. Daimon, S.H. Sun, Dumbbell-like Pt-Fe3O4 Nanoparticles and Their Enhanced Catalysis for Oxygen Reduction Reaction, Nano Lett 9(4) (2009) 1493-1496.
[66] C.J. Xu, B.D. Wang, S.H. Sun, Dumbbell-like Au-Fe3O4 Nanoparticles for Target-Specific Platin Delivery, J Am Chem Soc 131(12) (2009) 4216-+.
[67] N. Zhao, M.Y. Gao, Magnetic Janus Particles Prepared by a Flame Synthetic Approach: Synthesis, Characterizations and Properties, Adv Mater 21(2) (2009) 184-+.
[68] J. Qi, W. Zhang, R.J. Xiang, K.Q. Liu, H.Y. Wang, M.X. Chen, Y.Z. Han, R. Cao, Porous Nickel-Iron Oxide as a Highly Efficient Electrocatalyst for Oxygen Evolution Reaction, Adv Sci 2(10) (2015).
[69] M.M. Benjamin, J.O. Leckie, Multiple-Site Adsorption of Cd, Cu, Zn, and Pb on Amorphous Iron Oxyhydroxide, J Colloid Interf Sci 79(1) (1981) 209-221.
[70] J.A. Davis, J.O. Leckie, Surface-Ionization and Complexation at the Oxide-Water Interface .3. Adsorption of Anions, J Colloid Interf Sci 74(1) (1980) 32-43.
[71] J. Luo, X.H. Wang, L. Shen, H.C. Fu, X.H. Chen, L.L. Wu, Q. Zhang, H.Q. Luo, N.B. Li, Corrosion-Engineered Mo-Containing FeCo-(oxy)hydroxide Electrocatalysts for Superior Oxygen Evolution Reaction, Acs Sustain Chem Eng 9(36) (2021) 12233-12241.
[72] F. Zhou, X. Zhang, R.J. Sa, S. Zhang, Z.H. Wen, R.H. Wang, The electrochemical overall water splitting promoted by MoS 2 in coupled nickel ?iron (oxy)hydride/molybdenum sul fide/graphene composite, Chem Eng J 397 (2020).
[73] R. Arrigo, R. Blume, V. Streibel, C. Genovese, A. Roldan, M.E. Schuster, C. Ampelli, S. Perathoner, J.J.V. Velez, M. Havecker, A. Knop-Gericke, R. Schlogl, G. Centi, Dynamics at Polarized Carbon Dioxide-Iron Oxyhydroxide Interfaces Unveil the Origin of Multicarbon Product Formation, Acs Catal 12(1) (2022) 411-430.
[74] J.Y. Jin, W.Q. Wu, H. Min, H.M. Wu, S.F. Wang, Y. Ding, S.J. Yang, A glassy carbon electrode modified with FeS nanosheets as a highly sensitive amperometric sensor for hydrogen peroxide, Microchim Acta 184(5) (2017) 1389-1396.
[75] M.Y. Zhang, Z.H. Cui, H. Jiang, Relative stability of FeS2 polymorphs with the random phase approximation approach, J Mater Chem A 6(15) (2018) 6606-6616.
[76] C. Wadia, Y. Wu, S. Gul, S.K. Volkman, J.H. Guo, A.P. Alivisatos, Surfactant-Assisted Hydrothermal Synthesis of Single phase Pyrite FeS2 Nanocrystals, Chem Mater 21(13) (2009) 2568-2570.
[77] R. Li, H. Shen, E. Pervaiz, M. Yang, Facile in situ nitrogen-doped carbon coated iron sulfide as green and efficient adsorbent for stable lithium–sulfur batteries, Chem Eng J 404 (2021) 126462.
[78] K. Li, Z. Hu, R. Zhao, J. Zhou, C. Jing, Q. Sun, J. Rao, K. Yao, B. Dong, X. Liu, H. Li, Y. Zhang, J. Ji, A multidimensional rational design of nickel-iron sulfide and carbon nanotubes on diatomite via synergistic modulation strategy for supercapacitors, J Colloid Interface Sci 603 (2021) 799-809.
[79] W.B. Qi, J.A. Cowan, Structural, mechanistic and coordination chemistry of relevance to the biosynthesis of iron-sulfur and related iron cofactors, Coordin Chem Rev 255(7-8) (2011) 688-699.
[80] Y. Yuan, L.P. Wang, L.Z. Gao, Nano-Sized Iron Sulfide: Structure, Synthesis, Properties, and Biomedical Applications, Front Chem 8 (2020).
[81] C.F. Chyba, Atmospheric science - Rethinking Earth's early atmosphere, Science 308(5724) (2005) 962-963.
[82] M.A. Nino, E. Flores, C. Sanchez, J.M. Rojo, Reactivity of a FeS Surface under Room Temperature Exposure to Nitrogen and H2S, J Phys Chem B 122(2) (2018) 705-712.
[83] C.R. Usher, K.W. Paul, J. Narayansamy, J.D. Kubicki, D.L. Sparks, M.A.A. Schoonen, D.R. Strongin, Mechanistic aspects of pyrite oxidation in an oxidizing gaseous environment: An in situ HATR-IR isotope study, Environ Sci Technol 39(19) (2005) 7576-7584.
[84] R. Afrin, N. Ganbaatar, M. Aono, H.J. Cleaves, T. Yano, M. Hara, Size-Dependent Affinity of Glycine and Its Short Oligomers to Pyrite Surface: A Model for Prebiotic Accumulation of Amino Acid Oligomers on a Mineral Surface, Int J Mol Sci 19(2) (2018).

[85] N.H. de Leeuw, S.C. Parker, H.M. Sithole, P.E. Ngoepe, Modeling the surface structure and reactivity of pyrite: Introducing a potential model for FeS2, J Phys Chem B 104(33) (2000) 7969-7976.
[86] Y.T. He, J.T. Wilson, C. Su, R.T. Wilkin, Review of Abiotic Degradation of Chlorinated Solvents by Reactive Iron Minerals in Aquifers, Ground Water Monit R 35(3) (2015) 57-75.
[87] D. Santos-Carballal, A. Roldan, N.Y. Dzade, N.H. de Leeuw, Reactivity of CO2 on the surfaces of magnetite (Fe3O4), greigite (Fe3S4) and mackinawite (FeS), Philos T R Soc A 376(2110) (2018).
[88] K. Simeonidis, S. Liebana-Vinas, U. Wiedwald, Z. Ma, Z.A. Li, M. Spasova, O. Patsia, E. Myrovali, A. Makridis, D. Sakellari, I. Tsiaoussis, G. Vourlias, M. Farle, M. Angelakeris, A versatile large-scale and green process for synthesizing magnetic nanoparticles with tunable magnetic hyperthermia features, Rsc Adv 6(58) (2016) 53107-53117.
[89] K. Yang, G.B. Yang, L. Chen, L. Cheng, L. Wang, C.C. Ge, Z. Liu, FeS nanoplates as a multifunctional nano-theranostic for magnetic resonance imaging guided photothermal therapy, Biomaterials 38 (2015) 1-9.
[90] Q.T. Jin, J.J. Liu, W.J. Zhu, Z.L. Dong, Z. Liu, L. Cheng, Albumin-Assisted Synthesis of Ultrasmall FeS2 Nanodots for Imaging-Guided Photothermal Enhanced Photodynamic Therapy, Acs Appl Mater Inter 10(1) (2018) 332-340.
[91] M.A.A. Schoonen, C.A. Cohn, E. Roemer, R. Laffers, S.R. Simon, T. O'Riordan, Mineral-induced formation of reactive oxygen species, Rev Mineral Geochem 64 (2006) 179-221.
[92] L. Argueta-Figueroa, N. Torres-Gomez, R. Garcia-Contreras, A.R. Vilchis-Nestor, O. Martinez-Alvarez, L.S. Acosta-Torres, M.C. Arenas-Arrocena, Hydrothermal synthesis of pyrrhotite (Fex-1S) nanoplates and their antibacterial, cytotoxic activity study, Prog Nat Sci-Mater 28(4) (2018) 447-455.
[93] A.M.K. Pasha, M. Hosseini, A. Fakhri, V.K. Gupta, S. Agarwal, Investigation of photocatalytic process for iron disulfide-bismuth oxide nanocomposites by using response surface methodology: Structural and antibacterial properties, J Mol Liq 289 (2019).
[94] S. Agnihotri, T. Mohan, D. Jha, H.K. Gautam, I. Roy, Dual Modality FeS Nanoparticles with Reactive Oxygen Species-Induced and Photothermal Toxicity toward Pathogenic Bacteria, Acs Omega 5(1) (2020) 597-602.
[95] M. Feng, Y. Lu, Y. Yang, M. Zhang, Y.J. Xu, H.L. Gao, L. Dong, W.P. Xu, S.H. Yu, Bioinspired greigite magnetic nanocrystals: chemical synthesis and biomedicine applications, Sci Rep-Uk 3 (2013).
[96] X. Li, C. Deng, H. Wang, J. Si, S. Zhang, B. Huang, Iron Nitride@C Nanocubes Inside Core-Shell Fibers to Realize High Air-Stability, Ultralong Life, and Superior Lithium/Sodium Storages, ACS Appl Mater Interfaces 13(6) (2021) 7297-7307.
[97] M. Brumovsky, J. Oborna, V. Micic, O. Malina, J. Kaslik, D. Tunega, M. Kolos, T. Hofmann, F. Karlicky, J. Filip, Iron Nitride Nanoparticles for Enhanced Reductive Dechlorination of Trichloroethylene, Environ Sci Technol 56(7) (2022) 4425-4436.
[98] M. Chen, Y. Liu, J. Fan, B. Liu, N. Shi, Y. Lin, X. Li, W. Song, D. Xu, X. Xu, M. Han, Phase-Controlled Synthesis of Nickel-Iron Nitride Nanocrystals Armored with Amorphous N-Doped Carbon Nanoparticles Nanocubes for Enhanced Overall Water Splitting, Small 18(34) (2022) e2203042.
[99] Q.G. He, C.Y. Huang, J. Liu, Preparation, Characterization and Antibacterial Activity of Magnetic Greigite and Fe3S4/Ag Nanoparticles, Nanosci Nanotech Let 6(1) (2014) 10-17.
[100] T. Kinner, K.P. Bhandari, E. Bastola, B.M. Monahan, N.O. Haugen, P.J. Roland, T.P. Bigioni, R.J. Ellingson, Majority Carrier Type Control of Cobalt Iron Sulfide (CoxFe1-xS2) Pyrite Nanocrystals, J Phys Chem C 120(10) (2016) 5706-5713.
[101] H. Chai, L. Gao, J. Jin, Revealing the Essential Role of Iron Phosphide and its Surface-Evolved Species in the Photoelectrochemical Water Oxidation by Gd-Doped Hematite Photoanode, ChemSusChem 15(17) (2022) e202201030.
[102] D. Duan, D. Guo, J. Gao, S. Liu, Y. Wang, Electrodeposition of cobalt-iron bimetal phosphide on Ni foam as a bifunctional electrocatalyst for efficient overall water splitting, J Colloid Interface Sci 622 (2022) 250-260.
[103] Y.X. Wang, J.P. Yang, S.L. Chou, H.K. Liu, W.X. Zhang, D.Y. Zhao, S.X. Dou, Uniform yolk-shell iron sulfide-carbon nanospheres for superior sodium-iron sulfide batteries, Nat Commun 6 (2015).
[104] J.H. Yu, G.Z. Cheng, W. Luo, Ternary nickel-iron sulfide microflowers as a robust electrocatalyst for bifunctional water splitting, J Mater Chem A 5(30) (2017) 15838-15844.
[105] S. Rahimi, S. Shahrokhian, H. Hosseini, Ternary nickel cobalt iron sulfides ultrathin nanosheets grown on 3-D nickel nanocone arrays-nickel plate current collector as a binder free electrode for fabrication of highly performance supercapacitors, J Electroanal Chem 810 (2018) 78-85.
[106] N.D. Phu, T.X. Sy, H.T. Cao, N.N. Dinh, L.V. Thien, N.M. Hieu, N.H. Nam, N.H. Hai, Amorphous iron-chromium oxide nanoparticles prepared by sonochemistry, J Non-Cryst Solids 358(3) (2012) 537-543.
[107] L. Machala, R. Zboril, A. Gedanken, Amorphous iron(III) Oxide - A review, J Phys Chem B 111(16) (2007) 4003-4018.
[108] M. Kotzabasaki, E. Tylianakis, E. Klontzas, G.E. Froudakis, OH-functionalization strategy in Metal-Organic Frameworks for drug delivery, Chem Phys Lett 685 (2017) 114-118.
[109] H. Zheng, Y. Zhang, L. Liu, W. Wan, P. Guo, A.M. Nystrom, X. Zou, One-pot Synthesis of Metal-Organic Frameworks with Encapsulated Target Molecules and Their Applications for Controlled Drug Delivery, Journal of the American Chemical Society 138(3) (2016) 962-8.
[110] A. Petri-Fink, H. Hofmann, Superparamagnetic iron oxide nanoparticles (SPIONs): From synthesis to *in vivo* studies - A summary of the synthesis, characterization, in vitro, and *in vivo* investigations of SPIONs with particular focus on surface and colloidal properties, Ieee T Nanobiosci 6(4) (2007) 289-297.
[111] E. Haye, C.S. Chang, G. Dudek, T. Hauet, J. Ghanbaja, Y. Busby, N. Job, L. Houssiau, J.J. Pireaux, Tuning the Magnetism of Plasma-Synthesized Iron Nitride Nanoparticles: Application in Pervaporative Membranes, Acs Appl Nano Mater 2(4) (2019) 2484-2493.
[112] T.Y. Liang, J.X. Li, X. Liu, Z. Ma, X.J. Su, X.J. Meng, Z.Y. Zhanghuang, H.Q. Wang, J.T. Li, Q. Wang, M.L. Wang, Preparation of CD3 Antibody-Conjugated, Graphene Oxide Coated Iron Nitride Magnetic Beads and Its Preliminary Application in T Cell Separation, Magnetochemistry 7(5) (2021).
[113] Y.Y. Wang, D.D. Liu, Z.J. Liu, C. Xie, J. Huo, S.Y. Wang, Porous cobalt-iron nitride nanowires as excellent bifunctional

electrocatalysts for overall water splitting, Chem Commun 52(85) (2016) 12614-12617.
[114] C. Qian, F. Kim, L. Ma, F. Tsui, P.D. Yang, J. Liu, Solution-phase synthesis of single-crystalline iron phosphide nanorods/nanowires, J Am Chem Soc 126(4) (2004) 1195-1198.
[115] J.F. Callejas, J.M. McEnaney, C.G. Read, J.C. Crompton, A.J. Biacchi, E.J. Popczun, T.R. Gordon, N.S. Lewis, R.E. Schaak, Electrocatalytic and Photocatalytic Hydrogen Production from Acidic and Neutral-pH Aqueous Solutions Using Iron Phosphide Nanoparticles, Acs Nano 8(11) (2014) 11101-11107.
[116] L.H. Tian, X.D. Yan, X.B. Chen, Electrochemical Activity of Iron Phosphide Nanoparticles in Hydrogen Evolution Reaction, Acs Catal 6(8) (2016) 5441-5448.
[117] D.H. Xiong, X.G. Wang, W. Li, L.F. Liu, Facile synthesis of iron phosphide nanorods for efficient and durable electrochemical oxygen evolution, Chem Commun 52(56) (2016) 8711-8714.
[118] W.J. Zhang, M. Dahbi, S. Amagasa, Y. Yamada, S. Komaba, Iron phosphide as negative electrode material for Na-ion batteries, Electrochem Commun 69 (2016) 11-14.
[119] A. Okazaki, The Variation of Superstructure in Iron Selenide Fe7se8, J Phys Soc Jpn 14(1) (1959) 112-113.
[120] N. Hamdadou, J.C. Bernede, A. Khelil, Preparation of iron selenide films by selenization technique, J Cryst Growth 241(3) (2002) 313-319.
[121] J.G. Guo, S.F. Jin, G. Wang, S.C. Wang, K.X. Zhu, T.T. Zhou, M. He, X.L. Chen, Superconductivity in the iron selenide KxFe2Se2 (0 <= x <= 1.0), Phys Rev B 82(18) (2010).
[122] Z.Y. Wang, J.T. Li, X.C. Tian, X.P. Wang, Y. Yu, K.A. Owusu, L. He, L.Q. Mai, Porous Nickel-Iron Selenide Nanosheets as Highly Efficient Electrocatalysts for Oxygen Evolution Reaction, Acs Appl Mater Inter 8(30) (2016) 19386-19392.
[123] J.W. Nai, Y. Lu, L. Yu, X. Wang, X.W. Lou, Formation of Ni-Fe Mixed Diselenide Nanocages as a Superior Oxygen Evolution Electrocatalyst, Adv Mater 29(41) (2017).

Chapter 3. Green Synthesis of DOX-loaded Hollow MIL-100 (Fe) Nanoparticles for Anticancer Treatment by Targeting Mitochondria

3.1 Introduction, Significance and Commentary

Low drug loading capacity of traditional drug carriers (micelles, vesicles, dendrimers, etc.) has always been a problem in the drug delivery of anticancer drugs. The structural modification of Fe-MOFs can create more cavities for drug loading. In this work, a green synthesis method is developed to obtain the hollow structure of MIL-100 (Fe). Hollow MIL-100 (Fe) has a doxorubicin loading capacity up to 30%, which is significantly improved compared to traditional drug carriers. DOX-loaded Hollow MIL-100 (Fe) Nanoparticles possess the mitochondrial targeting function verified by in vitro experiments. Their therapeutic effect is evident according to the cell viability results.

3.2 Publication

This section is presented as the published paper by **Y.C. Zhang**, Z.X. Gu, S.H. Yun, K. Luo, J.X. Bi, Y. Jiao, H. Zhang, Green synthesis of DOX-loaded hollow MIL-100 (Fe) nanoparticles for anticancer treatment by targeting mitochondria, Nanotechnology 33(34) (2022).

Statement of Authorship

Title of Paper	**Green Synthesis of DOX-loaded Hollow MIL-100 (Fe) Nanoparticles for Anticancer Treatment by Targeting Mitochondria**
Publication Status	☑ Published ☐ Accepted for Publication ☐ Submitted for Publication ☐ Unpublished and Unsubmitted work written in manuscript style
Publication Details	**Y.C. Zhang**, Z.X. Gu, S.H. Yun, K. Luo, J.X. Bi, Y. Jiao, H. Zhang, Green synthesis of DOX-loaded hollow MIL-100 (Fe) nanoparticles for anticancer treatment by targeting mitochondria, Nanotechnology 33(34) (2022). (**IF=3.953**)

Principal Author

Name of Principal Author (Candidate)	Yechuan Zhang		
Contribution to the Paper	Designed the material and experiments, carried out experiments, analyzed experimental results, and wrote the manuscript.		
Overall percentage (%)	80%		
Certification:	This paper reports on original research I conducted during the period of my Higher Degree by Research candidature and is not subject to any obligations or contractual agreements with a third party that would constrain its inclusion in this thesis. I am the primary author of this paper.		
Signature		Date	05/09/2022

Co-Author Contributions

By signing the Statement of Authorship, each author certifies that:

i. the candidate's stated contribution to the publication is accurate (as detailed above);

ii. permission is granted for the candidate in include the publication in the thesis; and

iii. the sum of all co-author contributions is equal to 100% less the candidate's stated contribution.

Name of Co-Author	Zhengxiang Gu		
Contribution to the Paper	Modified the manuscript, figure corrections.		
Signature		Date	05/09/2022

Name of Co-Author	Seonho Yun		
Contribution to the Paper	Results analysis		
Signature		Date	05/09/2022

Please cut and paste additional co-author panels here as required.

Name of Co-Author	Kui Luo		
Contribution to the Paper	Modified the manuscript.		
Signature		Date	05/09/2022

Name of Co-Author	Jingxiu Bi		
Contribution to the Paper	Modified the manuscript.		
Signature		Date	05/09/2022

Name of Co-Author	Yan Jiao		
Contribution to the Paper	Modified the manuscript.		
Signature		Date	05/09/2022

Name of Co-Author	Hu Zhang		
Contribution to the Paper	Helped to design the experiment. Modified the manuscript.		
Signature		Date	05/09/2022

Nanotechnology **33** (2022) 345601 (12pp) https://doi.org/10.1088/1361-6528/ac6f10

Green synthesis of DOX-loaded hollow MIL-100 (Fe) nanoparticles for anticancer treatment by targeting mitochondria

Yechuan Zhang[1], Zhengxiang Gu[2], Seonho Yun[1], Kui Luo[2,*], Jingxiu Bi[1,*], Yan Jiao[1,*] and Hu Zhang[3,*]

[1] School of Chemical Engineering and Advanced Materials, The University of Adelaide, SA 5005, Australia
[2] Huaxi MR Research Center (HMRRC), Department of Radiology, National Clinical Research Center for Geriatrics, Frontiers Science Center for Disease-Related Molecular Network, State Key Laboratory of Biotherapy, West China Hospital, Sichuan University, Chengdu 610041, People's Republic of China
[3] Riggs School of Applied Life Sciences, Keck Graduate Institute, CA 91711, United States of America

E-mail: luokui@scu.edu.cn, jingxiu.bi@adelaide.edu.au, yan.jiao@adelaide.edu.au and hu_zhang@kgi.edu

Received 27 January 2022, revised 9 May 2022
Accepted for publication 12 May 2022
Published 1 June 2022

Abstract

Fe-based metal-organic frameworks (MOFs) are promising drug delivery materials due to their large surface area, high stability, and biocompatibility. However, their drug loading capacity is constrained by their small pore size, and a further improvement in their drug capacity is needed. In this work, we report an effective and green structural modification strategy to improve drug loading capacity for Fe-based MOFs. Our strategy is to grow MIL-100 (Fe) on carboxylate-terminated polystyrene (PS-COOH) via a sustainable route, which creates a large inner cavity as well as exposure to more functional groups that benefit drug loading capacity. We employ the scanning electron microscope and transmission electron microscope to confirm the hollow structure of MIL-100 (Fe). Up to 30% of drug loading capacity has been demonstrated in our study. We also conduct cell viability tests to investigate its therapeutic effects on breast cancer cells (MDA-MB-231). Confocal laser scanning microscopy imaging confirms cellular uptake and mitochondrial targeting function of doxorubicin-loaded H-M (DOX@H-M) nanoparticles. JC-1 staining of cancer cells reveals a significant change in the mitochondrial membrane potential, indicating the mitochondrial dysfunction and apoptosis of tumor cells. Our study paves the way for the facile synthesis of hollow structural MOFs and demonstrates the potential of applying Fe-based MOFs in breast cancer treatment.

Supplementary material for this article is available online

Keywords: metal-organic frameworks (MOFs), green synthesis, hollow structure, drug delivery, mitochondria targeting, cancer treatment

(Some figures may appear in colour only in the online journal)

1. Introduction

Cancer remains the second largest threat to human health [1]. Lung cancer and breast cancer are two leading causes of cancer death, with 18.4% and 11.6% fatality rates, respectively [2]. For the treatment of cancer, substantial attempts have been made to design better drug delivery platforms to increase drug loading capacity and to realize controlled and targeted drug release [3]. Doxorubicin (DOX) is one of the effective chemotherapeutic drugs applied in the treatment of a variety of cancers, including breast cancer and ovarian cancer [4]. However, doxorubicin has cytotoxicity

* Authors to whom any correspondence should be addressed.

towards normal cells as well as cancer cells. Therefore, the construction of an effective drug delivery system with tumor cell targeting and controlled drug release is important. Various drug nanocarriers have been designed to improve the therapeutic effect on cancer including liposomes [5], micelles [6], polymers [7], polymeric nanoparticles [8], and inorganic nanoparticles [9]. Nevertheless, metal-organic frameworks (MOFs), an emerging porous nanomaterial, have not been explored extensively [10]. Since a crystalline nanostructure of MOFs consists of metal ions and organic ligands in specific directional arrays, they hold enormous potential in many applications [11–13], including drug delivery [14].

In contrast with other drug carriers, nanoporous MOFs [15] possess a high loading capacity resulting from their large pore volume, high surface area, and tunable pore sizes by employing different organic ligands [16]. Many published studies focus on the modifications of one of the zinc-based MOFs (ZIF-8) for potential anticancer drug delivery application due to its effectiveness in pH-responsive. However, its limited pore size hampers further enhancement in the drug loading capacity. MIL-100 (Fe), which consists of metal iron trimers and trimesic acid (H_3BTC), exhibits an octahedral structure and a nanocage diameter of 29 Å, which is slightly larger than a single doxorubicin molecule [17]. This size similarity may contribute to the entrapment and controlled release of doxorubicin molecules. Previous studies employ the size similarity of MOFs and biomolecules for the purpose of the entrapment of guest molecules [18]. In this context, MIL-100 (Fe) might be a MOF candidate as an effective drug delivery carrier. Additionally, MIL-100 (Fe) has been demonstrated to have great biocompatibility for clinical application [19]. Ferey *et al* used MIL-100 (Fe) as a drug carrier for ibuprofen delivery [20]. The same group further demonstrated the feasibility of utilizing MIL-100 (Fe) as a drug carrier for doxorubicin with no observed burst release [21]. However, the drug loading capacity of MIL-100 (Fe) has not been significantly improved in these studies.

General approaches to boost the drug loading capacity of MOFs are mainly structural modifications; e.g. (1) modification of MOF surface by functional groups to enable the potential conjugation with anticancer drugs, or (2) construction of hollow structures within MOFs by growing them on templates. For the latter method, a hollow structure creates a 150 nm inner cavity in addition to the intrinsic pores possessed by MOF, and may potentially increase the drug loading capacity. For example, a hollow structural modification was realized on ZIF-8 [22], and hollow mesoporous ZIF-8-coated silica nanoparticles were used for the controlled release of doxorubicin[3b]. However, the particle size of ZIF-8-coated silica nanoparticles exceeds 500 nm, which makes it extremely challenging for the cellular internalization of these nanoparticles. In this regard, the synthesis of hollow structured MOFs with appropriate particle size is much needed and might be realized by adopting MIL-100 (Fe) due to its appropriate nanocages size for drugs like doxorubicin.

Herein, we explored the green synthesis of hollow structural MIL-100 (Fe) to achieve a higher loading capacity of doxorubicin. The formation process of H-M involves no hazardous chemicals and solvents while generating no toxic residues, and it consumes less energy. DMF was only used for washing off the PS-COOH template, and it can be recycled after the washing process. No autoclave and heating furnace was employed in our method, thus consuming less energy than the traditional solvothermal method. Hollow structural MIL-100 (Fe) nanoparticles (H-M NPs) were obtained through growing MIL-100 (Fe) on carboxylate-terminated polystyrene (PS-COOH) templates at room temperature under ambient pressure. The growth of the uniform MIL-100 (Fe) shell was achieved by controlling the molar ratio of Fe^{2+}, BTC^{3-}, and PS-COOH and dropwise addition of H_3BTC solution. Different from previous reports, H-M NPs in the present work were obtained without applying high pressure, high temperature, or organic solvent. This methodology is sustainable and enables up-scalable fabrication. The as-synthesized H-M NPs with high porosity demonstrated a high drug loading capacity, controlled release of DOX, efficient cellular uptake, and high biocompatibility owing to the facile removal of DMF with great potential as a drug delivery platform.

2. Materials and methods

2.1. Materials

Styrene (St), Acrylic acid (AA), Methyl methacrylate (MMA), Ammonium Bicarbonate (NH_4HCO_3), Ammonium Persulfate ($(NH_4)_2S_2O_8$), Ferrous chloride ($FeCl_2{\cdot}4H_2O$), Iron chloride ($FeCl_3{\cdot}6H_2O$), Trimesic acid (H_3BTC), Dimethylformamide (DMF), and Doxorubicin hydrochloride were purchased from Sigma-Aldrich without further purification. The most relevant materials synthesis methods are summarized in the following section. Apparatus and other methods are listed in the supporting information.

2.2. Fabrication of H-M NPs

The methodology of manufacturing H-M was developed from the literature [22, 23]. The schematic process of H-M NPs fabrication is shown in figure S1 (available online at stacks.iop.org/NANO/33/345601/mmedia). Solution 1 contained 2.26 g $FeCl_2{\cdot}4H_2O$ and 500 mg PS-COOH dissolved in 97.2 g H_2O. Solution 1 was ultrasonicated for 10 min. Solution 2 was prepared by dissolving 1.676 g trimesic acid in 23.72 g 1 M NaOH aqueous solution. After Solution 2 was completely clear, it was dropwise added to Solution 1 under magnetic stirring for 24 h at room temperature. The obtained solid MIL-100 (Fe) with PS-COOH cores were separated by centrifugation and then washed with deionized water and ethanol three times respectively. After the sample was dried under vacuum, it was dispersed in 150 ml DMF in a one-neck flask under magnetic stirring at 120 °C for 24 h to remove PS-COOH. H-M were washed with ethanol and deionized water three times, respectively. H-M was then dried at 160 °C for 6 h to ensure that DMF is completely evaporated. H-M was activated under vacuum before the drug loading process.

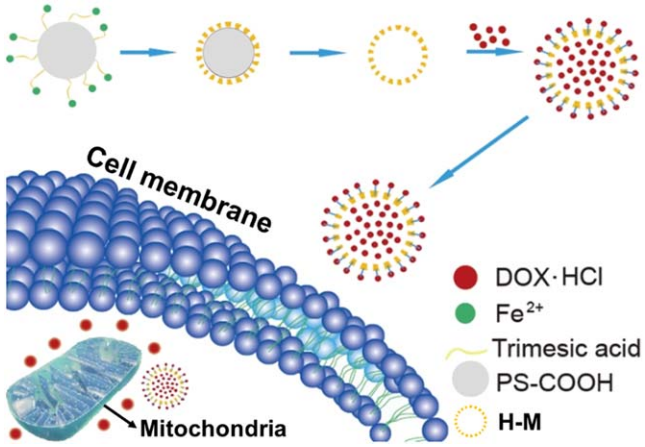

Figure 1. The schematic diagram for the synthesis procedure of H-M NP and its mitochondria-targeting process. Fe^{2+} coordinates with the −COOH on the surface of PS and reacts with trimesic acid to grow the outer shell of MIL-100 (Fe). PS-COOH core is then removed to obtain H-M. DOX·HCl molecules are loaded into H-M NPs after PS-COOH templates are removed. DOX@H-M are delivered into breast cancer cells to target mitochondria and induce apoptosis.

2.3. Fabrication of H-F NPs

The methodology of fabricating H-F NPs, a control sample for this study, was similar to that for H-M NPs. Solution 1 was prepared by dissolving 0.508 g $FeCl_3{\cdot}6H_2O$ and 0.250 g PS-COOH in 10 g H_2O. Solution 1 was ultrasonicated for 10 min and magnetically stirred for 15 min 0.263 g H_3BTC was added to 10.150 g 1 M NaOH aqueous solution as Solution 2. Solution 2 was dropwise added to Solution 1 under magnetic stirring. The reaction continued for two hours. Brownish orange solids were separated by centrifugation at 3800 rpm and then placed into a one-neck flask containing 150 ml DMF to remove PS-COOH. The removal of the template took place under magnetic stirring at 120 °C for 24 h. The H-F product was washed with ethanol and deionized water three times and dried under vacuum.

3. Results and discussion

3.1. Materials characterization

The scheme of fabricating H-M as well as its application in mitochondrial targeting are exhibited in figure 1. Different from traditional solvothermal methodology, green synthesis of H-M does not have organic solvent residues left in the nanopores of MOFs which may pose toxicity concerns for MOFs as drug carriers [23, 24]. To the best of our knowledge, it is the first time that hollow structural MIL-100 (Fe) is synthesized under an ambient environment without organic solvents. PS-COOH template (figure S2) possesses a negative charge, which enables the initial electrostatic interaction with Fe^{2+} in an aqueous solution during the synthetic process. MIL-100 (Fe) nanoparticles without a hollow structure, semi-amorphous Fe-BTC, and H-F were also synthesized as controls to investigate the impact of a larger surface area and an inner cavity on the efficiency in DOX loading and release. The structure of H-M and MIL-100 (Fe) nanoparticles was characterized via scanning electron microscopy (SEM) and transmission electron microscopy (TEM). An octahedral morphology of MIL-100 (Fe) synthesized by Fe^{2+} and H_3BTC is shown in figure 2(a). The observed structures are similar to those in other reports, which were also synthesized at room temperature [25], confirming the formation of a typical crystalline structure of MIL-100 (Fe). The diameter of the octahedral nanoparticles is around 500 nm. An irregular morphology of Fe-BTC obtained from $Fe3^+$ and H_3BTC is exhibited in figure 2(b). Compared with the Fe-BTC having the PS-COOH core (figure 2(c)), the hollow structure of H-F is observed under the TEM image in figure 2(d). The shell of H-F shows neither uniform nor smooth morphology due to its semi-amorphous nature. According to the comparison between figures 2(e) and (f), the formation of a solid MIL-100 (Fe) shell and an inner cavity is clearly shown by the contrast of black and light grey colors. The morphology of the H-M is smooth compared with H-F, which may be attributed to the process of crystallization on the surface of the PS-COOH template, intending to grow a shell cycle by cycle.

Powder x-ray diffraction (XRD) was applied to confirm the crystalline structures of MIL-100 (Fe) and H-M NPs. The XRD patterns of H-M NPs, MIL-100 (Fe), and Fe-BTC are shown in figure 2 (g). XRD patterns show two typical peaks at 2θ of 10.9° and 13.1° for H-M and MIL-100 (Fe) nanoparticles, indicating the crystal structure of MIL-100 (Fe). The relative intensity of these two peaks is consistent with samples prepared using similar synthesis conditions (room temperature, ambient pressure, and water as the solvent) [26], and is slightly different from published literature with an organic solvent at high pressure and temperature [27, 28]. Figure 2(g) also indicates the semi-amorphous nature of the Fe-BTC sample as no certain peak is observed in the XRD spectrum. Although Fe-BTC and MIL-100 (Fe) samples are formed from the same iron ion and organic ligand BTC^{3-}, the starting oxidation status of irons are different: Fe^{2+} and Fe^{3+} are used for Fe-BTC and MIL-100 (Fe) samples respectively. Therefore, the structural difference between the two samples lies in the oxidation process from Fe^{2+} to Fe^{3+} for MIL-100 (Fe) [23]. Fe^{3+} state is analyzed by the x-ray photoelectron spectroscopy (XPS) in figure S3, confirming the oxidation process from Fe^{2+} to Fe^{3+} in H-M NPs.

3.2. Inner cavity characterization

The drug loading capacity (table 1) and the loading mechanism of H-M nanoparticles were first investigated by the nitrogen adsorption/desorption curve (figure 2(h)).

A minor difference in the drug loading capacity between Fe-BTC and H-F may be due to the semi-amorphous nature of these materials. The outer shell of H-F is not composed of regular microporous channels according to its semi-amorphous nature, which does not allow doxorubicin molecules to flow into the inner cavity of H-F samples. In contrast, the difference in the drug loading capacity between MIL-100 (Fe) and H-M NPs is 7.7%, much greater than the difference of

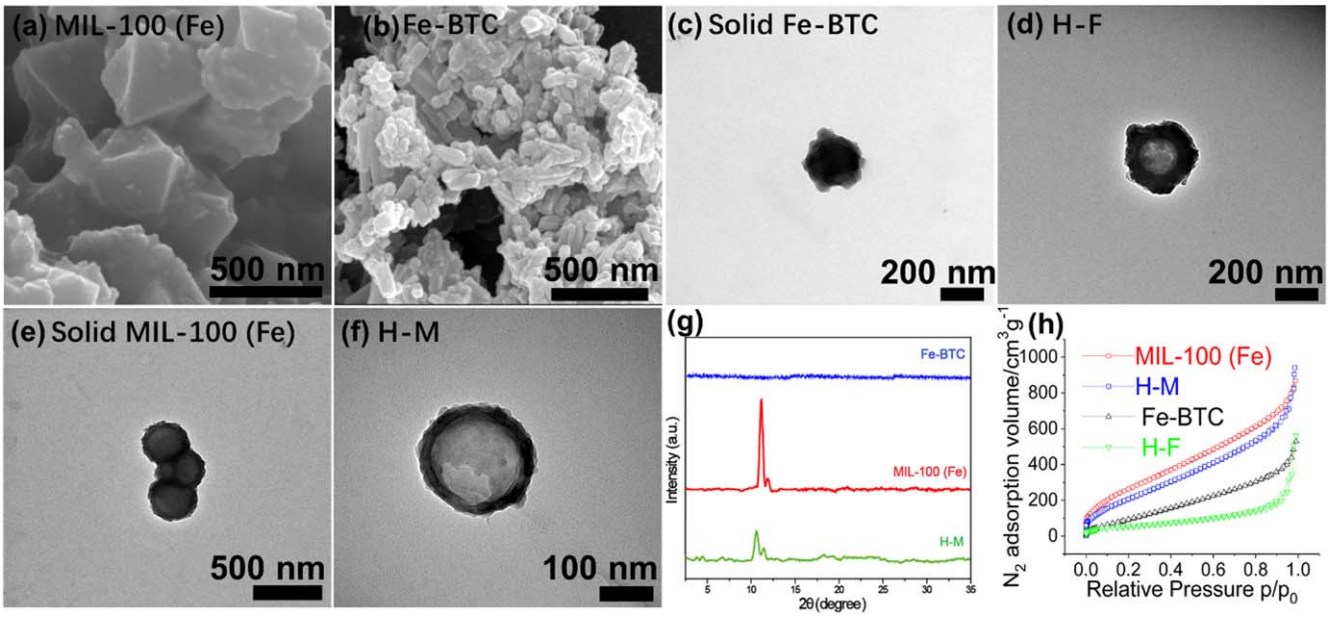

Figure 2. (a) SEM image of MIL-100 (Fe) prepared by green synthesis method. (b) SEM image of Fe-BTC synthesized by Fe^{3+} and H_3BTC. TEM images of (c) solid Fe-BTC with PS-COOH core, (d) H-F, (e) Solid MIL-100 (Fe) with PS-COOH core, and (f) H-M NPs. Figure 2(g) shows the XRD patterns of H-M, MIL-100 (Fe), and Fe-BTC. Figure (h) exhibits the N_2 adsorption/desorption isotherm curves of MIL-100 (Fe), H-M, Fe-BTC, and H-F.

Table 1. DOX loading capacity of four drug carriers, zeta potential of all samples, polydispersion index (PDI) and particle size of DOX@H-M measured in pH = 7.0 deionized water via DLS.

Sample	DOX loading capacity (%)	Zeta potential (mV)	PDI	Particle size (nm)
Fe-BTC	13.5	−10.7	—	—
H-F	14.7	−9.1	0.282	183
MIL-100 (Fe)	22.3	−17.6	—	—
H-M	30.0	−15.3	0.235	171
COOH-PS	—	−11.9	0.097	162
DOX@H-M	—	+12.0	0.268	170

Table 2. Textural properties of four samples prepared at room temperature. S_{BET}: BET surface area. $S_{langmuir}$: langmuir surface area. P_d: average pore diameter. V_p: BJH adsorption cumulative volume of pores.

Sample	S_{BET} ($m^2\ g^{-1}$)	$S_{langmuir}$ ($m^2\ g^{-1}$)	P_d (Å)	V_p ($cm^3\ g^{-1}$)
Fe-BTC	239	1448	5.43	0.49
H-F	155	479	8.90	0.25
MIL-100 (Fe)	679	2568	9.87	0.88
H-M	487	2261	9.98	0.83

1.2% between Fe-BTC and H-F. Therefore, the hollow structure Nitrogen adsorption and desorption experiment based on the Brunauer–Emmett–Teller (BET) and Langmuir theory is conducted to confirm a microporous structure and an inner cavity in H-M NPs.

MIL-100 (Fe) and H-M NPs exhibit a significantly higher nitrogen uptake than that of Fe-BTC and H-F at a relative pressure of less than 0.01, which indicates the microporous configuration of MIL-100 (Fe) [29]. The pattern of isotherms curves of MIL-100 (Fe) is similar to that in the published literature [30]. H-M NPs have a higher nitrogen uptake at a relative pressure greater than 0.95, demonstrating its characteristic microporous structure, also confirming a large inner cavity and a hollow structure in H-M NPs. The adsorption/desorption isotherms of Fe-BTC and H-F indicate low nitrogen uptakes at a relative pressure of less than 0.1 due to the absence of micropores in both nanoparticles. A sudden increase in nitrogen uptake and a large amount of nitrogen are observed for H-F at relative pressure higher than 0.9 since a great nitrogen uptake and a steep slope in the adsorption curve are often observed for macroporous and non-porous structures under this pressure condition.

The BET surface area, Langmuir surface area, average pore diameter, and Barrett–Joyner–Halenda (BJH) adsorption cumulative pore volume of four samples are listed in table 2. There is a distinct difference between semi-amorphous nanoparticles (Fe-BTC and H-F) and MOFs crystalline nanoparticles (MIL-100 (Fe) and H-M NPs) in terms of both microporous volume and surface area. Semi-amorphous Fe-BTC and H-F possess smaller nanocages than crystalline MIL-100 (Fe) and H-M NPs according to the pore diameter, which leads to lower BET surface area, Langmuir surface area, and cumulative pore volume. H-F and H-M nanoparticles have a larger average pore diameter than Fe-BTC and MIL-100 (Fe), possibly because of the inner cavity in both nanoparticles. A lower cumulative pore volume in H-F and H-M NPs than that in Fe-BTC and MIL-100 (Fe) suggested there is a large inner cavity and a hollow structure in both H-F and H-M NPs. The thickness of the film adsorbed

Table 3. FT-IR peaks and associated functional groups of MIL-100 (Fe).

Peaks wavenumbers (cm^{-1})	Functional group
710	C–H bending
759	C–H bending
1378	Symmetric –O–C–O–
1439	Asymmetric –O–C–O–
1615	C–O bond of the carboxylate group
3222	Associated –OH

on the pore wall is an important factor in the model for calculating the BJH pore volume. Therefore, the inner cavity occupies most of the space in the H-F and H-M NPs, resulting in fewer pores and pore walls than non-hollow Fe-BTC and MIL-100 (Fe).

3.3. Drug loading and release study

The drug loading capacity of both Fe-BTC and MIL-100 (Fe) is higher than that in the published reports [17, 31]. We hypothesized that the mechanism of loading doxorubicin could include electrostatic interactions apart from physical adsorption. In this section, the drug loading mechanism including the electrostatic interaction and the functional group on the surface of H-M are investigated via zeta potential (table 1) and FT-IR spectrum (table 3). Doxorubicin is highly protonated and has a positive charge in an aqueous solution because of the presence of hydrochloride in the drug molecule. The negative zeta potential of four samples is shown in table 1. MIL-100 (Fe) and H-M have a negative value of −17.6 and −15.3 mV, corresponding to a higher drug loading capacity of 22.3% and 30.0%. After incorporation of DOX·HCl, DOX@H-M NPs exhibit a positive charge of 12 mV. A high payload of highly protonated DOX·HCl molecules results in reversing the charge of H-M NPs. The zeta potential values from H-M and DOX@H-M obtained from dynamic light scattering (DLS) suggested there are electrostatic interactions between H-M NPs with a negative charge and doxorubicin with a positive charge. Fourier-transform infrared spectroscopy (FTIR) spectra of MIL-100 (Fe) indicate the negative zeta potential is derived from the carboxylate groups. A negative charge of four samples could be ascribed to carboxylate groups on a PS-COOH template which was confirmed from FTIR spectra of MIL-100 (Fe) and H-M (figure S4). Peaks of MIL-100 (Fe) are found to be identical to those reported in the [32]. The peak at 1615 cm^{-1} corresponds to the C–O bond of carboxylate groups (table 3). The bands of 1378 and 1439 cm^{-1} result from symmetric and asymmetric vibrational bands of –O–C–O– group [33]. The peaks at 759 and 710 cm^{-1} are ascribed to C–H bending vibrations of benzene [34]. The broad peak at 3222 cm^{-1} corresponds to the associated –OH in the carboxylate group. The FTIR spectrum of H-M is similar to that of MIL-100 (Fe), indicating the introduction of the hollow structure in H-M does not change the bending and vibrations of chemical bonds in MIL-100(Fe).

DOX release from four samples was monitored by recording its UV–vis absorbance values in the solution. The drug release pattern from four samples in the short-term and long-term are shown in figure 3. Figure 3(a) shows DOX release profiles in the first 4.5 h from four samples. More than 35% of DOX is released from DOX@Fe-BTC and DOX@H-F with a burst effect. The burst effect is controlled in DOX@MIL-100 (Fe) and DOX@H-M as less than 28% of DOX is released in the first 4.5 h. The difference in the percentage of DOX released in the first 4.5 h may lie in different electrostatic interaction strengths between nanoparticle carriers and protonated DOX molecules. MIL-100 (Fe) and H-M have a higher negative charge, leading to stronger electrostatic interactions and slower DOX release rates. 77% of DOX is released from DOX@MIL-100 (Fe) and DOX@H-M at 96 h, while more than 85% is released from DOX@Fe-BTC and DOX@H-F at the same time point. After 96 h, the drug release rate for all carriers starts to become slower but continues to release DOX until up to 264 h (figure 3(b)). The drug release pattern of four carriers can be divided into three stages: 0–24 h, 24–96 h, and 96–264 h. At the first stage (0–24 h), the release rate is higher due to the desorption of DOX molecules from the surface of carriers. In the second stage (24–96 h), DOX continues to release at a slower rate than in the first stage. The concentration gradient becomes the driving force for the diffusion of DOX molecules from porous channels in nanoparticle carriers. In the third stage (96–246 h), DOX is released at a very low rate as the driving force for releasing DOX molecules becomes weakened. The overall release pattern from DOX@Fe-BTC and DOX@H-F is quite similar. The release pattern of DOX@H-M in the second stage differs from that of DOX@MIL-100 (Fe). A smaller amount of DOX released from DOX@H-M than DOX@MIL-100 (Fe) could be due to its smaller pore volume with a large inner cavity. A minor burst release is observed from 18 to 24 h in the release profile from DOX@H-M, which may be explained by those DOX molecules trapped in the inner cavity of H-M starting to efflux after 18 h of incubation via orbital shaking. Furthermore, by combining the drug release pattern with confocal laser scanning microscope (CLSM) images of DOX@H-M (figures S5 and S6), the controlled release of DOX@H-M is achieved by incorporating the large inner cavity and its porous MIL-100 (Fe) shell. Regular porous channels contribute to the sustained release since the DOX requires a longer time to diffuse through porous channels to be released.

3.4. Cytotoxicity study

The cytotoxicities of H-M NPs, H-F NPs, DOX@H-M, DOX@H-F, and free DOX were evaluated by measuring the cell viability using the MTT assay. The human breast cancer cell line (MDA-MB-231) was used in this experiment. The cell viability results after incubation with DOX@H-M and DOX@H-F NPs or drug carriers alone are shown in figures 4(a) and (b), respectively. An equivalent DOX concentration was used for both DOX-incorporated NPs and an equivalent drug carrier concentration for DOX-loaded NPs or

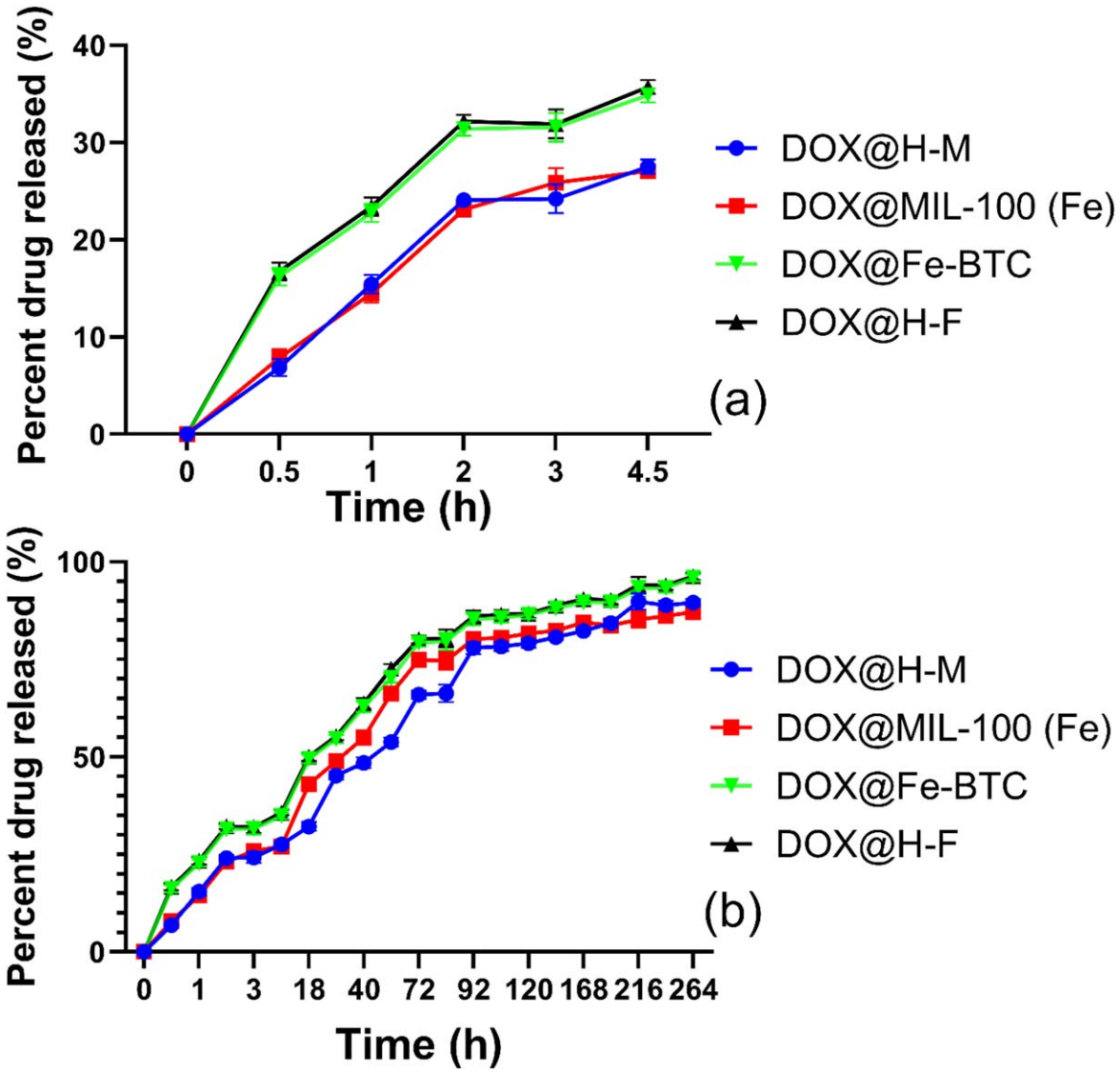

Figure 3. Drug (DOX) release performance for four DOX-loaded samples for (a) the first 4.5 h; and (b) 268 h.

NPs alone. After 24 h incubation, the cell viability decreases with an increase in the DOX concentration. It is found that the viability after treatment with both DOX@H-F and DOX@H-M is DOX dose-dependent. It is noticed that the difference in the cell viability between the treatments by DOX and DOX@H-M is pronounced in figure 4(a), indicating DOX incorporated in H-M NPs is more potent than free DOX at the equivalent DOX concentration. The cell viability after exposure to H-M NPs is similar to that with H-F NPs at the same drug carrier concentration, which indicates great cytocompatibility of H-M NPs. Semi-amorphous H-F NPs are less stable than crystalline H-M NPs in terms of degradation in an aqueous solution [35]. Figure 4(b) shows a minor difference in the cell viability after treatment with DOX and DOX@H-F. DOX@H-F shows no obvious therapeutic effect on breast cancer cells compared to free DOX. However, DOX@H-M kills more breast cancer cells compared to free DOX and DOX@H-F, which can be attributed to its higher loading capacity and porous MIL-100 (Fe) shell. The difference in the cell viability becomes evident with an increase in DOX concentration. To investigate the cytotoxicity of H-F and H-M NPs against human normal cells, human embryonic kidney cells (HEK-293T) were used. The cell viability results are shown in figure S7. A relatively high nanoparticle concentration of 100 μg ml^{-1} was applied to each sample in the experiment. The cell viability after incubation with both H-F and H-M NPs remains greater than 80% at such a high concentration. The cell viability results indicate good biocompatibility of H-F and H-M NPs, supporting the feasibility of using H-M NPs as anticancer drug carriers.

3.5. Cellular uptake

A CLSM was applied to monitor the cellular uptake of MDA-MB-231 as well as intracellular distribution of DOX@H-M and free DOX was used as a control. All fluorescence in CLSM images was captured using the pseudo colors defined by the default settings in the software. The excitation and emission wavelength of DOX used in the CLSM are 480 nm and 580 nm, respectively. The CLSM images are displayed in

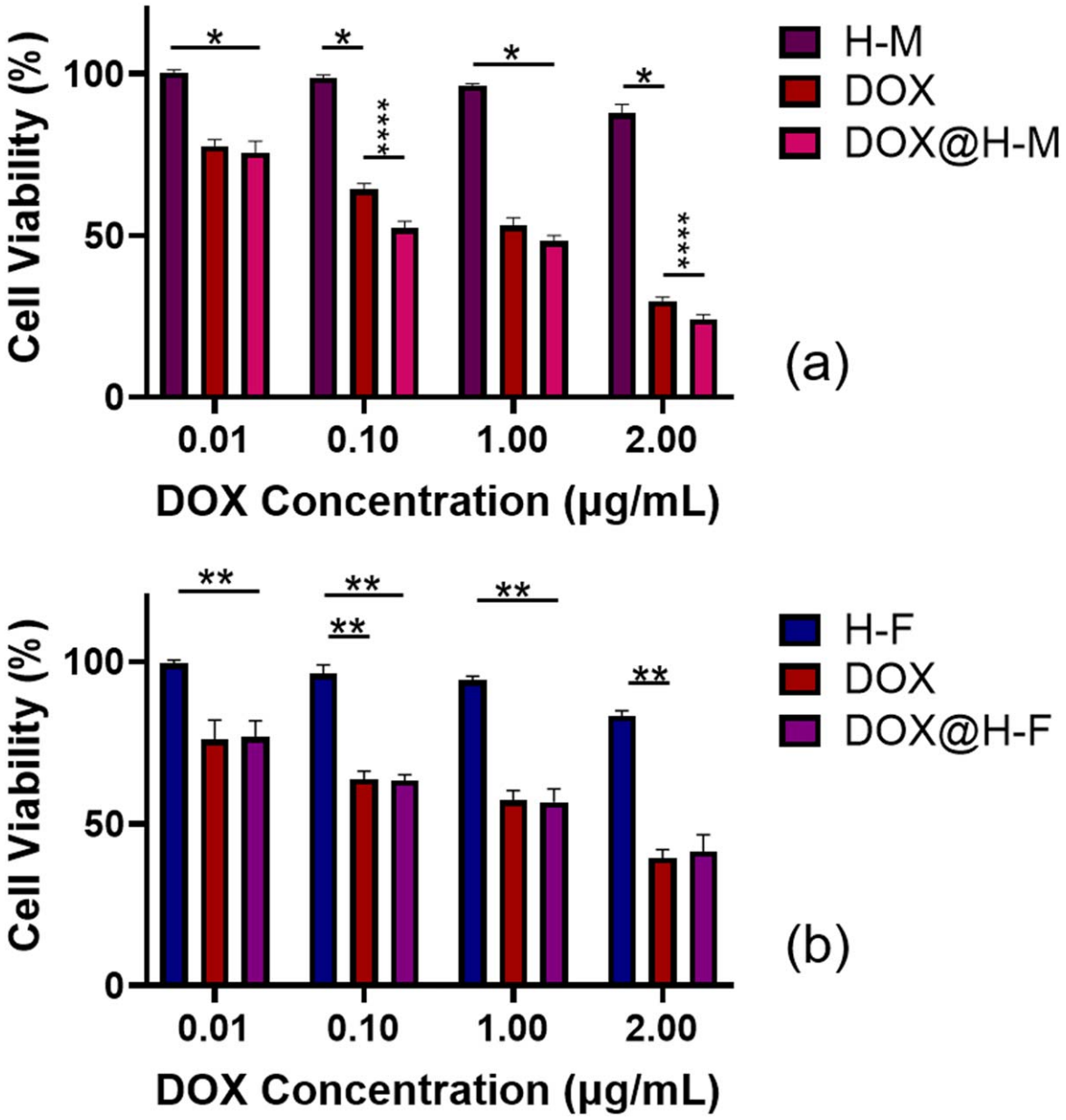

Figure 4. Cell viabilities of breast cancer cells (MDA-MB-231) after incubation with (a) H-M and (b) H-F for 24 h. DOX-loaded samples have the equivalent amount of DOX as the pure DOX group based on the drug loading capacity. One-way ANOVA results are statistically significant. *P* value summary from t-test is displayed ($P < 0.05$).

figure 5. Red fluorescence representing the cell membrane outlines breast cancer cells. In contrast with the control group without treatment with free DOX and H-M NPs, both free DOX and H-M NPs are internalized by breast cancer cells. Inside the cells, blue (nucleus) and green (DOX) are overlapped in the merged image to produce a cyan color in both free DOX- and DOX@H-M-treated groups, indicating DOX is located inside the nucleus. However, a difference in the distribution of green fluorescence (DOX) between the two groups. In the free DOX-treated cells, DOX is observed to accumulate in the nucleus. Free DOX molecules enter cells through molecular diffusion. Inside cells, they rapidly migrate into the nucleus and poison topoisomerase-II, leading to the damage of DNA chains, interference with replication, and finally cell death [36]. In the DOX@H-M-treated group, DOX not only localizes inside the nucleus but also distributes in the cytoplasm. However, DOX@H-M at a size of 170 nm may be endocytosed into cells. Due to its positive charge, DOX@H-M may escape from late endosomes/lysosomes. During this process, DOX may be released from the DOX-loaded nanoparticles and enter the nucleus. DOX-loaded nanoparticles with unreleased DOX are retained in the

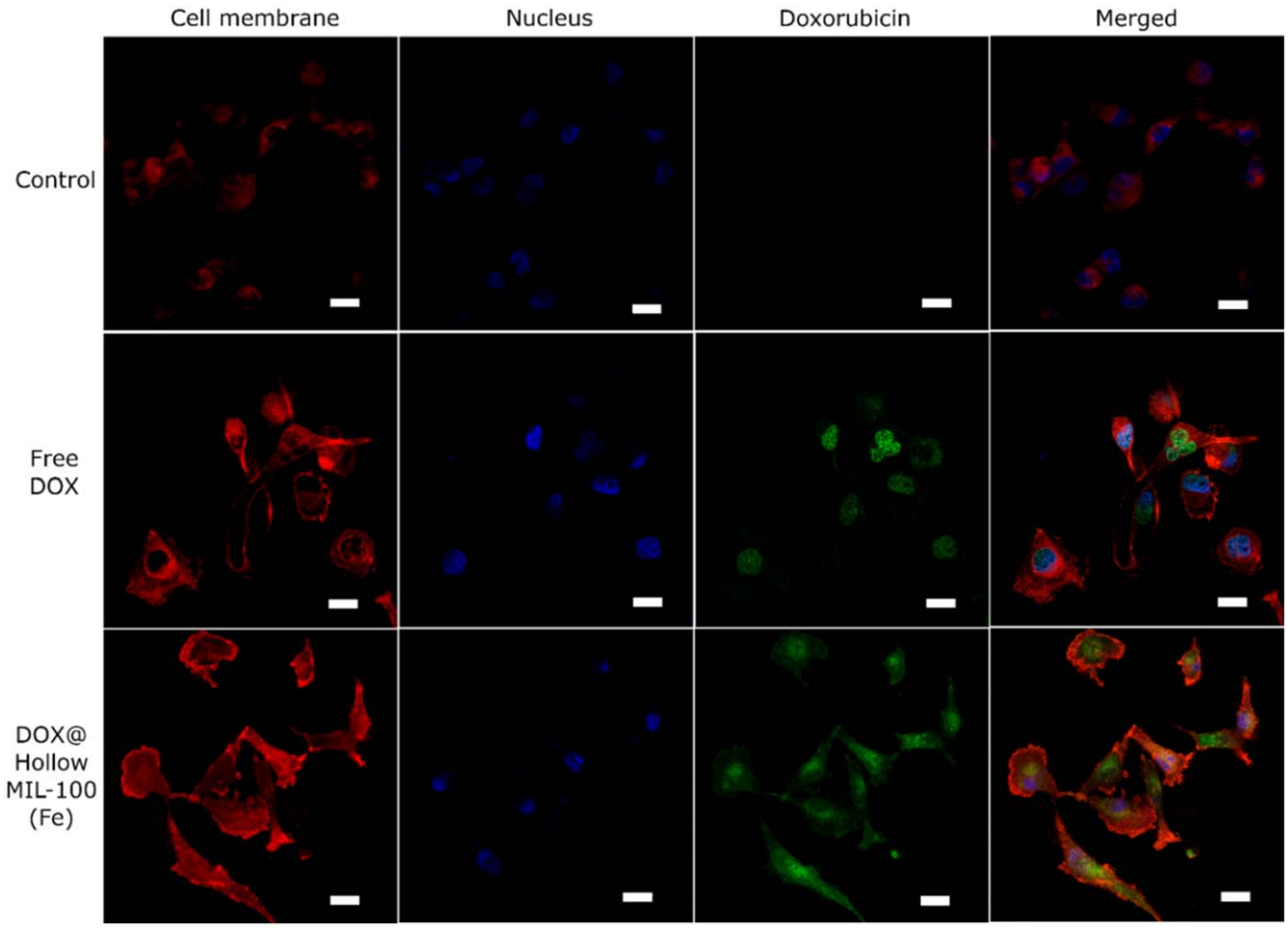

Figure 5. CLSM images of MDA-MB-231 cultured with the control group (untreated), free DOX (5 μg ml^{-1}), and DOX@Hollow MIL-100 (Fe) (5 μg DOX ml^{-1}) for 4 h, confirming the cellular uptake of DOX@Hollow MIL-100 (Fe). Red: Cell membrane. Blue: Cell nucleus. Green: Doxorubicin. Scale bar: 20 μm. (All colors are pseudo colors generated automatically by the CLSM.)

cytoplasm after they escape from late endosomes/lysosomes. The CLSM images may suggest the cytotoxic mechanisms from DOX@H-M nanoparticles may be different from free DOX.

3.6. Mitochondrial targeting

To further reveal the intracellular location of DOX@H-M NPs in the cytoplasm, MitoTracker™ Deep Red was applied to stain the mitochondria, and cells were then observed under a CLSM. Variations of DOX distribution inside MDA-MB-231 cells are detected after treatment with free DOX and DOX@H-M (figure 6). Distinct blue (nucleus) and red (mitochondria) fluorescence in the merged image are seen in the control group without any treatment. After four hours of incubation with free DOX, cyan as a result of overlapping blue and green is seen in the nucleus in the free DOX-treated group, which is in agreement with the images in figure 5. There is no overlapping of red (mitochondria) and green (DOX) in the group. This result indicates that free DOX barely targets the mitochondria but enters the nucleus [37]. Nevertheless, cyan and yellow as a result of overlapping red (mitochondria) and green (DOX) are observed in the cells treated with DOX@H-M nanoparticles, suggesting DOX@H-M nanoparticles are accumulated in the mitochondria after escaping from endosomes/lysosomes. Moreover, the blue signal (nucleus) is very strong in the merged image in DOX@H-M-treated cells, which indicates that the majority of DOX is still retained in DOX@H-M NPs accumulated in the mitochondria. DOX@H-M NPs have a similar intracellular distribution as triphenylphosphine-modified NPs which are also positively charged, [38] suggesting the positive-charged DOX@H-M NPs could target the mitochondria for exerting their therapeutic effect in tumor cells. The mechanism of mitochondrial targeting is based on the positive charge of the nanoparticles. One typical mitochondrial targeting component is triphenylphosphonium (TPP) cation, consisting of a positively charged phosphorus atom with three phenyl groups. The molecular structure of TPP determines its hydrophobic characteristic with the delocalized pi bond [39]. After DOX was conjugated with −COOH on the surface of hollow MIL-100 (Fe), the delocalized pi bond was added, which is similar to the TPP moiety. The mitochondrial targeting mechanism of DOX@H-M lies in the positive charge and delocalized pi bond of the molecule [40].

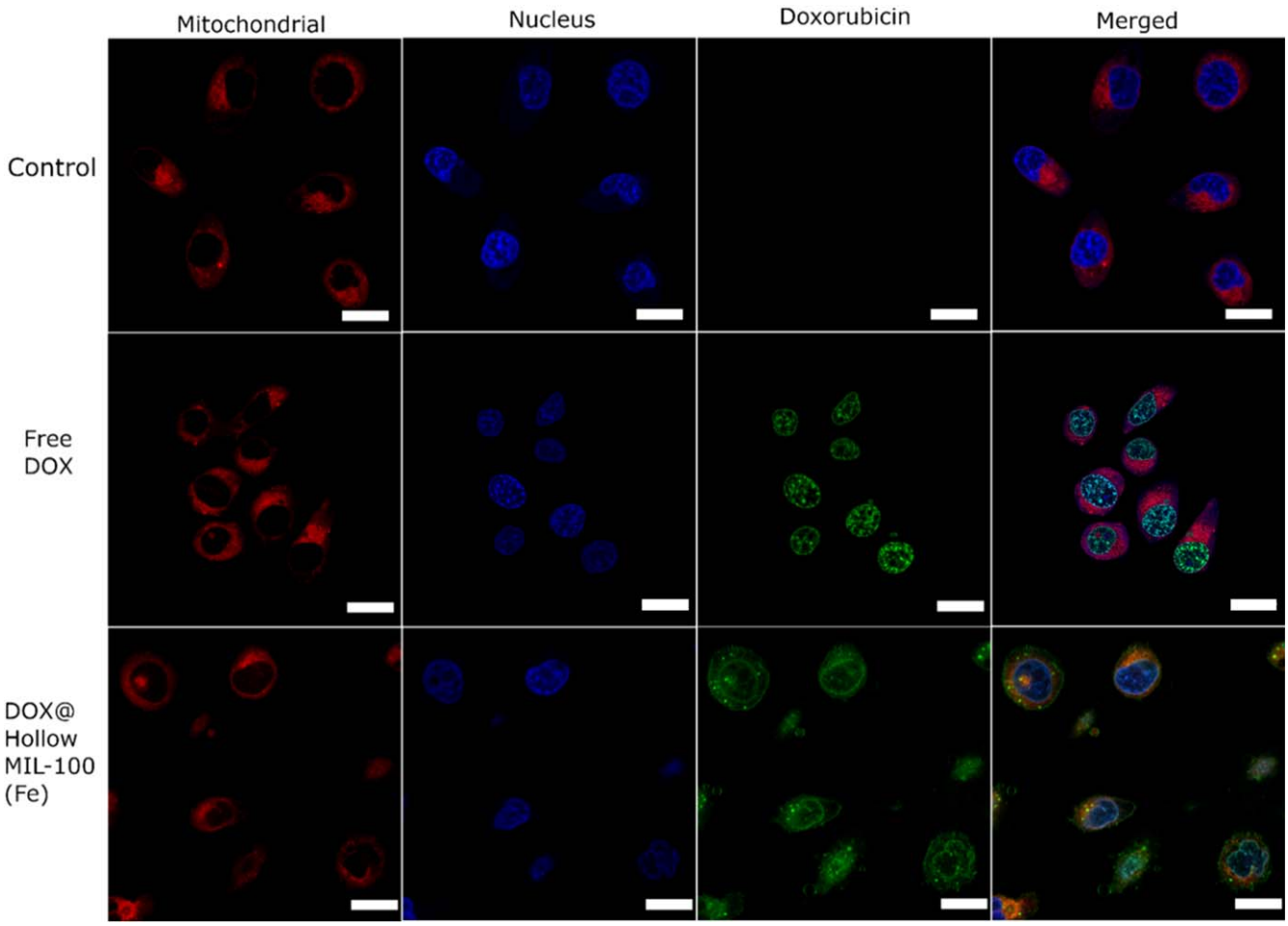

Figure 6. CLSM images of MDA-MB-231 cultured with the control group (untreated), free DOX (5 μg ml^{-1}), and DOX@Hollow MIL-100 (Fe) (5 μg DOX ml^{-1}) for 4 h, which demonstrates the mitochondrial targeting of DOX@Hollow MIL-100 (Fe). Red: Mitochondria. Blue: Cell nucleus. Green: Doxorubicin. Scale bar: 20 μm. (All colors are pseudo colors generated automatically by the CLSM.)

Mitochondrial dysfunction has been recognized as one of the mechanisms for DOX-induced apoptosis [41]. The mitochondrial transmembrane potential (MMP) results from a difference between a positive charge from the mitochondrial intermembrane space (IMS) and a negative charge from the mitochondrial matrix [42]. Delocalized lipophilic cations (DLC) are amphipathic cationic compounds with delocalized electrons, giving the whole molecule a positive charge. Triphenylphosphine (TPP) and dequalinium (DQA) are two typical DLC employed in drug delivery for mitochondrial targeting [43, 44]. In addition, nanoparticles with a strong positive surface charge, such as single-walled carbon nanotubes, have also been explored for targeting mitochondria [45, 46]. In our work, DOX@H-M nanoparticles are positively charged (table 1) after loading with DOX·HCl, and they have the potential of targeting mitochondria after they are internalized into cancer cells. Monitoring of the MMP change was conducted to confirm that DOX@H-M NPs may damage the mitochondria of MDA-MB-231 cells. A JC-1 dye was used as an indicator for changes in the MMP because of its interactions with respiring mitochondrial membrane [47]. The J-aggregate (green) dominates on the mitochondrial membrane of healthy cells at a higher MMP, while the J-monomer (red) appears on the mitochondrial membrane of injured cells as the MMP decreases. CLSM images of JC-1 stained MDA-MB-231 cells after treatment with free DOX (fuchsia) and DOX@H-M NPs are displayed in figure 7. DOX has an emission wavelength of 595 nm, and the JC-1 aggregate has an emission wavelength range of 570–600 nm. The overlapping of the emission wavelength from DOX and the JC-1 aggregate may interfere with the results of the MMP change. To address this issue, two control samples were used in this experiment: control sample 1 for cells treated with 2 × IC50 free DOX for 12 h without JC-1 staining and control sample 2 for cells stained by JC-1 without any pretreatment with DOX. No fluorescence signal is detected in the J-monomer channel of control sample 1, while fluorescence signals are captured in both channels for J-aggregate and DOX because of the overlapping of their emission wavelengths but they are located inside the nucleus. In control sample 2, both red and green fluorescence is seen on the mitochondrial membrane, and the fluorescence signals are around the nucleus. Although free DOX fluorescence may interfere with that from the J-aggregate channel, the fluorescence signal shows the solid oval pattern in the nucleus, while the JC-1 stained area shapes as a hollow oval pattern. A previous study confirmed a similar hollow oval pattern for the JC-1 dye [48]. An increase in the ratio of the red-to-green signal in the hollow oval area in the

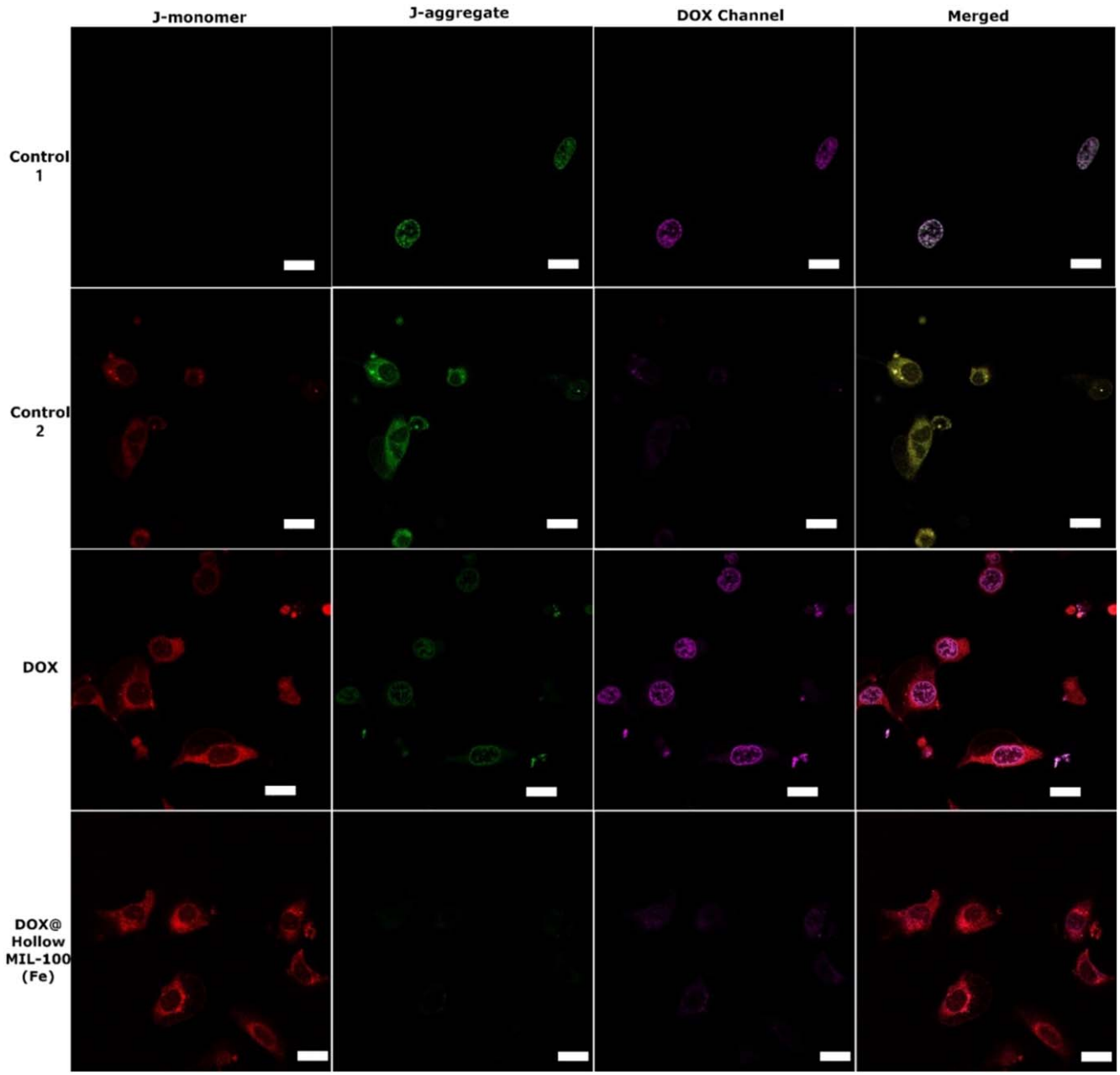

Figure 7. CLSM images for monitoring the mitochondrial membrane potential (MMP) after JC-1 staining of MDA-MB-231 cells incubated with DOX and DOX@Hollw MIL-100 (Fe) at a DOX concentration of 2 × IC50, illustrating the change of MMP and the damage of mitochondria after incorporating DOX@Hollow MIL-100 (Fe). Control 1: cells treated with 2 × IC50 DOX. Control 2: cells treated with 2.5 μg ml^{-1} JC-1. IC50 of DOX: 1.1 μg ml^{-1}. Red: J-monomer. Green: J-aggregate. Fuchsia: DOX. Scale bar: 20 μm. (All colors are pseudo colors generated automatically by the CLSM.)

DOX@H-M-treated group in comparison with control sample 2 indicates a decrease in the MMP. Thus, tumor cells could be killed due to the damage of mitochondria by the accumulated DOX@H-M NPs, apart from DNA damage by free DOX released from DOX@H-M NPs.

4. Conclusion

A green synthesis method was developed for the synthesis of H-M NPs by employing a PS-COOH template with carboxylate groups at room temperature and ambient pressure in an aqueous solution, resulting in great biocompatibility of the synthesized nanoparticles. A high loading capacity of up to 30.0%, much higher than the non-hollow structural one, is found for the H-M NPs as a drug carrier due to the presence of a large inner cavity up to 180 nm and a microporous outer shell as well as electrostatic interaction between a negative surface charge of the drug carrier and DOX·HCl [49]. In contrast with the previous report, the high anti-tumor efficacy of DOX@H-M NPs against breast cancer cells could be ascribed to the accumulation of DOX@H-M in the

mitochondria and damage to the mitochondria [50]. Our study opens a new avenue for green synthesis of hollow-structural MIL-100 (Fe) with great biocompatibility as a drug delivery carrier due to its, high DOX loading capacity as well as its ability to target and damage mitochondria in tumor cells. Structural modifications on MOFs will explore more potential in boosting drug loading capacity and tumor cell targeting in the near future.

Acknowledgments

This work is supported by The University of Adelaide International Wildcard Scholarship. We thank Prof. Colin Raston and Dr Daniel Mangos from Flinders University for providing the instrument of nitrogen adsorption/desorption.

Data availability statement

All data that support the findings of this study are included within the article (and any supplementary files).

Conflict of interest

The authors declare that they have no conflict of interest.

ORCID iDs

Yechuan Zhang https://orcid.org/0000-0002-9396-8234
Kui Luo https://orcid.org/0000-0002-3536-1485

References

[1] Siegel R L, Miller K D and Jemal A 2019 *Ca-Cancer J. Clin.* **69** 7–34
[2] Bray F, Ferlay J, Soerjomataram I, Siegel R L, Torre L A and Jemal A 2018 *Ca-Cancer J. Clin.* **68** 394–424
[3] Song M R, Li D Y, Nian F Y, Xue J P and Chen J J 2018 *J Mater Sci* **53** 2351–61
Jia X M *et al* 2018 *Chemmedchem* **13** 400–5
Wu Z F, Hao N, Zhang H, Guo Z Y, Liu R, He B and Li S 2017 *Biomater. Sci.* **5** 1032–40
[4] Wen J X *et al* 2019 *Biomed. Pharmacother.* **115** 108881
[5] Zhao G J, Huang Q, Wang F, Zhang X, Hu J G, Tan Y, Huang N, Wang Z G, Wang Z B and Cheng Y 2018 *Cancer Lett.* **418** 147–58
[6] Ran D N, Mao J N, Zhan C Y, Xie C, Ruan H T, Ying M, Zhou J F, Lu W L and Lu W Y 2017 *ACS Appl. Mater. Int.* **9** 25672–82
[7] Zhao J, Yang Y, Han X, Liang C, Liu J, Song X, Ge Z and Liu Z 2017 *ACS Appl. Mater. Int.* **9** 23555–63
[8] Kim T H, Jeong G W and Nah J W 2017 *J. Ind. Eng. Chem.* **54** 298–303
[9] Wuttke S, Lismont M, Escudero A, Rungtaweevoranit B and Parak W J 2017 *Biomaterials* **123** 172–83
[10] Yaghi O M and Li H L 1995 *J. Am. Chem. Soc.* **117** 10401–2
[11] Wang D, Sun L B, Liu Y C, Du J F, Wang S, Song X W and Liang Z Q 2017 *RSC Adv.* **7** 17697–703
[12] Ma L, Jiang F B, Fan X, Wang L Y, He C, Zhou M, Li S, Luo H R, Cheng C and Qiu L 2020 *Adv. Mater.* **32** 2003065
[13] Duan C X, Li F E, Luo S J, Xiao J, Li L B and Xi H X 2018 *Chem. Eng. J.* **334** 1477–83
[14] Zhu W, Liu Y, Yang Z, Zhang L, Xiao L J, Liu P, Wang J, Yi C F, Xu Z S and Ren J H 2018 *J. Mater. Chem. B* **6** 265–76
[15] Yaghi O M, O'Keeffe M, Ockwig N W, Chae H K, Eddaoudi M and Kim J 2003 *Nature* **423** 705–14
[16] Horcajada P, Serre C, Maurin G, Ramsahye N A, Balas F, Vallet-Regi M, Sebban M, Taulelle F and Ferey G 2008 *J. Am. Chem. Soc.* **130** 6774–80
[17] Horcajada P *et al* 2010 *Nat. Mater.* **9** 172–8
[18] Feng D W *et al* 2015 *Nat. Commun.* **6** 5979
[19] Yu S S, Wan J Q and Chen K Z 2016 *J. Colloid Interface Sci.* **461** 173–8
[20] Horcajada P, Serre C, Vallet-Regi M, Sebban M, Taulelle F and Ferey G 2006 *Angew. Chem.* **45** 5974–8
[21] Horcajada P *et al* 2010 *Nat. Mater.* **9** 172–8
[22] Lee H J, Cho W and Oh M 2012 *Chem. Commun.* **48** 221–3
[23] Guesh K, Caiuby C A D, Mayoral A, Diaz-Garcia M, Diaz I and Sanchez-Sanchez M 2017 *Cryst. Growth Des.* **17** 1806–13
[24] Julien P A, Mottillo C and Friščić T 2017 *Green Chem.* **19** 2729–47
[25] Yuan B Q, Wang X, Zhou X, Xiao J and Li Z 2019 *Chem. Eng. J.* **355** 679–86
[26] Yang W X, Guo G Q, Mei Z H and Yu Y H 2019 *RSC Adv.* **9** 21804–9
[27] Jeremias F, Henninger S K and Janiak C 2016 *Dalton Trans.* **45** 8637–44
[28] Pardo P, Kojdecki M A, Calatayud J M, Amigo J M and Alarcon J 2017 *Powder Diffraction* **32** S87–98
[29] Thommes M, Kaneko K, Neimark A V, Olivier J P, Rodriguez-Reinoso F, Rouquerol J and Sing K S W 2015 *Pure Appl. Chem.* **87** 1051–69
[30] Strzempek W, Menaszek E and Gil B 2019 *Microporous Mesoporous Mater.* **280** 264–70
[31] Anand R, Borghi F, Manoli F, Manet I, Agostoni V, Reschiglian P, Gref R and Monti S 2014 *J. Phys. Chem. B* **118** 8532–9
Sene S *et al* 2017 *Chem* **3** 303–22
[32] Lv H L, Zhao H Y, Cao T C, Qian L, Wang Y B and Zhao G H 2015 *J. Mol. Catal. A* **400** 81–9
[33] Lohe M R, Rose M and Kaskel S 2009 *Chem. Commun.* 6056–8
[34] Leclerc H, Vimont A, Lavalley J C, Daturi M, Wiersum A D, Llwellyn P L, Horcajada P, Ferey G and Serre C 2011 *Phys. Chem. Chem. Phys.* **13** 11748–56
Seo Y K, Yoon J W, Lee J S, Lee U H, Hwang Y K, Jun C H, Horcajada P, Serre C and Chang J S 2012 *Microporous Mesoporous Mater.* **157** 137–45
[35] Bezverkhyy I, Weber G and Bellat J P 2016 *Microporous Mesoporous Mater.* **219** 117–24
[36] Thorn C F, Oshiro C, Marsh S, Hernandez-Boussard T, McLeod H, Klein T E and Altman R B 2011 *Pharmacogenetics Genomics* **21** 440–6
[37] Laginha Y A, Verwoert S, Charrois G J R and Allen T M 2005 *Clin. Cancer Res.* **11** 6944–9
[38] Liu Y Q, Zhang X J, Zhou M J, Nan X Y, Chen X F and Zhang X H 2017 *ACS Appl. Mater. Int.* **9** 43498–507

[39] Li J, Wei Y J, Yang X L, Wu W X, Zhang M Q, Li M Y, Hu Z E, Liu Y H, Wang N and Yu X Q 2020 *ACS Appl. Mater. Int.* **12** 32432–45
[40] Mallick A, More P, Syed M M K and Basu S 2016 *ACS Appl. Mater. Int.* **8** 13218–31
[41] Wongrakpanich A, Geary S M, Joiner M L A, Anderson M E and Salem A K 2014 *Nanomedicine* **9** 2531–43
[42] Newmeyer D D and Ferguson-Miller S 2003 *Cell* **112** 873–873
[43] Han M, Vakili M R, Abyaneh H S, Molavi O, Lai R and Lavasanifar A 2014 *Mol. Pharm.* **11** 2640–9
[44] Mallick S, Song S J, Bae Y and Choi J S 2019 *Int. J. Biol. Macromol.* **132** 451–60
[45] Qi T, Chen B L, Wang Z H, Du H L, Liu D C, Yin Q Q, Liu B Y, Zhang Q and Wang Y G 2019 *Biomaterials* **213** 119219
[46] Chen Z G, Kang X X, Wu Y X, Xiao H H, Cai X Z, Sheng S H, Wang X F and Chen S G 2019 *Chem. Commun.* **55** 4781–4
[47] Reers M, Smith T W and Chen L B 1991 *Biochemistry* **30** 4480–6
Reers M, Smiley S T, MottolaHartshorn C, Chen A, Lin M and Chen L B 1995 *Method Enzymol.* **260** 406–17
[48] Chen K, Cai H, Zhang H, Zhu H Y, Gu Z W, Gong Q Y and Luo K 2019 *Acta Biomater.* **84** 339–55
[49] Adhikari C and Chakraborty A 2016 *Chem. Phys. Chem.* **17** 1070–7
[50] Chen X J, Zhang M J, Li S N, Li L, Zhang L Y, Wang T T, Yu M, Mou Z C and Wang C G 2017 *J. Mater. Chem. B* **5** 1772–8

Supporting Information

Green Synthesis of DOX-loaded Hollow MIL-100 (Fe) Nanoparticles for Anticancer Treatment by Targeting Mitochondria

Yechuan Zhang[1], Zhengxiang Gu[2], Seonho Yun[1], Kui Luo[2], Jingxiu Bi*[1], Yan Jiao*[1], Hu Zhang*[3]

[1]*School of Chemical Engineering and Advanced Materials, University of Adelaide, SA 5005, Australia*

[2] *Huaxi MR Research Center (HMRRC), Department of Radiology, National Clinical Research Center for Geriatrics, Frontiers Science Center for Disease-Related Molecular Network, State Key Laboratory of Biotherapy, West China Hospital, Sichuan University, Chengdu 610041, China*

[3] *Riggs School of Applied Life Sciences, Keck Graduate Institute, CA 91711, USA*

*Corresponding Authors.
Email Address: Jingxiu.bi@adelaide.edu.au; yan.jiao@adelaide.edu.au; hu_zhang@kgi.edu

Materials Characterization:

The crystal structure of the synthesized NPs was analyzed by X-ray diffraction (XRD) on a MiniFlex 600 (Rigaku, Cu Kα, λ = 0.15418 nm). The XRD was operated at 40 kV and 15 mA. The XRD spectra were collected at a scanning range from 2° to 35° with a step size of 0.02°. The particle size and morphology of NPs were observed under a scanning electron microscope (FEI Quanta 450 FEG). The hollow structure of NPs was confirmed via a transmission electron microscope (FEI Tecnai G2 Spirit TEM) which was operated at 120 kV accelerating voltage. The zeta-potential of NPs in aqueous suspensions (MilliQ water) was evaluated by Dynamic Light Scattering (DLS) (Zetasizer Nano, Malvern Instruments Ltd., UK). The BET and Langmuir surface areas of NPs were obtained by nitrogen adsorption (Micromeritics TriStar II 3020). Images of all stained cells were visualized under a confocal microscope (Olympus FV3000 Confocal Microscope).

Experimental Protocols

Synthesis of carboxylate terminated polystyrene template (PS-COOH):

The PS-COOH template was modified from a previously reported method.[22] 10.5 mL styrene was first washed with 10 wt% NaOH three times to remove the stabilizer. 0.55 mL methyl methacrylate, 0.46 mL acrylic acid, and 0.25 g NH_4HCO_3 were mixed with the previously washed styrene and then added to 50 mL of deionized water under mechanically stirring. 0.27 g ammonium persulfate was added to the mixture solution when the temperature reached 70 °C. The temperature was raised to 80 °C for further reaction of 12 h. The product was separated by centrifugation at 9000 rpm, then washed with ethanol and deionized water 3 times respectively, and finally obtained using freeze-drying.

Synthesis of MIL-100 (Fe):

MIL-100 (Fe) nanoparticles were produced according to the literature with some modifications.[23] 1.676 g trimesic acid (H_3BTC) was dissolved in 23.72 g 1 M NaOH aqueous solution as Solution 1 (pH≈11). 2.26 g ferrous chloride tetrahydrate ($FeCl_2 \cdot 4H_2O$) added into 97.2 g H_2O as Solution 2 (pH≈2.7). After both solutions became completely clear, Solution 1 was dropwise added to Solution 2 under magnetic stirring (pH = 5.2). The molar ratio of all components in the mixture was controlled to be 1.5 Fe/1.0 H_3BTC/3.0 NaOH/880 H_2O. The reaction continued for 24 h under magnetic stirring at room temperature. The color of the mixture changed from green to orange-

brown after 4 h. MIL-100 (Fe) nanoparticles were separated by centrifugation at 3700 rpm and washed with deionized water and ethanol three times. The obtained nanoparticles were dried under vacuum.

Synthesis of Fe-BTC:

Semi-amorphous Fe-BTC was produced using the methodology previously published.[24] Two solutions were prepared for the synthesis: Solution 1 containing 0.263 g H_3BTC dissolved in 10.150 g 1 M NaOH aqueous solution; Solution 2 containing 0.508 g $FeCl_3 \cdot 6H_2O$ in 10 g H_2O. Solution 2 was dropwise added into Solution 1 under magnetic stirring with immediate appearance of brownish-orange precipitates. The molar composition of the mixture was the same as that of the synthesis of MIL-100 (Fe). The reaction was maintained under stirring for 1 h. The brownish-orange solids were washed by deionized water and ethanol 3 times and dried under vacuum.

Doxorubicin loading:

The drug loading method was adapted from a previously reported method.[4] 5 mg of Fe-BTC and MIL-100 (Fe) were dried at 100 °C for 24 h to remove the moisture. For H-F and H-M, the drying process was conducted at 153 °C for 2 h to ensure the removal of DMF residues in the pores. Samples were dispersed in 2 mL 10 mg/mL DOX solution. The drug loading process continued for 24 h using an orbital shaker. After the 24 h loading process, doxorubicin-loaded samples were washed with deionized water to remove doxorubicin on the surface and dried under vacuum. The doxorubicin loading capacity was calculated according to the difference of UV-vis values measured before and after drug loading.

$$\text{Drug loading capacity } (\%) = \frac{Mass\ of\ the\ loaded\ drug}{Mass\ of\ dried\ drug\ loaded\ carriers} \times 100\% \quad (1)$$

Doxorubicin Release:

The DOX release experiments were conducted by the protocol in the published literature with modifications.[25] 5 mg doxorubicin-loaded nanoparticles were placed into 80 mL phosphate buffer saline (PBS) at pH=7.4 to monitor the drug release behavior. The experiment was carried out in a sealed orbital shaker at 200 rpm under 37 °C. At each time point, 2.0 mL sample was taken out to centrifuge at 10000 rpm for 10 min, and 1.5 mL of the supernatant was used to determine the DOX concentration via a UV-vis spectrophotometer. Meanwhile, 2.0 mL of PBS was added to the bulk solution to maintain the same liquid volume. The drug release process continued for 11 days.

The percentage of DOX released was calculated from the following equation.

$$Percent\ DOX\ released = \frac{M_r}{M_l} \quad (2)$$

where M_r is the total specific mass (mg) DOX released in PBS, ML is the mass (mg) of DOX loaded in 5 mg carriers.

MTT Assay in MDA-MB-231 and HEK-293T:

Human breast cancer cells (MDA-MB-231) were incubated in L-15 medium with 10% fetal bovine serum (FBS) and 1% penicillin/streptomycin (L-15 based medium) for 48 h in a humified incubator (37 °C, 5% CO_2). Cell viability results were obtained using a standard MTT assay in a 96-well plate. Three groups were designed to study the cytotoxicity of H-F and H-M against the cell line MDA-MB-231. Group 1 cells were incubated with H-M at a nanoparticle concentration of 0.023, 0.23, 2.3, 4.6 μg/mL; Group 2 cells free DOX at a concentration of 0.01, 0.1, 1 and 2 μg/mL; and Group 3 cells with DOX@H-M at the equivalent DOX concentration as free DOX group. After 24 h incubation, the medium was removed, and 100 μL fresh medium and 10 μL 1 × MTT were added to each well for another four hours incubation. 150 μL dimethyl sulfoxide (DMSO) was added to each well after removing all media. After 10 min, the absorbance of each well was measured by the microplate reader. The same experimental procedure was applied to HEK-293T cells using the Dulbecco's Modified Eagle's Medium (DMEM).

The cell viability was calculated by the following equation:

$$\text{Cell Viability} = \frac{S-B}{C-B} \times 100\% \quad (3)$$

S, B and C are the absorbance value of samples (S) in each well, the background group (B) and the control group (C), respectively. All experiments were quadruplicated, and the results were presented as mean ± SD (Standard Deviation).

Intracellular uptake of DOX@H-M and Free DOX:

Intracellular uptake of DOX@H-M and DOX was monitored via a confocal laser scanning microscopy (CLSM) (Olympus FV 3000). MDA-MB-231 cells were seeded in 3 wells of the ibidi 8-well plate with L-15 based medium for 24 h. After 24 h incubation, one well was used as a control. The second well was incubated with DOX@H-M at a DOX concentration of 2 × IC50. The third well was incubated with 2 × IC50 free DOX. After four hours of incubation, cells were fixed by 4% formaldehyde and incubated for 10 min. After cells were washed with warm PBS three times, they

in three wells were treated with 5 μg/mL CellMask™ Deep Red Plasma Membrane Stain for 5 min and then washed with PBS three times to remove the residue. 1 μg/mL bisBenzimide H 33258 was added to three wells afterwards and incubated for another 5 min, and three wells were washed by PBS another three times. Fluorescent images were captured via the CLSM.

Mitochondria Targeting in MDA-MB-231

To identify the localization difference of free DOX and DOX@H-M NPs inside cells after the cellular uptake, mitochondria and nuclei were stained by MitoTracker™ Deep Red FM and bisBenzimide H 33258, respectively. Briefly, MDA-MB-231 cells were seeded in 3 wells of an ibidi 8-well plate with L-15 based medium for 24 h. One well was used as a control. The second and third wells were incubated with free DOX and DOX@H-M at the same concentration of 2×IC50 DOX. After 4 hours of incubation, cells were fixed by 4% formaldehyde and incubated for 10 min. Cells were stained by 0.1 μg/mL (~200 nM) MitoTracker™ Deep Red FM, incubated for 15 min and washed with PBS three times. Afterwards, cells were incubated with 1 μg/mL bisBenzimide H 33258 for five minutes and washed with PBS another three times. Fluorescent images were obtained by the CLSM.

Mitochondria Membrane Potential (MMP) Analysis:

A JC-1 dye was applied to investigate the change in the MMP. MDA-MB-231 cells were seeded in 6 wells of an ibidi 8-well plate with L-15 based medium for 24 hours first. MDA-MB-231 cells in Well 1 were used as a background control. Cells in Well 2 were incubated with 2×IC50 DOX for 12 h without JC-1 dye staining as Control 1. Cells in Well 3 were simply stained by JC-1 dye without any treatment as Control 2. Cells in Well 4 and Well 5 were incubated with free DOX and DOX@H-M at 2×IC50 DOX for 12 h. After incubation, cells were stained with 2.5 μg/mL JC-1 dye for 30 min and washed with PBS three times to remove any staining residue. Cells were then fixed by 4% formaldehyde and washed by PBS another three times. Cells were immediately observed under a CLSM. 488 nm was selected as the excitation wavelength for JC-1. The excitation wavelength of 480 nm and the emission wavelength of 580 nm were used for DOX. The excitation wavelength of 488 nm was selected for the JC-1; and the emission wavelengths of 515–545 nm and 570–600 nm were set for JC-1 monomers and for JC-1 aggregates respectively.

Figures:

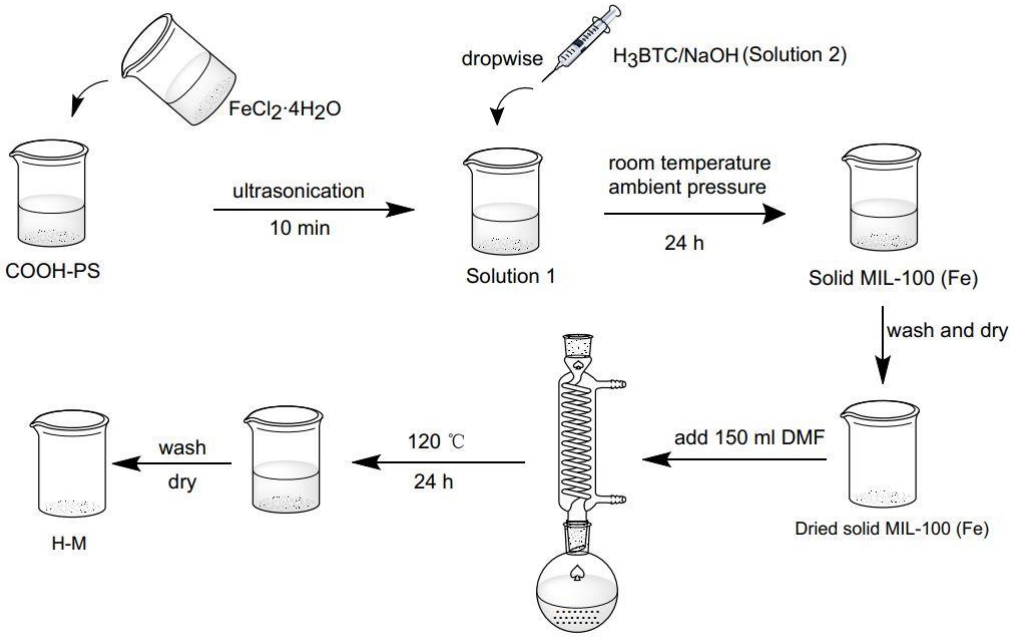

Figure S1. Schematic process of fabricating H-M NPs.

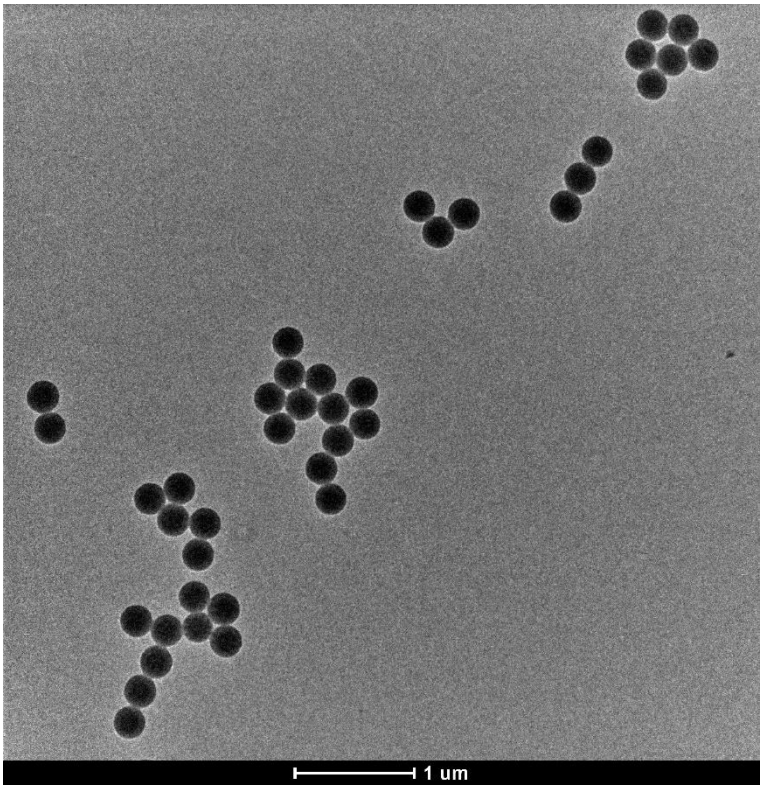

Figure S2. TEM image of carboxylate-terminated polystyrene (PS-COOH).

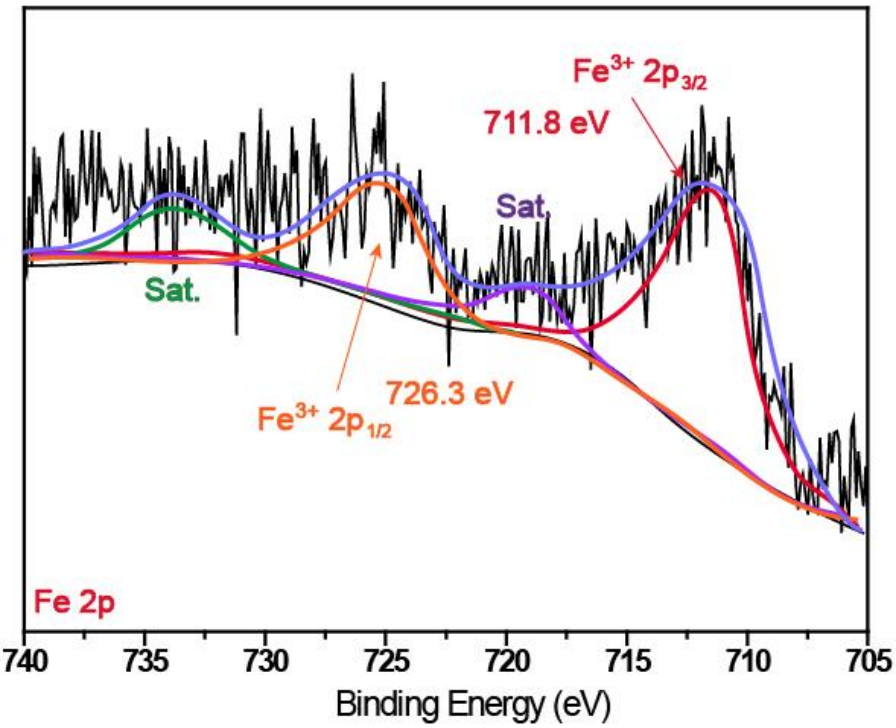

Figure S3. XPS spectra of Fe in H-M.

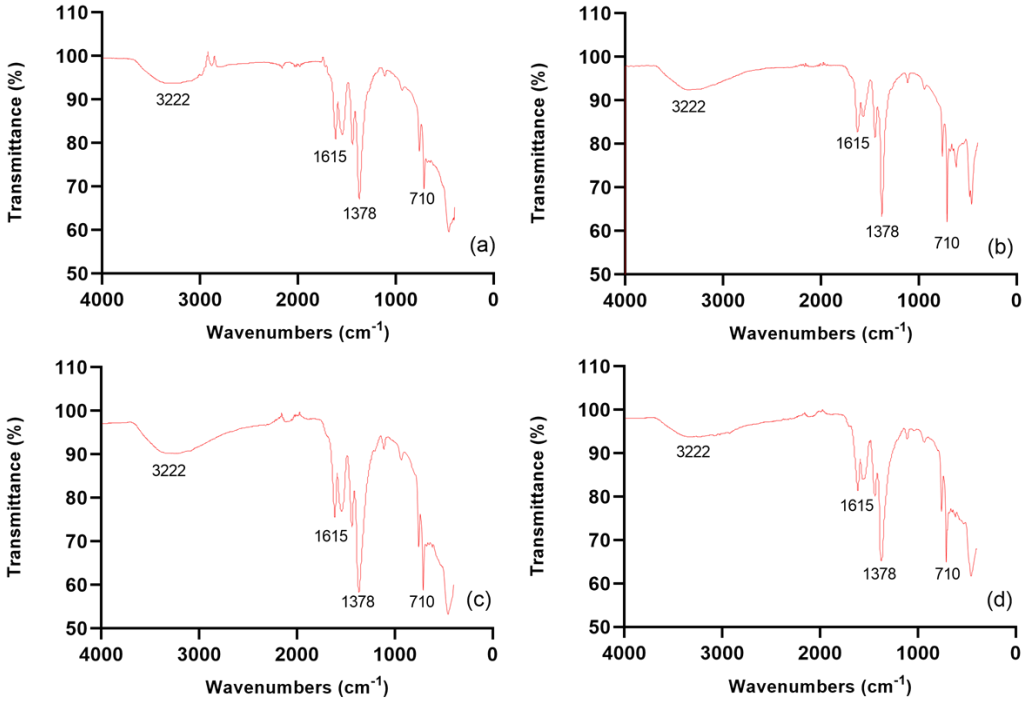

Figure S4. FTIR spectra of: (a) Fe-BTC, (b) H-F, (c) MIL-100 (Fe), (d) H-M.

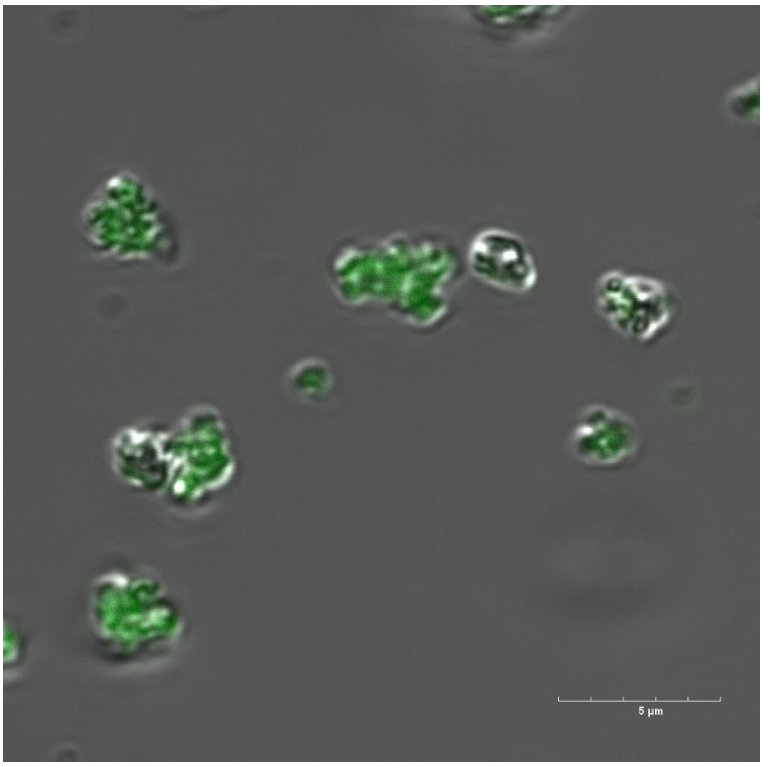

Figure S5. CLSM image of DOX@H-M. Green: DOX.

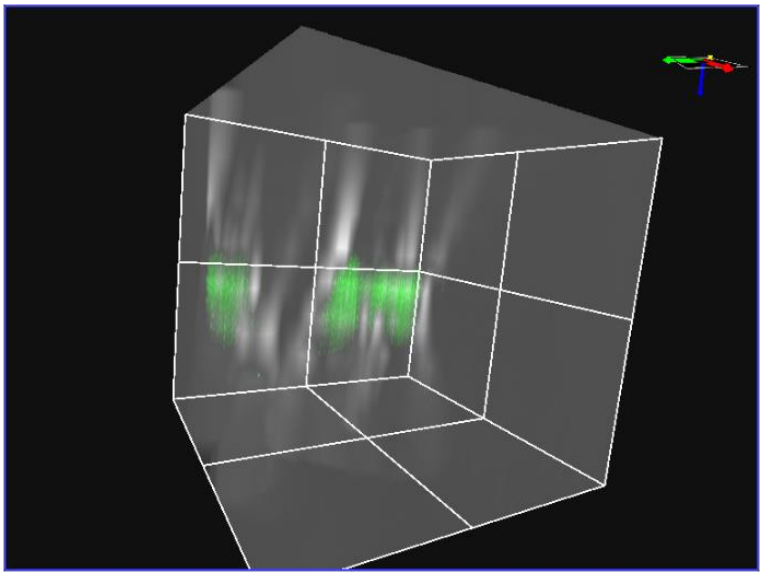

Figure S6. Z-axis stacked CLSM image of DOX loaded H-M.

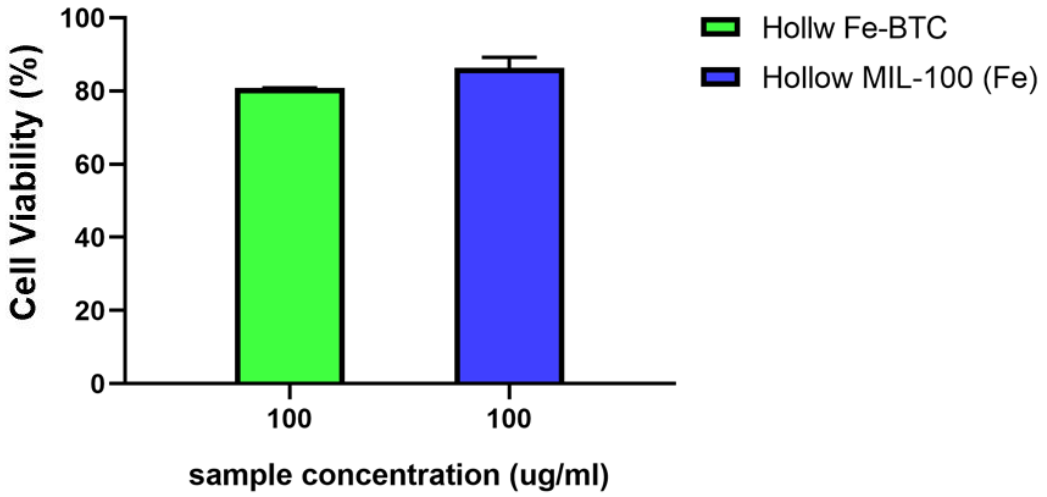

Figure S7. Cell viabilities of human kidney cells HEK-293T after incubation with 100 μg/mL hollow Fe-BTC and hollow MIL-100 (Fe).

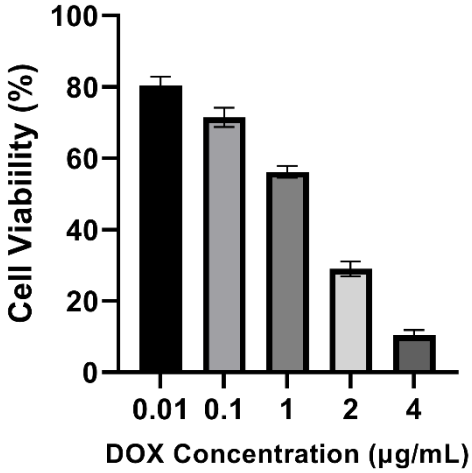

Figure S8. Preliminary cell viability test using different concentration of DOX against MDA-MB-231 cells. Cells are incubated with DOX for 24 h. The trend of cell viability reflects the dose-dependent characteristic of DOX against MDA-MB-231 cells.

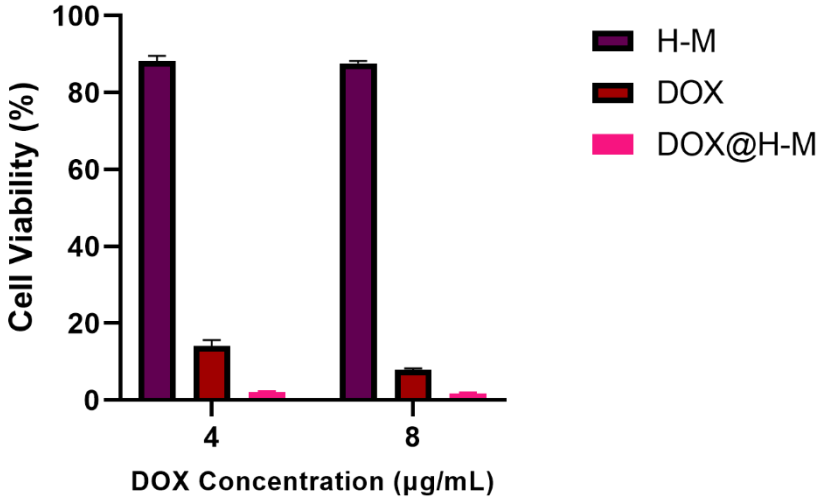

Figure S9. Cell viability test using higher concentration of DOX (4 μg/mL, 8 μg/mL) and longer incubation time (48 h).

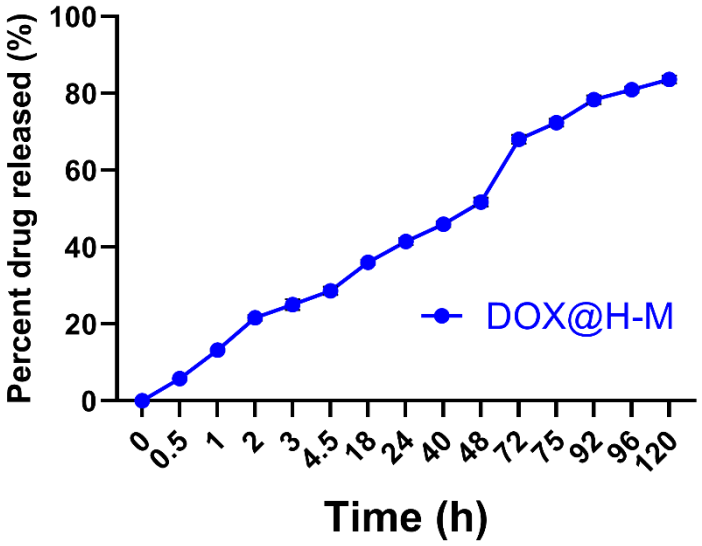

Figure S10. Drug release pattern of DOX@H-M at pH=6.5 for 120 h.

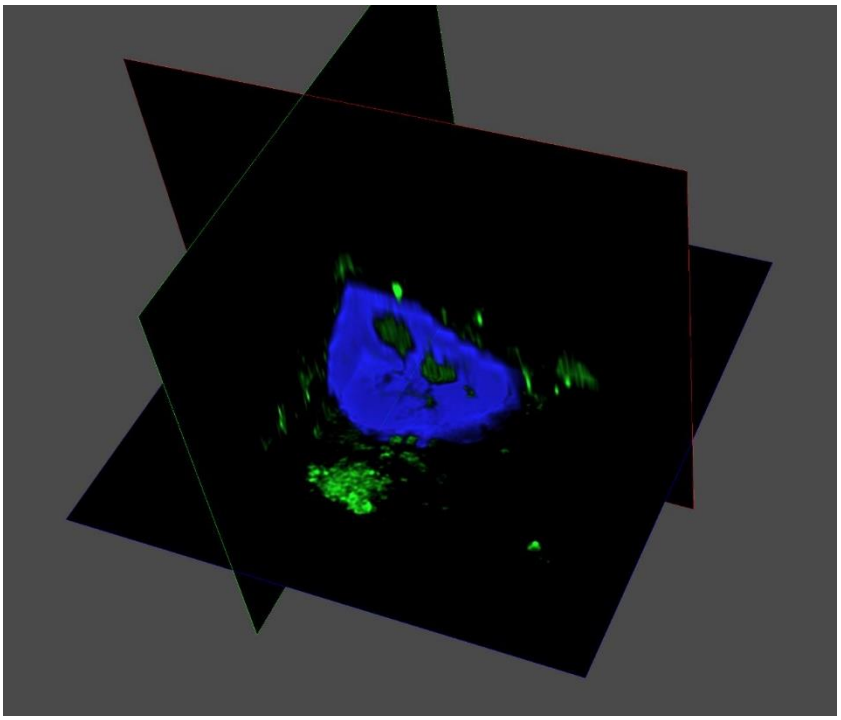

Figure S11. The Z-stack projection confocal image of MDA-MB-231 cell after uptake of DOX@H-M. Blue: nucleus; Green: DOX@H-M.

Appendix

CLSM parameters.

"[General]" ""
"Path" "F:/DATA/Yechuan Zhang/cell"
"Name" "DLS_0001.oir"
"Scan Mode" "XY"
"Date" "11/07/2019 01:54:06.345 PM"
"File Version" "2.1.2.3"
"System Name" "FV3000"
"System Version" "2.3.1.163"
"[Dimensions]" ""
"X Dimension" "1024, 0.0 - 212.132 [um], 0.207 [um/pixel]"
"Y Dimension" "1024, 0.0 - 212.132 [um], 0.207 [um/pixel]"
"Channel Dimension" "3 [Ch]"
"[Image]"""
"Primary Dimensions" "X * Y"
"Image Size" "1024 * 1024 [pixel]"
"Image Size(Unit Converted)" "212.132 [um] * 212.132 [um]"
"[Acquisition]" ""
"Objective Lens" "PLAPON 60XOSC2"
"Objective Lens Mag." "60.0X"
"Objective Lens NA" "1.4"
"Scan Device" "Galvano"
"Scan Direction" "Oneway"
"Sampling Speed" "2.0 [us/pixel]"
"Sequential Mode" "Line"
"Integration Type" "Line"
"Integration Count" "3"
"Region Mode" "None"
"Find Mode" "x1"
"Rotation" "0.0 [deg]"
"Pan X" "0.0 [um]"
"Pan Y" "0.0 [um]"
"Zoom" "x1.0"
"ADM" "Empty"
"MirrorTurret 1" "MIRROR"
"ZDC DM" "Out"
"Z Drift Compensation in SeriesScan" "OFF"
"[Channel 1]" ""
"Channel Name" "HSD1"
"Dye Name" "DAPI"
"Emission WaveLength" "461 [nm]"
"PMT Voltage" "638 [V]"
"Excitation DM Name" "DM405/488/561/640"

"C.A." "225 [um]"
"Bits/Pixel" "12 [bits]"
"Laser Wavelength" "405 [nm]"
"Laser Transmissivity" "1.17 [%]*"
"AOTF/AOM Transmissivity" "11.7 [%]"
"Laser ND Filter" "10 [%]"
"Detection Wavelength" "430 - 470 [nm]"
"[Channel 2]" ""
"Channel Name" "HSD2"
"Dye Name" "Alexa Fluor 488"
"Emission WaveLength" "520 [nm]"
"PMT Voltage" "703 [V]"
"Excitation DM Name" "DM405/488/561/640"
"C.A." "225 [um]"
"Bits/Pixel" "12 [bits]"
"Laser Wavelength" "488 [nm]"
"Laser Transmissivity" "5.02 [%]*"
"AOTF/AOM Transmissivity" "50.2 [%]"
"Laser ND Filter" "10 [%]"
"Detection Wavelength" "582 - 622 [nm]"
"[Channel 3]" ""
"Channel Name" "HSD3"
"Dye Name" "Alexa Fluor 647"
"Emission WaveLength" "671 [nm]"
"PMT Voltage" "500 [V]"
"Excitation DM Name" "DM405/488/561/640"
"C.A." "225 [um]"
"Bits/Pixel" "12 [bits]"
"Laser Wavelength" "640 [nm]"
"Laser Transmissivity" "1.35 [%]*"
"AOTF/AOM Transmissivity" "13.5 [%]"
"Laser ND Filter" "10 [%]"
"Detection Wavelength" "650 - 750 [nm]"

Reference:

[1] F. Zhang, Y. Y. Wei, X. T. Wu, H. Y. Jiang, W. Wang, H. X. Li, *J Am Chem Soc* 2014, *136*, 13963-13966.

[2] K. Guesh, C. A. D. Caiuby, A. Mayoral, M. Diaz-Garcia, I. Diaz, M. Sanchez-Sanchez, *Cryst Growth Des* **2017**, *17*, 1806-1813.

[3] M. Sanchez-Sanchez, I. de Asua, D. Ruano, K. Diaz, *Cryst Growth Des* **2015**, *15*, 4498-4506.

[4] P. Horcajada, T. Chalati, C. Serre, B. Gillet, C. Sebrie, T. Baati, J. F. Eubank, D. Heurtaux, P. Clayette, C. Kreuz, J. S. Chang, Y. K. Hwang, V. Marsaud, P. N. Bories, L. Cynober, S. Gil, G. Ferey, P. Couvreur, R. Gref, *Nat. Mater* 2010, *9*, 172-178.

[5] P. F. Gao, L. L. Zheng, L. J. Liang, X. X. Yang, Y. F. Li, C. Z. Huang, *J Mater Chem B* **2013**, *1*, 3202-3208.

Chapter 4. Efficient Cancer Therapy Through Conversion of Encapsulated Prodrug via Immobilized Enzyme in PCN-333 (Fe)

4.1 Introduction, Significance and Commentary

The increasing interest of converting prodrugs via enzymes for cancer therapy requires stable and unique structural carriers for simultaneous loading of both prodrugs and enzymes. Metal-organic frameworks (MOFs) with large hierarchical pores have the potential of immobilizing enzymes and loading prodrugs based on size difference. In this work, PCN-333 (Fe) was obtained using the hydrothermal method. Horseradish peroxidase (HRP) and indole-3-acetic acid (IAA) loaded PCN-333 (Fe) (HRP/IAA@PCN-333 (Fe)) exhibited a continuous generation of reactive oxygen species (ROS), which could kill breast cancer cells (MDA-MB-231) efficiently. The *in vivo* experiments also verified the therapeutic effect of HRP/IAA@PCN-333 (Fe) towards the Patient-Derived Tumor Xenograft (PDX) model built in nude mice.

4.2 Manuscript

This section is presented as the prepared manuscript submitted to Nanoscale.

Statement of Authorship

Title of Paper	Efficient Cancer Therapy Through Conversion of Encapsulated Prodrug via Immobilized Enzyme in PCN-333 (Fe)
Publication Status	☐ Published ☐ Accepted for Publication ☑ Submitted for Publication ☐ Unpublished and Unsubmitted work written in manuscript style
Publication Details	

Principal Author

Name of Principal Author (Candidate)	Yechuan Zhang		
Contribution to the Paper	Designed the material and experiments, carried out experiments, analyzed experimental results, and wrote the manuscript.		
Overall percentage (%)	80%		
Certification:	This paper reports on original research I conducted during the period of my Higher Degree by Research candidature and is not subject to any obligations or contractual agreements with a third party that would constrain its inclusion in this thesis. I am the primary author of this paper.		
Signature		Date	09/05/2022

Co-Author Contributions

By signing the Statement of Authorship, each author certifies that:

i. the candidate's stated contribution to the publication is accurate (as detailed above);

ii. permission is granted for the candidate in include the publication in the thesis; and

iii. the sum of all co-author contributions is equal to 100% less the candidate's stated contribution.

Name of Co-Author	Zhengxiang Gu		
Contribution to the Paper	Modified the manuscript, figure corrections.		
Signature		Date	09/05/2022

Name of Co-Author	Zhiqian Li		
Contribution to the Paper	Assisted to conduct in vivo experiments.		
Signature		Date	09/05/2022

Name of Co-Author	Hu Zhang		
Contribution to the Paper	Modified the manuscript		
Signature		Date	09/05/2022

Name of Co-Author	Jingxiu Bi		
Contribution to the Paper	Modified the manuscript		
Signature		Date	09/05/2022

Name of Co-Author	Kui Luo		
Contribution to the Paper	Analyzed the experimental results, modified the manuscript		
Signature		Date	09/05/2022

Name of Co-Author	Yan Jiao		
Contribution to the Paper	Analyzed experimental results, modified the manuscript		
Signature		Date	09/05/2022

Please cut and paste additional co-author panels here as required.

PAPER

Efficient Cancer Therapy Through Conversion of Encapsulated Prodrug via Immobilized Enzyme in PCN-333 (Fe)

Received 00th January 20xx,
Accepted 00th January 20xx

DOI: 10.1039/x0xx00000x

Yechuan Zhang[1], Zhengxiang Gu[2], Zhiqian Li[2], Kui Luo[2], Hu Zhang*[3], Jingxiu Bi*[1], Yan Jiao*[1]*

Release of active pharmaceutical ingredients (APIs) from prodrugs catalyzed by specific enzymes in the tumor microenvironment improves the biocompatibility and efficiency of the drug delivery system. However, due to biodegradability and membrane-impermeability of exogeneous enzymes, it is vital to explore stable carriers for protection and simultaneous delivery of exogeneous enzymes and anticancer prodrugs. Herein, a porous metal-organic framework (MOF), PCN-333 (Fe), was fabricated for the dual loading of horseradish peroxidase (HRP) and a prodrug indole-3-acetic acid (IAA), producing HRP/IAA@PCN-333 (Fe). Cavities at a large size inside PCN-333 (Fe) are used to store HRP, while cavities at a small size for IAA, thus preventing the premature catalysis of the prodrug inside the MOF. HRP and IAA are loaded into PCN-333 (Fe) with a high loading capacity of 317 and 258 mg per gram of PCN-333 (Fe), respectively. PCN-333 (Fe) provides the protection for HRP and its enzymatic activity is maintained in a physiological-mimicking condition. In vitro experiments confirm cellular uptake of HRP/IAA@PCN-333 (Fe) and distribution inside MDA-MB-231 cells via confocal laser scanning microscopy. In vivo experiments further demonstrate the feasibility of utilizing PCN-333 (Fe) as a carrier for the enzyme and the prodrug for the treatment of breast cancer. HRP/IAA@PCN-333 (Fe) effectively inhibit the tumor growth in the patient-derived tumor xenograft (PDX) mice model via intravenous injection as the prodrug is catalyzed by the encapsulated HRP to generate reactive oxygen species (ROS). The tumor grow inhibition rate reaches 43 % based on the excised tumor weight. Therefore, the hierarchical porous MOF, PCN-333 (Fe), could be used to accommodate both exogeneous enzymes and prodrugs, and the prodrug could be catalyzed in the tumor microenvironment to release the API for effectively exerting its anti-cancer therapeutic function.

Introduction

The enzyme-activated prodrug therapy (EAPT) is an effective strategy to treat cancer by catalyzing a non-toxic prodrug to a cytotoxic anticancer drug as an active pharmaceutical ingredient (API) in the tumor microenvironment, thus exerting its therapeutic effect and diminishing its side effects to normal tissues.[1, 2] The conventional methodology employs the overexpressed enzymes by tumor cells inside the tumor microenvironment to activate the prodrug.[3] However, endogenous enzymes may not be sufficient to catalyze the prodrugs to produce the API at a dose above its therapeutic threshold due to their low concentration, thus weakening the therapeutic effect of EAPT.[4, 5] In addition, some of the prodrugs may not be activated by endogenous enzymes. Different carriers have been explored to simultaneously deliver exogenous enzymes and prodrugs into cancer cells.[6, 7] Nevertheless, simultaneous loading of enzymes and prodrugs in the same compartment of the carrier may lead to premature activation of prodrugs.[8] Moreover, asynchronous release and distribution of enzymes and prodrugs at different locations may reduce the therapeutic effect of EAPT.[9] Therefore, it is vital to develop nanocarriers for simultaneous loading of exogenous enzymes and prodrugs, but prevent premature activation of prodrugs and maintain the enzyme activity before reaching the tumor site.

Metal-Organic Frameworks (MOFs) are a series of porous nanocarriers, and their biocompatibility for drug delivery have been realized by selecting appropriate metal ions and organic ligands.[10-12] Particularly, high porosity, an adjustable pore structure, and nanocages with different sizes endow MOFs with the feasibility of using them as nanocarriers for immobilization of biomolecules with different sizes.[13-15] The mesoporous structure of MOFs can facilitate the immobilization of large biomolecules.[16-18] However, this structure cannot be used to load small molecular prodrugs to realize EAPT. [19, 20] Iron-based

[1] *School of Chemical Engineering and Advanced Materials, University of Adelaide, SA 5005, Australia.*
[2] *Huaxi MR Research Center (HMRRC), Department of Radiology, State Key Laboratory of Biotherapy, West China Hospital, Sichuan University, Chengdu 610041, China.*
[3] *Riggs School of Applied Life Sciences, Keck Graduate Institute, CA 91711, USA*
**Corresponding Authors.*
†Electronic Supplementary Information (ESI) available: [details of any supplementary information available should be included here]. See DOI: 10.1039/x0xx00000x

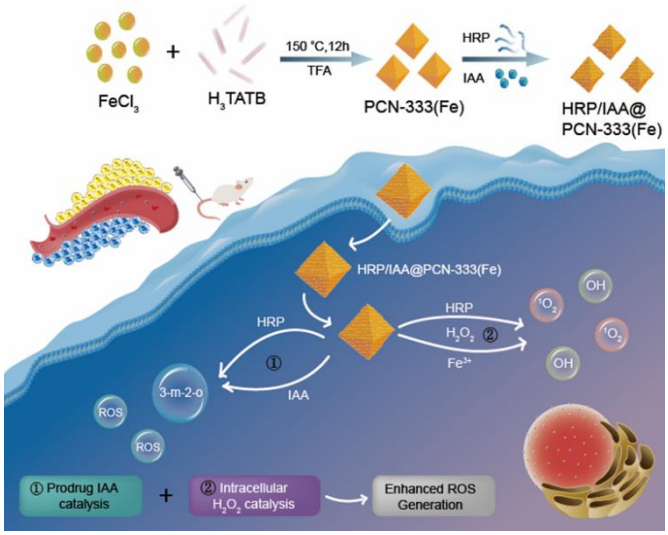

Figure 1. Scheme of the synthetic process of HRP/IAA@PCN-333 (Fe) and its EAPT against breast cancer cells. In Process 1, HRP catalyzes IAA to generate ROS and cytotoxic 3-methylene-2-oxindole (3-m-2-o) as an API. In Process 2, HRP catalyzes intracellular H_2O_2 in breast cancer cells with the assistance of Fe^{3+} from the nanocarrier. Strong potent therapeutic effects could be achieved through both the API and ROS.

MOFs as a drug delivery system possess advantages including great biocompatibility and high catalytic activity of iron ions. Previous study has investigated the potential of PCN-333 (Al) as the carrier for various enzymes.[6] PCN-333 (Fe), a hierarchical mesoporous MOF with a similar topology as PCN-333 (Al), has the capability of immobilizing enzymes.

Indole-3-acetic acid (IAA), a non-toxic natural plant growth hormone, is barely oxidized by mammalian peroxidases.[21, 22] However, it can be catalyzed by horseradish peroxidase (HRP) to generate a cytotoxic compound, 3-methylene-2-oxindole, as an API. Meanwhile, HRP can catalyze intracellular H_2O_2 to reactive oxygen species (ROS), thus the utilization of HRP and IAA could destroy cancer cells through membrane and DNA damage.[23, 24] However, interaction between HRP and IAA in a nanocarrier may result in premature leakage of the API in the blood stream, inducing severe adverse effects.[25, 26] Release of HRP and IAA for EAPT from the nanocarrier would decrease the concentration of HRP and/or IAA, leading to a diminished therapeutic effect due to instability of the nanocarrier in the blood stream.[27, 28] Therefore, the nanocarrier should hold a hierarchically porous structure to simultaneously deliver HRP and IAA but at different locations, preventing release of HRP, IAA and the API before the nanocarrier is internalized by tumor cells.

Herein, we synthesized a hierarchically porous MOF, PCN-333 (Fe), for dual loading and delivery of HRP and IAA. Figure 1 exhibited the synthetic process of HRP and IAA loaded PCN-333 (Fe) (HRP/IAA@PCN-333 (Fe)), and its EAPT mechanism against breast cancer cells. PCN-333 (Fe) is composed of Fe-O clusters and 4,4',4''-s-triazine-2,4,6-triyltribenzoic acid (TATB) ligands. It possesses three cavities: a large hexacaidecahedral mesoporous cage (4.9 nm), a small dodecahedral mesoporous cage (3.7 nm) and a micropore cage (0.8 nm). Those cages can be utilized to load molecules at different sizes. The encapsulation of HRP and IAA into different cavities of this hierarchical porous structure PCN-333 (Fe) could prevent premature activation of the prodrug.[29] According to the size screening effect, HRP at a size of 4.0 x 4.4 x 6.8 nm^3 could be loaded into the large mesoporous cage of PCN-333 (Fe).[6] The small mesoporous cage and the micropore cage are vacant after loading of HRP, and small molecules IAA can be effectively encapsulated in these cages because of strong affinity between its carboxylic groups and metal nodes. HRP/IAA@PCN-333 (Fe) could be internalized into breast cancer cells (MDA-MB-231) to release the API for its therapeutic effect as well as generate the ROS to enhance apoptosis of tumor cells. In addition, in vivo experiments support that the growth of the planted tumors in the BALB/c-nu mice model is significantly inhibited after intravenous injection of HRP/IAA@PCN-333 (Fe) into these mice.

Experimental section

Synthesis of PCN-333 (Fe)

The synthetic method of PCN-333 (Fe) was adapted from a published study [6]. H_3TATB (50 mg) and anhydrous $FeCl_3$ (60 mg) were dissolved in 10 ml DMF, and 0.5 ml trifluoroacetic acid was then added. The mixture was transferred to a pressure vessel and heated up at 150 °C in an oven for 12 h until brown precipitates were observed. The brown precipitate was centrifuged and washed with fresh DMF several times. The obtained product was finally dried at 160 °C to completely remove DMF.

HRP and IAA loading

Two milligrams of PCN-333 was suspended in 5 mL of HRP aqueous solution (2.0 mg mL^{-1} HRP). The mixture was stirred at 4 °C for 2 h in the dark. HRP-loaded PCN-333 (Fe) (HRP@PCN-333) NPs were obtained after centrifugation. To quantitatively analyze the loading capacity of HRP into PCN-333, HRP standard solutions were prepared in deionized water at concentrations of 0.0625, 0.125, 0.25, 0.5 and 1.0 mg mL^{-1}. The absorbances of HRP standard solutions were acquired via a UV-vis spectroscopy (company and country). The absorption values at 402 nm were plotted against the concentration to establish the standard

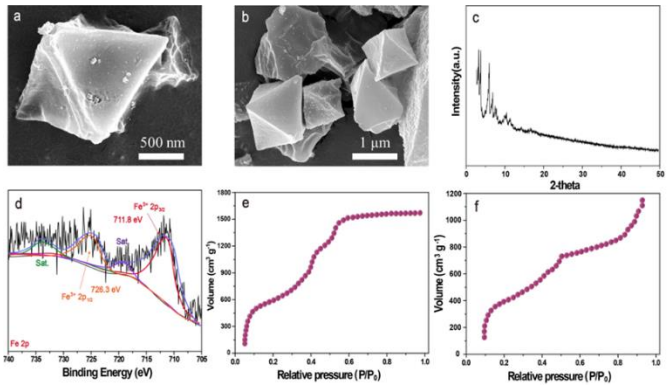

Figure 2. (a) (b) SEM images of PCN-333 (Fe) at different scales. (c) XRD pattern of PCN-333 (Fe). (d) XPS analysis of PCN-333 (Fe). (e) BET curve of N_2 adsorption onto PCN-333 (Fe) before HRP and IAA loading. (f) BET curve of N_2 adsorption onto PCN-333 (Fe) after HRP and IAA loading.

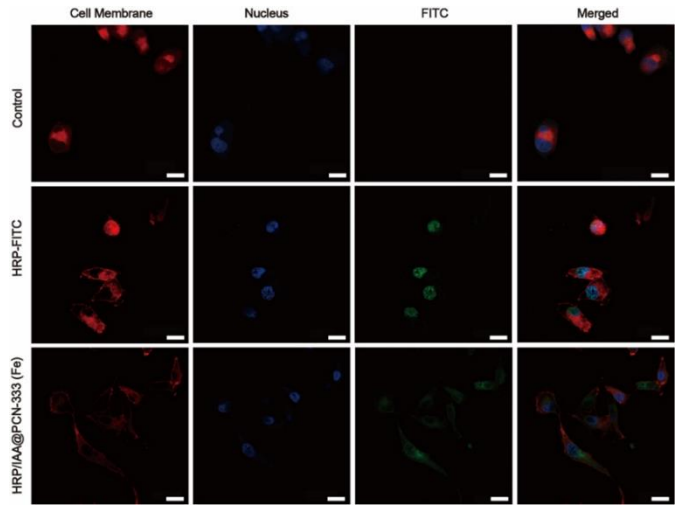

Figure 3. CLSM images of MDA-MB-231 cells incubated with HRP-FITC and HRP/IAA@PCN-333 (Fe) for 12 h. Red: cell membrane, blue: nucleus, green: FITC signal. Scale bar: 20 μm.

curve. The amount of the loaded HRP was calculated from the difference in the absorbance of the supernatant before and after HRP loading at 402 nm. Measurements were performed on four parallel samples, and the results were averaged.

Two milligrams of HRP@PCN-333 was suspended in 5 mL of IAA deoxygenated aqueous solution (1 mg mL^{-1} IAA). The deoxygenated solution was used to prevent premature activation of the prodrug. The mixture was stirred at 4 °C for 24 h in the dark. IAA/HRP@PCN-333 NPs were collected by centrifugation. Measurements of the amount of the loaded IAA were performed on four parallel samples. IAA standard solutions were prepared in water at concentrations of 3.91, 7.82, 15.64, 31.28 and 62.5 mg mL^{-1}. The absorbances of IAA standard at 280 nm via the UV-vis spectroscopy (company, country) were plotted against the concentrations to build a standard curve for IAA. The amount of the loaded IAA onto HRP@PCN-333 was calculated from the difference in the absorbance of the supernatant before and after IAA loading at 280 nm. The leaked HRP from HRP@PCN-333 during the IAA encapsulation process was calculated by measuring the absorbance of the 5x concentrated supernatant after IAA loading at 402 nm.

Materials and other experimental protocols are provided in the Supporting Information (SI).

Results and Discussion

The as-synthesized PCN-333 (Fe) was characterized by SEM and XRD to reveal its morphology and crystalline nature. Figure 2a and 2b present the SEM images of PCN-333 (Fe) while its XRD pattern is exhibited in Figure 2c. PCN-333 (Fe) displays a uniform octahedral morphology according to the SEM image, which is in line with that in the previously published study.[5] The XRD pattern reveals characteristic peaks of PCN-333 (Fe) from 1.0 to 3.5, confirming its crystallinity and crystalline structure compared to the reported XRD pattern[6]. In Figure 2d, XPS results further supports that the valence state of Fe ion in PCN-333 (Fe) is 3+, in alignment with the coordination type and the MTN topology.

The loading amount of HRP into PCN-333 (Fe) and IAA into HRP@PCN-333 is 253 mg and 332 mg per gram of PCN-333 (Fe), and the loading capacity of HRP and IAA was 20.2% and 24.9%, respectively. Figure 2e and 2f exhibit the BET curves before and after HRP/IAA loading. The BET curve for nitrogen adsorption on PCN-333 (Fe) before HRP and IAA loading displays the combining type IV and VI adsorption isotherm curve, indicating there is a stepwise or hierarchical mesoporous structure in PCN-333 (Fe). The pore size of hierarchical pores is estimated to be 4.9 nm, 3.7 nm, and 0.8 nm from the nitrogen adsorption/desorption curves (Table S2). After PCN-333 (Fe) is loaded with HRP and IAA, the BET curve of HRP/IAA@PCN-333 (Fe) exhibits a type II nitrogen adsorption isotherm, indicating a decrease in the porous space in the material, thus confirming successful loading of HRP and IAA into mesopores and micropores. Moreover, the value of BET surface area decreased significantly after loading PCN-333 (Fe) with HRP and IAA (Table S2). Figure S1(a) shows the release profile of HRP in a PBS solution from HRP@PCN-333 (Fe). The UV-vis spectrum of the supernatant was acquired to quantify the released HRP. The release pattern of HRP from HRP-loaded PCN-333 (Fe) reveals two stages of the release process. Since HRP has a similar size to that of large mesopores of PCN-333 (Fe), only a trace amount of HRP is released in the first stage of the HRP release pattern starting from 0 h to 120 h. Only 0.7% of HRP is detected in the supernatant after the first 1 h, and 2.8% of HRP after the 12-h stirring. A slight increase up to 5.3 % of HRP is seen after 72 h. The accumulative release of HRP from HRP@PCN-333 (Fe) is 9.5% after 120 h. An increase in the HRP release is observed in the second stage starting from 120 h to 168 h, which could be ascribed to swelling of the porous structure in PCN-333 (Fe). The amount of the released HRP into the supernatant increases to 17.1% at 144 h, and accumulatively to 24.3% at 168 h. The loaded HRP into PCN-333 (Fe) are well retained inside the porous sites up to 120 h, which could efficiently prevent premature activation of IAA. In the second stage, an increase in the released HRP from PCN-333 (Fe) could contribute to activation of IAA and catalysis of intracellular H_2O_2, inducing a potent therapeutic effect on breast cancer cells. Figure S1(b) revealed the IAA release pattern of HRP/IAA@PCN-333 (Fe). IAA, as the small prodrug molecules, were loaded into PCN-333 (Fe) by physical adsorption. The IAA release pattern showed that more than 70% of IAA was released into PBS after 168 h,

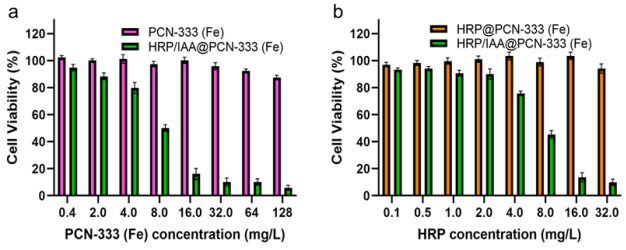

Figure 4. (a) Cell viability of MDA-MB-231 cells incubated with PCN-333 (Fe) and HRP/IAA@PCN-333 (Fe) for 24 h. (b) Cell viability of MDA-MB-231 cells incubated with HRP@PCN-333 (Fe) and HRP/IAA@PCN-333 (Fe) for 24 h.

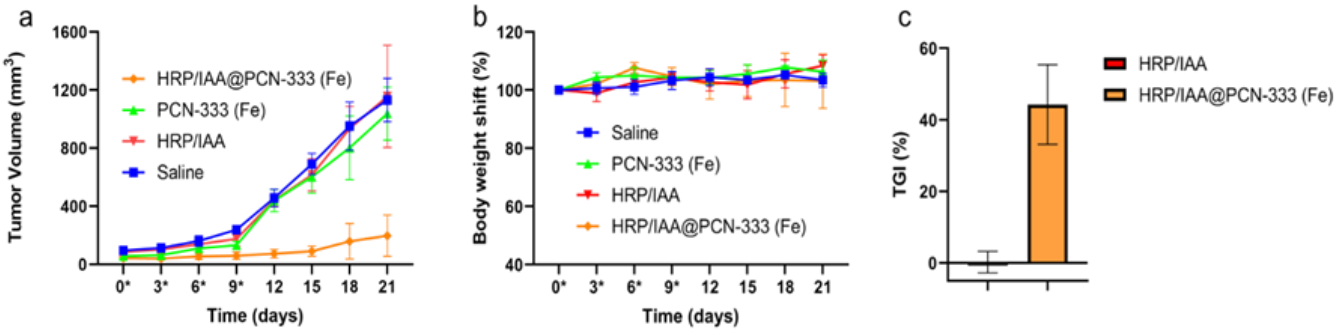

Figure 5. (a) Tumor growth curve in the mice groups based on the measurement of the tumor volume. The nude mice were intravenous injected with saline (control), HRP/IAA, PCN-333 (Fe) and HRP/IAA@PCN-333(Fe) at a dose of IAA of 250 μg/mL on day 0, 3, 6, and 9. (b) Body weight shift of the nude mice with different drug administrations. (c) Tumor growth inhibition of HRP/IAA and HRP/IAA@PCN-333 (Fe). *On the horizontal axis of (a) and (b) indicates the day of drug administration.

indicating that IAA molecules were not immobilized due to their smaller molecular size, which is different from the loaded HRP. Higher release rate and continuous release of IAA may contribute to its effective activation by HRP, thus facilitating the generation of ROS and toxic moiety for killing breast cancer cell. To reveal the ROS generation by HRP/IAA@PCN-333 (Fe), the enzymatic activity of HRP@PCN-333 (Fe) was investigated compared with free HRP. The enzymatic activity of HRP@PCN-333 (Fe) is comparable to that of native HRP when *o*-PD was used as the enzyme substrate, confirming that PCN-333 (Fe) could preserve the activity of the loaded HRP. The Michaelis–Menten plots in Figure S2 and Figure S3 show the effect of an increase in the concentration of o-PD on the initial reaction rate of native HRP and HRP@PCN-333. The kinetic parameters including K_m (μM), V_{max} (μm s^{-1}), and K_{cat} (s^{-1}) are listed in Table S1. K_m represents the concentration of the substrate when the enzymatic catalytic rate reaches the half of the maximum catalytic rate. It is found that the K_m of HRP@PCN-333 (Fe) is 2.5 times as that of native HRP, which indicates more substrates are needed for HRP@PCN-333 (Fe) to achieve the same catalytic rate as native HRP, which may be due to the diffusion of substrates and products through the pores of PCN-333 (Fe).[30] The difference in the V_{max} and K_{cat} between native HRP and HRP@PCN-333 (Fe) is negligible. Therefore, these results support successful encapsulation of HRP into PCN-333 (Fe) and preservation of the catalytic activity of HRP in HRP@PCN-333 (Fe).

Figure S4 and Figure S5 confirm the generation of ROS inside tumor cells by HRP/IAA and HRP/IAA@PCN-333 (Fe). MDA-MB-231 cells were incubated with HRP/IAA@PCN-333 (Fe) for different time periods to monitor the generation of ROS (1 h, 2 h, 4 h, 12 h). The culture medium without HRP/IAA@PCN-333 (Fe) is used as the control group to compare the catalytic performance of HRP/IAA@PCN-333 (Fe). The FITC channel (Excitation: 488 nm, Emission: 525 nm) was selected to monitor the amount of ROS generated. Flowcytometry results indicate that a low level of ROS is generated from HRP-loaded PCN-333 (Fe) at different time points (1 h, 2 h, 4 h, and 12 h) compared to the control group. At a time point of 12 h, a low ROS value of 5.98% is detected in the cells treated with HRP-loaded PCN-333 (Fe). The result suggest that without IAA, a quite low level of ROS could be generated by catalysis of intracellular H_2O_2 in the cancer cell microenvironment by HRP released from HRP-loaded PCN-333 (Fe).[31] However, a remarkable increase in the ROS generated is seen in cancel cells treated with HRP/IAA@PCN-333 (Fe) after a 12-h incubation, and up to 73.6% of cells display ROS signals. Flow cytometry results also confirm continuous catalysis of IAA by HRP in HRP/IAA@PCN-333 (Fe) to produce ROS after a 12-h incubation.

CLSM images in Figure 3 support uptake of HRP/IAA@PCN-333 (Fe) by MDA-MB-231 cells. To monitor the cellular uptake of HRP-loaded PCN-333 (Fe), HRP was labelled with FITC before it was loaded into PCN-333 (Fe) (HRP-FITC@PCN-333 (Fe)). MDA-MB-231 cells were incubated with HRP-FITC@PCN-333 (Fe) for 12 h. After PCN-333 (Fe) was loaded with FITC-labelled HRP, HRP-FITC@PCN-333 (Fe) was rinsed to remove the HRP-FITC residue. The green fluorescence representing FITC-labelled HRP is observed in the nucleus of breast cancer cells, which overlaps the blue fluorescence for the nucleus. Figure 4 exhibits the in vitro cytotoxicity induced by PCN-333 (Fe), HRP@PCN-333 (Fe) and HRP/IAA@PCN-333 (Fe) in contrast with the control group with the cell culture medium only. According to CCK8 analysis data, cells treated with PCN-333 (Fe) show non-toxicity toward MDA-MB-231 cells (Figure 4a), suggesting great biocompatibility of PCN-333 (Fe) as an enzyme/prodrug carrier. However, it is interesting to note that HRP treatment at

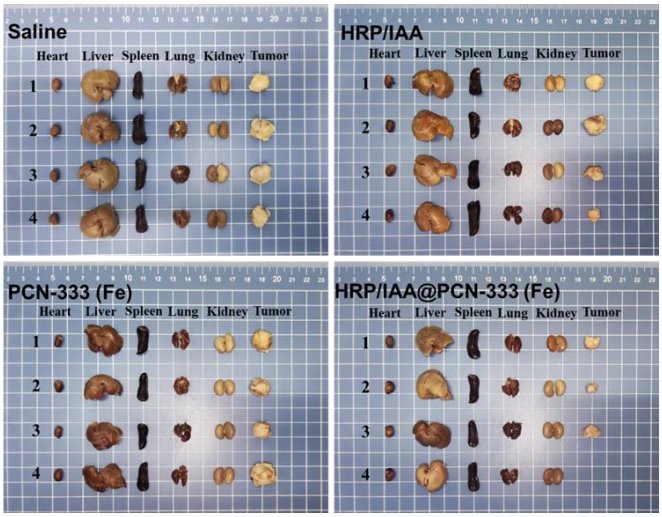

Figure 6. Viscera organs harvested from the BALB/c-nu mice after 21-day treatments with different formulations: saline, HRP/IAA, PCN-333 (Fe), and HRP/IAA@PCN-333 (Fe). Organs/tissues from left to right in each image in this figure: heart, liver, spleen, lung, kidney, tumor tissue.

different concentrations promotes the proliferation of breast cancer cells (Figure S6), which is in line with the observation from previous reports.[32, 33] The HRP@PCN-333 (Fe)-treated cell group (Figure 4b) exhibits a minor therapeutic effect on MDA-MB-231 cells, and a 91% of cell viability is maintained even at a high concentration of 32 mg/L of HRP@PCN-333 (Fe). In contrast, a high level of cytotoxicity for MDA-MB-231 cells is induced by HRP/IAA@PCN-333 (Fe). Up to 95% of cancer cells are not viable after their incubation with HRP/IAA@PCN-333 (Fe) at a concentration 128 mg/L for 24 h. The cell viability results support the feasibility of using HRP/IAA@PCN-333 (Fe) for the treatment of breast cancer.

In vivo experiment was conducted to reveal the therapeutic effect of HRP/IAA@PCN-333 (Fe) on breast cancer in an animal model. A patient-derived tumor xenograft (PDX) model was employed by planting MDA-MB-231 tumors into the BALB/c-nu mice. PDX model construction method is described in the Supporting Information. Saline (control), PCN-333 (Fe) at 550 μg/mL, HRP/IAA, and HRP/IAA@PCN-333(Fe) at a dose of IAA of 250 μg/mL at a nanoparticle concentration of 1 mg/mL were administrated four times on day 0, 3, 6, and 9. The tumor size changes in all mice were monitored up to 21 days. All results in each group were averaged from the quadruplicated samples. The tumor growth curve is displayed in Figure 5a. In comparison with the control group, HRP/IAA@PCN-333 (Fe) treatment effectively inhibits the growth of breast cancer tumor. after day 15, the tumor growth in the mice group treated with HRP/IAA@PCN-333 (Fe) is effectively inhibited and a lower level of growth in this group is observed compared to other groups, indicating sustainable catalysis of IAA by HRP to release the cytotoxic API and ROS helps curbing the growth of tumor cells. It is also noted that the mice group treated with HRP/IAA group exhibits a negligible therapeutic effect, no significant difference in the tumor volume is observed between the groups treated with HRP/IAA and the control, which could result from premature activation of IAA and inactivation of HRP without the protection of PCN-333 (Fe).

HRP/IAA@PCN-333 (Fe) do not induce systemic side effect in the tumor-planted nude mice, thus verifying great biocompatibility of this enzyme/prodrug delivery system. The tumor growth inhibition rate (TGI) was calculated and it is displayed in Figure 5c. The TGI of HRP/IAA@PCN-333 (Fe) is significantly higher in contrast with that of HRP/IAA, indicating the vital role of the enzyme/prodrug carrier PCN-333 (Fe) in prevention of premature IAA activation and protection of HRP. Furthermore, viscera organs (heart, liver, spleen, lung, kidney) from these nude mice were collected and compared with them from the control group. Figure 6 show the viscera organs harvested from the mice at the end of the treatment. According to these images, no obvious difference in the size of these organs is observed in the mice treated with HRP/IAA@PCN-333 (Fe) compared to the saline-treated group. No distinct shrinkage or swelling are observed in these organs in the mice after the treatment with saline, the drug carrier and HRP/IAA@PCN-333 (Fe). Therefore, HRP/IAA@PCN-333 (Fe) can effectively inhibit the growth of breast cancer cells but does not induce systemic side effects on the tumor-planted nude mice. The experimental results in the PDX model could facilitate transition of our enzyme/prodrug delivery system in clinical trial. The delivery of HRP/IAA@PCN-333 (Fe) can be achieved via the enhanced permeability and retention effect (EPR) as the size of nanoparticles is in the range of 100-800 nm.[34] Further work needs to be done to verify the assumption.

Conclusion

In summary, the hierarchical mesoporous PCN-333 (Fe) was fabricated for dual loading and delivery of HRP and IAA with a high loading capacity. The enzymatic activity of HRP is maintained after the immobilization, and the premature activation of IAA is prevented. CLSM images confirm successful intracellular uptake of HRP/IAA@PCN-333 (Fe) into breast cancer cells MDA-MB-23. Inside the tumor cells, HRP catalyzes the prodrug to produce cytotoxic components and ROS, which induces apoptosis of tumor cells, while the carrier PCN-333 (Fe) shows great biocompatibility. In a PDX animal model, the enzyme/prodrug delivery system effectively inhibit the tumor growth and the TGI is around 43%. The use of hierarchical PCN-333 (Fe) for the immobilization of exogeneous enzymes and encapsulation of products may provide a promising strategy for EAPT of cancer.

Conflicts of interest

The authors declare no conflict of interest.

Acknowledgements

We would like to thank the Analytical & Testing Center of Sichuan University for SEM and TEM work. We are grateful to Dr. Yong Liu for her help with SEM analysis and Dr Shanling Wang for her assistance with TEM analysis. We thank Dr. Long Ren in Huaxi MR Research Center (HMRRC) for his assistance of analyzing the results of enzymatic activity regarding HRP and *o*-PD substrate.

References

1. K. M. Bernt, D. S. Steinwaerder, S. H. Ni, Z. Y. Li, S. R. Roffler and A. Lieber, *Cancer Res*, 2002, **62**, 6089-6098.
2. M. A. Robinson, S. T. Charlton, P. Garnier, X. T. Wang, S. S. Davis, A. C. Perkins, M. Frier, R. Duncan, T. J. Savage, D. A. Wyatt, S. A. Watson and B. G. Davis, *P Natl Acad Sci USA*, 2004, **101**, 14527-14532.
3. I. T. Mohuiddin, X. B. Cao and W. R. Smythe, *Cancer Gene Ther*, 2000, **7**, S20-S20.
4. H. X. Zhang, H. H. Lin, D. Su, D. C. Yang and J. Y. Liu, *Mol Pharmaceut*, 2022, **19**, 630-641.
5. P. Ghosh, X. C. Yang, R. Arvizo, Z. J. Zhu, S. S. Agasti, Z. H. Mo and V. M. Rotello, *J Am Chem Soc*, 2010, **132**, 2642-2645.
6. D. W. Feng, T. F. Liu, J. Su, M. Bosch, Z. W. Wei, W. Wan, D. Q. Yuan, Y. P. Chen, X. Wang, K. C. Wang, X. Z. Lian, Z. Y. Gu, J. Park, X. D. Zou and H. C. Zhou, *Nat Commun*, 2015, **6**.
7. X. Z. Lian, A. Erazo-Oliveras, J. P. Pellois and H. C. Zhou, *Nat Commun*, 2017, **8**.
8. L. Xu, X. H. Liu, Y. P. Li, Z. H. Yin, L. Jin, L. L. Lu, J. Y. Qu and M. Xiao, *Appl Microbiol Biot*, 2019, **103**, 7997-8008.
9. F. Wang, J. Yang, Y. S. Li, Q. X. Zhuang and J. L. Gu, *J Mater Chem B*, 2020, **8**, 6139-6147.

10. O. M. Yaghi and H. L. Li, *Journal of the American Chemical Society*, 1995, **117**, 10401-10402.
11. P. Horcajada, T. Chalati, C. Serre, B. Gillet, C. Sebrie, T. Baati, J. F. Eubank, D. Heurtaux, P. Clayette, C. Kreuz, J. S. Chang, Y. K. Hwang, V. Marsaud, P. N. Bories, L. Cynober, S. Gil, G. Ferey, P. Couvreur and R. Gref, *Nat Mater*, 2010, **9**, 172-178.
12. P. Horcajada, C. Serre, G. Maurin, N. A. Ramsahye, F. Balas, M. Vallet-Regi, M. Sebban, F. Taulelle and G. Ferey, *J Am Chem Soc*, 2008, **130**, 6774-6780.
13. X. Li, D. W. Li, Y. N. Zhang, P. F. Lv, Q. Feng and Q. F. Wei, *Nano Energy*, 2020, **68**.
14. Q. B. Li, Y. X. Pan, H. Li, L. Alhalhooly, Y. Li, B. C. Chen, Y. Choi and Z. Y. Yang, *Acs Appl Mater Inter*, 2020, **12**, 41794-41801.
15. S. M. Huang, G. S. Chen, N. R. Ye, X. X. Kou, R. Zhang, J. Shen and G. F. Ouyang, *Acs Appl Mater Inter*, 2020, **12**, 57343-57351.
16. Z. Wang, J. S. Niu, C. Q. Zhao, X. H. Wang, J. S. Ren and X. G. Qu, *Angew Chem Int Edit*, 2021, **60**, 12431-12437.
17. T. Simon-Yarza, M. Gimenez-Marques, R. Mrimi, A. Mielcarek, R. Gref, P. Horcajada, C. Serre and P. Couvreur, *Angew Chem Int Edit*, 2017, **56**, 15565-15569.
18. I. A. Lazaro and R. S. Forgan, *Coordin Chem Rev*, 2019, **380**, 230-259.
19. H. M. Wang, Y. Q. Chen, H. Wang, X. Q. Liu, X. Zhou and F. Wang, *Angew Chem Int Edit*, 2019, **58**, 7380-7384.
20. Z. Wang, S. G. Hu, J. Yang, A. J. Liang, Y. S. Li, Q. X. Zhuang and J. L. Gu, *Adv Funct Mater*, 2018, **28**.
21. L. R. M. B. Mourao, R. S. S. Santana, L. M. Paulo, S. M. P. Pugine, L. M. Chaible, H. Fukumasu, M. L. Z. Dagli and M. R. de Melo, *Cell Biochem Funct*, 2009, **27**, 16-22.
22. M. Dai, J. Liu, D. E. Chen, Y. Rao, Z. J. Tang, W. Z. Ho and C. Y. Dong, *Cancer Gene Ther*, 2012, **19**, 77-83.
23. L. K. Folkes and P. Wardman, *Biochem Pharmacol*, 2001, **61**, 129-136.
24. A. Baeza, E. Guisasola, A. Torres-Pardo, J. M. Gonzalez-Calbet, G. J. Melen, M. Ramirez and M. Vallet-Regi, *Adv Funct Mater*, 2014, **24**, 4625-4633.
25. N. I. Marupudi, J. E. Han, K. W. Li, V. M. Renard, B. M. Tyler and H. Brem, *Expert Opin Drug Saf*, 2007, **6**, 609-621.
26. N. Milosavljevic, C. Duranton, N. Djerbi, P. H. Puech, P. Gounon, D. Lagadic-Gossmann, M. T. Dimanche-Boitrel, C. Rauch, M. Tauc, L. Counillon and M. Poet, *Cancer Res*, 2010, **70**, 7514-7522.
27. D. P. Nolan, S. Rolin, J. R. Rodriguez, J. Van Den Abbeele and E. Pays, *Eur J Biochem*, 2000, **267**, 18-27.
28. T. O. Harris, D. W. Shelver, J. F. Bohnsack and C. E. Rubens, *J Clin Invest*, 2003, **111**, 61-70.
29. I. A. Lazaro, S. Haddad, J. M. Rodrigo-Munoz, C. Orellana-Tavra, V. del Pozo, D. Fairen-Jimenez and R. S. Forgan, *Acs Appl Mater Inter*, 2018, **10**, 5255-5268.
30. A. K. Poulsen, A. M. Scharff-Poulsen and L. F. Olsen, *Anal Biochem*, 2007, **366**, 29-36.
31. T. Jiang, X. X. Sun, L. L. Wei and M. G. Li, *Anal Chim Acta*, 2020, **1135**, 132-141.
32. P. L. Thi, Y. Lee, D. L. Tran, T. T. H. Thi and K. D. Park, *J Biomater Appl*, 2020, **34**, 1216-1226.
33. J. W. Bae, J. H. Choi, Y. Lee and K. D. Park, *J Tissue Eng Regen M*, 2015, **9**, 1225-1232.
34. M. C. García, in Stimuli-Responsive Nanocarriers (Eds.: V. Gajbhiye, K. R. Gajbhiye, S. Hong), Academic Press, 2022, pp. 429-450.

Supporting Information

Efficient Cancer Therapy Achieved by Enzyme Immobilization and Prodrug Encapsulation using PCN-333 (Fe)

Yechuan Zhang[1], Zhengxiang Gu[2], Zhiqian Li[2], Kui Luo*[2], Hu Zhang*[3], Jingxiu Bi*[1], Yan Jiao*[1],

[1]School of Chemical Engineering and Advanced Materials, University of Adelaide, SA 5005, Australia
[2]Huaxi MR Research Center (HMRRC), Department of Radiology, National Clinical Research Center for Geriatrics, Frontiers Science Center for Disease-Related Molecular Network, State Key Laboratory of Biotherapy, West China Hospital, Sichuan University, Chengdu 610041, China
[3] Riggs School of Applied Life Sciences, Keck Graduate Institute, CA 91711, USA
*Corresponding Authors.
E-mail address: luokui@scu.edu.cn; hu_zhang@kgi.edu; jingxiu.bi@adelaide.edu.au; yan.jiao@adelaide.edu.au.

Materials

Trifluoroacetic acid (TFA), hydrochloric acid, rhodamine-B (RhB), dimethyl sulfoxide (DMSO), N-2-hydroxyethylpiperazine-N'-2-ethanesulfonic acid (HEPES) dichloromethane (CH_2Cl_2), N,N-dimethylformamide (DMF), hydrogen peroxide (H2O2), sodium chloride (NaCl), sodium bicarbonate ($NaHCO_3$), H_3TATB, IAA and o-phenylenediamine (o-PD) were purchased from Shanghai Aladdin Biochemical Technology Co., Ltd. $FeCl_3$, HRP, ethanol, sodium citrate, acetone, Fluorescein isothiocyanate (FITC) and CCK8 were obtained from Sigma-Aldrich. DMEM and Fetal bovine serum (FBS) were provided by Gibco, Switzerland. All reagents were of analytical grade and were used without further purification.

Experimental Methods

Enzymatic activity of HRP

The oxidation of *o*-PD was employed to evaluate the enzymatic activity of free HRP and HRP@PCN-333 (Fe) at room temperature. During the catalytic reaction, various substrate concentrations of *o*-PD, 0.2 mM H_2O_2 and 0.015 mM native HRP or HRP@PCN-333 (Fe) solutions were prepared in a citric acid–sodium citrate buffer (0.1 M, pH = 6.0). The catalytic reaction was continuously monitored via an ultraviolet-visible spectrophotometer (UV-3600, country), and the absorption value of the product, 2,3-diamino-phenazine (DAP), was recorded at 418 nm. The difference in the absorption value at 418 nm between test samples and blank samples was transformed to the molar concentrations of the DAP product via its reported molar absorption coefficient. The initial reaction rate (V) for the catalytic reaction was calculated using the following equation (1), and the Michaelis–Menten model was used to correlate the reaction rate and the substrate concentration (Equation 2). The kinetic parameters were obtained from linear regression, where V (mM s^{-1}) is the initial reaction rate of HRP@PCN-333 (Fe) catalyzing the *o*-PD substrate to produce DAP; S (mM) is the substrate concentration of *o*-PD; V_{max} (mM s^{-1}) is the maximum rate of the reaction; and K_m (mM) is the Michaelis–Menten constant.

$$\text{Reaction rate } (V) = \frac{\text{Amount of DAP product}}{\text{Reaction Time}} \quad (1)$$

$$\frac{1}{V} = \frac{1}{Vmax} + \frac{Km}{Vmax} \times \frac{1}{[S]} \quad (2)$$

Release of HRP from PCN-333 (Fe)

PCN-333 (Fe) NPs were separately loaded with HRP and IAA for the release studies. 1 mg of HRP@PCN-333 was dispersed in 1 mL of PBS buffer solution (10 mM, pH = 7.4) at 37 °C and the dispersion was mechanically shaken at 200 rpm. At different time intervals, the supernatant was withdrawn after centrifugation, and the material was re-dispersed in 1 mL of fresh PBS to continue the release process. The amount of HRP released was analyzed via a UV-vis spectrometer. Measurements were performed on three parallel samples.

Cytotoxicity studies

MDA-MB-231 cells were seeded at a density of 10^4 cells per well in 96-well plates, and 100 uL of DMEM containing 10% FBS was added to each well. The cells were cultured for 24 h at 37 °C under 95% humidity and in a 5% CO_2 atmosphere. After removing the spent medium, 100 uL of PCN-333(Fe), HRP@PCN-333(Fe), IAA/HRP@PCN-333(Fe) per well was added to the cells, and fresh DMEM (100 uL per well) was used as the blank control group. They were incubated for 24 h. The residual of the nanoparticles was washed with PBS solution (pH = 7.4, 10 mM). 10 uL of the CCK8 (1 mg /mL) solution in 100 uL DEME solution was added to each well and incubated for 30 min at 37 °C under 95% humidity and in a 5% CO_2 atmosphere. The absorbance of each well was measured using a microplate reader.

Labelling HRP with FITC

5 mg of HRP was dissolved in 2 mL of $NaHCO_3$ (0.1 M, pH = 9) buffer solution. 50 uL of FITC solution (10 mg/mL in DMSO) was then added to the above HRP solution, and the mixture was stirred in an ice bath at 4 °C for 12 h in the dark. HRP-FITC was purified and collected from a chromatographic column using the Sepharose 4b matrix.

Flow cytometry analysis

To quantify the ROS generation of the present EAPT system, MDA-MB-231 cells were

seeded at a density of 5×10^4 cells per well in 12-well plates. 0.5 mL of DMEM containing 10% FBS was added to each well. The cells were cultured for 24 h at 37 ° C under 95% humidity and in a 5% CO_2 atmosphere. After removing the media, the cells were incubated with 0.5 mL of medium containing HRP/IAA@PCN-333 (Fe) or HRP/IAA at different concentrations for 1 h, 2 h, 4 h, and 12 h as experimental groups, and fresh DMEM (0.5 mL per well) was used as the blank control group. The nanoparticles in each well were removed by washing twice with PBS (pH = 7.4, 10 mM), and 50 uL of trypsin was added to each well to harvest cells. The cells were collected by low-speed centrifugation and washed three times with PBS. Finally, the collected cells were dispersed in PBS solution for flow cytometry analysis.

Confocal fluorescence microscopy (CLSM)

MDA-MB-231 cells (10^4 cells) were seeded in an ibidi 8-well plate, and 100 uL of DMEM containing 10% FBS was added to each well. The cells were grown for 24 h at 37°C under 95% humidity and in a 5% CO_2 atmosphere. After removing the media, the cells were incubated with 100 uL of medium containing HRP-FITC or HRP-FITC@PCN-333 (Fe) for 12 h. The nanomaterial residue was removed by washing 3 times with PBS. Cells were then treated with 5 μg/mL CellMask™ Deep Red Plasma Membrane Stain for 5 min and then washed with PBS three times to remove the residue. 1 μg/mL bisBenzimide H 33258 was added to three wells afterwards and incubated for another 5 min, and three wells were washed by PBS another three times. Fluorescent images were captured via a CLSM (company name, country).

***In vivo* experiment**

BALB/c-nu nude mice were used for *in vivo* experiments. PDX model based on MDA-MB-231 cells was built in each nude mouse. For each nude mice, 2 x 10^7 cells (previously cultured in 150 mm cell culturing dish) were planted subcutaneously at the abdomen near the left leg. After the cell planting, the PDX model growed for 21 days to start the drug administration. The concentration of HRP/IAA@PCN-333 (Fe) for

administration was 1.0 mg/mL. Based on the loading capacity of HRP and IAA, the dose of HRP and IAA was estimated. PCN-333 (Fe) and saline were used as control groups. Four nude mice were used in each group. Drug administration via intravenous injection of 200 uL of HRP/IAA@PCN-333 (Fe), HRP/IAA, PCN-333 (Fe) and saline was conducted on day 0, 3, 6, and 9. The tumor size and body weight were recorded every three days. The entire treatment continued for 21 days, and nude mice were executed on day 21 by following the animal ethical protocols of West China Hospital, Sichuan University. All animal experiment procedure were approved by the ethic committee of West China Hospital, Sichuan University.

Tables:

Table S1. Kinetic parameters of the catalytic reaction toward *o*-PD using native HRP and HRP@PCN-333 (Fe).

Samples	**K_m (mM)**	**V_{max} (mM s^{-1})**	**k_{cat} (s^{-1})**
Native HRP	88.63	0.063	4.2
HRP@PCN-333 (Fe)	221.58	0.061	4.1

Table S2. BET surface area and pore diameter of hierarchical pores of PCN-333 (Fe) and HRP/IAA@PCN-333 (Fe).

Sample	**S_{BET} (m^2 g^{-1})**	**P_d (Å)**
PCN-333 (Fe)	1587	48.53/36.67/7.72
HRP/IAA@PCN-333 (Fe)	1165	29.34/16.85/4.26

Figures:

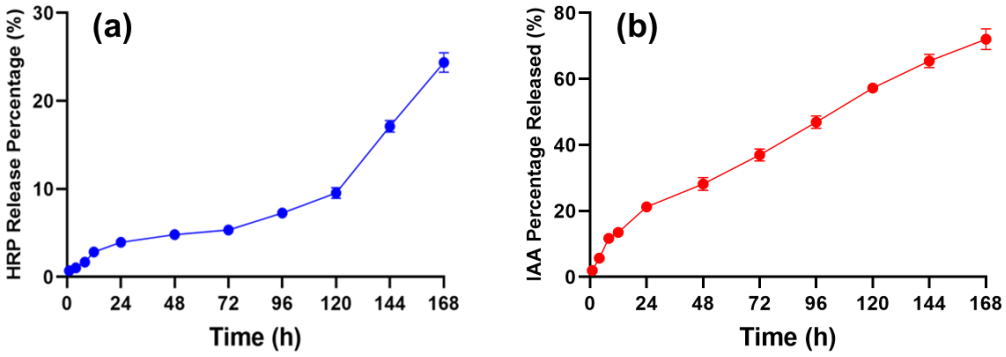

Figure S1. (a) HRP released from HRP/IAA@PCN-333 (Fe) in PBS for 168 h; (b) IAA released from HRP/IAA@PCN-333 (Fe) in PBS for 168 h.

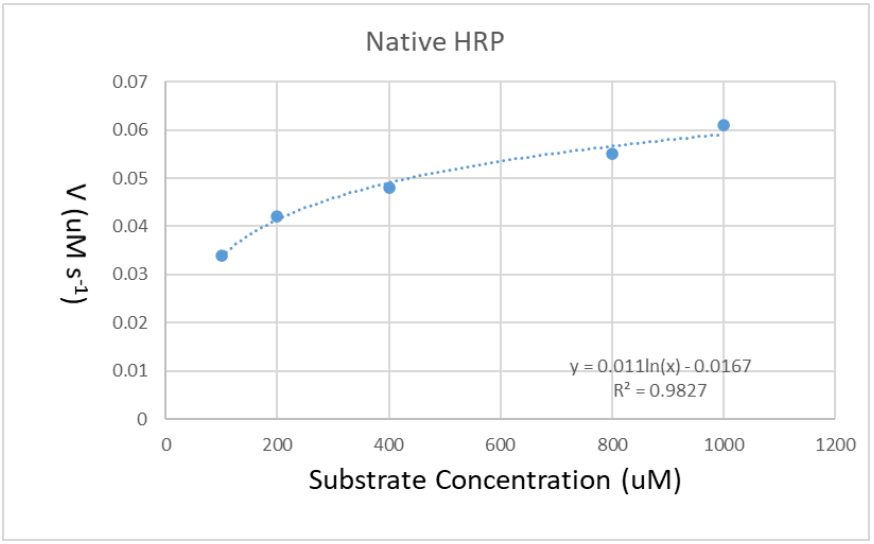

Figure S2. The Michaelis–Menten plots illustrating the effect of the increasing concentration of *o*-PD on the initial reaction rate of native HRP.

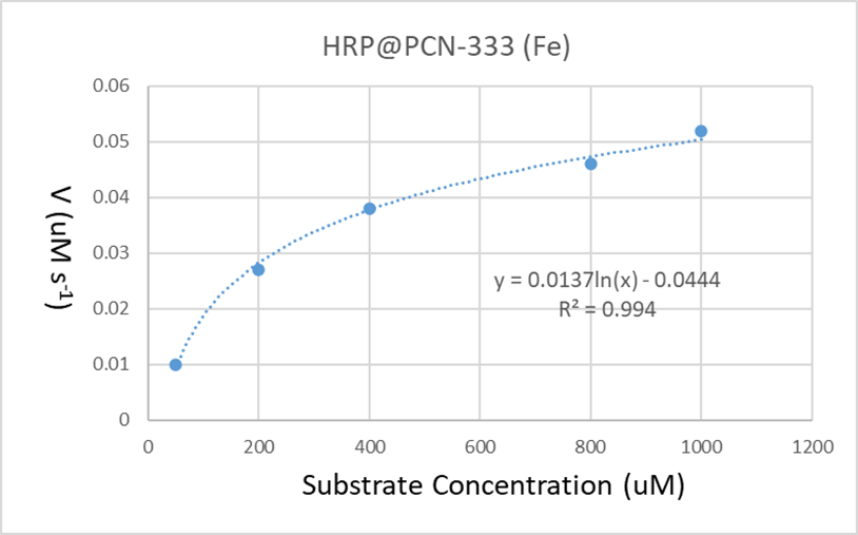

Figure S3. The Michaelis–Menten plots illustrating the effect of the increasing concentration of *o*-PD on the initial reaction rate of HRP@PCN-333 (Fe).

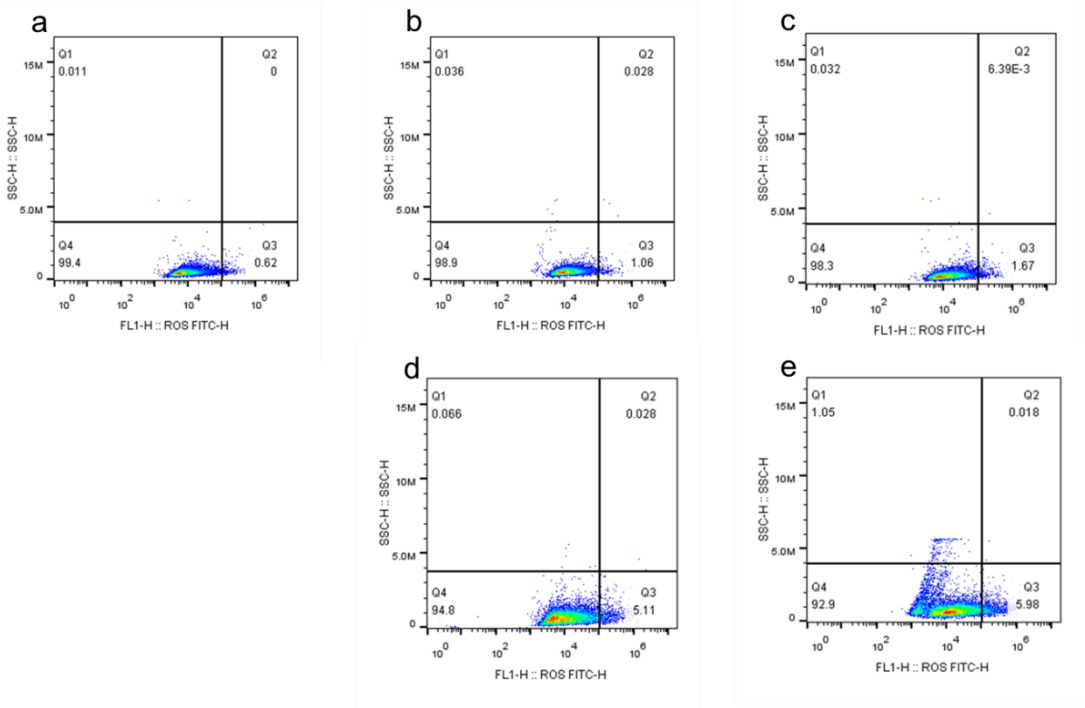

Figure S4. (a) Control group of flow cytometry using MDA-MB-231 cells. Flow cytometry results of MDA-MB-231 cells incubated with HRP/IAA with different time periods (b) 1, (c) 2 h, (d) 4 h, and (e) 12 h.

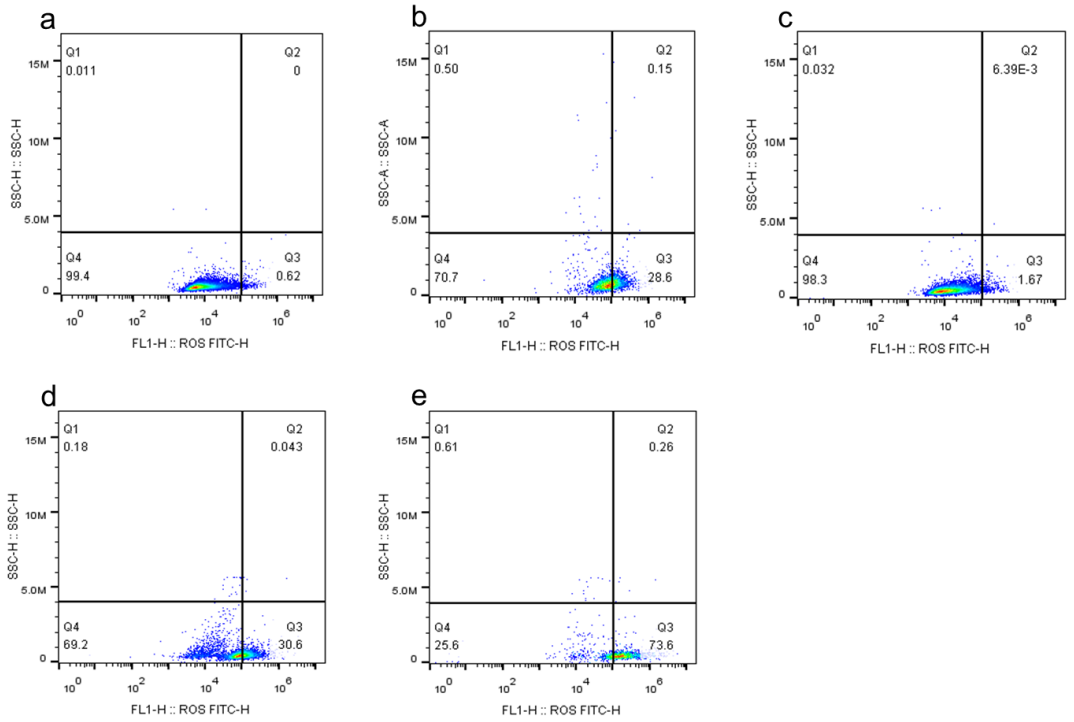

Figure S5. (a) Control group of flow cytometry using MDA-MB-231 cells. Flow cytometry results of MDA-MB-231 cells incubated with HRP/IAA@PCN-333 (Fe) with different time periods (b) 0.5 h, (c) 1 h, (d) 2 h, and (e) 4 h.

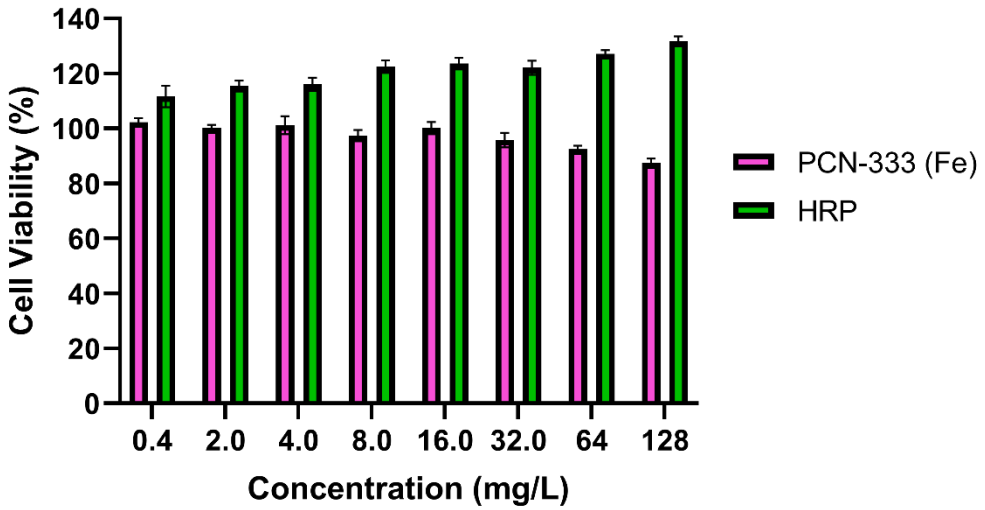

Figure S6. Cell proliferation caused by HRP with different concentrations compared to PCN-333 (Fe).

Chapter 5. Molybdenum-Iron-Cobalt Oxyhydroxide with Rich Oxygen Vacancies for Oxygen Evolution Reaction

5.1 Introduction, Significance and Commentary

The sluggish kinetics of OER limited the development of water splitting technology. Transition metals possess the advantages of being the OER catalysts due to faster electron transfer. In this work, trimetallic oxyhydroxide constructed from three transition metals: molybdenum, iron, and cobalt was synthesized by the a facile and robust cation exchange method. The material presented in this work exhibited abundant oxygen vacancies and active metal sites for OER catalysis. The excellent OER performance of the molybdenum-iron-cobalt oxyhydroxide proved the potential of ternary transition metal oxyhydroxide with rich oxygen vacancies as OER catalysts.

5.2 Publication

This section is presented as the published paper by **Y.C. Zhang**, Z.X. Gu, J.X. Bi, Y. Jiao, Molybdenum-iron–cobalt oxyhydroxide with rich oxygen vacancies for the oxygen evolution reaction, Nanoscale 14(30) (2022) 10873-10879.

Statement of Authorship

Title of Paper	Molybdenum-iron–cobalt oxyhydroxide with rich oxygen vacancies for the oxygen evolution reaction
Publication Status	☑ Published ☐ Accepted for Publication ☐ Submitted for Publication ☐ Unpublished and Unsubmitted work written in manuscript style
Publication Details	**Y.C. Zhang**, Z.X. Gu, J.X. Bi, Y. Jiao, Molybdenum-iron–cobalt oxyhydroxide with rich oxygen vacancies for the oxygen evolution reaction, Nanoscale 14(30) (2022) 10873-10879. (**IF=8.307**) https://doi.org/10.1039/D2NR02568J

Principal Author

Name of Principal Author (Candidate)	Yechuan Zhang		
Contribution to the Paper	Designed the material and experiments, carried out experiments, analyzed experimental results, and wrote the manuscript.		
Overall percentage (%)	50%		
Certification:	This paper reports on original research I conducted during the period of my Higher Degree by Research candidature and is not subject to any obligations or contractual agreements with a third party that would constrain its inclusion in this thesis. I am the primary author of this paper.		
Signature		Date	05/09/2022

Co-Author Contributions

By signing the Statement of Authorship, each author certifies that:

i. the candidate's stated contribution to the publication is accurate (as detailed above);

ii. permission is granted for the candidate in include the publication in the thesis; and

iii. the sum of all co-author contributions is equal to 100% less the candidate's stated contribution.

Name of Co-Author	Zhengxiang Gu		
Contribution to the Paper	Designed experiments, analyzed results, modified the manuscript, figure corrections.		
Signature		Date	08/08/2022

Name of Co-Author	Jingxiu Bi		
Contribution to the Paper	Modified the manuscript.		
Signature		Date	08/08/2022

Name of Co-Author	Yan Jiao		
Contribution to the Paper	Analyzed experimental results, modified the manuscript.		
Signature		Date	08/08/2022

Please cut and paste additional co-author panels here as required.

Nanoscale

PAPER

View Article Online
View Journal | View Issue

Cite this: *Nanoscale*, 2022, **14**, 10873

Molybdenum-iron–cobalt oxyhydroxide with rich oxygen vacancies for the oxygen evolution reaction†

Yechuan Zhang, ‡[a,b] Zhengxiang Gu,‡[a] Jingxiu Bi[b] and Yan Jiao *[b]

Received 10th May 2022,
Accepted 30th June 2022

DOI: 10.1039/d2nr02568j

rsc.li/nanoscale

The sluggish kinetics of the oxygen evolution reaction (OER) restrains the development of water splitting technologies and the efficiency of producing sustainable resources. To this end, the introduction of iron and molybdenum in catalytic systems has been employed as a crucial strategy for the enhancement of catalytic activity toward the oxygen evolution reaction (OER), but the relationship between catalyst components and catalytic performance is still evasive. In this study, by doping iron and molybdenum into cobalt hydroxide *via* a cation-exchange method, rich oxygen vacancies and active metal centers are introduced to the trimetallic oxyhydroxide, endowing the catalyst with a low overpotential of 223 mV at 10 mA cm^{-2}, a low Tafel slope of 43.6 mV dec^{-1}, and a long stable operation time (>50 h) in alkaline media, comparable to the current best OER catalyst. Moreover, it is demonstrated that the doping of iron favors the generation of oxygen vacancies. It is also found in this work that using a certain amount (5 mg) of iron dopant can alter the electronic structure of the catalyst by tuning the electronic density around the metal ions, thus optimizing the binding energy of intermediates. The present work unveils the doping effect of iron and molybdenum on the construction of trimetallic oxyhydroxide catalysts, and sheds light on the relationship between the catalyst components and catalytic performance of the OER.

Introduction

The challenges of increasing energy consumption and global warming have prompted the exploration of water electrolysis to produce H_2, in which the oxygen evolution reaction (OER) is the vital half reaction.[1–4] However, the OER is a four-electron coupled reaction with a high kinetic barrier, restrained by a high overpotential and low efficiency.[5] The design and fabrication of highly efficient and economical catalysts is essential for optimizing the OER process. Conventionally, iridium (Ir) and ruthenium (Ru)-based materials[6,7] are often used as OER catalysts, but the scarcity and high cost of noble metals hinder their broad application in water splitting.[8,9] The development of low-cost electrocatalysts with the capability of reducing the high overpotential and the associated energy loss in the OER process has been widely investigated for practical applications.[10,11] Among the reported OER electrocatalysts, transition metal (such as Co, Ni, Mo and Fe) nanomaterials have drawn considerable attention and have been demonstrated as promising electrocatalysts in alkaline media.[12–15] In particular, various transition-metal doped Co-based electrocatalysts exhibit distinct properties in terms of the OER. For instance, Wen *et al.* developed a trimetallic catalyst with outstanding performance for the OER, which resulted from the synergistic effects of Fe, Co, and Cr.[16]

However, the rational design of OER electrocatalysts with optimal catalytic performance, namely low overpotential and long-term stability, remains a major challenge. Currently, two design strategies are mainly employed to enhance the catalytic activity. One is to utilize a controllable alloy composition with rich oxygen vacancies (O_v) to favor local coordination and energetics,[17,18] while the other is to take advantage of surface effects from the engineered nanostructure to enhance the exposure of active metal sites and to accelerate the ion transfer.[19–23] As a typical strategy for improving the OER catalytic activity, introducing oxygen vacancies into catalysts has been intensively studied. Oxygen vacancies can facilitate the adsorption of OH^- on the surface of electrocatalysts, resulting in extensive OH^- interaction with metal sites, and modifying the electronic structure of the materials to improve electrical conductivity, thus optimizing its dynamic performance for the

[a]*Huaxi MR Research Center (HMRRC), Department of Radiology, State Key Laboratory of Biotherapy, West China Hospital, Sichuan University, Chengdu 610041, China*
[b]*School of Chemical Engineering and Advanced Materials, University of Adelaide, SA 5005, Australia. E-mail: yan.jiao@adelaide.edu.au*

†Electronic supplementary information (ESI) available. See DOI: **https://doi.org/10.1039/d2nr02568j**

‡These authors contributed equally to this work.

OER.[24] The effective methods to obtain O_v in catalysts include heat treatment, reduction processing, anion/cation doping, plasma treatment, *etc*. Among them, cation doping will maintain the original physical structure of the material.[25] Zeng *et al.* designed an ultrathin amorphous iron-doped cobalt–molybdenum hydroxide nanosheet with excellent OER performance using the cation doping method.[26] To introduce the oxygen vacancy into water splitting electrocatalysts, Fang *et al.* employed a Mo-doping strategy for the fabrication of a $BiVO_4$ homojunction, leading to the crystal orientation reconstruction, thus achieving high oxygen evolution reaction activity.[27]

In the present work, we have developed a simple and robust cation-exchange methodology to successfully fabricate iron/molybdenum doped trimetallic oxyhydroxide (donated as $MoFe_{0.5}O_xCo(OH)_{2-x}$) with enriched oxygen vacancies and metal centers as active sites. The cation-exchange process of fabricating $MoFe_{0.5}O_xCo(OH)_{2-x}$ and its electrocatalysis of the OER are shown by the scheme in Fig. 1. Owing to the appropriate amount of molybdenum and iron doped into the $Co(OH)_2$ precursor, $MoFe_{0.5}O_xCo(OH)_{2-x}$ exhibited outstanding stability as highly active OER electrocatalysts. The high activity of catalysts results from the doping effect of iron and molybdenum. With the introduction of molybdenum, it can promote the generation of O_v when doping iron into the catalyst due to its electronic structure.[28] Doping of iron and molybdenum was achieved *via* a cation-exchange route with $Co(OH)_2$ at 60 °C. A series of Fe–Mo–Co trimetallic oxyhydroxides were obtained with various amounts of $FeCl_3$ (*e.g.*, 2.5, 5 to 10 mg), denoted as $MoFe_{0.25}O_xCo(OH)_{2-x}$, $MoFe_{0.5}O_xCo(OH)_{2-x}$, and $MoFeO_xCo(OH)_{2-x}$, respectively. The actual Co/Mo/Fe ratio in the samples was readily tuned and characterized by inductively coupled plasma mass spectrometry (ICP-MS) (Table S1, ESI†). The extended X-ray absorption fine structure (EXAFS) spectrum reveals the synergetic interaction of Co, Mo and Fe cations in the $MoFe_{0.5}O_xCo(OH)_{2-x}$ catalyst. Consequently, the $MoFe_{0.5}O_xCo(OH)_{2-x}$ catalyst exhibits excellent OER catalytic activity with an overpotential (η) of 223 mV to deliver an anodic current density of 10 mA cm^{-2} (j_{10}), possessing a low Tafel slope of 43.6 mV dec^{-1}. The remarkable OER catalytic performance exceeds that of the state-of-the-art RuO_2 (η = 387 mV) catalyst. Furthermore, the $MoFe_{0.5}O_xCo(OH)_{2-x}$ catalyst shows durability that exceeds 50 hours under continuous operation at 1.46 V *vs.* Reversible Hydrogen Electrode (RHE). The presented work contributes to the understanding of the doping effect of iron and molybdenum on optimizing the electrochemical properties of trimetallic oxyhydroxide, and provides a strategy for developing a low-cost and highly efficient OER catalytic system.

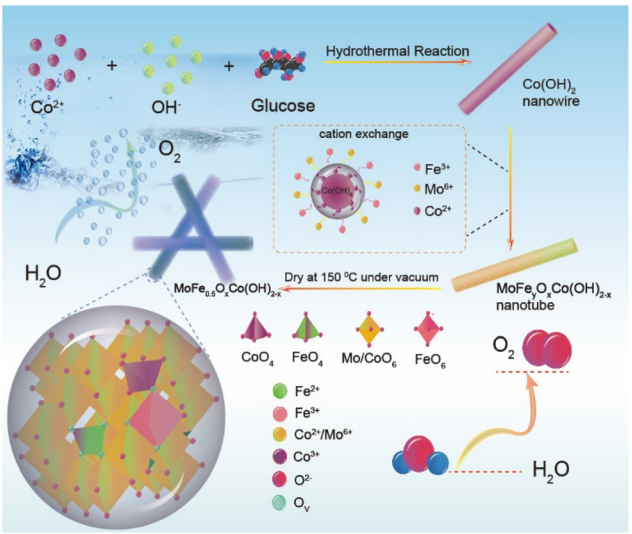

Fig. 1 Synthetic procedure of the heterostructural $MoFe_yO_xCo(OH)_{2-x}$ (*y*: atom ratio) nanotube using different amounts of Fe^{3+} dopant (2.5, 5, 10 mg) based on the *in situ* growth of $Co(OH)_2$ nanowire templates, showing the cation exchange process of Fe^{3+}/Mo^{6+} and the $Co(OH)_2$ nanowire templates.

Experimental section

Synthesis of $Co(OH)_2$

2 mmol $CoCl_2{\cdot}6H_2O$, 4 mmol NH_4F, and 10 mmol glucose were mixed in 50 ml of deionized water, and stirred for 30 min. The previous mixture was transferred to a 100 ml pressure vessel and reacted at 120 °C for 9 h. $Co(OH)_2$ was washed with water and ethanol 3 times, respectively.

Synthesis of $MoFe_yO_xCo(OH)_{2-x}$

Fe/Mo-doped $MoFe_yO_xCo(OH)_{2-x}$ were prepared *via* a cation-exchange method. First, 100 mg of as-prepared $Co(OH)_2$ and 10 mg of $Na_2MoO_4{\cdot}2H_2O$ were added to 20 mL of ethanol using an oil bath at 60 °C. Different amounts of $FeCl_3$ (2.5, 5, and 10 mg) were then added to the solution and continuously stirred for 2 h. The obtained products were centrifuged and washed with DI water and ethanol several times, and eventually dried under vacuum at 150 °C. The final products were denoted as $MoFe_yO_xCo(OH)_{2-x}$, where *y* represents the atomic ratio of Fe, which was evaluated by ICP-MS measurement.

Other information such as materials synthesis, materials characterization, and experimental protocols of this work are provided in the ESI.†

Results and discussion

X-ray powder diffraction (XRD) results confirmed the composition and crystal structure of $MoFe_{0.5}O_xCo(OH)_{2-x}$, exhibiting the XRD patterns of $MoFe_{0.25}O_xCo(OH)_{2-x}$/$MoFe_{0.5}O_xCo(OH)_{2-x}$/$MoFeO_xCo(OH)_{2-x}$, $MoO_xCo(OH)_{2-x}$, and $Co(OH)_2$ (Fig. S1, ESI†). The amorphous nature of $Co(OH)_2$ was confirmed as no obvious peak was observed. The presence of various crystalline peaks in the XRD pattern indicates that the heterostructure of $MoFe_{0.5}O_xCo(OH)_{2-x}$ has been formed. Fig. S2† shows the Raman spectra of $MoFe_{0.5}O_xCo(OH)_{2-x}$, $MoO_xCo(OH)_{2-x}$, and $Co(OH)_2$. The highest strength peak of Co–O–Mo had a red shift in which Fe can regulate the elec-

tronic structure of the Co center to reduce the energy barrier required for the reaction and optimize the adsorption and desorption of the active center to the reaction intermediate, thus improving its electrocatalytic performance.[29] From scanning electron microscopy (SEM) images (Fig. S3a, ESI†), it can be seen that $Co(OH)_2$ nanowire arrays were uniformly grown with a smooth surface at a high magnification (Fig. S3b, ESI†), confirming that the $Co(OH)_2$ nanowire arrays were used as a sacrificial template for the next reaction. Fast Fourier transform (FFT) images also confirmed the lattice spacing of $MoFe_{0.5}O_xCo(OH)_{2-x}$ corresponding to SEM images (Fig. S4†). Afterwards, doping of Fe^{3+} and Mo^{6+} into $Co(OH)_2$ was achieved *via* a cation exchange route, and it can be found (Fig. S5, ESI†) that the formed $MoFe_{0.5}O_xCo(OH)_{2-x}$ exhibited the nanotube morphology developed from the $Co(OH)_2$ nanowire precursor while the previously smooth surface of the precursor turned into a rough surface with a porous structure in the final product. As shown in Fig. S6 in the ESI,† all samples presented a nanotube-like structure with the lateral size ranging from 200 to 400 nm.

Fig. 2a shows the high-resolution transmission electron microscopy (HRTEM) image with the nanotube structure of $MoFe_{0.5}O_xCo(OH)_{2-x}$ displayed in Fig. 2b, of which the crystalline phase shows lattice spacing values of 0.309, 0.339, and 0.382 nm, corresponding to the (311), (220), and (021) planes. Fig. 2c shows the HRTEM pattern at the interface with lattice spacing values of 0.239 and 0.249 nm, in accord with the (111) and (200) planes, respectively. The selected area electron diffraction (SAED) diagram showed a clear diffraction ring, proving the hierarchical structure of $MoFe_{0.5}O_xCo(OH)_{2-x}$ as shown in Fig. 2d. The presence of oxygen vacancies could be further

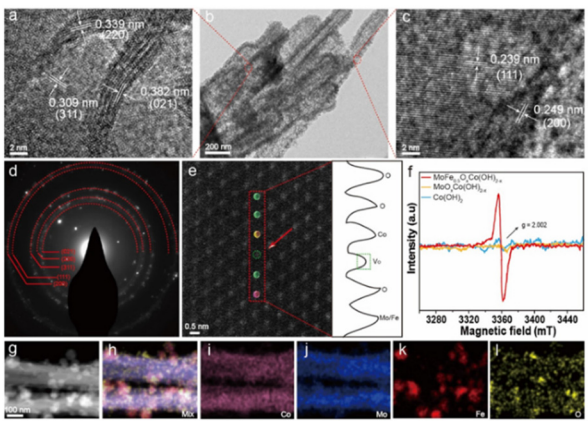

Fig. 2 (a) High resolution TEM (HRTEM) image of the selected area marked by a red-dotted circle in the left section of the $MoFe_{0.5}O_xCo(OH)_{2-x}$ sample in the (b) TEM image of as-prepared $MoFe_{0.5}O_xCo(OH)_{2-x}$. (c) High resolution TEM (HRTEM) image of the selected area marked by a red-dotted circle in the right section of $MoFe_{0.5}O_xCo(OH)_{2-x}$. (d) SAED pattern in the rectangle of $MoFe_{0.5}O_xCo(OH)_{2-x}$. (e) Spherical aberration-corrected STEM of $MoFe_{0.5}OxCo(OH)_{2-x}$. (f) EPR spectra of $Co(OH)_2$, $MoO_xCo(OH)_{2-x}$, and $MoFe_{0.5}O_xCo(OH)_{2-x}$. (g–l) HAADF-mapping images of Co, Mo, Fe, and O elements for $MoFe_{0.5}O_xCo(OH)_{2-x}$.

demonstrated by the high-angle annular dark-field scanning transmission electron microscopy (HAADF-STEM) image of $MoFe_{0.5}O_xCo(OH)_{2-x}$, in which abundant defects of oxygen atoms were clearly observed (marked by red arrows in Fig. 2e). Furthermore, the electron paramagnetic resonance (EPR) spectra of the as-prepared $Co(OH)_2$ and $MoO_xCo(OH)_{2-x}$ did not present any unpaired electrons while $MoFe_{0.5}O_xCo(OH)_{2-x}$ exhibited a pair of opposite peaks at $g = 2.002$, suggesting the existence of unpaired electrons due to the oxygen vacancies (Fig. 2f).[30,31] The EPR spectrum of $MoFe_{0.25}O_xCo(OH)_{2-x}$ showed opposite peaks at $g = 2.002$ in Fig. S7,† indicating its unpaired electrons due to the oxygen vacancies. The intensity of opposite peaks at $g = 2.002$ of $MoFeO_xCo(OH)_{2-x}$ is much lower than $MoFe_{0.25}O_xCo(OH)_{2-x}$ and $MoFe_{0.5}O_xCo(OH)_{2-x}$, implying fewer oxygen vacancies than the other two samples. Fig. 2g–l display the HAADF-STEM image and the corresponding elemental mapping of $MoFe_{0.5}O_xCo(OH)_{2-x}$, showing the distribution of elements (Co, Mo, Fe, and O) in the sample. The uneven distribution of the Fe element in $MoFe_{0.5}O_xCo(OH)_{2-x}$ nanotubes reflected in Fig. 2k may also demonstrate that oxygen vacancies are generated by the unsaturated coordination between Fe and O atoms since Fe atoms cannot be doped into $MoFe_{0.5}O_xCo(OH)_{2-x}$ evenly by coordination, which will be discussed later based on Fig. 3.

X-ray photoelectron spectroscopy (XPS) was utilized to characterize the electronic state of metal ions in $MoFe_{0.5}O_xCo(OH)_{2-x}$, displayed in Fig. 3a–d. The Fe 2p spectra (Fig. 3a) showed intensity peaks at 718.2/712.6 eV and 717.8/708.6 eV, suggesting the dual existence of Fe^{3+} and Fe^{2+} in the compound.[32] In Co 2p XPS spectra, Co 2p 3/2 and Co 2p 1/2 are located at 781.3/797.4 eV and 785.7/799.6 eV, respectively, revealing the coexistence of Co^{2+} and Co^{3+} (Fig. 3b).[33] Moreover, for the Mo 3d orbital of $MoFe_{0.5}O_xCo(OH)_{2-x}$ (Fig. 3c), two groups of dual peaks corresponding to Mo $3d_{3/2}$ and Mo $3d_{5/2}$ are situated at 235.3 and 232.1 eV, respectively, in line with the +6 oxidation state for Mo. According to Fig. 3d, three peaks in the O 1s orbital energy level spectrum of $MoFe_{0.5}O_xCo(OH)_{2-x}$ can be ascribed to the coexistence of lattice oxygen species (O_{latt}, 529.8 eV), surface adsorbed oxygen (O_{ads}, 531.9 eV), and oxygen vacancies (531.1 eV).[34,35] The comparison of the O 1s peaks showed the lack of oxygen vacancies in $MoO_xCo(OH)_{2-x}$ and $Co(OH)_2$ (Fig. S8†). Meanwhile, after the introduction of Fe atoms into $MoFe_{0.5}O_xCo(OH)_{2-x}$, the content of oxygen defects was obviously higher than $MoO_xCo(OH)_{2-x}$ and $Co(OH)_2$. This result further demonstrated that the introduction of Fe induced by cation-exchange can favor the formation of surface oxygen defect sites. This speculation is further supported by the Fe and Co K-edge XANES spectra shown in Fig. 3e and g. In the Fe K-edge XANES spectra (Fig. 3e), a reduction in the electronic state of Fe ions in $MoFe_{0.5}O_xCo(OH)_{2-x}$ is observed. The comparative analysis of XPS and XANES spectra indicated that the doping of Fe into the $Co(OH)_2$ lattice *via* a cation-exchange reaction resulted in enhanced electron transfer from Co/Mo to Fe compared to that prepared *via* the one-step chemical coprecipitation method. The doping effect of Fe could tune the electronic density

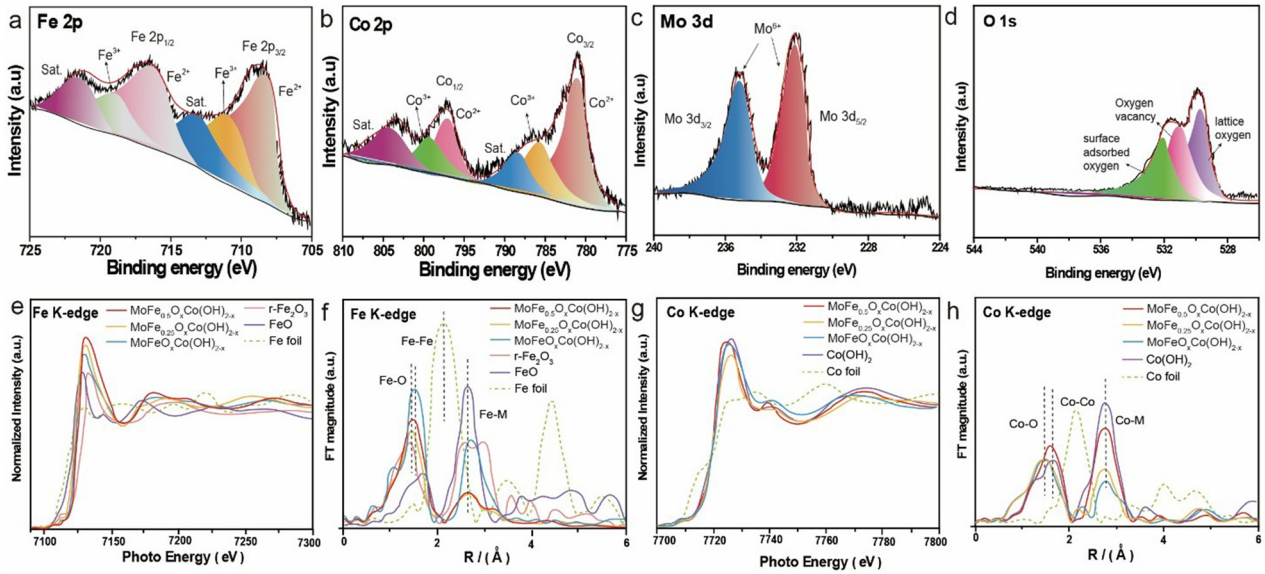

Fig. 3 (a–d) XPS spectra of $MoFe_{0.5}O_xCo(OH)_{2-x}$: (a) Fe 2p, (b) Co 2p, (c) Mo 3d, and (d) O 1s. (e) The Fe K-edge XANES spectra of $MoFe_{0.25}O_xCo(OH)_{2-x}$, $MoFe_{0.5}O_xCo(OH)_{2-x}$, $MoFeO_xCo(OH)_{2-x}$, and the standard reference Fe foil, r-Fe_2O_3 and FeO powder. (f) Fourier-transform EXAFS spectra at the Fe K-edge. (g) The Co K-edge XANES spectra of $MoFe_{0.25}O_xCo(OH)_{2-x}$, $MoFe_{0.5}O_xCo(OH)_{2-x}$, $MoFeO_xCo(OH)_{2-x}$, $Co(OH)_2$, and the standard reference of Co foil. (h) Fourier-transform EXAFS spectra at the Co K-edge.

around the metal ions (Co, Mo, and Fe) and optimize the binding energies of intermediates during the electrocatalytic OER process using $MoFe_{0.5}O_xCo(OH)_{2-x}$. Previous studies have proved that after doping Fe into the material the synergistic interactions between the triple transition metals of oxyhydroxide generate the favorable coordination environment and electronic structure that could optimize the adsorption energy of OER intermediates, thus reducing the required overpotential.[36–38] The Co K-edge XANES spectra (Fig. 3g) show that the Co absorption-edge and the red-line of $MoFe_{0.5}O_xCo(OH)_{2-x}$ gradually shift to the lower-energy side in contrast to $Co(OH)_2$, $MoO_xCo(OH)_{2-x}$, $MoFe_{0.25}O_xCo(OH)_{2-x}$, and $MoFeO_xCo(OH)_{2-x}$, suggesting partial electron transfer from Co to the substitutional Fe or Mo. This result further demonstrated that a certain amount of Fe dopant introduced a change in the electronic structure of $MoFe_{0.5}O_xCo(OH)_{2-x}$. In the Fourier transform Fe K-edge EXAFS of $MoFe_{0.5}O_xCo(OH)_{2-x}$ (Fig. 3f), both the Fe–O and Fe–M (M = Co, Mo, Fe) bonds in $MoFe_{0.25}O_xCo(OH)_{2-x}$ shift to low-R with a relatively weak peak intensity owing to the lattice distortion.[39] In terms of Co (Fig. 3h), the Co–O distance in the first shell is 1.52 Å, shorter than the 1.58 Å of $Co(OH)_2$ and the 1.57 Å of $MoFe_{0.25}O_xCo(OH)_{2-x}$ and $MoFeO_xCo(OH)_{2-x}$, which indicated the generation of lattice distortion and coordination deficiency in the $MoFe_{0.5}O_xCo(OH)_{2-x}$ sample, further verifying the change in the electronic structure in the format of bonding, explaining the mechanism of generating O_v induced by the doping effect of Fe using 5 mg of $FeCl_3$.[40] Furthermore, the lower intensity of the Co–M (M: Fe, Mo) featured in $MoFe_{0.5}O_xCo(OH)_{2-x}$ also suggested the generation of structural distortion including disordered atoms and dangling bonds,[41] which could reduce the surface energy of $MoFe_{0.5}O_xCo(OH)_{2-x}$ and enable the catalyst with excellent structural durability. The above results demonstrated that the cation-exchange process facilitates the formation of the defective lattice and coordinatively unsaturated metal centers, functioning as the active sites in the OER.

Conversions based on the oxidation and reduction of triple metal ions will improve the electrocatalytic capacity of $MoFe_{0.5}O_xCo(OH)_{2-x}$ compared to $Co(OH)_2$, $MoO_xCo(OH)_{2-x}$, $MoFe_{0.25}O_xCo(OH)_{2-x}$, $MoFeO_xCo(OH)_{2-x}$, and RuO_2. The electrocatalytic OER activity was investigated *via* linear sweep voltammetry (LSV). The electrocatalytic activity of $MoFe_{0.5}O_xCo(OH)_{2-x}$ towards the OER was investigated under an alkaline electrolyte (1 M KOH) by a three-electrode system (electrochemical measurements, ESI†). Polarization curves were measured by linear sweep voltammetry (LSV) with a scan rate of 5 mV s^{-1} under *iR*-correction. In addition, all potentials were converted to those at a reversible hydrogen electrode (RHE) scale (Fig. 4a and c). At a lower overpotential of 223 mV, the current density of $MoFe_{0.5}O_xCo(OH)_{2-x}$ reached 10 mA cm^{-2} and then increased to 50 mA cm^{-2} rapidly with a lowest overpotential of 287 mV, which is comparable to the best OER catalyst reported before.[42] In contrast to the previously reported OER catalysts, it is found that the catalyst, with the introduction of Fe and Mo dopants, exhibits better OER catalytic performance.[43–48] The capacity of $MoFe_{0.5}O_xCo(OH)_{2-x}$ regarding overpotentials is comparable to recently reported Earth-abundant OER catalysts with excellent performance (Table S2, ESI†). The catalytic kinetics of the presented catalysts were further evaluated by the Tafel slopes (Fig. 4b). As expected, $MoFe_{0.5}O_xCo(OH)_{2-x}$ possesses a distinctly smaller

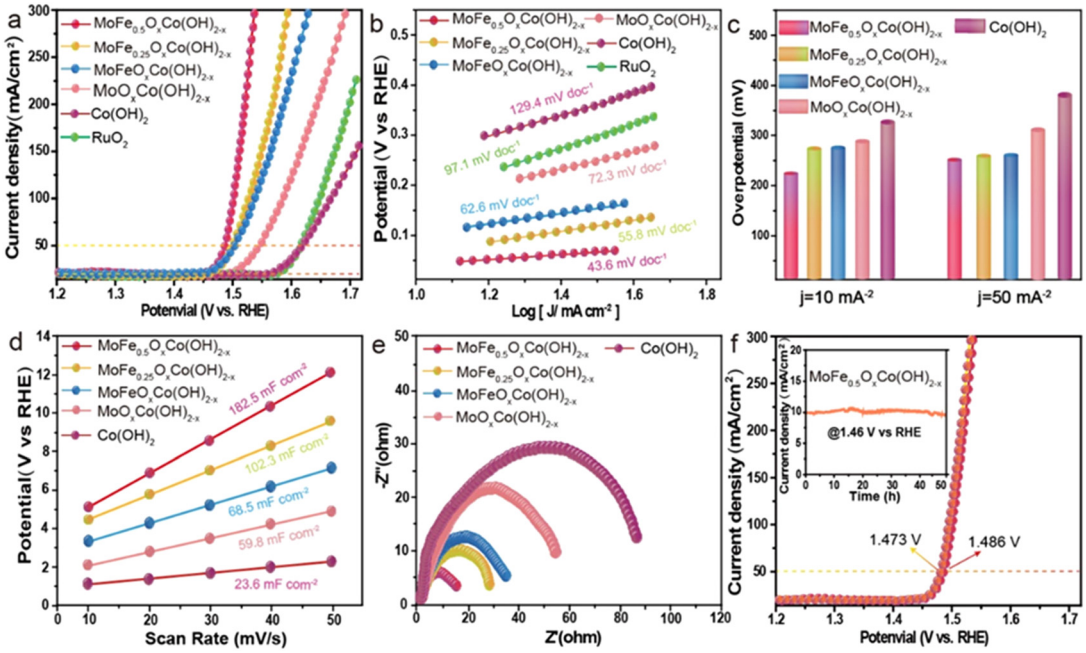

Fig. 4 OER performances of as-synthesised catalysts. (a) LSV curves of different electrocatalysts in 1.0 M KOH solution. (b) Corresponding OER Tafel plots. (c) Overpotential histogram of LSV. (d) ECSA estimated by C_{dl} values and (e) Nyquist plots. (f) LSV polarization curves of the $MoFe_{0.5}O_xCo(OH)_{2-x}$ catalyst after 1000 cycles with current density *vs.* time (*i*–*t*) curves for the OER for over 50 h shown in the inset.

Tafel slope of 43.6 mV dec^{-1} than $Co(OH)_2$, $MoO_xCo(OH)_{2-x}$, $MoFe_{0.25}O_xCo(OH)_{2-x}$, $MoFeO_xCo(OH)_{2-x}$, and RuO_2, suggesting its excellent OER kinetics. The ratio of the electrochemically active surface area (ECSA) to the two-layer capacitance (C_{dl}) can reveal the electrocatalytic activity of catalysts.[49] To measure the electrochemical property, the ECSA of $MoFe_{0.5}O_xCo(OH)_{2-x}$ was further analyzed by cyclic voltammetry (CV) in 1.0 M KOH solution (Fig. S9, ESI†). It is revealed in Fig. 4d that $MoFe_{0.5}O_xCo(OH)_{2-x}$ exhibited the top C_{dl} value (182.5 mF cm^{-2}) among all samples. This result indicates that $MoFe_{0.5}O_xCo(OH)_{2-x}$ has more active sites corresponding to the LSV results. In addition, the reaction kinetics of the as-synthesized samples were investigated by electrochemical impedance spectroscopy (EIS), shown in Fig. 4e. According to EIS, in contrast to other samples, the R_{ct} value of $MoFe_{0.5}O_xCo(OH)_{2-x}$ decreased in the high frequency region, which indicated a change in the electronic structure of $MoFe_{0.5}O_xCo(OH)_{2-x}$ with the introduction of Fe, facilitating the charge transfer between the active site and the proton in the electrolyte.[50] The LSV curves (Fig. 4f) remained virtually unchanged after 1000 cycles, with an error of less than 1%, confirming the excellent durability of $MoFe_{0.5}O_xCo(OH)_{2-x}$. The OER stability of $MoFe_{0.5}O_xCo(OH)_{2-x}$ was investigated by chronopotentiometry at 1.46 V *vs.* RHE in 1 M KOH solution. $MoFe_{0.5}O_xCo(OH)_{2-x}$ exhibited long-term stability as the current density remained stable for 50 hours (the inset part in Fig. 4f). $Co(OH)_2$ and $MoO_xCo(OH)_{2-x}$ exhibited inferior stability and a higher overpotential at a current density of 10 mA cm^{-2} (Fig. S10, ESI†), further proving that the stability and OER catalytic performance have been optimized by $MoFe_{0.5}O_xCo(OH)_{2-x}$. The SEM and TEM image of $MoFe_{0.5}O_xCo(OH)_{2-x}$ after the stability test (Fig. S11†) revealed that the morphology of the sample was maintained after a 50 h electrochemical operation. Furthermore, the characteristic crystalline peaks of $MoFe_{0.5}O_xCo(OH)_{2-x}$ in the XRD pattern (Fig. S12†) were maintained after the stability test, only with a decrease in the intensity of the peaks. The above results synergistically proved that $MoFe_{0.5}O_xCo(OH)_{2-x}$ maintained its crystalline property and morphology after the 50 h operation in alkaline media.

Conclusions

In summary, a series of Fe/Mo doped Co–Mo–Fe trimetallic electrocatalysts with different dopant contents were prepared by a simple cation-exchange method. The heterophased $MoFe_{0.5}O_xCo(OH)_{2-x}$ exhibited excellent catalytic performance towards OER catalytic activity and stability compared to $Co(OH)_2$, $MoO_xCo(OH)_{2-x}$, $MoFe_{0.25}O_xCo(OH)_{2-x}$, $MoFeO_xCo(OH)_{2-x}$, and RuO_2. The doping of Fe^{3+} possesses a higher regulation degree on the electronic structure of $MoFe_{0.5}O_xCo(OH)_{2-x}$, which not only results in the formation of abundant surface O_v to favor the exposure of active sites, but also tunes the adsorption of OH^- by adjacent metal cations,[29] contributing to the reduced charge transfer resistance and the improved kinetics of the OER process. Moreover, the $MoFe_{0.5}O_xCo(OH)_{2-x}$ catalyst showed a low overpotential of only 223 mV at a current density of 10 mA cm^{-2} with a small Tafel slope of 43.6 mV dec^{-1}. Therefore, the present work provides a feasible strategy for the design and fabrication of highly efficient

Earth-abundant trimetallic electrocatalysts and further illustrates the relationship between iron/molybdenum dopants and the optimized catalytic properties of molybdenum–iron–cobalt oxyhydroxide catalysts.

Conflicts of interest

The authors declare no conflict of interest.

Acknowledgements

We would like to thank the Analytical & Testing Center of Sichuan University for SEM and TEM work. We are grateful to Dr Yong Liu for her help with SEM analysis and Dr Shanling Wang for her assistance with TEM analysis.

References

1 M. G. Walter, E. L. Warren, J. R. McKone, S. W. Boettcher, Q. X. Mi, E. A. Santori and N. S. Lewis, *Chem. Rev.*, 2010, **110**, 6446–6473.
2 Y. Jiao, Y. Zheng, M. T. Jaroniec and S. Z. Qiao, *Chem. Soc. Rev.*, 2015, **44**, 2060–2086.
3 L. Xu, Q. Q. Jiang, Z. H. Xiao, X. Y. Li, J. Huo, S. Y. Wang and L. M. Dai, *Angew. Chem., Int. Ed.*, 2016, **55**, 5277–5281.
4 W. T. Hong, M. Risch, K. A. Stoerzinger, A. Grimaud, J. Suntivich and Y. Shao-Horn, *Energy Environ. Sci.*, 2015, **8**, 1404–1427.
5 F. M. Wang, T. A. Shifa, X. Y. Zhan, Y. Huang, K. L. Liu, Z. Z. Cheng, C. Jiang and J. He, *Nanoscale*, 2015, **7**, 19764–19788.
6 H. Y. Guo, Z. W. Fang, H. Li, D. Fernandez, G. Henkelman, S. M. Humphrey and G. H. Yu, *ACS Nano*, 2019, **13**, 13225–13234.
7 Y. L. Xing, J. G. Ku, W. Fu, L. Z. Wang and H. H. Chen, *Chem. Eng. J.*, 2020, **395**.
8 P. W. Du and R. Eisenberg, *Energy Environ. Sci.*, 2012, **5**, 6012–6021.
9 D. J. Chen, C. Chen, Z. M. Baiyee, Z. P. Shao and F. Ciucci, *Chem. Rev.*, 2015, **115**, 9869–9921.
10 M. W. Kanan and D. G. Nocera, *Science*, 2008, **321**, 1072–1075.
11 H. Dau, C. Limberg, T. Reier, M. Risch, S. Roggan and P. Strasser, *ChemCatChem*, 2010, **2**, 724–761.
12 J. H. Wang, W. Cui, Q. Liu, Z. C. Xing, A. M. Asiri and X. P. Sun, *Adv. Mater.*, 2016, **28**, 215–230.
13 O. Diaz-Morales, I. Ledezma-Yanez, M. T. M. Koper and F. Calle-Vallejo, *ACS Catal.*, 2015, **5**, 5380–5387.
14 L. Han, S. J. Dong and E. K. Wang, *Adv. Mater.*, 2016, **28**, 9266–9291.
15 X. D. Jia, Y. F. Zhao, G. B. Chen, L. Shang, R. Shi, X. F. Kang, G. I. N. Waterhouse, L. Z. Wu, C. H. Tung and T. R. Zhang, *Adv. Energy Mater.*, 2016, **6**(10), 1502585.
16 L. L. Wen, X. L. Zhang, J. Y. Liu, X. Y. Li, C. C. Xing, X. J. Lyu, W. P. Cai, W. C. Wang and Y. Li, *Small*, 2019, **15**(35), 1902373.
17 B. Zhang, X. L. Zheng, O. Voznyy, R. Comin, M. Bajdich, M. Garcia-Melchor, L. L. Han, J. X. Xu, M. Liu, L. R. Zheng, F. P. G. de Arquer, C. T. Dinh, F. J. Fan, M. J. Yuan, E. Yassitepe, N. Chen, T. Regier, P. F. Liu, Y. H. Li, P. De Luna, A. Janmohamed, H. L. L. Xin, H. G. Yang, A. Vojvodic and E. H. Sargent, *Science*, 2016, **352**, 333–337.
18 Y. P. Liu, Q. J. Li, R. Si, G. D. Li, W. Li, D. P. Liu, D. J. Wang, L. Sun, Y. Zhang and X. X. Zou, *Adv. Mater.*, 2017, **29**(13), 1606200.
19 J. H. Huang, J. T. Chen, T. Yao, J. F. He, S. Jiang, Z. H. Sun, Q. H. Liu, W. R. Cheng, F. C. Hu, Y. Jiang, Z. Y. Pan and S. Q. Wei, *Angew. Chem., Int. Ed.*, 2015, **54**, 8722–8727.
20 S. L. Zhao, Y. Wang, J. C. Dong, C. T. He, H. J. Yin, P. F. An, K. Zhao, X. F. Zhang, C. Gao, L. J. Zhang, J. W. Lv, J. X. Wang, J. Q. Zhang, A. M. Khattak, N. A. Khan, Z. X. Wei, J. Zhang, S. Q. Liu, H. J. Zhao and Z. Y. Tang, *Nat. Energy*, 2016, **1**, 1–10.
21 K. Fan, H. Chen, Y. F. Ji, H. Huang, P. M. Claesson, Q. Daniel, B. Philippe, H. Rensmo, F. S. Li, Y. Luo and L. C. Sun, *Nat. Commun.*, 2016, **7**, 1–9.
22 H. J. Yin and Z. Y. Tang, *Chem. Soc. Rev.*, 2016, **45**, 4873–4891.
23 H. J. Yin, S. L. Zhao, K. Zhao, A. Muqsit, H. J. Tang, L. Chang, H. J. Zhao, Y. Gao and Z. Y. Tang, *Nat. Commun.*, 2015, **6**, 6430.
24 Y. M. Zhu, X. Liu, S. G. Jin, H. J. Chen, W. Lee, M. L. Liu and Y. Chen, *J. Mater. Chem. A*, 2019, **7**, 5875–5897.
25 K. Y. Zhu, F. Shi, X. F. Zhu and W. S. Yang, *Nano Energy*, 2020, **73**, 104761.
26 L. J. Zeng, B. B. Cao, X. Wang, H. D. Liu, J. R. Shang, J. P. Lang, X. Q. Cao and H. W. Gu, *Nanoscale*, 2021, **13**, 3153–3160.
27 M. Fang, Q. A. Cai, Q. Qin, W. T. Hong and W. Liu, *Chem. Eng. J.*, 2021, **421**(2), 127796.
28 S. C. Wang, G. Liu and L. Z. Wang, *Chem. Rev.*, 2019, **119**, 5192–5247.
29 Y. H. Dou, C. T. He, L. Zhang, H. J. Yin, M. Al-Mamun, J. M. Ma and H. J. Zhao, *Nat. Commun.*, 2020, **11**(1), 1664.
30 C. Peng, G. Luo, J. B. Zhang, M. H. Chen, Z. Q. Wang, T. K. Sham, L. J. Zhang, Y. F. Li and G. F. Zheng, *Nat. Commun.*, 2021, **12**(1), 1580.
31 X. Wang, Y. W. Zhang, H. N. Si, Q. H. Zhang, J. Wu, L. Gao, X. F. Wei, Y. Sun, Q. L. Liao, Z. Zhang, K. Ammarah, L. Gu, Z. Kang and Y. Zhang, *J. Am. Chem. Soc.*, 2020, **142**, 4298–4308.
32 J. Liu, J. S. Wang, B. Zhang, Y. J. Ruan, L. Lv, X. Ji, K. Xu, L. Miao and J. J. Jiang, *ACS Appl. Mater. Interfaces*, 2017, **9**, 15364–15372.
33 X. Y. Gao, Y. F. Zhao, K. Q. Dai, J. T. Wang, B. Zhang and X. J. Shen, *Chem. Eng. J.*, 2020, **384**, 123373.
34 S. Deng, X. Xiao, X. Xing, J. Wu, W. Wen and Y. Wang, *J. Mol. Catal. A: Chem.*, 2015, **398**, 79.

35 Z. Wang, W. Z. Wang, L. Zhang and D. Jiang, *Catal. Sci. Technol.*, 2016, **9**, 3845.
36 M. Fang, D. Han, W. B. Xu, Y. Shen, Y. M. Lu, P. J. Cao, S. Han, W. Y. Xu, D. L. Zhu, W. J. Liu and J. C. Ho, *Adv. Energy Mater.*, 2020, **10**(27), 2001059.
37 B. Zhang, X. L. Zheng, O. Voznyy, R. Comin, M. Bajdich, M. Garcia-Melchor, L. L. Han, J. X. Xu, M. Liu, L. R. Zheng, F. P. G. de Arquer, C. T. Dinh, F. J. Fan, M. J. Yuan, E. Yassitepe, N. Chen, T. Regier, P. F. Liu, Y. H. Li, P. De Luna, A. Janmohamed, H. L. L. Xin, H. G. Yang, A. Vojvodic and E. H. Sargent, *Science*, 2016, **352**, 333–337.
38 J. Jiang, F. F. Sun, S. Zhou, W. Hu, H. Zhang, J. C. Dong, Z. Jiang, J. J. Zhao, J. F. Li, W. S. Yan and M. Wang, *Nat. Commun.*, 2018, **9**, 2885.
39 M. Z. Gu, X. Y. Deng, M. Lin, H. Wang, A. Gao, X. M. Huang and X. J. Zhang, *Adv. Energy Mater.*, 2021, **11**, 2102361.
40 S. Z. Song, J. Zhou, X. Z. Su, Y. Wang, J. Li, L. J. Zhang, G. P. Xiao, C. Z. Guan, R. D. Liu, S. G. Chen, H. J. Lin, S. Zhang and J. Q. Wang, *Energy Environ. Sci.*, 2018, **11**, 2945–2953.
41 Q. He, D. Tian, H. L. Jiang, D. F. Cao, S. Q. Wei, D. B. Liu, P. Song, Y. Lin and L. Song, *Adv. Mater.*, 2020, **32**(11), 1906972.
42 A. Bergmann, T. E. Jones, E. M. Moreno, D. Teschner, P. Chernev, M. Gliech, T. Reier, H. Dau and P. Strasser, *Nat. Catal.*, 2018, **1**, 711–719.
43 S. F. Hung, Y. Y. Hsu, C. J. Chang, C. S. Hsu, N. T. Suen, T. S. Chan and H. M. Chen, *Adv. Energy Mater.*, 2018, **8**, 1701686.
44 M. Zhang, Y. Liu, B. Liu, Z. Chen, H. Xu and Y. Yan, *ACS Catal.*, 2020, **10**, 5179–5189.
45 P. Zhou, P. Niu, J. Liu, N. Zhang, H. Bai, M. J. Feng, D. Liu, L. Wang, S. Chen, C. T. Kwok, Y. Tang, R. Li, S. Wang and H. Pan, *Adv. Funct. Mater.*, 2022, 2202068.
46 J. Liu, Y. Ji, J. Nai, X. Niu, Y. Luo, L. Guo and S. Yang, *Energy Environ. Sci.*, 2018, **11**, 1736–1741.
47 B. Liu, M. Zhang, Y. Wang, Z. Chen and K. Yan, *J. Alloys Compd.*, 2021, **852**, 156949.
48 Q. Guo, J. Mao, J. Huang, Z. Wang, Y. Zhang, J. Hu, J. Dong, S. Sathasivam, Y. Zhao, G. Xing, H. Pan, Y. Lai and Y. Tang, *Small*, 2020, **16**, 1907029.
49 X. Cao, E. Johnson and M. Nath, *ACS Sustainable Chem. Eng.*, 2019, **7**, 9588–9600.
50 M. Kuang, J. M. Zhang, D. B. Liu, H. T. Tan, K. N. Dinh, L. Yang, H. Ren, W. J. Huang, W. Fang, J. D. Yao, X. D. Hao, J. W. Xu, C. T. Liu, L. Song, B. Liu and Q. Y. Yan, *Adv. Energy Mater.*, 2020, **10**, 2002215.

Supporting Information

Molybdenum-Iron-Cobalt Oxyhydroxide with Rich Oxygen Vacancies for Oxygen Evolution Reaction

Yechuan Zhang,[ab, ‡] *Zhengxiang Gu,*[a, ‡] *Jingxiu Bi,*[b] *Yan Jiao*[b,]*

Y. Zhang, Dr. Z. Gu,

Huaxi MR Research Center (HMRRC), Department of Radiology, State Key Laboratory of Biotherapy, West China Hospital, Sichuan University, Chengdu 610041, China.

E-mail: zxgu16@scu.edu.cn

Y. Zhang, A/Prof. Jingxiu Bi, A/Prof. Y. Jiao,

School of Chemical Engineering and Advanced Materials, University of Adelaide, SA 5005, Australia.

*E-mail: yan.jiao@adelaide.edu.au

[‡]Y. Z. and Z.G. contributed equally to this work.

*Corresponding author.

Experimental Section

All materials were of analytical grade and used without further purification.

Synthesis of $MoO_xCo(OH)_{2-x}$

In a typical synthesis, 2 mmol of $Na_2MoO_4 \cdot 2H_2O$ and 4 mmol of glucose were dissolved into 50 mL of DI water. The mixture was treated with an intense ultrasonication for a few minutes and then transferred to a 1000 mL Teflon stainless steel autoclave. Afterwards, $Co(OH)_2$ nanowires supported was immersed in the reaction solution. The autoclave was sealed and maintained at 150 ℃ for 6 h and then cooled to room temperature.

Structure Characterizations

A field emission scanning electron microscopy (FESEM; ZEISS-Merlin), a transmission electron microscopy (TEM, JEOL-2010) with energy dispersive X-ray spectroscopy (EDX), and a high-resolution TEM (HRTEM, JEOL-2010) were used to characterize the morphology and composition of samples. (XRD) curves of samples were recorded on Rigaku at 40 kV and 40 mA, and X-ray photoelectron spectroscopy (XPS) curves are obtained on a PHI Quantera SXM (ULVAC-PHI) instrument to determine the compositions and the valence states of the elements in the samples.

Electrochemical measurements.

All electrochemical measurements were performed on a CHI 760E electrochemical work station with a typical three-electrode setting at room temperature. A graphite rod and a Hg/HgO electrode were selected as a counter and reference electrode, respectively. The self-supporting array grown on carbon cloth (1×1 cm, mass loading ~ 2.5 mg/cm^{-2}) was directly used as a working electrode. The electrochemical data were collected in an electrolyte of 1.0 M KOH. The measured potentials via the Hg/HgO electrode were converted to those based on a reversible hydrogen electrode (RHE) by the Nernst equation: E(RHE) = E(Hg/HgO) + 0.0591*pH + 0.098. The overpotential (η) was calculated according to the following equation: η = E(RHE)-1.23 V. Linear sweep voltammetry curves for OER were established at a scanning rate of 5 mV/s before 50 cycles of the cyclic voltammetry tests at a scan rate

of 50 mV/s were conducted to obtain stable curves. The Tafel slopes were obtained from the polarization curves by the equation, η = a + b log (i). The chronoamperometry was operated to evaluate the stability under different current densities. Electrochemical impedance spectroscopy (EIS) measurements were performed over a frequency range of 0.1-10^6 Hz by applying an AC amplitude of 50 mV. All data presented were within 90% iR-correction.

Figures

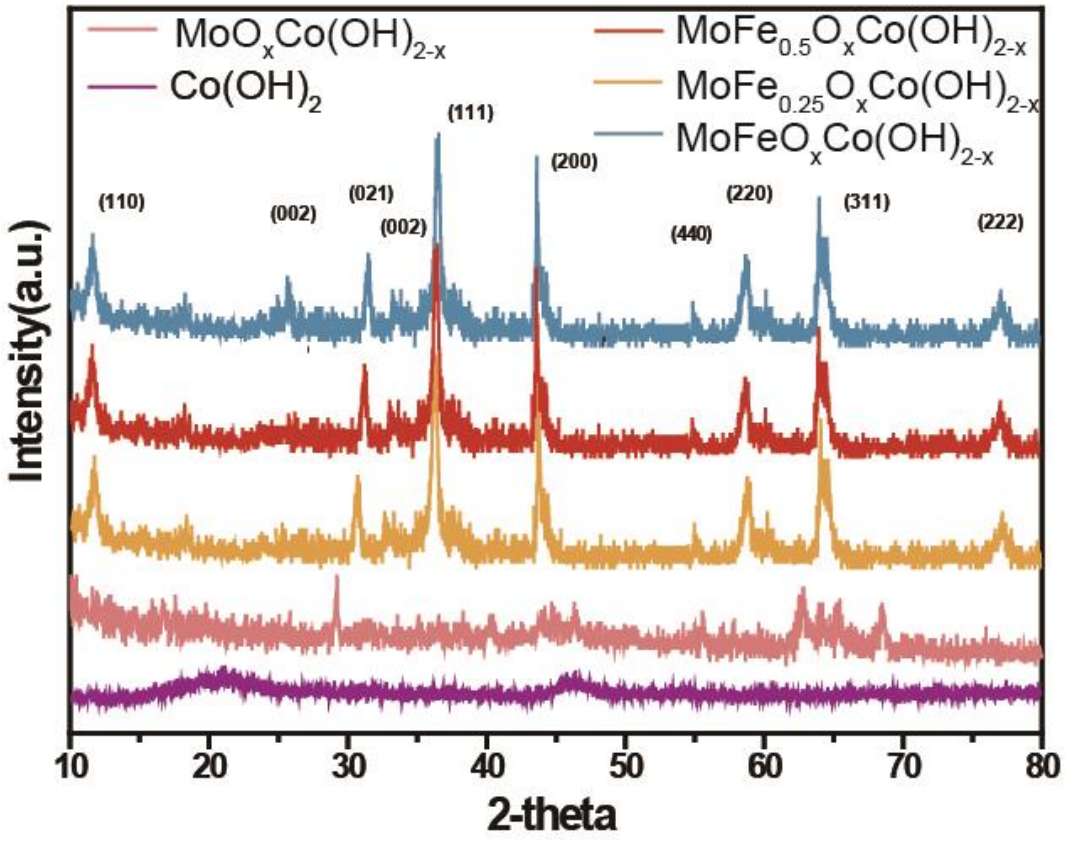

Figure S1. (a) XRD patterns of different electrocatalysts.

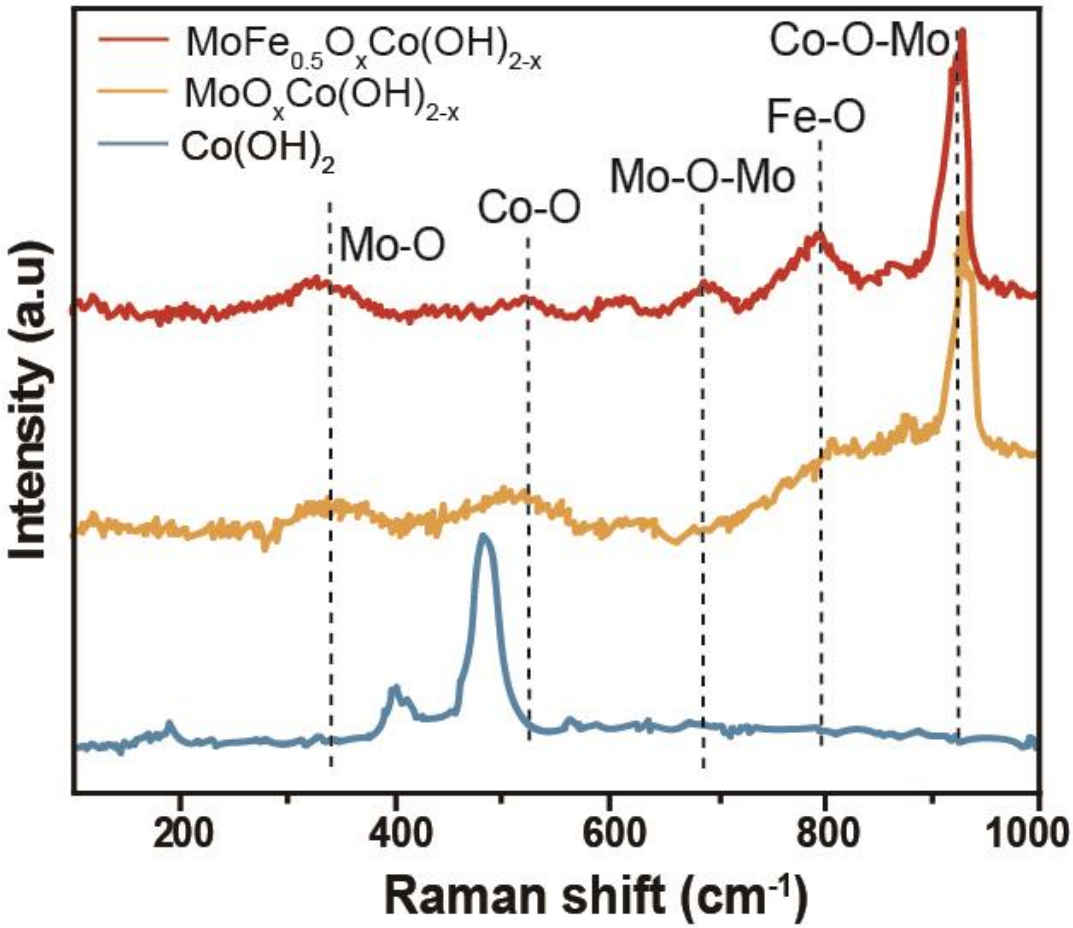

Figure S2. (a) Raman spectra of $MoO_xCo(OH)_{2-x,}$ $MoFe_{0.5}O_xCo(OH)_{2-x}$, and $Co(OH)_2$ electrocatalysts.

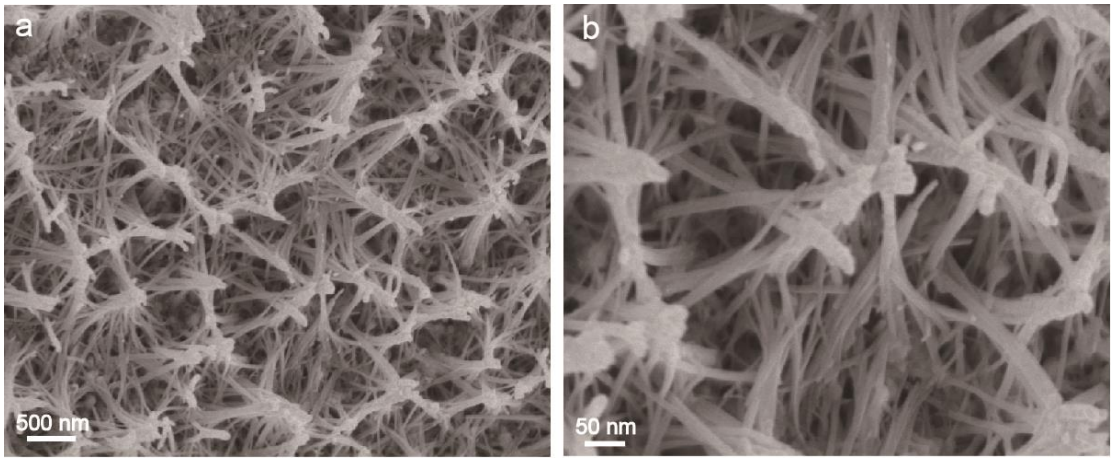

Figure S3. (a, b) SEM images of $Co(OH)_2$.

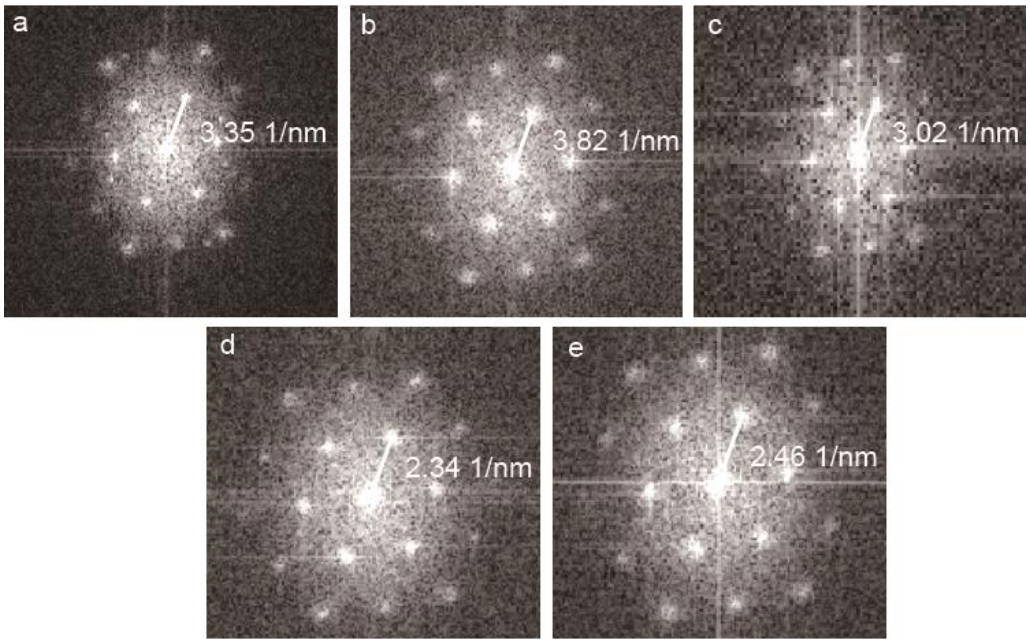

Figure S4. Images of Fourier transform corresponding to Fig 2a and 2c that reveal the lattice spacing of $MoFe_{0.5}O_xCo(OH)_{2-x}$.

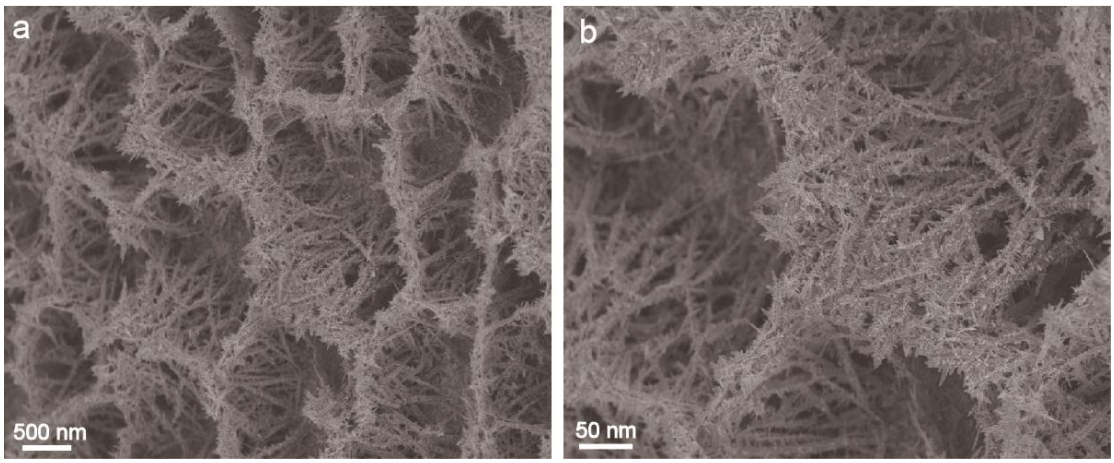

Figure S5. (a, b) SEM images of $MoFe_{0.5}O_xCo(OH)_{2-x}$.

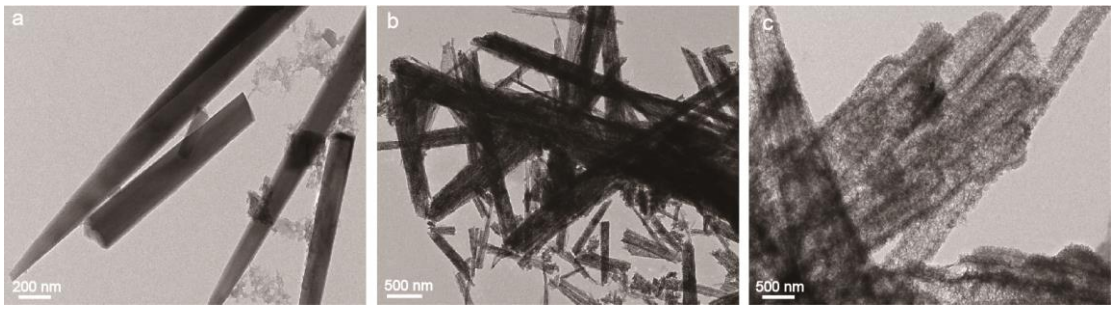

Figure S6. TEM images of (a)$Co(OH)_2$, (b) $MoFeO_xCo(OH)_{2-x}$, (c) $MoFe_{0.5}O_xCo(OH)_{2-x}$.

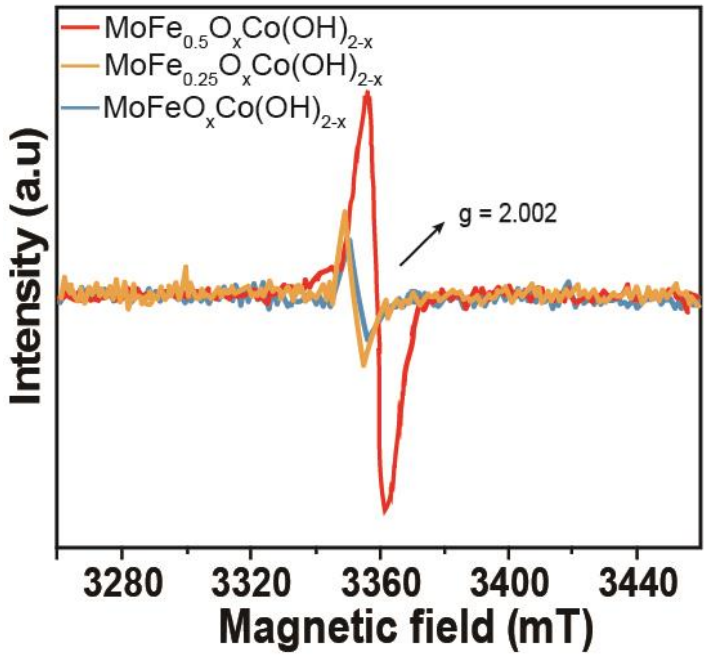

Figure S7. EPR spectra of $MoFeO_xCo(OH)_{2-x}$, $MoFe_{0.25}O_xCo(OH)_{2-x}$, and $MoFe_{0.5}O_xCo(OH)_{2-x}$.

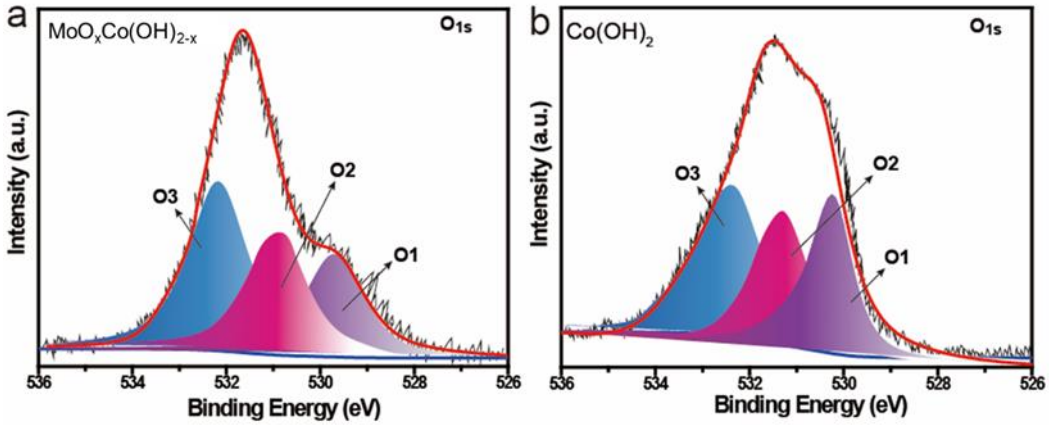

Figure S8. O1s XPS of comparative (a) $MoO_xCo(OH)_{2-x}$ and (b) $Co(OH)_2$.

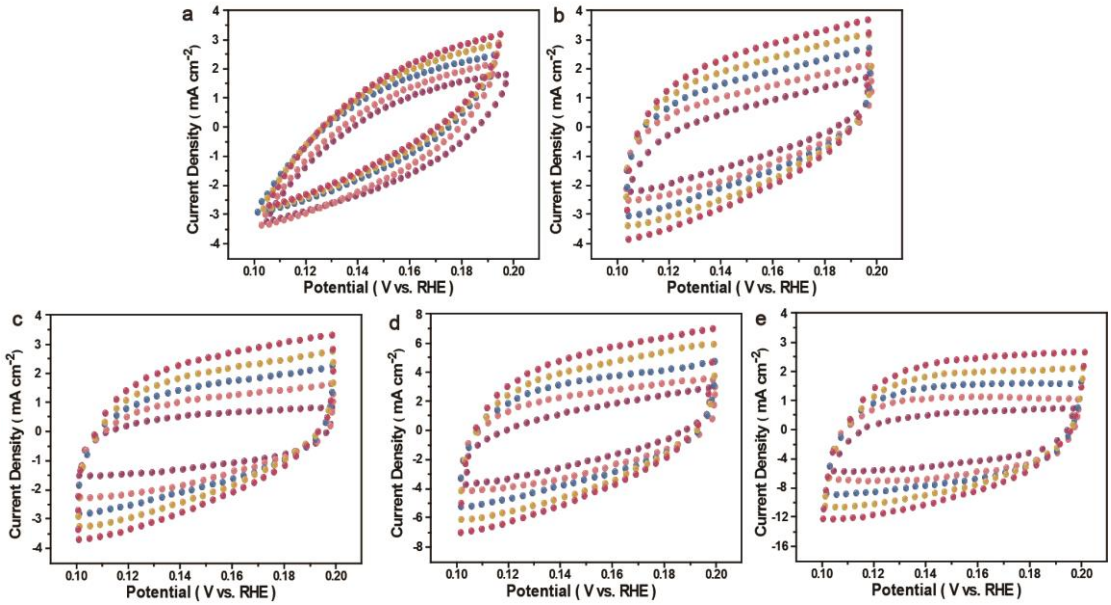

Figure S9. (a) CV curves of (a) $Co(OH)_2$, (b) $MoO_xCo(OH)_{2-x}$, (c) $MoFe_{0.25}O_xCo(OH)_{2-x}$, (d) $MoFe_{0.5}O_xCo(OH)_{2-x}$, (e) $MoFeO_xCo(OH)_{2-x}$ electrocatalysts at scan rates from 10 to 50 mV s^{-1}.

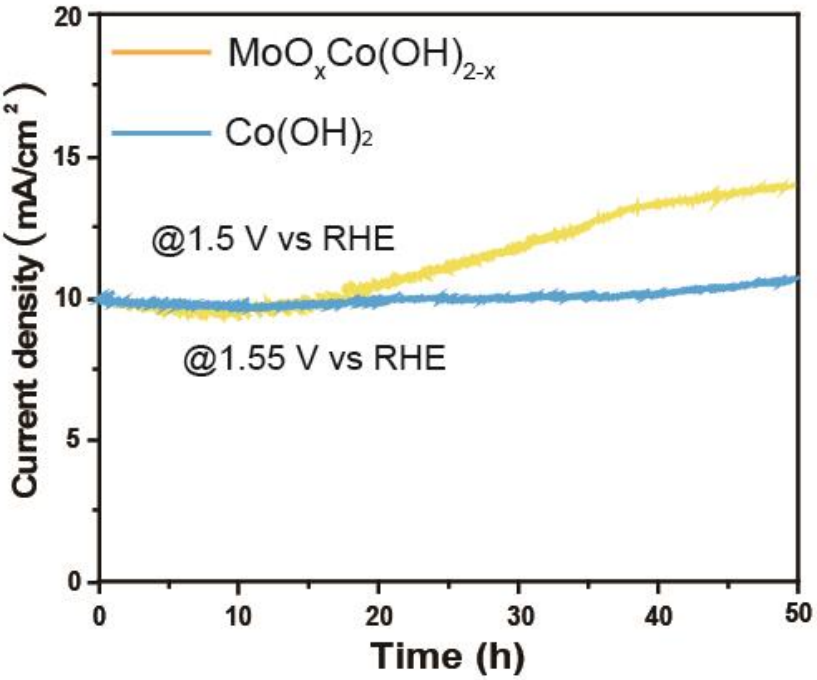

Figure S10. Long-term durability test of $Co(OH)_2$ and $MoO_xCo(OH)_{2-x}$ at different potentials for OER.

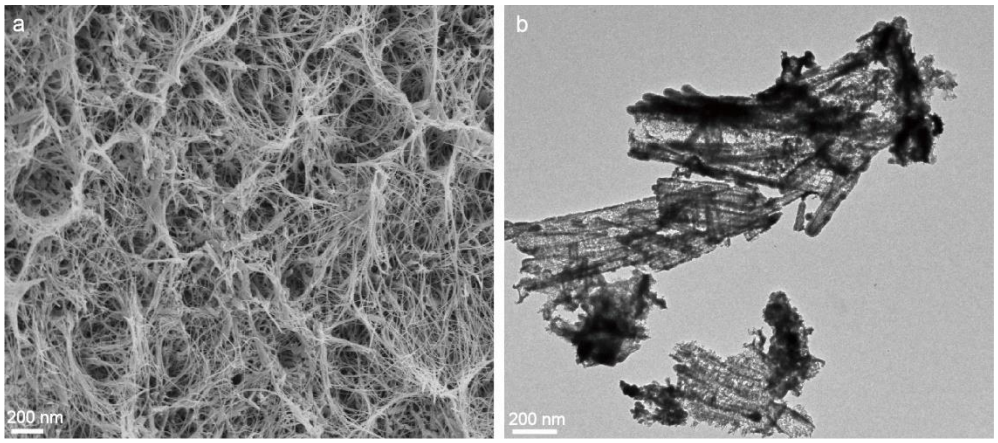

Figure S11. (a) SEM image and (b) TEM image of $MoFe_{0.5}O_xCo(OH)_{2-x}$ after the stability test.

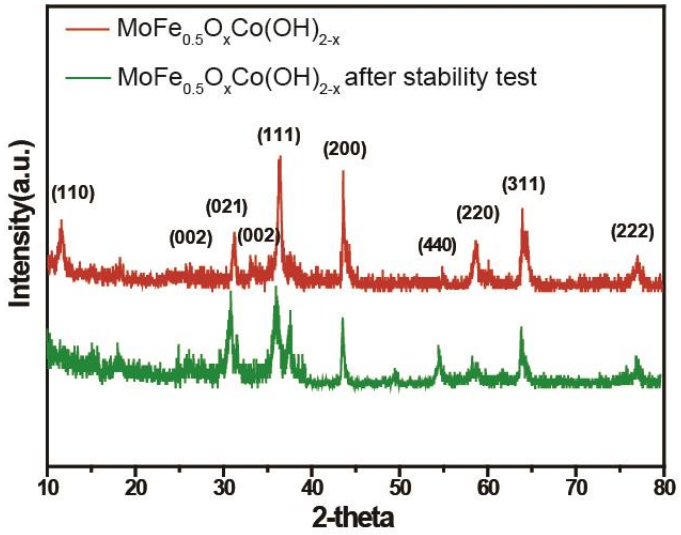

Figure S12. XRD pattern of $MoFe_{0.5}O_xCo(OH)_{2-x}$ before and after the stability test.

Table S1. The metallic composition of $MoO_xCo(OH)_{2-x}$, $MoFe_{0.5}O_xCo(OH)_{2-x}$, $MoFe_{0.25}O_xCo(OH)_{2-x}$, and $MoFeO_xCo(OH)_{2-x}$, catalyst by ICP-MS. Regardless of oxygen in this characterization.

Sample	Co (at.%)	Mo (at.%)	Fe (at.%)
$MoO_xCo(OH)_{2-x}$	90.13	9.87	-
$MoFe_{0.25}O_xCo(OH)_{2-x}$	88.46	9.01	2.53
$MoFe_{0.5}O_xCo(OH)_{2-x}$	86.97	7.51	5.52
$MoFeO_xCo(OH)_{2-x}$	83.61	6.21	10.18

Table S2. Comparison of the OER activities of the $MoFe_{0.5}O_xCo(OH)_{2-x}$ sample in this work with recently-reported catalysts.

catalysts	Overpotential (mV)	j /(mA cm^{-2})	Tafel slope (mV dec^{-1})	Reference
$MoFe_{0.5}O_xCo(OH)_{2-x}$	**223**	**10**	**43.6**	**This work**
CoFeV-LDH	242	10	57	S1
CoMoV-LDH	270	10	106	S2
CoMo hydr(oxy)oxide	377	10	41.88	S3
CoFe-LDH	320	10	53	S4
$Fe_xCo_{1-x}OOH$	266	10	30.0	S5
Ir-doped $NiV(OH)_2$	260	10	55.3	S6
$NiCo_{16-x}P_6$	290	10	66	S7
$CoP-CeO_2$	224	10	90.3	S8
$Pt-Cu@Cu_xO$	250	10	56	S9
NiCoMo	304	10	56.4	S10

References:

S1. Y. M. Hu, Z. L. Wang, W. J. Liu, L. Xu, M. L. Guan, Y. P. Huang, Y. Zhao, J. Bao and H. M. Li, *Acs Sustain Chem Eng*, 2019, **7**, 16828-16834.

S2. J. Bao, Z. L. Wang, J. F. Xie, L. Xu, F. C. Lei, M. L. Guan, Y. Zhao, Y. P. Huang and H. M. Li, *Chem Commun*, 2019, **55**, 3521-3524.

S3. S. Bera, W. J. Lee, E. K. Koh, C. M. Kim, S. Ghosh, Y. Yang and S. H. Kwon, *J Phys Chem C*, 2020, **124**, 16879-16887.

S4. Q. Zhou, Y. P. Chen, G. Q. Zhao, Y. Lin, Z. W. Yu, X. Xu, X. L. Wang, H. K. Liu, W. P. Sun and S. X. Dou, *Acs Catal*, 2018, **8**, 5382.

S5. S. H. Ye, Z. X. Shi, J. X. Feng, Y. X. Tong and G. R. Li, *Angew Chem Int Edit*, 2018, **57**, 2672-2676.

S6. S. Li, C. Xi, Y. Z. Jin, D. Y. Wu, J. Q. Wang, T. Liu, H. B. Wang, C. K. Dong, H. Liu, S. A. Kulinich and X. W. Du, *Acs Energy Lett*, 2019, **4**, 1823-1829.

S7. Y. F. Zhao, J. Q. Zhang, Y. H. Xie, B. Sun, J. J. Jiang, W. J. Jiang, S. B. Xi, H. Y. Yang, K. Yan, S. J. Wang, X. Guo, P. Li, Z. J. Han, X. Y. Lu, H. Liu and G. X. Wang, *Nano Lett*, 2021, **21**, 823-832.

S8. M. Li, X. C. Pan, M. Q. Jiang, Y. F. Zhang, Y. W. Tang and G. T. Fu, *Chem Eng J*, 2020, **395**.

S9. D. T. Tran, H. T. Le, T. L. L. Doan, N. H. Kim and J. H. Lee, *Nano Energy*, 2019, **59**, 216-228.

S10. S. Y. Hao, L. C. Chen, C. L. Yu, B. Yang, Z. J. Li, Y. Hou, L. C. Lei and X. W. Zhang, *Acs Energy Lett*, 2019, **4**, 952-959.

Chapter 6. Conclusion and Future Direction

6.1 Conclusion

The aim of this thesis is to design and synthesize multifunctional iron-based nanomaterials for various applications with optimized performance, and to develop facile synthetic methodology based on green chemistry concepts. According to the drawback of traditional drug delivery system, we first developed a green synthetic method for the fabrication of hollow structural MIL-100 (Fe) with significant high drug loading capacity. The oxidation of Fe^{2+} to Fe^{3+} promotes the successful synthesis of hollow MIL-100 (Fe) under room temperature and ambient pressure. Particularly, in vitro experiment indicated that DOX loaded hollow MIL-100 (Fe) possessed excellent therapeutic effect on MDA-MB-231 breast cancer cells with mitochondrial targeting function. The as-synthesized hollow MIL-100 (Fe) without additional moiety significantly improved the DOX loading capacity compared to traditional drug carriers, and achieved mitochondrial damage and targeting function with such simplified components. Afterwards, we explored the potential of utilizing PCN-333 (Fe) for HRP immobilization and IAA encapsulation to achieve efficient enzyme activated prodrug therapy (EAPT). The creativity of this work lies in the dual loading of enzyme and prodrug in hierarchical cavities to prevent premature activation. As far as we know, it is the first time that MOF-based EAPT system was proved effective by *in vivo* experiments, which makes the results and conclusion more convincing. PCN-333 (Fe) enzyme/prodrug delivery system efficiently generates ROS with the assistance of Fe^{3+} due to Fenton reactions in the tumor microenvironment. As iron-based nanomaterials are most widely applied in biomedical and energy field, the other direction of this thesis mainly focuses on the energy conversion application of iron-based nanomaterials, especially electrochemical catalysis. We optimized Molybdenum-Iron-Cobalt oxyhydroxide with enriched oxygen vacancies by the introduction of molybdenum and iron. The obtained Mo-Fe-Co oxyhydroxide exhibited excellent OER catalytic

performance, which is top-level among all reported transition metal based OER catalysts. Abundant oxygen vacancies contribute to the adsorption of OH^- on the surface of electrocatalysts, resulting in extensive OH^- interaction with metal sites, and modify the electronic structure of the materials to improve electrical conductivity, thus optimizing its dynamics performance of OER. The cation exchange method makes it feasible to produce such OER catalysts in large scale with low cost. Furthermore, we continue to investigate the effect of iron on transition metal sulfides in terms of their overall water splitting catalytic performance. It is found that with the introduction of iron, heterostructure with crystalline/amorphous interface (CAI) can be obtained. Based on materials characterization and HER/OER catalytic performance, the number of CAI is the key factor that impact the overall water splitting catalysis. This finding is further verified by theoretical calculation based on computational simulations. Atoms on CAI exhibited favorable capability for intermediates adsorption and desorption, which is vital in promoting stepwise reactions in the entire water splitting catalytic process.

In summary, the function of iron is significant in the synthesis of iron-based nanomaterials in that it can facilitate the successful synthesis of the material as well as altering the nanostructure. The mechanisms of iron for effective anticancer treatment and electrochemical catalysis are deeply investigated in the presented thesis. However, the presented thesis still has limitations in terms of the following aspects. As the anticancer drug carrier, iron-based nanomaterial needs to overcome the problem of low solubility, which would have a significant impact on its body circulation. The balance between crystallinity and solubility has always been an issue. For instance, metal-organic frameworks with high crystallinity usually have more porous volume to load anticancer drugs while their solubility stay very low, which can be difficult to conduct further cell and animal experiments. Moreover, further optimization on the balance of amorphous phase and crystalline phase of iron-based nanomaterial as bifunctional catalyst for water splitting is required. Amorphous phases can facilitate the electron transfer among active centers. Crystalline phases can favor the catalytic performance toward OER, which also improve the stability of the entire catalyst. Therefore, further research focusing on the balance and relationship between amorphous and crystalline phases is vital for developing highly efficient water splitting catalysts.

6.2 Future direction

Iron-based nanomaterials will be more widely applied in the anticancer treatment due to deeper study of ferroptosis of cancer cells. Novel techniques can be achieved based on the important functions of iron in biomedical fields. For instance, I have successfully synthesized nanoparticles with uniform morphologies based on the coordination between Fe^{2+} and carboxylate groups from G1-Glu-4COOH, which provides an idea of using peptides with symmetric carboxylate groups as organic ligands for further incorporation of properties of different peptides.

1) The direction of using iron-based nanomaterials to induce ferroptosis can be meaningful. Synergistic effect from iron nodes and organic ligands can be employed to damage cancer cells.
2) The direct use of biomolecules such as enzymes, proteins, and peptides as a part of the iron-based nanomaterials will be interesting, which will significantly improve the biocompatibility of iron-based nanomaterials. For instance, G1-Glu-4COOH as a peptide has the function of promoting the proliferation of liver cells. Fe ions can facilitate the working function of liver. Therefore, Fe coordinating with G1-Glu-4COOH can be promising for the application of liver repair.
3) Using peptides with symmetric carboxyl as ligands to coordinate with Fe^{2+} and Fe^{3+} has the potential to fabricate porous bio-frameworks (PBF). For the application of water splitting catalysis, iron-based nanomaterials will have a great value based on the idea of equilibrium of valence state.
4) Future direction can be determined based on the synthesis of a stable Fe-based nanomaterials with equal Fe^{2+} and Fe^{3+} within the material. The hypothesis is that this Fe-based catalyst can be used as a bifunctional catalyst for HER and OER. The loss of electrons of Fe^{2+} will favor the production hydrogen while the gain of electrons of Fe^{3+} will facilitate the generation of oxygen. The dynamic stability of the catalyst will be achieved by the transformation from Fe^{2+} to Fe^{3+} and Fe^{3+} to Fe^{2+} while the absolute composition of Fe^{2+} and Fe^{3+} maintains.

Appendix

Unveiling the Accelerated Water Electrolysis Kinetics of Heterostructural Iron-Cobalt-Nickel Sulfides by Probing into Crystalline/Amorphous Interfaces in Stepwise Catalytic Reactions

Introduction, Significance and Commentary

Transition-metal-based sulfide have been extensively studied for the catalysis hydrogen evolution reaction (HER) due to its active sites and favorable electron transfer. However, the stability of iron-based sulfides and its catalytic reactivity in OER have not been well developed. In this work, heterostructural iron-cobalt-nickel sulfide with crystalline/amorphous interfaces (CAI) was synthesized via an ion-exchange method. The catalytic behavior of CAI in both HER and OER was analyzed by DFT in stepwise catalytic reactions to unveil the catalytic mechanism behind the water splitting catalysis. The experimental results also confirmed that CAI could contribute to the bifunctional catalysis in water splitting.

Publication

This section is presented as the published paper by Z.X. Gu, **Y.C. Zhang**, X.L. Wei, Z.Y. Duan, L. Ren, J.C. Ji, X.Q. Zhang, Y.X. Zhang, Q.Y. Gong, H. Wu, K. Luo, Unveiling the Accelerated Water Electrolysis Kinetics of Heterostructural Iron-Cobalt-Nickel Sulfides by Probing into Crystalline/Amorphous Interfaces in Stepwise Catalytic Reactions. Adv. Sci. 2022, 2201903.

Statement of Authorship

Title of Paper	Unveiling the Accelerated Water Electrolysis Kinetics of Heterostructural Iron-Cobalt-Nickel Sulfides by Probing into Crystalline/Amorphous Interfaces in Stepwise Catalytic Reactions
Publication Status	☑ Published ☐ Accepted for Publication ☐ Submitted for Publication ☐ Unpublished and Unsubmitted work written in manuscript style
Publication Details	Z.X. Gu, **Y.C. Zhang**, X.L. Wei, Z.Y. Duan, L. Ren, J.C. Ji, X.Q. Zhang, Y.X. Zhang, Q.Y. Gong, H. Wu, K. Luo, Unveiling the Accelerated Water Electrolysis Kinetics of Heterostructural Iron-Cobalt-Nickel Sulfides by Probing into Crystalline/Amorphous Interfaces in Stepwise Catalytic Reactions. Adv. Sci. 2022, 2201903. (**IF=17.521**)

Principal Author

Name of Principal Author (Candidate)	Yechuan Zhang		
Contribution to the Paper	Designed the material and experiments, carried out experiments, analyzed experimental results, help to analyse the computational study, and wrote the manuscript.		
Overall percentage (%)	40%		
Certification:	This paper reports on original research I conducted during the period of my Higher Degree by Research candidature and is not subject to any obligations or contractual agreements with a third party that would constrain its inclusion in this thesis. I am the primary author of this paper.		
Signature		Date	09/05/2022

Co-Author Contributions

By signing the Statement of Authorship, each author certifies that:

i. the candidate's stated contribution to the publication is accurate (as detailed above);

ii. permission is granted for the candidate in include the publication in the thesis; and

iii. the sum of all co-author contributions is equal to 100% less the candidate's stated contribution.

Name of Co-Author	Zhengxiang Gu		
Contribution to the Paper	Designed the material and experiments, carried out experiments, analyzed experimental results, and did the computational simulations.		
Signature		Date	09/05/2022

Name of Co-Author	Xuelian Wei		
Contribution to the Paper	Modified the manuscriot.		
Signature		Date	09/05/2022

Name of Co-Author	Zhanyu Duan		
Contribution to the Paper	Figure corrections.		
Signature		Date	09/05/2022

Name of Co-Author	Long Ren		
Contribution to the Paper	Modified the manuscript.		
Signature		Date	09/05/2022

Name of Co-Author	Jiecheng Ji		
Contribution to the Paper	Materials characterization results analysis.		
Signature		Date	09/05/2022

Name of Co-Author	Xiaoqin Zhang		
Contribution to the Paper	Modified the manuscript.		
Signature		Date	09/05/2022

Name of Co-Author	Yuxin Zhang		
Contribution to the Paper	Modified the manuscript, literature review.		
Signature		Date	09/05/2022

Name of Co-Author	Qiyong Gong		
Contribution to the Paper	Modified the manuscript.		
Signature		Date	09/05/2022

Name of Co-Author	Hao Wu		
Contribution to the Paper	Instructions on experiments. Modified the manuscript.		
Signature		Date	09/05/2022

Name of Co-Author	Kui Luo		
Contribution to the Paper	Instructions on the analysis of experimental results. Modified the manuscript.		
Signature		Date	09/05/2022

Please cut and paste additional co-author panels here as required.

ADVANCED SCIENCE Open Access
www.advancedscience.com

Unveiling the Accelerated Water Electrolysis Kinetics of Heterostructural Iron-Cobalt-Nickel Sulfides by Probing into Crystalline/Amorphous Interfaces in Stepwise Catalytic Reactions

Zhengxiang Gu, Yechuan Zhang, Xuelian Wei, Zhenyu Duan, Long Ren, Jiecheng Ji, Xiaoqin Zhang, Yuxin Zhang, Qiyong Gong, Hao Wu, and Kui Luo**

Amorphization and crystalline grain boundary engineering are adopted separately in improving the catalytic kinetics for water electrolysis. Yet, the synergistic effect and advance in the cooperated form of crystalline/amorphous interfaces (CAI) have rarely been elucidated insightfully. Herein, a trimetallic $FeCo(NiS_2)_4$ catalyst with numerous CAI ($FeCo(NiS_2)_4$-C/A) is presented, which shows highly efficient catalytic activity toward both hydrogen and oxygen evolution reactions (HER and OER). Density functional theory (DFT) studies reveal that CAI plays a significant role in accelerating water electrolysis kinetics, in which Co atoms on the CAI of $FeCo(NiS_2)_4$-C/A catalyst exhibit the optimal binding energy of 0.002 eV for H atoms in HER while it also has the lowest reaction barrier of 1.40 eV for the key step of OER. H_2O molecules are inclined to be absorbed on the interfacial Ni atoms based on DFT calculations. As a result, the heterostructural CAI-containing catalyst shows a low overpotential of 82 and 230 mV for HER and OER, respectively. As a bifunctional catalyst, it delivers a current density of 10 mA cm^{-2} at a low cell voltage of 1.51 V, which enables it a noble candidate as metal-based catalysts for water splitting. This work explores the role of CAI in accelerating the HER and OER kinetics for water electrolysis, which sheds light on the development of efficient, stable, and economical water electrolysis systems by facile interface-engineering implantations.

1. Introduction

The exploration of highly active catalysts for water electrolysis (hydrogen and oxygen evolution reactions, HER and OER) is vital to the sustainable production of high-purity hydrogen and oxygen. In pursuit of kinetics-favorable catalysts beyond scarce noble metals and compounds, the activation of electrochemically passive catalysts provides a promising solution. Amorphization,[1,2] defect engineering,[3,4] phase engineering,[5,6] downsizing,[7,8] heterostructure construction,[9,10] and grain boundary engineering[11] have been involved in the design strategies to achieve this goal. Amorphization, among these methods, is capable of improving the catalytic activity due to the increased active sites, rich surface defects, and available dangling bonds in the amorphous phase. Intrinsically, because the lattice distortion and surface dangling bonds in the amorphous phase could favor the generation of active *OOH intermediates of OER, the amorphous counterparts could exhibit

Z. Gu, Y. Zhang, Z. Duan, L. Ren, J. Ji, X. Zhang, Y. Zhang, Q. Gong, K. Luo
Huaxi MR Research Center (HMRRC)
Animal Experimental Center
Department of Radiology
National Clinical Research Center for Geriatrics
Frontiers Science Center for Disease-Related Molecular Network
State Key Laboratory of Biotherapy
West China Hospital
Sichuan University
Chengdu 610041, P. R. China
E-mail: luokui@scu.edu.cn

The ORCID identification number(s) for the author(s) of this article can be found under https://doi.org/10.1002/advs.202201903

DOI: 10.1002/advs.202201903

Y. Zhang
School of Chemical Engineering and Advanced Materials
University of Adelaide
Adelaide, SA 5005, Australia

X. Wei
National Engineering Research Center for Biomaterials
Sichuan University
29 Wangjiang Road, Chengdu 610064, P. R. China

Q. Gong, K. Luo
Functional and Molecular Imaging Key Laboratory of Sichuan Province and Research Unit of Psychoradiology
Chinese Academy of Medical Sciences
Chengdu 610041, P. R. China

H. Wu
Institute of Molecular Sciences and Engineering
Institute of Frontier and Interdisciplinary Science
Shandong University
Qingdao, Shandong 266237, P. R. China
E-mail: haowu2020@sdu.edu.cn

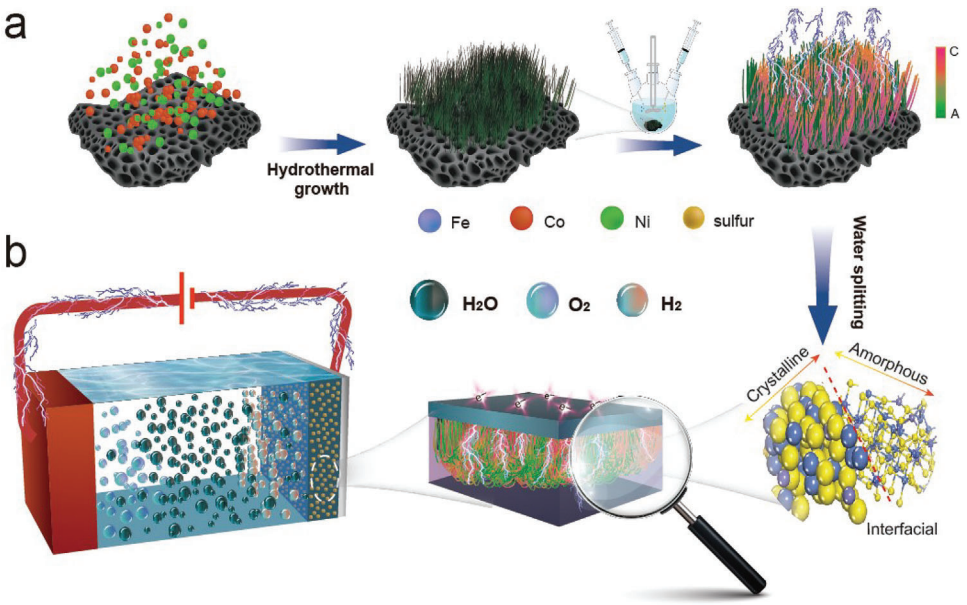

Figure 1. a) Synthesis process for amorphous/crystalline heterostructure $FeCo(NiS_2)_4$-C/A on Ni foam. b) Schematic illustration of $FeCo(NiS_2)_4$-C/A as bifunctional electrocatalysts.

superior activity. For instance, Indra et al.[12] reported that amorphous cobalt iron oxide exhibits better OER performance than their crystalline counterparts under the same electrochemical environment. Liu et al.[13] illustrated that amorphous cobalt could contribute to the transformation of its ultrathin, amorphous and alloyed structure into active phases, leading to optimized electrocatalytic performance for OER. Yet, the poor crystallinity and defective structure of amorphous material would induce high solubility and poor stability in aqueous solution.[14–16]

Though crystalline non-noble transition metal has the advantage in intermediate adsorption free energy, the water dissociation kinetics itself remains sluggish, which is still unsatisfactory for practical alkaline water electrolysis.[17,18] Grain boundaries as bulk defects in polycrystalline materials, on the other hand, could stabilize dislocations and generate high-energy surfaces. This will favor the catalytic kinetics owing to the lattice strain of the catalyst although the active sites in grain boundaries are normally unable to fully exposed.[11,19] As a result, the separate drawbacks of polycrystalline and amorphous materials limit their further performance improvement in water electrolysis. Therefore, it is of importance to develop electrocatalysts with judicious configurations that can maintain stability and fully expose the active sites concurrently for further advance of the performance. Previous research has demonstrated that heterostructural transition-metal based electrocatalysts could favor the catalytic performance. However, most studies have been focused on crystalline grain boundaries and crystalline–crystalline heterostructures, where the character and function of crystalline–amorphous interfaces (CAI) in the catalyst for water electrolysis have scarcely been investigated deeply. It is envisioned that the coexistence of crystalline and amorphous phases in one transition-metal compound in the form of CAI could be a feasible strategy to accelerate the water electrolysis kinetics.[20,21]

Other than interface engineering, the physicochemical properties and electronic structure of the catalyst could be optimized by tuning the components. For example, trimetallic sulfides normally have a lower activation energy than that of monometallic and bimetallic sulfides, which is conducive to electron transfer, thus leading to better electron conductivity.[22–24] Moreover, the synergistic effects between trimetallic ions allow for the modification of electronic structures, which leads to more active sites and faster reaction kinetics in HER/OER.[25–27] Therefore, trimetallic sulfides have more applicable features as electrocatalysts and have the potential to outperform monometallic and bimetallic sulfides in terms of electrocatalytic property.[2,22] Herein, we report a trimetallic crystalline/amorphous co-containing $FeCo(NiS_2)_4$ catalyst (denoted as $FeCo(NiS_2)_4$-C/A), which shows excellent performance toward both HER and OER. This bifunctional $FeCo(NiS_2)_4$-C/A catalyst was obtained via a series of component transformations as illustrated in **Figure 1**a. It originates from cobalt-nickel bimetal (oxy)hydroxides, which were converted into corresponding bimetal sulfides (denoted as $CoNiS_x$) and finally underwent a cation-exchange implementation (details are stated in the Experimental Procedures of the Supporting Information). The as-obtained $FeCo(NiS_2)_4$-C/A is composed of both crystalline and amorphous phases, which form abundant CAI. Owing to their unique heterostructure and CAI, the $FeCo(NiS_2)_4$-C/A exhibits excellent catalytic performances in both HER and OER in alkaline electrolytes (Figure 1b) with fairly low onset overpotentials of 82 and 230 mV, respectively. Density functional theory (DFT) calculations demonstrate that Co atoms on CAI exhibit superior catalytic activity for both HER and OER. Moreover, the bifunctional $FeCo(NiS_2)_4$-C/A catalyst shows outstanding durability and a low operation voltage of 1.51 V to reach 10 mA cm^{-2} in the two-electrode configuration for full water splitting.

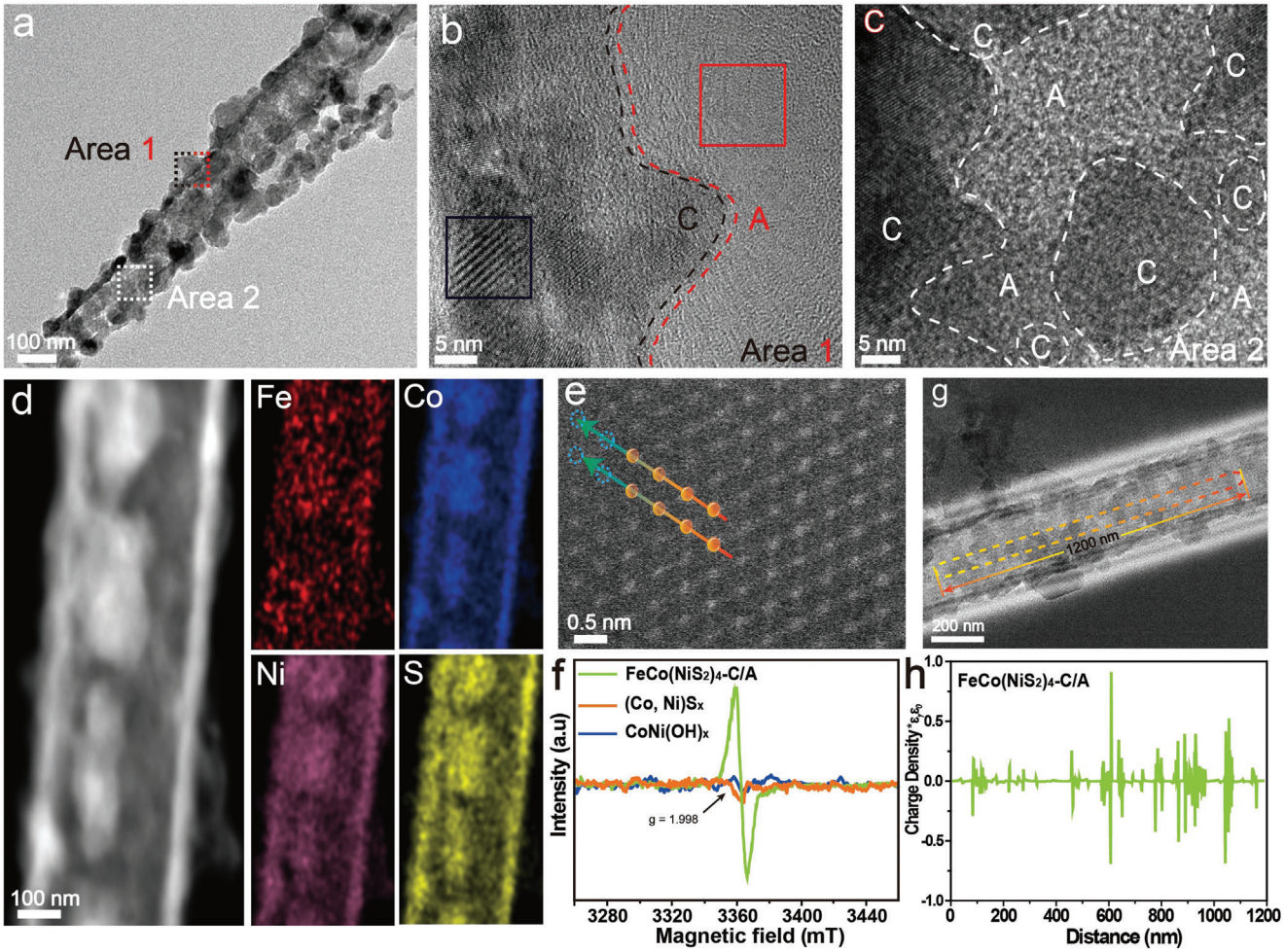

Figure 2. a) TEM of as-prepared $FeCo(NiS_2)_4$-C/A. b,c) High-resolution TEM (HRTEM) image of $FeCo(NiS_2)_4$-C/A sample. d) HAADF-mappings and e) spherical aberration-corrected STEM of $FeCo(NiS_2)_4$-C/A. f) EPR spectra of $CoNi(OH)_x$, $CoNiS_x$, and $FeCo(NiS_2)_4$-C/A. Electron holography of g) $FeCo(NiS_2)_4$-C/A sample and h) corresponding profiles for charge density distributions.

2. Results

2.1. Morphology and Electronic Structure Characterizations

To confirm the composition and crystal structure of $FeCo(NiS_2)_4$-C/A, X-ray powder diffraction (XRD) experiments were conducted. (Figure S1, Supporting Information) exhibits the XRD patterns of $FeCo(NiS_2)_4$-C/A, $CoNiS_x$, and $CoNi(OH)_x$. The XRD pattern of $CoNi(OH)_x$ showed several peaks with extreme low intensity, indicating it was not well grown via certain crystalline planes. As for $CoNiS_x$, few XRD peaks exhibited high intensity, which suggested a poor crystallinity of the material. From scanning electron microscopy (SEM) images in (Figure S2a, Supporting Information), it can be seen that $CoNi(OH)_x$ nanoneedle arrays are uniformly grown on Ni foam with a smooth surface at high magnification (Figure S2b, Supporting Information), indicating the well-prepared bimetallic $CoNi(OH)_x$ nanoneedle arrays are ready as a sacrifice template for the next reaction. After the vulcanization process, the needle-like sample becomes tubular, which is more conducive for $CoNiS_x$ to transport ions (Figure S3, Supporting Information). Next, doping of Fe^{3+} into $CoNiS_x$ was achieved by an ion exchange process with $Fe(NO_3)_3$ at 80 °C, and it can be observed (Figure S4, Supporting Information) that the formed $FeCo(NiS_2)_4$-C/A maintains a nanoneedle morphology of the bimetallic $CoNiS_x$ precursor while the previous smooth surface of the precursor becomes a rough and nanosheet-like structure in the final product. Above all, novel heterostructural (crystalline/amorphous) $FeCo(NiS_2)_4$-C/A were obtained via cation exchange route after incorporating Fe^{3+} into $CoNiS_x$, which would favor both HER and OER. $FeCo(NiS_2)_4$-C/A exhibited tubular structures with a rough surface and the attached flakes, in which dark and light areas can be observed (**Figure 2**a). The high-resolution TEM (HRTEM) image of Figure 2b reveals that the $FeCo(NiS_2)_4$-C/A is composed of crystalline/amorphous mixture, which was also verified by the bright spots (Figure S5a, Supporting Information) and diffused ring (Figure S5b, Supporting Information) in the corresponding selected area of fast Fourier transform (FFT) patterns. Figure 2c confirmed the coexistence of various crystalline and amorphous sections in Area 2, resulting in abundant CAI labeled by dash lines. High-angle annular dark-field scanning transmission electron microscopy (HAADF-TEM) was used to characterize the elemental mapping Fe, Co, Ni,

and S that are homogeneously distributed in the hollow structure of $FeCo(NiS_2)_4$-C/A, and it shows that the material is obtained by cation exchange rather than simple coating (Figure 2d). Spherical aberration-corrected HAADF-STEM images revealed that the $FeCo(NiS_2)_4$-C/A exhibited the typical rhombic phase, where sulfur vacancies sites were observed at the edge of the nanostructure (highlighted as blue dashed circles in Figure 2e). Furthermore, the electron paramagnetic resonance (EPR) spectra of the as-prepared $CoNi(OH)_x$ and $CoNiS_x$ did not present any unpaired electrons. In contrast, for $FeCo(NiS_2)_4$-C/A, a pair of opposite peaks were observed with a signal at $g = 1.998$, suggesting the existence of unpaired electrons due to the sulfur vacancies (Figure 2f).[28,29] Off-axis electron holography was utilized to visualize lattice defects and CAI,[30] and the polarization charge density distribution was also quantified (Figure 2g,h). Compared to $CoNi(OH)_x$ and $CoNiS_x$, $FeCo(NiS_2)_4$-C/A exhibited an obvious fluctuation of negative and positive charge density, confirming a higher CAI density of $FeCo(NiS_2)_4$-C/A (Figures S6 and S7, Supporting Information).

Brunauer–Emmett–Teller (BET) surface area and pore diameter of the three samples are characterized by N_2 sorption isotherm measurements. As plotted in (Figure S8, Supporting Information), the isotherm of $FeCo(NiS_2)_4$-C/A exhibits a typical H3-type hysteresis loop in the relative pressure range of 0.3–0.9 P/P_0 as type IV according to IUPAC protocol.[31] This typical curve demonstrates the mesoporous characteristic of $FeCo(NiS_2)_4$-C/A, and it could be attributed to the porous shell of the hollow-tube structure. Results calculated out of BET equations indicate the surface area of 662.5 $m^2\ g^{-1}$ and the average pore size obtained from Barrett–Joyner–Halenda (BJH) method of $FeCo(NiS_2)_4$-C/A show two mesopore sizes of 8.9 and 13.5 nm. The mesopores of $FeCo(NiS_2)_4$-C/A demonstrate the high surface area and exposure of electrochemically active sites. This structure enables the facile absorption of ions on the surface of electrodes.

X-ray photoelectron spectroscopy (XPS) was applied to investigate the electronic states of metal ions for $FeCo(NiS_2)_4$-C/A as shown in **Figure 3**a–d. The Fe 2p spectra (Figure 3a) show the intensity peaks at 718.1/713.2 and 717.3/711.8 eV, indicating the existence of both Fe^{3+} and Fe^{2+} in the compound.[32] In Co 2p XPS spectra, Co 2p 3/2 and Co 2p 1/2 are located at 779.3/795.1 and 781.3/796.3 eV, respectively.[33] The coexistence of Co^{2+} and Co^{3+} can be revealed from the intensity peaks (Figure 3b). Moreover, for Ni 2p spectra (Figure 3c), two intensity peaks at 855.2/873.1 and 856.9/874.9 eV attributed to Ni 2p 3/2 and Ni 2p 1/2 reveal the valences state of Ni are 2 and 3.[34] Therefore, the above results partially prove that a portion of Co^{2+}, Ni^{2+}, and Fe^{2+} can be oxidized to Co^{3+}, Ni^{3+}, and Fe^{3+} correspondingly. In Figure 3d, the S 2p XPS peaks at 161.2/163.9/166.6 and 168.3 eV are assigned to S^{2-} and SO_x species. It should be noted that the valence state of Fe, Co, and Ni are 2 and 3, which will contribute to the stability of electrode in water splitting in that the valence state could be relatively fixed during the reduction and oxidation circulation on the surface of electrodes.

The X-ray absorption spectroscopy (XAS) measurements were performed to further investigate the coordination environment and the chemical state of metal species (Fe, Co, and Ni) at the atomic level. The X-ray absorption near edge structure (XANES) spectra of three samples and corresponding reference at K-edge are shown in Figure 3e,g,i. The XANES spectra of $FeCo(NiS_2)_4$-C/A and the reference samples at K-edge (Figure 3e) reveal that the line position (absorption edge) of $FeCo(NiS_2)_4$-C/A is located between FeO and Fe_2O_3, which indicates that the valence state of Fe species in $FeCo(NiS_2)_4$-C/A is between Fe^{2+} and Fe^{3+}. The Co K-edge XANES spectra (Figure 3g) show that the Co absorption edge and the green line of $FeCo(NiS_2)_4$-C/A gradually shifts to the higher-energy side compared with Co foil, $CoNiS_x$, and $CoNi(OH)_x$, indicating partial electron transfer from Co to the substitutional Fe or Ni. In the Ni K-edge XANES spectra (Figure 3i), the binding energy of Ni in $FeCo(NiS_2)_4$-C/A is a bit higher than that of $CoNiS_x$ and $CoNi(OH)_x$, implying the average oxidation state of nickel in $FeCo(NiS_2)_4$-C/A is higher than bivalency. The Fourier transform (FT) k^3-weighed extended X-ray absorption fine structure (EXAFS) spectra of three samples are shown in Figure 3f,h,j. The EXAFS spectrum of $FeCo(NiS_2)_4$-C/A shows that the main peak is located at 1.79 Å, which is attributed to the Fe–S coordination in the structure (Figure 3f). In addition, Fe–M bonds in $FeCo(NiS_2)_4$-C/A shift to high-R with relatively weak peak intensity compared to FeO, caused by the lattice distortion. In the Fourier transformed Co K-edge EXAFS of the three samples (Figure 3h), $CoNi(OH)_x$ presents a dominant peak located at ≈1.52 Å because of the Co–O scattering path. Another deviation peak at ≈1.81 Å is also observed, which matches with the Co–S bond length in $FeCo(NiS_2)_4$-C/A and $CoNiS_x$.[35] In addition, the lower intensity of the Co–M (M = Co, Ni, Fe) featured in $FeCo(NiS_2)_4$-C/A verifies the existence of structural distortion (i.e., disordered atoms and dangling bonds) that reduces the surface energy of $FeCo(NiS_2)_4$-C/A and improves the structural durability of the catalyst.[2,15] In the Fourier transform of the Ni K-edge EXAFS spectra of $FeCo(NiS_2)_4$-C/A, $CoNiS_x$, and $CoNi(OH)_x$ (Figure 3j), both Fe–S and Fe–M bonds in $FeCo(NiS_2)_4$-C/A shift to high-R with relatively high peak intensity, which is attributed to the valence state of nickel ($>2^+$). After the introduction of iron, the peak of Ni-M in $FeCo(NiS_2)_4$ did not shift compared to two control groups. The peak of Co–M in $FeCo(NiS_2)_4$ shifted to left by 0.1 Å, indicating the ligancy of Co and other metals increased. At the same time, the peak of Co–S in $FeCo(NiS_2)_4$ shifted to right by 0.05 Å, suggesting the ligancy of Co and S decreased. Therefore, the coordination between Co and S changed after the introduction of Fe, more Co atoms coordinated with Ni and Fe atoms rather than S atoms, thus contributing to the generation of sulfur vacancies. The above results demonstrate that the cation-exchange process led to the formation of defective lattice and coordinatively unsaturated metal centers, which will function as the active sites in OER.[2]

2.2. DFT Calculations of Crystalline/Amorphous Interface

In this work, the DFT and ab initio molecular dynamics (AIMD) simulations are coupled to reveal the high-performance water splitting mechanism of $FeCo(NiS_2)_4$-C/A. Previously reported research lacks theoretical study on the function of CAI in water splitting process, where the completed and accurate construction of CAI model is the key. Herein, we employ the AIMD simulation to establish the $FeCo(NiS_2)_4$-C/A. Experimental results found abundant sulfur vacancies in $FeCo(NiS_2)_4$-C/A, which may explain the formation of amorphous structure. Thus, the sulfur vacancies were created in part I to build the amorphous

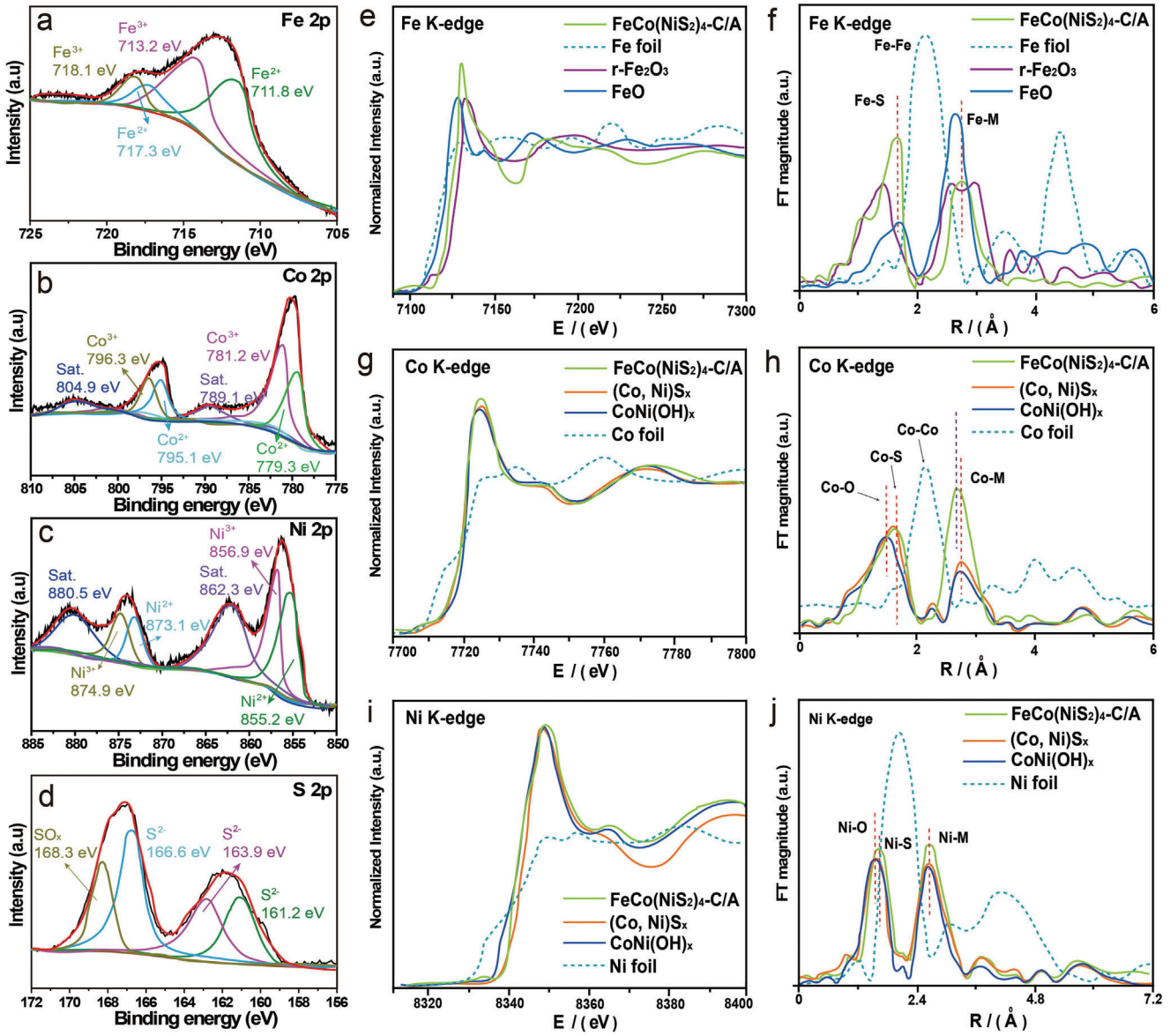

Figure 3. XPS spectra of a) Fe 2p for $FeCo(NiS_2)_4$-C/A; b) Co 2p for $FeCo(NiS_2)_4$-C/A; c) Ni 2p and (d) S 2p for $FeCo(NiS_2)_4$-C/A, respectively. e) Fe K-edge XANES spectra of $FeCo(NiS_2)_4$-C/A, and the standard reference Fe foil and FeO powder. g) Co K-edge XANES spectra of the three samples, and the standard reference Co powder. i) Ni K-edge XANES spectra of the three samples, and the standard reference Ni foil. Fourier-transformed EXAFS spectra at the f) Fe K-edge, h) Co K-edge, and j) Ni K-edge collected for $FeCo(NiS_2)_4$-C/A, $(Co,Ni)S_x$, and $CoNi(OH)_x$, and the corresponding references.

counterpart near CAI in $FeCo(NiS_2)_4$-C/A, shown in (Figure S9a, Supporting Information). After 10 ps MD simulations, the temperature and potential energy tend to be stable (Figure S9b, Supporting Information), confirming the successful formation of amorphous/crystalline heterostructure in $FeCo(NiS_2)_4$-C/A (Figure S9c, Supporting Information). H_2O molecules adsorption behavior regarding different counterparts of $FeCo(NiS_2)_4$-C/A are analyzed to investigate the catalytic kinetics of water splitting. H_2O molecules adsorbed on Ni atoms on the crystalline surface of $FeCo(NiS_2)_4$-C/A (see the position of a1) exhibit an adsorption energy of −0.07 eV (Figure S9d, Supporting Information). At the CAI of $FeCo(NiS_2)_4$-C/A, the H_2O molecule adsorbed on the sulfur atom shows a lower adsorption energy of −0.18 eV, decreased by 0.11 eV (Figure S9e, Supporting Information). The adsorption energy continues to decrease when it comes to the adsorption between H_2O molecules and interfacial Ni atoms (−0.26 eV, Figure S8f, Supporting Information). The adsorption energy then increases to −0.12 eV on Ni atoms on the amorphous surface (Figure S9g, Supporting Information). The above theoretical study indicates that H_2O molecules are inclined to be adsorbed on the CAI of $FeCo(NiS_2)_4$-C/A, especially on the interfacial Ni atoms. To study H atoms adsorption configurations of $FeCo(NiS_2)_4$-C/A heterostructure, different adsorption sites from crystalline to amorphous counterparts are taken into account. For instance, H atom adsorbed on the Ni atom at position e1 has an adsorption energy of 0.53 eV (Figure S8h, Supporting

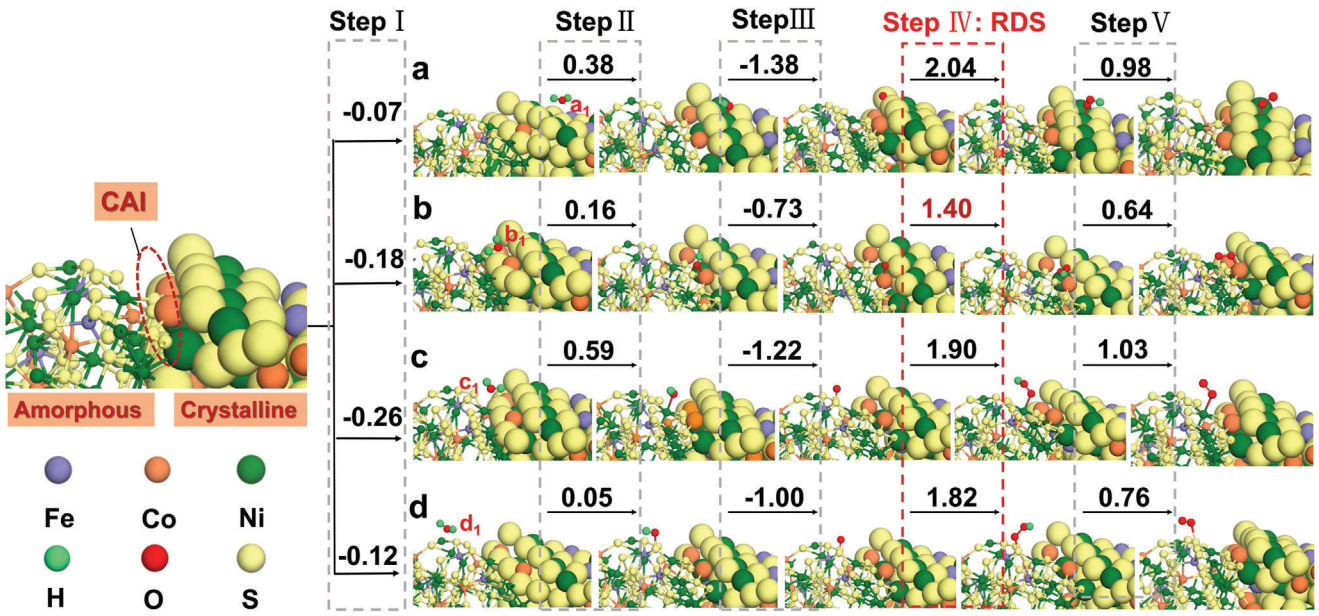

Figure 4. Oxygen evolution reaction (OER) processes on the amorphous/crystalline $FeCo(NiS_2)_4$-C/A heterostructure at a) a_1, b) b_1, c) c_1, and d) d_1 positions, respectively.

Information), suggesting a weak interaction between the H atom and crystalline counterparts of $FeCo(NiS_2)_4$. Co atoms at CAI exhibit a low H-atom adsorption energy of 0.002 eV, favoring both H_2 capture and release (Figure S9i, Supporting Information). When it comes to the adsorption between H atoms and interfacial Ni atoms, the adsorption energy of 0.72 eV (Figure S9j, Supporting Information) indicates H atoms are less prone to interact with interfacial Ni atoms. The S atom on the surface of amorphous counterparts of $FeCo(NiS_2)_4$-C/A has an adsorption energy of 0.2 eV toward the H atom (Figure S9k, Supporting Information). This transition of the H-atom adsorption energy from crystalline to amorphous counterparts through the interface regarding different host atoms demonstrates that Co atoms at CAI will contribute to the better catalytic performance of HER.

The exploration of OER catalytic pathways in terms of different counterparts from the crystalline through CAI to the amorphous (position a_1, b_1, c_1, and d_1) are displayed in **Figure 4**. Step I shows the H_2O molecule adsorption energy. Steps II and III depict the dehydrogenation process of forming *OH and *O species, respectively. Steps IV and V describe the required energy to form *OOH intermediate and O_2. For Step IV, it has a higher reaction energy barrier over other steps in the pathway, defined as the rate-determining step (RDS), which is the key step to perform the OER catalytic process. Position b_1 retains a remarkably lower energy barrier of 1.40 eV in the RDS than other selected positions (Figure 4b). For step I and II, position b_1 at CAI exhibits an excellent activity over the H_2O molecule adsorption and *OH formation, very close to position c_1 and d_1 that possess the best performance of step I and II, respectively (Figure 4c,d). For step III, it is an exothermal reaction, thus this step will not be the barrier of the whole OER pathway. Furthermore, *OOH catalyzed on the position b1 to generate O_2 at step V requires the lowest energy of 0.64 eV in contrast with other catalytic positions. Overall, position b_1 exhibits the leading OER catalytic activity over other selected positions based on the above theoretical study, verifying that CAI will promote the OER process. It is noteworthy that Co atoms at CAI will avail the catalytic activity of OER.

2.3. Electrochemical Water Splitting

These conversions based on the oxidation and reduction of triple metal ions will increase the electrocatalytic capacity compared with $CoNiS_x$ and $CoNi(OH)_x$. The electrocatalytic OER and HER activity were studied via the linear sweep voltammetry (LSV). The electrocatalytic activity of $FeCo(NiS_2)_4$-C/A toward HER was investigated under alkaline electrolyte (1 M KOH) using a three-electrode system (Experimental Section). Polarization curves were measured by LSV with a scan rate of 5 mV s^{-1} under *iR*-correction. In addition, all potentials were converted to those at a reversible hydrogen electrode (RHE) scale. $FeCo(NiS_2)_4$-C/A showed comparable electrocatalytic performance to Pt/C (**Figure 5**). Tafel slope can be used as an indicator of HER and OER activity of catalysts as the smaller Tafel slope represents the faster chemical reaction kinetics. Figure 5b shows the Tafel slope for all samples $FeCo(NiS_2)_4$-C/A (69.57 mV dec^{-1}), $CoNiS_x$ (116.36 mV dec^{-1}), $CoNi(OH)_x$ (176.28 mV dec^{-1}), and Pt/C (51 mV dec^{-1}). The lower Tafel slope of $FeCo(NiS_2)_4$-C/A indicates a faster chemical reaction kinetic of HER.[36] Meanwhile, $FeCo(NiS_2)_4$ only needs an overpotential of 82 mV to reach the current density of −10 mA cm^{-2}, which is 91 and 254 mV lower than that of $CoNiS_x$ and $CoNi(OH)_x$, respectively (Figure 5c). Furthermore, the current density of $FeCo(NiS_2)_4$-C/A can be scaled up to 50 mA cm^{-2} at an overpotential of 198 mV, which can be compared favorably to those reported metal chalcogenides and other earth-abundant electrocatalysts (Table S1, Supporting Information). In addition, the reaction kinetics of the as-synthesized samples were investigated by electrochemical impedance spectroscopy (EIS), shown

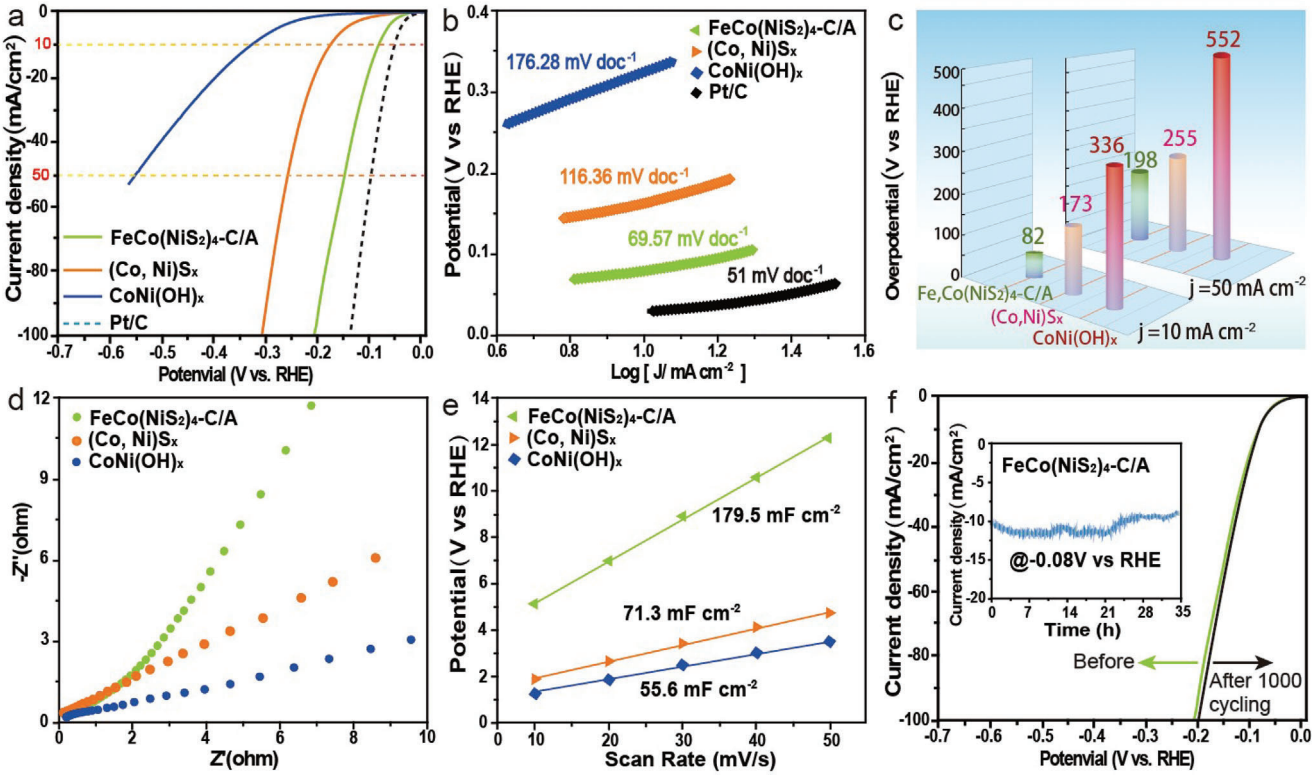

Figure 5. HER performances of as-synthesis catalysis. a) LSV curves of different electrocatalysts in 1.0 M KOH solution. b) Corresponding HER Tafel plots. c) Overpotential histogram of LSV. d) Nyquist plots and e) ECSA estimated by C_{dl} values. f) LSV polarization curves of the $CoFe(NiS_2)_4$-C/A catalyst after 1000 cycles with current density versus time (*i*–*t*) curves of HER for over 35 h shown in the inset.

in Figure 5d. It is clear that $FeCo(NiS_2)_4$-C/A has the smallest R_{ct} value among all samples, implying that the energy barrier of electrode transfer was reduced at the electrode–electrolyte interface, thus leading to the enhanced reaction kinetics. The ratio of the electrochemical active surface (ECSA) to the two-layer capacitance (C_{dl}) can reflect the electrocatalytic activity.[37] To measure the electrochemical property, the ECSA of sample $FeCo(NiS_2)_4$-C/A was further analyzed by cyclic voltammetry (CV) at 1.0 M KOH (Figure S10, Supporting Information). It is revealed by Figure 5e that the C_{dl} value of the $FeCo(NiS_2)_4$-C/A is the top (179.5 mF cm^{-2}) among all samples. This result indicates that $FeCo(NiS_2)_4$-C/A has more reaction surface active sites to be the ideal electrocatalyst corresponding to the LSV results. The durability of the sample of $FeCo(NiS_2)_4$-C/A in the KOH electrolyte was detected by 1000 scanning cycles of the electrocatalyst (Figure 5f). Cyclic stability of $FeCo(NiS_2)_4$-C/A was evaluated by chronopotentiometry at 0.08V versus RHE (Figure 5f, inset). After continuous electrolysis for 35 h, the current density of the $FeCo(NiS_2)_4$-C/A remained with a minor fluctuation, verifying the outstanding HER-stability of $FeCo(NiS_2)_4$-C/A in the strongly alkaline medium, significantly improved compared to $CoNiS_x$ and $CoNi(OH)_x$ (Figure S11, Supporting Information). In addition, $Fe_{0.5}Co(NiS_2)_4$-C/A and $Fe_{1.5}Co(NiS_2)_4$-C/A were synthesized at different amounts of Fe introduced into the compounds and their catalytic performances were evaluated (Figure S12, Supporting Information). The Holo experiment results revealed that $Fe_{0.5}Co(NiS_2)_4$-C/A and $Fe_{1.5}Co(NiS_2)_4$-C/A did exhibit amorphous/crystalline interfaces (Figure S12a–d, Supporting Information). Moreover, $Fe_{0.5}Co(NiS_2)_4$-C/A and $Fe_{1.5}Co(NiS_2)_4$-C/A exhibited poor catalytic performance compared to $FeCo(NiS_2)_4$-C/A. Therefore, the above results indicated that $FeCo(NiS_2)_4$-C/A possesses a superior nanostructure with an appropriate amount of Fe, leading to the best performance in terms of both HER and OER.

The electrocatalytic ability of the $FeCo(NiS_2)_4$-C/A for OER was measured under the same condition as that of HER. The OER performance of $CoNiS_x$, $CoNi(OH)_x$, and IrO_2 on carbon sheet were also tested for comparison. In contrast with IrO_2, $CoNiS_x$, and $CoNi(OH)_x$, $FeCo(NiS_2)_4$-C/A showed a low onset potential of ≈1.46 V (**Figure 6**a,c). At a lower overpotential of 230 mV, the current density of $FeCo(NiS_2)_4$ reached 10 mA cm^{-2} and further increased to 200 mA cm^{-2} rapidly with the lowest overpotential of 292 mV, which is comparable to the reported best OER catalyst. The capacity of $FeCo(NiS_2)_4$-C/A regarding overpotentials is comparable to those of recently reported earth-abundant OER catalysts with high performance (Table S2, Supporting Information). The catalytic kinetics of the presented catalysts was further evaluated by the Tafel slopes (Figure 6b). As expected, $FeCo(NiS_2)_4$-C/A possesses a much smaller Tafel slope of 39.62 mV dec^{-1} than that of $CoNiS_x$, $CoNi(OH)_x$, and IrO_2, suggesting its distinct OER kinetics. The LSV curves (Figure 6d) remained almost unchanged after 1000 cycles, with an error of less than 1%, proving the excellent durability of the $FeCo(NiS_2)_4$-C/A. OER stability of $FeCo(NiS_2)_4$-C/A was tested by chronopotentiometry at 0.08V vs

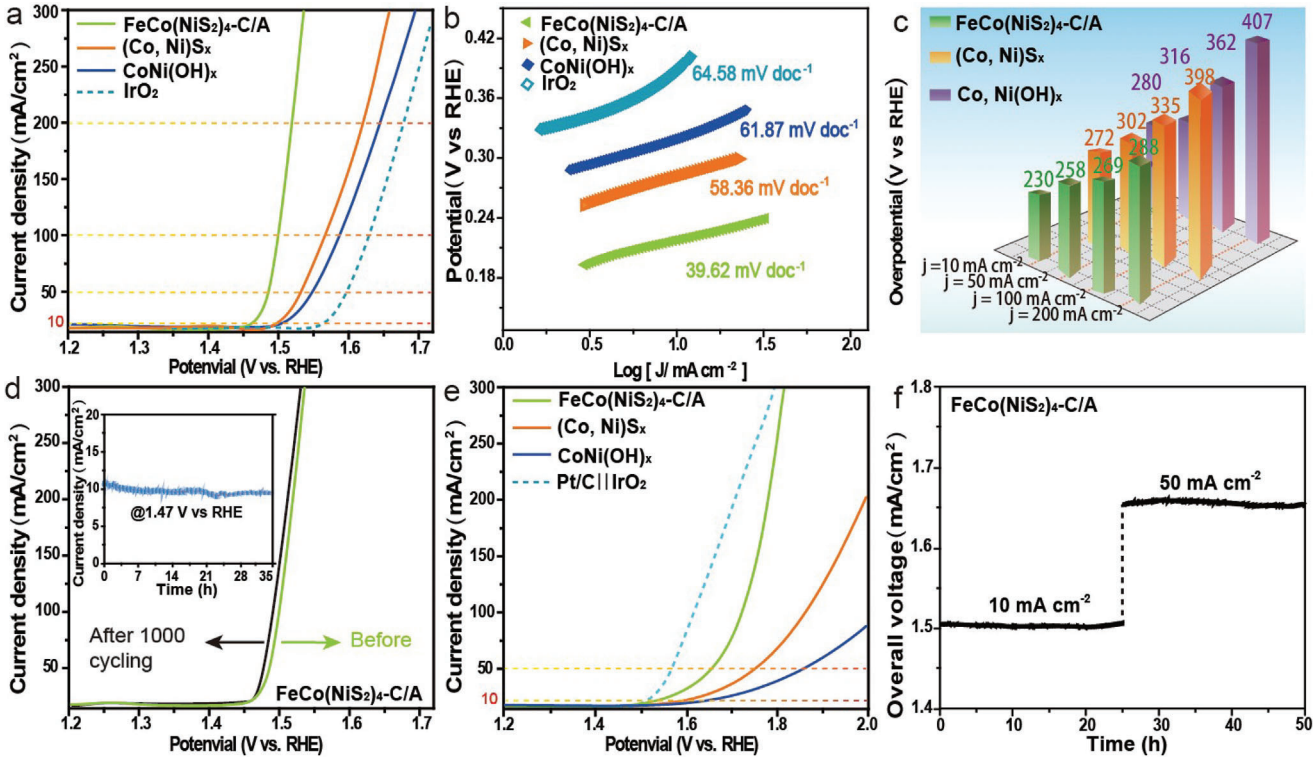

Figure 6. OER performances of as-synthesis catalysis. a) LSV curves of different electrocatalysts in 1.0 M KOH solution. b) Corresponding HER Tafel slopes. c) Overpotential histogram of LSV. d) LSV polarization curves of the $CoFe(NiS_2)_4$-C/A catalyst after 1000 cycles with current density versus time (*i*–*t*) curves of OER for over 35 h shown in the inset. e) $CoFe(NiS_2)_4$-C/A for overall water splitting electrocatalysis in 1 M KOH in two-electrode system. f) Long-term stability tests carried out at 10 and 50 mA cm^{-2} for over 50 h.

RHE in 1 M KOH solution. $FeCo(NiS_2)_4$-C/A exhibited long-term stability as the current density remained stable for 35 h (the inset part in Figure 6d). $CoNiS_x$ and $CoNi(OH)_x$ exhibited lower stability and higher overpotential under the current density of 10 mA cm^{-2} (Figure S13, Supporting Information), further confirming that the stability and OER catalytic performance have been optimized by $FeCo(NiS_2)_4$-C/A. The OER catalytic performance of $FeCo(NiS_2)_4$-C/A is mainly attributed to the high surface area generated by the outer film of nanotubes, the exposed active sites resulting from amorphous structure, and the optimized electroconductivity and charge transfer anchored in the CAI between amorphous and crystalline counterparts. To further verify the stability of $FeCo(NiS_2)_4$-C/A, the testing condition of 50 mA cm^{-2} for 35 h was applied. It is found that $FeCo(NiS_2)_4$-C/A maintained its stability after the 35-h IT test (Figure S14, Supporting Information). Moreover, CAI of $FeCo(NiS_2)_4$-C/A was not transformed or destructed after the stability test, displayed in Figure S15 (Supporting Information).

In order to investigate the effect of CAI on the catalytic performance of water splitting, $FeCo(NiS_2)_4$ with different composition of crystalline and amorphous counterparts were fabricated (denoted as $FeCo(NiS_2)_4$-A^+, $FeCo(NiS_2)_4$-C^+, and $FeCo(NiS_2)_4$-C^{++}). The XRD pattern revealed the crystalline structure and of the above mentioned three samples in Figure S16 (Supporting Information). ECSA results demonstrated the electrochemical active area of $FeCo(NiS_2)_4$-C^+ and $FeCo(NiS_2)_4$-C^{++} in Figure S17 (Supporting Information). Heterostructural $FeCo(NiS_2)_4$ containing more amorphous counterparts and less crystalline counterparts (denoted as $FeCo(NiS_2)_4$-A^+) was fabricated via tuning the reaction condition (Materials Synthesis, Supporting Information) to study the function and mechanism of CAI in water splitting performance. Thin films affiliated to the tubal structure can be seen from (Figure S18a, Supporting Information), exhibiting an amorphous characteristic in the HRTEM image (Figure S18b, Supporting Information). Figure S18c (Supporting Information) shows the boundary of the thin film and hollow tube while the amorphous and crystalline counterparts are clearly revealed by areas A and C in the HRTEM image. Crystalline structure with different crystallinity inside the hollow tube is characterized through divided area C in (Figure S18d, Supporting Information). According to Figure S18e,f (Supporting Information), HER performance of $FeCo(NiS_2)_4$-C/A is superior to $FeCo(NiS_2)_4$-A^+. $FeCo(NiS_2)_4$-C/A showed a lower onset potential of −0.2 V and Tafel slope of 69.57 mV doc^{-1} compared to $FeCo(NiS_2)_4$-A^+. For OER, $FeCo(NiS_2)_4$-A^+ exhibited similar performance to $FeCo(NiS_2)_4$-C/A, and its Tafel slope is 42.25 mV doc^{-1}, which is very close to that of $FeCo(NiS_2)_4$-C/A (39.62 mV doc^{-1}) (Figure S12g,h, Supporting Information). It can be concluded that the amorphous counterpart in $FeCo(NiS_2)_4$ A^+ may contribute to its OER performance. Nevertheless, $FeCo(NiS_2)_4$-C/A possesses outstanding catalytic activity in both HER and OER due to more CAI components.

Heterostructural $FeCo(NiS_2)_4$ containing more crystalline counterparts and less amorphous counterparts ($FeCo(NiS_2)_4$-C^+)

was synthesized by altering the synthesis methodology (Materials Synthesis, Supporting Information) to further demonstrate the importance of CAI in water splitting catalysts. Flake-like structure in the outer part of $FeCo(NiS_2)_4$-C^+ hollow tube (Figure S19a, Supporting Information) is characterized by HRTEM. Crystalline structure dominates in the $FeCo(NiS_2)_4$-C^+ hollow tube, marked as area C in the HRTEM image (Figure S19b, Supporting Information). The HER performance of $FeCo(NiS_2)_4$-C^+ is close to $FeCo(NiS_2)_4$-C/A (Figure S19c, Supporting Information). Tafel slope of $FeCo(NiS_2)_4$-C^+ is 78.25 mV doc^{-1}, a bit higher than that of $FeCo(NiS_2)_4$ C/A (69.57 mV doc^{-1}, Figure S13d, Supporting Information). Overall, the HER catalytic activity of $FeCo(NiS_2)_4$-C^+ is comparable to $FeCo(NiS_2)_4$-C/A. For OER catalysis, $FeCo(NiS_2)_4$-C^+ exhibited a moderate activity compared to $FeCo(NiS_2)_4$-C/A (Figure S13e, Supporting Information). Tafel slope (Figure S19f, Supporting Information) reveals the difference of OER performance between $FeCo(NiS_2)_4$-C/A (39.62 mV doc^{-1}) and $FeCo(NiS_2)_4$-C^+ (60.16 mV doc^{-1}), indicating the crystalline counterpart is more favorable to HER performance. $FeCo(NiS_2)_4$-C/A still outperforms $FeCo(NiS_2)_4$-C^+ in both HER and OER owing to the existence of CAI.

To further demonstrate the function of CAI in water splitting catalysts, the comparison of grain boundaries and CAI regarding HER and OER catalytic performance is addressed. $FeCo(NiS_2)_4$-C^{++} rich in grain boundaries (Figure S20a, Supporting Information) that generated from anisotropic crystalline counterparts is obtained via a multistep synthetic route (Materials Synthesis, Supporting Information). Anisotropic crystalline counterparts are segmented and marked as area C, and grain boundaries are labeled as dot lines on the edge of different area C, characterized by HRTEM (Figure S20b, Supporting Information). $FeCo(NiS_2)_4$ C^{++} rich in grain boundaries showed moderate catalytic activity in HER and OER compared to $FeCo(NiS_2)_4$-C/A with abundant CAI (Figure S20c–f, Supporting Information). Therefore, based on the above discussion of computational study and experimental results, $FeCo(NiS_2)_4$-C/A with abundant CAI surpasses $FeCo(NiS_2)_4$-A^+, $FeCo(NiS_2)_4$-C^+, and $FeCo(NiS_2)_4$-C^{++} in terms of both HER and OER catalysis. The existence of CAI in $FeCo(NiS_2)_4$-C/A is the key factor in improving water splitting efficiency. The significance of CAI in optimizing the bifunctional water splitting catalysts is conclusive. The stability of $FeCo(NiS_2)_4$-C/A, $FeCo(NiS_2)_4$-C^+, and $FeCo(NiS_2)_4$-C^{++} was investigated at a current density of 10 mA cm^{-2} for 75 h. All samples maintained its stability before 40 h. Minor difference was observed after comparing all samples with different compositions of crystalline counterparts from 40 to 75 h (Figure S21, Supporting Information), indicating great stability $FeCo(NiS_2)_4$-C/A at a current density of 10 mA cm^{-2}. The stability of $FeCo(NiS_2)_4$-C/A, $FeCo(NiS_2)_4$-C^+, and $FeCo(NiS_2)_4$-C^{++} was also studied at a current density of 50 mA cm^{-2} for 75 h. $FeCo(NiS_2)_4$-C/A maintained its stability before 40 h. $FeCo(NiS_2)_4$-C^+ and $FeCo(NiS_2)_4$-C^{++} with more crystalline counterparts exhibited better stability for 75 h (Figure S22, Supporting Information). The stability results confirmed that a high percentage of crystalline in the nanomaterial favors long-term stability of the catalyst, and the stability of $FeCo(NiS_2)_4$-C/A at a higher current density is stronger than that at a lower current density.[16,38]

Single $FeCo(NiS_2)_4$-C/A electrode bifunctionally catalyzing both HER and OER could greatly simplify the water splitting system and reduce the production cost. Encouraged by the impressive catalytic activity of the $FeCo(NiS_2)_4$-C/A in terms of both HER and OER, we then assembled a water electrolyzer employing the $FeCo(NiS_2)_4$-C/A as anode and cathode for overall water splitting test in 1 M KOH. The $CoNiS_x||CoNiS_x$, $CoNi(OH)_x||CoNi(OH)_x$, and $Pt/C||IrO_2$ were all loaded on the carbon sheet to be compared as control groups. As shown in Figure 6e, water splitting catalyzed by $CoNi(OH)_x$ and $CoNiS_x$ requires cell voltages of 1.65 and 1.59 V to drive 10 mA cm^{-2}, respectively. In contrast, the cell voltage demanded for $FeCo(NiS_2)_4$-C/A is as low as 1.51 V, quite close to that of $Pt/C||IrO_2$ (1.5 V). It is noteworthy that $FeCo(NiS_2)_4$-C/A electrodes can drive high current densities (e.g., 300 mA cm^{-2}) at cell voltages that are comparable to those of $Pt/C||IrO_2$, which is beneficial to practical H_2 production, making itself a competitive electrocatalyst for water splitting (Table S3, Supporting Information). In addition, $FeCo(NiS_2)_4$-C/A also showed potent durability, tested by the chronopotentiometry for over 50 h (Figure 6f). The cell voltage of $FeCo(NiS_2)_4$-C/A regarding HER/OER remained stable for 50 h. The current density was increased from 10 to 50 mA cm^{-2} after 25 h of operation. The faradaic efficiency of $FeCo(NiS_2)_4$ was calculated to be ≈97% by comparing the experimental H_2/O_2 production with theoretical values (Figure S23, Supporting Information).

3. Conclusion

In summary, $FeCo(NiS_2)_4$-C/A with abundant CAI that possesses an outstanding catalytic performance of water electrolysis has been constructed via a cation-exchange route. The incorporation of Fe ions not only tunes the amorphous/crystalline heterogeneity that induces rich surface defects, the exposure of active sites, and a higher density of CAI, but also alters the morphology of $FeCo(NiS_2)_4$-C/A to hollow nanotubes with porous structure, favoring the ion exchange and charge transfer in water splitting. Consequently, the heterostructural $FeCo(NiS_2)_4$-C/A presents low overpotentials, high current densities, and prominent stability for both HER and OER. The overall current density of 10 mA cm^{-2} can be achieved at a low cell voltage of 1.51 V using $FeCo(NiS_2)_4$-C/A as electrodes in 1 M KOH. Based on rigorous experimental and computational studies, the superiority and function of CAI in bifunctional $FeCo(NiS_2)_4$-C/A electrocatalysts have been demonstrated, explaining the kinetics behind the excellent performance of $FeCo(NiS_2)_4$-C/A in water electrolysis. The presented work pointed out the value of CAI of electrocatalysts, which may give a direction on the path of designing the ideal electrocatalysts for water splitting.

Supporting Information

Supporting Information is available from the Wiley Online Library or from the author.

Acknowledgements

The authors would like to thank the Analytical and Testing Center of Sichuan University for morphology characterization work, and the authors

are grateful to Dr. Yong Liu for her help of SEM analysis and Dr. Shanling Wang for her assistance of TEM analysis. The authors would like to thank Shuyi Kong (Ph.D.) from Shanghai Institute of Ceramics, Chinese Academy of Sciences and Ximeng Lv (Ph.D.) from Fudan University for his help of XRD data analysis. This research was financially supported by the National Natural Science Foundation of China (51873120, 52073193, 81621003), 1 3 5 project for disciplines of excellence, West China Hospital, Sichuan University (ZYJC21013), and TheFundamental Research Funds for the Central Universities (20826041E4067).

Conflict of Interest

The authors declare no conflict of interest.

Data Availability Statement

The data that support the findings of this study are available from the corresponding author upon reasonable request.

Keywords

crystalline/amorphous interfaces, electrocatalysis, heterostructures, water splitting

Received: June 8, 2022
Revised: July 20, 2022
Published online:

[1] J. Cui, P. Li, J. Zhou, W. Y. He, X. Huang, J. Yi, J. Fan, Z. Ji, X. Jing, F. Qu, Z. G. Cheng, C. Yang, L. Lu, K. Suenaga, J. Liu, K. T. Law, J. Lin, Z. Liu, G. Liu, *Nat. Commun.* **2019**, *10*, 2044.
[2] M. Kuang, D. Liu, H. Tan, K. N. Dinh, L. Yang, H. Ren, W. Huang, W. Fang, J. Yao, Q. Yan, *Adv. Energy Mater.* **2020**, *10*, 2002215.
[3] Y. Zhou, J. Zhang, E. Song, J. Lin, J. Zhou, K. Suenaga, W. Zhou, Z. Liu, J. Liu, J. Lou, H. J. Fan, *Nat. Commun.* **2020**, *11*, 2253.
[4] H. Wang, X. Xiao, S. Liu, C. L. Chiang, X. Kuai, C. K. Peng, Y. C. Lin, X. Meng, J. Zhao, J. Choi, Y. G. Lin, J. M. Lee, L. Gao, *J. Am. Chem. Soc.* **2019**, *141*, 18578.
[5] W. Zhang, X. Liao, X. Pan, M. Yan, Y. Li, X. Tian, Y. Zhao, L. Xu, L. Mai, *Small* **2019**, *15*, 1900964.
[6] Q. Tang, D.-E. Jiang, *ACS Catal.* **2016**, *6*, 4953.
[7] Y. Yang, H. Fei, G. Ruan, J. M. Tour, *Adv. Mater.* **2015**, *27*, 3175.
[8] R. Ma, Y. Zhou, Y. Chen, P. Li, Q. Liu, J. Wang, *Angew. Chem., Int. Ed.* **2015**, *54*, 14723.
[9] X. Li, Y. Wang, J. Wang, Y. Da, J. Zhang, L. Li, C. Zhong, Y. Deng, X. Han, W. Hu, *Adv. Mater.* **2020**, *32*, 2003414.
[10] D. Gao, R. Liu, J. Biskupek, U. Kaiser, Y. F. Song, C. Streb, *Angew. Chem., Int. Ed.* **2019**, *58*, 4644.
[11] R. G. Mariano, K. McKelvey, H. S. White, M. W. Kanan, *Science* **2017**, *358*, 1187.
[12] A. Indra, P. W. Menezes, N. R. Sahraie, A. Bergmann, C. Das, M. Tallarida, D. Schmeißer, P. Strasser, M. Driess, *J. Am. Chem. Soc.* **2014**, *136*, 17530.
[13] J. Liu, Y. Ji, J. Nai, X. Niu, Y. Luo, L. Guo, S. Yang, *Energy Environ. Sci.* **2018**, *11*, 1736.
[14] G. Wu, X. Zheng, P. Cui, H. Jiang, X. Wang, Y. Qu, W. Chen, Y. Lin, H. Li, X. Han, Y. Hu, P. Liu, Q. Zhang, J. Ge, Y. Yao, R. Sun, Y. Wu, L. Gu, X. Hong, Y. Li, *Nat. Commun.* **2019**, *10*, 4855.
[15] A. Bergmann, T. Jones, T. Moreno, D. Teschner, P. Chernev, M. Gliech, T. Reier, H. Dau, P. Strasser, *Nat. Catal.* **2018**, *1*, 711.
[16] J. Xie, H. Zhang, S. Li, R. Wang, X. Sun, M. Zhou, J. Zhou, X. W. Lou, Y. Xie, *Adv. Mater.* **2013**, *25*, 5807.
[17] X. Chen, Q. Li, Q. Che, Y. Chen, X. Xu, *ACS Sustainable Chem. Eng.* **2019**, *7*, 2437.
[18] K. Ji, H. Arandiyan, P. Liu, L. Zhang, J. Han, Y. Xue, J. Hou, H. Dai, *Nano Energy* **2016**, *27*, 515.
[19] X. She, X. Zhu, Y. S. J. Yang, Y. She, D. Liu, J. Wu, Q. Yu, H. Li, Z. Liu, P. M. Ajayan, H. Xu, *Nano Energy* **2021**, *84*, 105869.
[20] C. Wan, B. M. Leonard, *Chem. Mater.* **2015**, *27*, 4281.
[21] X. Peng, L. Hu, L. Wang, X. Zhang, J. Fu, K. Huo, L. Y. S. Lee, K.-Y. Wong, P. K. Chu, *Nano Energy* **2016**, *26*, 603.
[22] T. Jiang, P. Dai, W. Zhang, M. Wu, *Electrochim. Acta* **2021**, *373*, 137903.
[23] H. Z. Yang, B. Wang, H. Y. Li, B. Ni, K. Wang, Q. Zhang, X. Wang, *Adv. Energy Mater.* **2018**, *8*, 1801839.
[24] W. H. Luo, X. X. Cao, S. Q. Liang, J. W. Huang, Q. Su, Y. Wang, G. Z. Fang, L. T. Shan, J. Zhou, *ACS Appl. Energy Mater.* **2019**, *2*, 4567.
[25] J. Liu, J. Nai, T. You, P. An, J. Zhang, G. Ma, X. Niu, C. Liang, S. Yang, L. Guo, *Small* **2018**, *14*, 1703514.
[26] L. Kuai, J. Geng, C. Chen, E. Kan, Y. Liu, Q. Wang, B. Geng, *Angew. Chem., Int. Ed.* **2014**, *53*, 7547.
[27] R. D. Smith, M. S. Prévot, R. D. Fagan, Z. Zhang, P. A. Sedach, M. K. J. Siu, S. Trudel, C. P. Berlinguette, *Science* **2013**, *340*, 60.
[28] C. Peng, G. Luo, J. Zhang, M. Chen, Z. Wang, T.-K. Sham, L. Zhang, Y. Li, G. Zheng, *Nat. Commun.* **2021**, *12*, 1580.
[29] X. Wang, Y. Zhang, H. Si, Q. Zhang, J. Wu, L. Gao, X. Wei, Y. Sun, Q. Liao, Z. Zhang, K. Ammarah, L. Gu, Z. Kang, Y. Zhang, *J. Am. Chem. Soc.* **2020**, *142*, 4298.
[30] Z. Gu, H. Shen, Z. Cheng, Y. Yang, C. Yang, Y. Ji, Y. Wang, C. Zhu, J. Liu, J. Li, T.-K. Sham, X. Xu, G. Zheng, *Joule* **2021**, *5*, 429.
[31] Z. Li, M. Shao, L. Zhou, R. Zhang, C. Zhang, M. Wei, D. G. Evans, X. Duan, *Adv. Mater.* **2016**, *28*, 2337.
[32] J. Liu, J. Wang, B. Zhang, Y. Ruan, L. Lv, X. Ji, K. Xu, L. Miao, J. Jiang, *ACS Appl. Mater. Interfaces* **2017**, *9*, 15364.
[33] X. Gao, Y. Zhao, K. Dai, J. Wang, B. Zhang, X. Shen, *Chem. Eng. J.* **2020**, *384*, 123373.
[34] J. Yang, C. Yu, C. Hu, M. Wang, S. Li, H. Huang, K. Bustillo, X. Han, C. Zhao, W. Guo, Z. Zeng, H. Zheng, J. Qiu, *Adv. Funct. Mater.* **2018**, *28*, 1803272.
[35] J. Zhang, Y. Zhao, C. Chen, Y.-C. Huang, C.-L. Dong, C.-J. Chen, R.-S. Liu, C. Wang, K. Yan, Y. Li, G. Wang, *J. Am. Chem. Soc.* **2019**, *141*, 20118.
[36] K. Tu, D. Tranca, F. Rodriguez-Hernandez, K. Jiang, S. Huang, Q. Zheng, M. X. Chen, C. Lu, Y. Su, Z. Chen, H. Mao, C. Yang, J. Jiang, H. W. Liang, X. Zhuang, *Adv. Mater.* **2020**, *32*, 2005433.
[37] X. Cao, E. Johnson, M. Nath, *ACS Sustainable Chem. Eng.* **2019**, *7*, 9588.
[38] Y. Zhou, W. Hao, X. Zhao, J. Zhou, Y.u H, B. Lin, Z. Liu, S. J. Pennycook, S. Li, H. Fan, *Adv. Mater.* **2022**, *34*, 2100537.

